

Investigations of Interactions in The Earth's Upper  
Atmosphere Using Optical and Radio Wave Techniques

A THESIS

submitted to

SARDAR PATEL UNIVERSITY

For the Award of

DOCTOR OF PHILOSOPHY

in Physics

by

Ravindra Pratap Singh

Under the Supervision of

Prof. Duggirala Pallamraju

Space and Atmospheric Sciences Division

Physical Research Laboratory

Ahmedabad, India

Dr. N. K. Bhatt

Department of Physics

Sardar Patel University

Vallabh Vidyanagar, India

November 2017



Date: 07/11/2017

## CERTIFICATE

Certified that the work incorporated in this Thesis entitled “**Investigations of Interactions in The Earth’s Upper Atmosphere Using Optical and Radio Wave Techniques**” submitted by **Mr. Ravindra Pratap Singh** comprises the result of independent and original investigations carried out. The materials obtained from other sources and used in the thesis have been acknowledged appropriately. The work contained in this thesis has not been submitted for the award of any other degree/diploma anywhere.

Place: Vallabh Vidyanagar

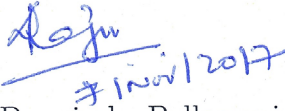
Date: 07/11/2017

Registration No.: 557, date: 16/10/2012



Ravindra Pratap Singh  
(Research Student)

Certified that the work mentioned above was carried out under my/our guidance.



Prof. Duggirala Pallamraju  
(Research Guide)

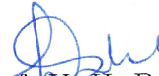


Prof. N. K. Bhatt  
(Research Co-Guide)

Forwarded Through:



Prof. P. Janardhan  
Dean  
PRL, Ahmedabad



Prof. U. H. Patel  
Head, Department of Physics  
Sardar Patel University  
Vallabh Vidyanagar - 388 120



प्रो. जनार्दन पद्मनाभन  
**Prof. Janardhan Padmanabhan**  
डीन, भौतिक अनुसंधान प्रयोगशाला  
Dean, Physical Research Laboratory  
(भारत सरकार, अंतरिक्ष विभाग की यूनिट)  
(Unit of Department of Space, Govt. of India)  
नवरंगपुरा, अहमदाबाद-380 009 भारत  
Navrangpura, Ahmedabad-380 009 India

**HEAD**  
**DEPARTMENT OF PHYSICS**  
**SARDAR PATEL UNIVERSITY**  
**VALLABH VIDYANAGAR**



*Dedicated to*  
*Mummy-Papa*  
*and*  
*Garima-Aanya-Aashvi*



# Contents

<b>List of Tables</b>	<b>xiii</b>
<b>List of Figures</b>	<b>xv</b>
<b>Acknowledgment</b>	<b>xxi</b>
<b>Abstract</b>	<b>xxvii</b>
<b>List of publications</b>	<b>xxxix</b>
<b>1 Introduction</b>	<b>1</b>
1.1 Background . . . . .	1
1.2 The Mesosphere and Lower Thermosphere (MLT) Dynamics . . .	3
1.3 Temperature and Wind Dynamics in MLT Region . . . . .	6
1.4 Wave Dynamics . . . . .	12
1.5 Short Time Scale Variations in MLT region . . . . .	15
1.5.1 Gravity Waves (GWs) . . . . .	15
1.5.2 Topographic Generation . . . . .	18
1.5.3 Convective Activity Generation . . . . .	19
1.5.4 Wind Shear Generation . . . . .	20
1.5.5 Atmospheric Tides . . . . .	21
1.5.6 Planetary Waves (PWs) . . . . .	22
1.6 Long Time Scale Oscillations in the MLT region . . . . .	25
1.7 Sudden Stratospheric Warming (SSW) . . . . .	28

1.8	Mesospheric Inversion Layers (MILs)	31
1.9	Measurement Techniques for MLT investigation	33
1.9.1	Ground-based Techniques	33
1.9.2	Rocket-borne Techniques	35
1.9.3	Satellite-based Techniques	35
1.10	Airglow emissions in MLT region	36
1.10.1	OI 557.7 nm Green Line Emission	39
1.10.2	O <sub>2</sub> (0–1) Atmospheric Band Emission	39
1.10.3	NaD Line Emission	41
1.10.4	OH Meinel Band Emission	42
1.11	Scientific Questions Addressed	42
1.12	Scope and Layout of the Thesis	43
<b>2</b>	<b>Instrumentation and Data Analysis</b>	<b>49</b>
2.1	Introduction	49
2.2	Near InfraRed Imaging Spectrograph (NIRIS)	50
2.2.1	Primary mirror	52
2.2.2	Secondary Mirror and slit assembly	52
2.2.3	Off-axis Paraboloid	53
2.2.4	Diffraction Grating	53
2.2.5	Converging Optics	54
2.2.6	Detector and Data Acquisition System	54
2.3	Calibration of NIRIS	55
2.3.1	Wavelength Calibration	55
2.3.2	Angle Calibration	57
2.4	Mesospheric Nightglow Intensity Determination	58
2.5	Derivation of Mesospheric Temperatures	61
2.5.1	OH(6-2) Meinel Band Emission	62
2.5.2	O <sub>2</sub> (0-1) Atmospheric Band Emission	64



2.5.3	Nocturnal Variation in OH(6-2) and O <sub>2</sub> (0-1) Band Intensities and Temperatures . . . . .	65
2.6	NIRIS and SABER Temperatures Comparison . . . . .	67
2.7	CCD-based Multi-wavelength Airglow Photometer (CMAP) . . . . .	69
2.7.1	Optical Configuration of CMAP . . . . .	69
2.7.2	Filters and Filter Wheel Assembly . . . . .	71
2.7.3	Detector and Data Acquisition System . . . . .	74
2.7.4	Derivation of Nightglow Emission Intensities . . . . .	75
2.8	Supplementary Datasets . . . . .	75
2.8.1	Sounding of the Atmosphere using Broadband Emission Radiometry (SABER) . . . . .	75
2.8.2	Optical Spectrograph and Infrared Imaging System (OSIRIS) . . . . .	77
2.8.3	Solar Occultation For Ice Experiment (SOFIE) . . . . .	77
2.8.4	Kalpana-1 . . . . .	78
2.8.5	Modern Era Retrospective-analysis for Research and Application (MERRA) . . . . .	78
2.8.6	F10.7 cm Radio Flux and SSN Numbers . . . . .	79
2.9	Time Series Analysis (TSA) Methods . . . . .	79
2.9.1	Lomb-Scargle Analysis . . . . .	80
2.9.1.1	Fast Computation of Lomb-Scargle Periodogram . . . . .	81
2.9.1.2	Phase and Amplitude Spectra . . . . .	82
2.9.1.3	Uncertainty in the frequency . . . . .	83
2.9.1.4	REDFIT . . . . .	84
2.9.2	Wavelet Analysis . . . . .	84
2.9.2.1	Continuous Wavelet Transform (CWT) . . . . .	85
2.9.2.2	Wavelet Functions . . . . .	86
2.9.2.3	Wavelet Power Spectrum . . . . .	87
2.9.2.4	Cone of Influence (COI) . . . . .	87
2.9.2.5	Significance Levels . . . . .	88
2.10	Wave Characteristics using NIRIS data . . . . .	88

2.10.1	Derivation of Wave Period ( $\tau$ ) . . . . .	89
2.10.2	Derivation of vertical phase speed ( $c_z$ ) and vertical wave-length ( $\lambda_z$ ) . . . . .	91
2.10.3	Derivation of Meridional Wavelength ( $\lambda_y$ ) . . . . .	93
2.10.4	Wavelet Spectrum . . . . .	95
2.11	Schematic of the Wave Propagation . . . . .	96
2.12	Summary . . . . .	98
<b>3</b>	<b>Large- and Small-Timescale Variations in the MLT region</b>	<b>101</b>
3.1	Background . . . . .	101
3.2	Data set . . . . .	102
3.3	Large-time Scale Variations . . . . .	103
3.3.1	Introduction . . . . .	103
3.3.2	Results and Discussion . . . . .	105
3.3.3	Conclusion of Large-Time Scale Variations . . . . .	112
3.4	Short-Time Scale Variations . . . . .	113
3.4.1	Introduction . . . . .	113
3.4.2	Results and Discussion . . . . .	115
3.4.3	Conclusion of Short-Time Scale Variations . . . . .	123
3.5	Summary . . . . .	125
<b>4</b>	<b>Vertical Coupling of the Atmospheres</b>	<b>127</b>
4.1	Background . . . . .	127
4.2	Introduction . . . . .	129
4.3	Data set . . . . .	133
4.3.1	Spectroscopic Observations . . . . .	134
4.3.2	Photometric Observations . . . . .	134
4.3.3	Outgoing Longwave Radiation (OLR) Measurements . . . . .	135
4.4	Observations . . . . .	135
4.4.1	Tropospheric activity . . . . .	135
4.4.2	Activity in MLT region . . . . .	137

4.5	Data Analyses and Results . . . . .	140
4.5.1	Wave Period ( $\tau$ ) . . . . .	140
4.5.2	Vertical Phase Speed ( $c_z$ ) and Vertical Wavelength ( $\lambda_z$ ) .	146
4.6	Discussion . . . . .	147
4.7	Conclusion of Vertical Coupling of Atmospheres During Cyclone Nilofar . . . . .	155
4.8	Anomalous Increase in O <sub>2</sub> Temperatures . . . . .	157
4.8.1	Introduction . . . . .	157
4.8.2	Observations . . . . .	159
4.8.3	Results . . . . .	160
4.9	Summary . . . . .	163
<b>5</b>	<b>Mesospheric Temperature Variations During SSW Events</b>	<b>165</b>
5.1	Background . . . . .	165
5.2	Introduction . . . . .	166
5.3	Measurement Techniques . . . . .	168
5.4	Observations . . . . .	169
5.4.1	NIRIS Temperatures for January 2013 . . . . .	169
5.4.2	MERRA Temperatures and Winds for 2004-2013 . . . . .	172
5.5	Results and Discussion . . . . .	172
5.5.1	SABER, OSIRIS, and SOFIE Temperatures for 2009 and 2013 SSW Events . . . . .	174
5.5.2	SABER Temperatures for 2006 and 2010 Major SSW Events . . . . .	177
5.5.3	SABER Temperatures for 2011 and 2012 Minor SSW Events . . . . .	178
5.5.4	SABER Temperatures for 2008 SSW Events . . . . .	179
5.5.5	Difference in Stratospheric vs Mesospheric Temperatures for 2009 and 2013 SSW Events . . . . .	181

5.5.6	$\Delta T_S$ vs $\Delta T_M$ for Major and Minor SSW Events from SABER Data . . . . .	183
5.5.7	$\Delta T_S$ vs $\Delta T_M$ for Major SSW events from SOFIE and OSIRIS Data . . . . .	186
5.5.8	Slope ( $\Delta T_M/\Delta T_S$ ) vs Geographic Latitude for Major and Minor SSW Events . . . . .	187
5.5.9	Relationship between SRL with $T_{Smax}$ and D with $T_{Smax}$	190
5.5.10	SABER vs CIRA Temperatures Comparison During SSW Events . . . . .	192
5.6	Summary and Conclusion . . . . .	195
<b>6</b>	<b>Summary and Scope for Future Work</b>	<b>197</b>
6.1	Summary and Conclusions . . . . .	197
6.1.1	Atmospheric Waves and Coupling in the Earths Upper Atmosphere . . . . .	199
6.1.2	Solar Influences in the MLT Nightglow Emissions and Temperatures . . . . .	200
6.1.3	Mesospheric Temperature Inversions and their Possible Sources . . . . .	200
6.1.4	Global Mesospheric Temperatures During SSW Events .	201
6.1.5	Techniques to Measure MLT Nightglow Emission Intensities and Temperatures . . . . .	202
6.2	Scope for Future Work . . . . .	203
	<b>Bibliography</b>	<b>207</b>

# List of Tables

1.1	Different types of oscillations/waves in the low-latitude middle atmosphere. . . . .	14
1.2	Different types of airglow emissions . . . . .	37
2.1	Characteristics of Near Infrared Imaging Spectrograph (NIRIS)	52
5.1	List of SSW events considered for this study . . . . .	174



# List of Figures

1.1	Schematic of lower and middle atmosphere showing thermal and dynamical structure [Adapted from Meriwether and Gerrard, 2004]. . . . .	5
1.2	Vertical distribution of heating rates due to absorption of solar short wave radiation [Adapted from <i>London (1980)</i> ]. . . . .	7
1.3	Zonal mean temperature from SABER retrievals and from WACCM [Adapted from <i>Smith (2012a)</i> ]. . . . .	9
1.4	Zonal mean zonal wind from the URAP climatology and simulated by WACCM [Adapted from <i>Smith (2012a)</i> ]. . . . .	11
1.5	A Summary of atmospheric waves [Adapted from <i>Lin (2007)</i> ]. . . . .	13
1.6	A surrealistic representation of atmospheric gravity waves [Adapted from <i>Hines (1974)</i> ]. . . . .	16
1.7	Vertical distribution of the amplitude of the MQBO, MSAO, SSAO, SQBO, and annual component at the equator [Adapted from <i>Baldwin et al. (2001)</i> ]. . . . .	27
1.8	Temperature and zonal wind for 2013 SSW event . . . . .	29
1.9	Schematic of upper and lower mesospheric inversion layers [Adapted from <i>Meriwether and Gerrard (2004)</i> ]. . . . .	32
1.10	Red, green, and yellow airglow emission from the Earth's upper atmosphere photographed by the International Space Station. ( <a href="http://auroranightglow.blogspot.in/2012/05/night-glow.html">http://auroranightglow.blogspot.in/2012/05/night-glow.html</a> ) . . . . .	37

1.11	Schematic of the peak emission altitudes for the various nightglow emissions in the MLT region. . . . .	38
1.12	Schematic of the simplified energy level diagram along with various emissions of the atomic oxygen. . . . .	40
2.1	(a) Optical layout of Near InfraRed Imaging Spectrograph (NIRIS) [ <i>Singh and Pallamraju (2017a)</i> ]. . . . .	51
2.2	Schematic of a reflection grating. . . . .	53
2.3	NIRIS obtained spectral images . . . . .	56
2.4	(a) View angles calibration of NIRIS. . . . .	58
2.5	A nocturnal spectral image and spectral lines obtained by NIRIS	60
2.6	Nocturnal variation of three different rotational lines of OH(6-2) Meinel band and O <sub>2</sub> (0-1) atmospheric band emissions . . . . .	61
2.7	Nocturnal variations in O <sub>2</sub> and OH intensities and rotational temperatures on the night of 16 April 2013 and 04 May 2013 . . . . .	66
2.8	Vertical profile of SABER and NIRIS derived temperatures . . . . .	68
2.9	Optical configuration and photograph of CMAP . . . . .	70
2.10	The filter wheel assembly and bipolar temperature controller along with Peltier elements to control the temperature . . . . .	73
2.11	Typical temperature stability achieved in our in-house developed temperature controlled chamber used in CMAP . . . . .	74
2.12	Nocturnal variations in the OI(630.0), OI(557.7 nm), and sodium (589.0 and 589.6 nm) nightglow emission intensities as measured by CMAP at Gurushikhar, Mount Abu on the night of 24-25 October 2014 . . . . .	76
2.13	Real part (solid) and imaginary part (dashed) for the Morlet wavelet in the time domain. . . . .	87
2.14	Periods that are present in nocturnal variation in O <sub>2</sub> and OH emission intensities . . . . .	90



2.15	Nocturnal variation in I(O <sub>2</sub> ) and I(OH) intensities and Lomb-Scargle periodograms of the residuals . . . . .	91
2.16	Residuals of the nightglow emission intensities for both O <sub>2</sub> and OH emissions showing downwards phase propagation which indicate an upwards propagation of gravity wave . . . . .	92
2.17	(Variations in the O <sub>2</sub> and OH intensities along N-S meridian and statistically significant meridional wavelengths for O <sub>2</sub> and OH intensity variation throughout the night of 4 May 2013 . . . .	94
2.18	The wavelet transform of the residuals of I(O <sub>2</sub> ) and I(OH) showing occurrence of the same periodicities as seen from Lomb-Scargle method along with their temporal occurrences . . . . .	96
2.19	A schematic of the propagation of gravity wave in which the phase is shown to be progressing downwards (upward propagating wave) . . . . .	97
3.1	Details of the duration of observations obtained from the Near InfraRed Imaging Spectrograph (NIRIS) at Gurushikhar, Mount Abu (24.6°N, 72.8°E), in India. . . . .	103
3.2	Variations in nightly mean O <sub>2</sub> and OH intensities, daily mean sunspot numbers and F10.7 cm radio flux, and corresponding O <sub>2</sub> and OH temperatures . . . . .	106
3.3	Lomb-Scargle periodograms of the O <sub>2</sub> and OH intensities and corresponding temperatures and solar parameters for different durations . . . . .	108
3.4	Four-day running averages of O <sub>2</sub> and OH intensities and SSN and correlation coefficients in between these parameters . . . . .	111
3.5	The procedure used to derive gravity wave periodicities from the nocturnal variations of the nightglow intensity data is shown for a sample night of 10 June 2015 . . . . .	116

3.6	Gravity wave periodicities obtained from the O <sub>2</sub> and OH emission intensities for all the 437 nights of observations are shown which are folded into a one year interval . . . . .	118
3.7	Same as in Figure 3.6 but for the temperatures obtained from the O <sub>2</sub> (0-1) atmospheric and OH(6-2) band emissions intensities.	120
3.8	Statistical results of the GW occurrence frequency observed by all sky camera [Adapted from <i>Wu and Killeen (1996)</i> ]. . . . .	123
3.9	Same as in Figures 3.6 and 3.7 (a, b, d, e) but for the periods that have been derived from only those nights of observation for which the total duration of observation was greater than 6 h . .	124
4.1	Time sequence of difference OH images in geographic coordinates from 0340 to 0500 UT on 11 May 2004 [Adapted from <i>Yue et al. (2009)</i> ] . . . . .	132
4.2	Outgoing longwave radiation (OLR) on 26 October 2014 as derived from VHRR on-board Indian meteorological satellite (Kalpana-1) . . . . .	136
4.3	Nocturnal variations in the OI (557.7 nm), O <sub>2</sub> (0-1) atmospheric band, Na (589.3 nm), and OH(6-2) Meinel band nightglow emission intensities as measured by CMAP and NIRIS at Gurushikhar, Mount Abu . . . . .	138
4.4	Nocturnal variation in OI, O <sub>2</sub> , Na, and OH nightglow emission intensities on the night of 26 October 2014. Variation of OLR values at the location ‘P’ for 24-hour duration . . . . .	141
4.5	Lomb-Scargle periodograms of the zero mean unit variance for the parameters shown in Figures 4.4 for the night of 26 October 2014. . . . .	143
4.6	Periods obtained using Lomb-Scargle analyses for OI, O <sub>2</sub> , Na, and OH nightglow emission intensities and in OLR(P) data obtained for each night during 16–27 October 2014. . . . .	145

4.7	Normalized wavelet spectra of the corresponding zero mean unit variances of the O <sub>2</sub> , Na, and OH nightglow emission intensities as shown in Figure 4.4 and OLR(CR1) showing temporal evolution of the periods seen in Figure 4.5 . . . . .	148
4.8	Schematic showing the wave propagation direction and distance from the source region to the observational location. . . . .	150
4.9	Nocturnal variation in meridional and zonal wind at 94 km altitude as obtained from HWM14 and in vertical wavelength calculated using GW linear dispersion relation with the HWM14 winds . . . . .	152
4.10	TIDI (TIMED Doppler Interferometer) winds showing the presence of shear in the zonal/ meridional winds. . . . .	154
4.11	The difference in T(O <sub>2</sub> ) and T(OH) on the night of (a) 16 April 2013, and (b) 6 May 2013 . . . . .	159
4.12	The five rows in the different subplots represent the difference in T(O <sub>2</sub> ) and T(OH), I(O <sub>2</sub> ) and I(OH), residuals of O <sub>2</sub> and OH emission intensities, and the periodicities present in the O <sub>2</sub> and OH emission intensities, respectively. . . . .	162
5.1	NIRIS derived O <sub>2</sub> and OH rotational temperatures over Gurushikhar, Mount Abu for a few selected nights during 2013 SSW period. . . . .	170
5.2	Temperatures in the polar cap poleward of 60°N and longitudinally averaged zonal wind at 60°N at 10 hPa pressure level obtained from MERRA dataset for eleven SSW events which occurred during 2004–2013 . . . . .	173
5.3	Longitudinally averaged mesospheric temperatures derived from the SABER, SOFIE, and OSIRIS dataset at 10° latitude interval for 2009 and 2013 SSW events . . . . .	176
5.4	Similar to Figure 5.3 but for 2006 major SSW event. . . . .	177

5.5	Similar to Figure 5.3 but for 2010 major SSW event. . . . .	178
5.6	Similar to Figure 5.3 but for 2011 minor SSW event. . . . .	179
5.7	Similar to Figure 5.3 but for 2012 minor SSW event. . . . .	180
5.8	Similar to Figure 5.3 but for 2008 SSW event. . . . .	181
5.9	Differences in SSW temperatures ( $\Delta T_S$ ) over $60^\circ$ – $90^\circ$ N at 10 hPa pressure level vs difference in mesospheric temperatures ( $\Delta T_M$ ) for six selected latitude ranges for 2013 and 2009 SSW event as derived from SABER datasets . . . . .	183
5.10	Difference in SSW temperatures ( $\Delta T_S$ ) over $60^\circ$ – $90^\circ$ N at 10 hPa pressure level vs difference in mesospheric temperatures ( $\Delta T_M$ ) at $10^\circ$ latitude intervals as derived from SABER dataset from both the hemispheres for three major and five minor SSW events as shown in Figure 5.2 . . . . .	184
5.11	Same as in Figure 5.9 but for SOFIE data at two latitudinal ranges in NH and SH for three major SSW events of 2009, 2010, and 2013 combined together and for OSIRIS data for two major SSW events of 2009 and 2010 . . . . .	187
5.12	Slopes ( $\Delta T_M/\Delta T_S$ ) derived from analyses for each individual major SSW event using SABER data with respect to the geographic latitude for all major and minor SSW events . . . . .	189
5.13	Peak stratospheric temperature for all the eleven selected SSW events with slope reversal latitudes in the poleward direction in both hemispheres. Latitudinal difference in peak slopes of the “double-humped” structure with respect to the peak stratospheric temperatures are also shown . . . . .	191
5.14	Daily mean mesospheric temperatures derived from SABER data for all the eleven SSW events with respect to geographic equator and CIRA-86 derived temperatures. The differences in the SABER measured and CIRA-86 estimated mesospheric temperature are also shown . . . . .	193

# Acknowledgments

This thesis is the outcome of the support, inspiration, and encouragement of a large group of people, in one way or another, and without which it would not have been possible to finish it in present form. Though, only a few of them are mentioned below by name I am grateful to all my well-wishers for their direct or indirect support.

First of all, I would like to express my deep sense of gratitude to my thesis supervisor Prof. Duggirala Pallamraju for his constant support, guidance, and enduring encouragement he has provided in the completion of my thesis. I am highly influenced by his in-depth knowledge in multidisciplinary fields. Throughout this period, I have been greatly benefited from his positive attitude in life. I thank him for his patience, providing an opportunity for independent thinking, and giving importance to my views and ideas. I highly value his concern in both scientific and personal front. I thank him for his critical comments and making important suggestions to improve this thesis. My sincere thanks also go to Prof. Nisarg K. Bhatt for agreeing to be co-guide of my thesis work. His continued support, untiring help, encouragement, and co-operation on various issues have been of immense help to finish this work.

I am thankful to former PRL Director Prof. J. N. Goswami for allowing me to pursue my thesis work. I express my sincere gratitude to the Director Dr. Anil Bhardwaj and the Dean Prof. P. Janardhan for their generous support and taking a personal interest in my thesis work. I am also thankful to former Deans Profs., U. Sarkar, A. S. Joshipura, and S. Rindani; former Registrars Shree Y. M. Trivedi and present Registrar Prof. J. S. Ray for providing necessary facilities and encouragements to pursue my research work.

I am highly indebted to Prof. S. R. Kulkarni (Hon. Vice Chancellor, Sardar Patel University), Dr. R. H. Rajput (Registrar, Sardar Patel University), Prof. P. N. Dave (Department of Chemistry, Sardar Patel University), and Dr. Mayank Bhatt (Assistant Registrar, Sardar Patel University) for their

help and concern in resolving administrative issues.

I am extremely thankful to Prof. U. H. Patel, Head, Department of Physics, Sardar Patel University and DRC Committee member Profs., P. C. Vinodkumar, V. M. Pathak, M. R. Deshpande, and B. Y. Thakore for their guidance and support. I am thankful to Rajani and Dhaval for their help during submission of my thesis. I am also thankful to all the faculty members and supporting staff members of the Physics Department and University office for their continuous support and help.

I am thankful to Narayanan jee for his unconditional support and enthusiasm for all experimental works and field campaigns we have done together. I am thankful to Kedar for “never say no attitude” who has accompanied me on several trips to Mount Abu and other lab activities; I wish him all the best for his bright future. I am thankful to all my group colleagues, Fazlul, Sneha, Deepak, Parshv, Subir, and Pradip for always being friendly and creating eventful atmosphere around.

I am extremely happy to express my sincere thanks to the principal investigators and team members of SABER and TIDI on-board TIMED satellite mission, OSIRIS on-board Odin satellite mission, and SOFIE on-board AIM satellite mission for providing temperature data up to MLT altitudes. I extend my thanks to team members of MOSDAC at SAC, Ahmedabad for enabling access to Kalpana-1 OLR data. I thank team members of GMAO for providing MERRA data for stratospheric temperatures and winds.

I feel honoured working in a cordial group of researchers working in Space and Atmospheric Sciences Division. I express my sincere thanks to all past and present faculty members of SPA-SC Division, Profs., R. Sekar, S. A. Haider, S. Ramachandran, Harish Chandra, R. Sridharan, Shyam Lal, Varun Sheel, K. P. Subramaniam, H. S. S. Sinha, and Bhas Bapat; Drs., L. K. Sahu, Som Kumar Sharma, D. Chakrabarty, Harish Gadhvi, Y. B. Acharya, S. B. Banerjee, B. Sivaraman, and A. Guharay; Mr., S. Venkataramani, T. A. Rajesh, Atul Manke, A. P. Gohil, Narain Dutt, K. S. Modh, and I. A. Prajapati; staff

members Mr. Sunil Kumar, Mitesh Bhavsar, Pradip, Malaidevan, Utkarsh, Aaditya, Sneha, Anil, Vishnu for their valuable co-operation and support during my tenure at PRL. The presence of PDF's and Research Scholars of our division; Fazlul, Sneha, Deepak, Subir, Dipti, Kuldeep, Ravi, Nidhi, Naveen, Debrup, Krishna, Ashimanand, Masoom, Siddhi, Thirupathaiah, and Jagat provided delightful atmosphere in our division during course of this work.

I extend my sincere thanks to former academic committee members Profs., Shyam Lal, S. Mohanty, P. Janardhan, S. K. Singh, S. Ramachandran, A. D. K. Singh, N. Srivastava, and D. Banerjee for reviewing my proposal and allowing me to carry out Ph.D. course work at PRL. I thank my course work instructors Profs., S. Ramachandran, V. Sheel, J. R. Bhatt, M. M. Sarin, and A. Chakraborty Drs. D. Chakrabarty, A. K. Singhal, K. K. Marhas, and B. Joshi for refreshing the required background for my thesis work.

Many individuals from PRL family have always been extremely helpful and supportive throughout my carrier at PRL. I would like to acknowledge the generous help I got from the PRL workshop, library, computer centre, purchase, stores, maintenance, administration, medical services, and accounts section. My special thanks are due to Mr., G. P. Ubale, H. R. Vaghela, Rajesh Kaila, and other members of workshop; Dr. Nishtha Anilkumar and all other members of PRL library; Jigar bhai, Tejas bhai, Alok, Mishra jee, Rahul, Girish bhai and all other members of computer centre; Hemal Bhai, Sivadasan jee, Rashmi jee, Nandini madam, Priti madam, Sunil bhai and all other members of purchase and stores; Mahirale jee, Sanjay bhai, Viral bhai, Ketan bhai, Ram lakhan and all other members of CMD; Anand Mehta jee, R. S. Gupta jee, Senthil, Pradeep, Kartik bhai, Richa and all other members of PRL administration; Dr. Shital Madam, Dr. Sameer bhai, Sasikumar jee, Jaishree madam and all other members of medical services; Deekshitulu jee, Geetha madam, Yugal bhai, Gandhi bhai, Parul madam, Keyur bhai and all other members of accounts section.

Thanks to Mr. Rajesh Kaila for his help in fabricating mechanical struc-

tures to mount the optical instruments and assisting their installations at Gurushikhar. The entire members of Mount Abu observatory has been always co-operative. To name a few, I wish to thank Rajesh jee, Mathur jee, Kothari jee, Patwal jee, Jain Sahab, Rajpurohit jee, Narayan jee, Padam jee, Nafees and other staff members and the entire canteen and housekeeping staff at Mount Abu for their help.

Thanks to my friends Lokesh, Sanjeev, Neeraj, Dinesh, Sudheer, Ravi-da, Jyoti, Sunil Singh, Shukla jee, Harish jee, Arvind, and Vinai for providing a refreshing change in my hectic work schedule during tea breaks.

I have nostalgic memories of my initial years at PRL hostel where I made so many friends. Being a sportsman, I had an opportunity to interact a large spectrum of peoples. Through which, I learned true sportsmanship that taught me graceful handling of victory or defeat in every moment of life. It would not be possible to name all of them individually for their direct or indirect support either academic or non-academic but they do have special place in my memories.

I am thankful to Vikramnagar fraternity for providing home away from home atmosphere my special thanks goes to them and their family members especially, Neeraj, Lokesh, Partha, Sanjeev, Dinesh, Deepak Dhingra, Subbu, Rindani, Neeraj Srivastava, Raghu, Navinder, Bijaya, Sudheer, T. A. Rajesh, Kuljeet, Panda, Ashish, Jerry, Mohanty, Ram, Santosh, Sunil, Srubabati, Hiranmaya, Sachindra, Shashikiran, Venkat, R. P. Jee, Goutam, J. Banerjee, Bhala, Jyoti, A. D. Shukla, Som Kumar Sharma, Amit Basu, Shanmugam, Shiv kumar, Atul, Alok, Rajiv Ranjan, Girish Padia, Nandini, Sasi kumar, Bhushit, Gupta Jee, and Tejas. I have fond memory of yesteryears "VBA" group at Vikramnagar.

Above all, words are not enough to express my gratitude towards my Mummy and Papa who sailed against all odds to make me a better person. I simply thank my parents for their sacrifices and blessings, which will keep me motivated throughout my life. I shall always remain grateful to my sis-



ters, brothers, Jija jee, in-laws, and niblings for their constant support and encouragement.

Unflagging and unconditional support and care of my wife Garima were biggest strengths for me. My cheerful daughters Aanya and Aashvi made our home a small paradise on earth. Their smiles and playing with them always awaken my inner child that gave me happiness, contentment, and inner peace. I wish and promise to give them more quality time.

**Ravindra Pratap Singh**



## ABSTRACT

The Earth's upper atmosphere is influenced by the incoming solar radiation from above and upward propagating atmospheric waves from lower atmosphere. The present thesis deals with the understanding of these two influences on the Earth's upper atmosphere. While Earth's upper atmosphere have been studied in the past using all sort of available techniques, there still exist large gap in our understanding of mesosphere lower thermosphere (MLT) region. MLT region is the part of the upper atmosphere where most of the atmospheric waves deposit their energy and momentum affecting overall structure and composition of the middle atmosphere. Therefore, quantitative understanding of the various processes that influence MLT region becomes essential. In this work, the main atmospheric parameters that have been used to understand the various coupling processes in the MLT region are nightglow emission intensities and mesospheric temperatures. Nightglow is a very weak emission occurring in the Earth's upper atmosphere in the infrared, visible, and ultraviolet wavelength regions. These nightglow emissions comes mainly from the recombination processes e.g., when two oxygen atoms recombine to form molecular oxygen. Therefore, intensity of these nightglow emissions depends upon the number densities of the reactants. Hence, by measuring the variations in nightglow emission intensities provides information on the densities of the reactants that is mainly affected by the atmospheric waves and/or solar influences. Measurements of these parameters are carried out mostly by ground- and space-based remote sensing techniques and less frequently using in-situ rocket-based measurements.

In this work, the main focus was to characterize various coupling processes in the MLT region, wave dynamical couplings under varying geophysical conditions, effect of the solar influences in the MLT region, lower- and upper-atmosphere coupling during cyclones, and latitudinal couplings during sudden stratospheric warming (SSW) events. These investigations were carried out

mainly by using ground-based long-term data obtained from couple of in house built instruments namely, Near InfraRed Imaging Spectrograph (NIRIS) and CCD-based Multi-Wavelength Airglow Photometer (CMAP). NIRIS provides nightglow emission intensities and temperatures corresponding to 87 and 94 km altitudes using OH(6-2) Meinel and O<sub>2</sub>(0-1) atmospheric band emissions, CMAP provides nightglow emission intensities using sodium doublet line (589.0 and 589.6 nm), OI green line (557.7 nm), and OI red line (630.0 nm) which emanate from 92, 100, and 250 km altitudes, respectively. In addition to these nightglow emission intensities and temperatures, mesospheric temperatures obtained from multiple satellite-based observations, data of F10.7 cm radio flux and SSN number, stratospheric zonal winds and temperatures from reanalysis dataset, OLR data from Kalpna-1 satellite etc. have been used. In the present doctoral thesis entitled **“Investigations of Interactions in The Earth’s Upper Atmosphere Using Optical and Radio Wave Techniques”** an attempt has been made for a detailed investigations on the basis of the above stated broad topics. The work carried out in this thesis is presented in six chapters.

In this thesis work, development of a new spectrograph, NIRIS, which is capable of simultaneous measurements of OH(6-2) Meinel and O<sub>2</sub>(0-1) atmospheric band nightglow emission intensities have been described. In this spectrographic technique, rotational line ratios are obtained to derive temperatures corresponding to the emission altitudes of 87 and 94 km. In addition to NIRIS, development of a new nightglow photometer, CMAP, to measure the nightglow emission intensities at multiple wavelength is also described. These two instruments have been commissioned for continuous operation from optical aeronomy observatory, Gurushikhar, Mount Abu (24.6°N, 72.8°E).

Large- and small-timescale variations in the mesosphere have been investigated using three (2013-2015) years of O<sub>2</sub>(0-1) and OH(6-2) bands nightglow emission intensities and corresponding rotational temperatures as tracers of mesospheric dynamics. The solar activity show different small- and large-time

periods along with well known 27 days and 11 years periods. Both  $O_2$  and OH intensities show variations similar to those of number of sunspots and F10.7 cm radio flux indicating a strong solar influence on mesospheric dynamics. In addition, both mesospheric airglow intensities also showed periodicities which are of atmospheric origin. Statistical study were performed using the periodicities derived from the nocturnal variations in all the four parameters ( $O_2$  and OH intensities and their respective temperatures) in order to understand mesospheric gravity wave behaviour over long term.

Vertical coupling of atmospheres during cyclone Nilofar have been studied, wherein, we have observed a common periodicity of around 4-hours in mesospheric nightglow intensities at three emissions ( $O_2(0-1)$ , OH(6-2) bands, and Na(589.3 nm)) from Gurushikhar, Mount Abu on the night of 26 October 2014. A convective activity due to the cyclone Nilofar, which had developed in the Arabian Sea during 25–31 October 2014, was found to be the source as this too showed a gravity wave period coherent with that of the mesospheric emissions on the 26<sup>th</sup>. The periodicities at the source region were obtained using Outgoing Longwave Radiation (OLR) fluxes (derived from Kalpana-1 satellite) which were used as a tracer of tropospheric activity. We have derived all the GW parameters (wave period,  $\tau$ , horizontal phase speed,  $c_h$ , horizontal wavelength,  $\lambda_h$ , vertical phase speed,  $c_z$ , vertical wavelength,  $\lambda_z$ , and vertical propagation angle,  $\theta_v$ ) which were obtained experimentally from ground-based optical data that exist during cyclone Nilofar. These results thus provide not only unambiguous evidence on the vertical coupling of atmospheres engendered by the tropical cyclone Nilofar, but also the characteristics of waves that exist during such cyclonic events.

Significant enhancements observed in the NIRIS derived mesospheric rotational temperatures at 87 and 94 km altitudes during the major sudden stratospheric warming (SSW) event of January 2013 provided motivation for the further investigation on the global scale. To investigate the relationship of these enhancements in the context of SSW occurrences, a detailed study

was carried out for eleven SSW events that occurred during 2004–2013 using SABER (Sounding of the Atmosphere using Broadband Emission Radiometry) data. In addition to SABER, Optical Spectrograph and InfraRed Imaging System (OSIRIS) and Solar Occultation For Ice Experiment (SOFIE) mesospheric temperatures were also used which showed similar latitudinal behaviour as obtained by SABER. The longitudinal mean mesospheric temperatures at different latitudes of northern and southern hemispheres have been derived. It is found that, during SSW events the well-known mesospheric cooling over the northern hemispheric high-latitudes turns to heating over mid-latitudes and then reverts to cooling closer to equatorial regions. This trend continues into the southern hemisphere as well. These variations in the mesospheric temperatures at different latitudes have been characterized based on northern hemispheric stratospheric temperature enhancements at high-latitudes during SSW periods. In comparison with the CIRA-86 derived temperatures the SABER temperatures show an increase/decrease in southern/northern hemisphere. Such a characterization in mesospheric temperatures with respect to latitudes reveals an hitherto unknown intriguing nature of the latitudinal coupling in the mesosphere that gets set up during the SSW events.

**Keywords:** Nightglow emissions, Mesospheric temperatures, OH(6-2) and O<sub>2</sub>(0-1) rotational temperatures, Mesosphere Lower Thermospheric (MLT) dynamics, Gravity wave characteristics, Tropical cyclone generated gravity waves, Atmospheric coupling, Low-latitude MLT dynamics, Stratospheric mesospheric coupling, Inter-hemispheric mesospheric couplings, Sudden Stratospheric Warming (SSW), Mesospheric inversion layers, Mesospheric temperature inversions, Optical techniques, Near Infrared Imaging spectrograph (NIRIS), CCD-based Multi-Wavelength Airglow Photometer (CMAP).

## LIST OF PUBLICATIONS

### A. Publications in Peer Reviewed Journals

1. **Singh, R. P.**, and D. Pallamraju (2017), Near Infrared Imaging Spectrograph (NIRIS) for ground-based mesospheric OH(6–2) and O<sub>2</sub>(0–1) intensity and temperature measurements, **J. Earth Sys. Sci.**, 126:88, doi:10.1007/s12040-017-0865-4.
2. **Singh, R. P.**, and D. Pallamraju (2017), Large- and small-scale periodicities in the mesosphere as obtained from variations in O<sub>2</sub> and OH nightglow emissions, **Ann. Geophys.**, 35, 227–237, doi:10.5194/angeo-35-227-2017.
3. **Singh, R. P.**, and D. Pallamraju (2016), Effect of cyclone Nilofar on mesospheric wave dynamics as inferred from optical nightglow observations from Mt. Abu, India, **J. Geophys. Res. Space Phys.**, 121, 5856–5867, doi:10.1002/2016JA022412.
4. **Singh, R. P.**, and D. Pallamraju (2015), On the latitudinal distribution of mesospheric temperatures during sudden stratospheric warming events, **J. Geophys. Res. Space Phys.**, 120, 2926–2939, doi:10.1002/2014JA020355.
5. Pallamraju, D., J. Baumgardner, **R. P. Singh**, F. I. Laskar, C. Mendillo, T. Cook, S. Lockwood, R. Narayanan, T. K. Pant, and S. Chakrabarti (2014), Daytime wave characteristics in the mesosphere lower thermosphere region: Results from the Balloon-borne Investigations of Regional-atmospheric Dynamics experiment, **J. Geophys. Res. Space Phys.**, 119, 2229–2242, doi:10.1002/2013JA019368.
6. Pallamraju, D., F. I. Laskar, **R. P. Singh**, J. Baumgardner, and S. Chakrabarti (2013), MISE: A Multiwavelength Imaging Spectrograph

using Echelle grating for daytime optical aeronomy investigations, **J. Atmos. Sol-Terr. Phys.**, 103, 176-183, doi: 10.1016/j.jastp.2012.12.003.

## **B. Peer-Reviewed Technical Publications**

1. Phadke, K. A., R. Narayanan, **R. P. Singh**, and D. Pallamraju (2014), An Automated CCD-based Multi-wavelength Airglow Photometer (CMAP) for Optical Aeronomy Studies, PRL Technical Note, PRL-TN-2014-107.
2. **Singh, R. P.**, D. Pallamraju, and R. Narayanan (2012), Development of Automated Digital Optical Imagers for Photography of Vapour Cloud Releases by Rocket, PRL Technical Note, PRL-TN-2012-102.



### C. Papers in International Conferences/ Symposia/ Workshops/ Meetings

Sr. No.	Paper title	Name of the Conference/ Symposia/ workshops	Mode of presentation
1.	Low-latitude mesospheric wave dynamical variability over large- and short-timescales <b>Singh, R. P.</b> and D. Pallamraju	IAPSO-IAMAS-IAGA Joint Assembly 2017, 27 August–1 September 2017, Cape Town, South Africa	Oral presentation
2.	Mesospheric temperature inversions over a low latitude location and their possible causes <b>Singh, R. P.</b> and D. Pallamraju	IAPSO-IAMAS-IAGA Joint Assembly 2017, 27 August–1 September 2017, Cape Town, South Africa	Oral presentation
3.	Results from first three dimensional waves in the daytime obtained from dayglow emissions and their comparison with those derived from ionospheric measurements Pallamraju, D., D. K. Karan, S. Mandal, and <b>R. P. Singh</b>	14 <sup>th</sup> Asia Oceania Geo Sciences (AOGS) meeting 6–11 August, 2017, Singapore	Oral presentation
4.	On the nature of latitudinal distribution of mesospheric temperatures during sudden stratospheric warming events <b>Singh, R. P.</b> and D. Pallamraju	9 <sup>th</sup> workshop on Long-Term Changes and Trends in the Atmosphere, 19-23 September 2016, IAP, Kühlungsborn, Germany	Oral Presentation
5.	Effect of cyclone Nilofar on mesospheric wave dynamics as inferred from optical nightglow observations from Mt. Abu, India <b>Singh, R. P.</b> and D. Pallamraju	9 <sup>th</sup> workshop on Long-Term Changes and Trends in the Atmosphere, 19-23 September 2016, IAP, Kühlungsborn, Germany	Poster Presentation

Sr. No.	Paper title	Name of the Conference/ Symposia/ workshops	Mode of presentation
6.	<p>“Double-humped” structure in latitudinal distribution of mesospheric temperatures revealed during sudden stratospheric warming events</p> <p><b>Singh, R. P.</b> and D. Pallamraju</p>	<p>14<sup>th</sup> International Symposium on Equatorial Aeronomy (ISEA-14), 19–23 October 2015, Bahir Dar, Ethiopia</p>	<p>Oral Presentation</p>
7.	<p>Effect of Sudden Stratospheric Warming (SSW) events on the latitudinal distribution of mesospheric temperatures</p> <p><b>Singh, R. P.</b> and D. Pallamraju</p>	<p>40<sup>th</sup> COSPAR Scientific Assembly, 2–10 August 2014, Moscow, Russia</p>	<p>Poster Presentation</p>
8.	<p>Results on the Wave Dynamics in the Lower Thermosphere Obtained From Balloon-borne Investigations of Regional-atmospheric Dynamics (BIRD) Experiment</p> <p>Pallamraju, D., J. Baumgardner, <b>R. P. Singh</b>, et al.</p>	<p>International CAWSES-II Symposium, 18–22 November 2013, Nagoya, Japan</p>	<p>Oral Presentation</p>
9.	<p>A search for seeds of equatorial plasma irregularities: Results from ground- and balloon-borne optical measurements</p> <p>Chakrabarti, S., D. Pallamraju, J. Baumgardner, <b>R. P. Singh</b>, et al.</p>	<p>American Geophysical Union, Fall Meeting, 9–13 December 2013, San Francisco</p>	<p>Oral Presentation</p>

## D. Papers in National Conferences/Symposia/ Meetings

Sr. No.	Paper title	Name of the Conference/Symposia/Meetings	Mode of presentation
1.	Gravity waves in the ionosphere as derived from digisonde measurements at Ahmedabad, India Pallamraju, D., S. Mandal, K. A. Phadke, D. K. Karan, and <b>R. P. Singh</b>	3rd URSI-Regional Conference on Radio Science, 1–4 March 2017, Tirupati, India	Oral Presentation
2.	Anomalous distribution in mesospheric temperatures: Causes and Implications <b>Singh, R. P.</b> , D. Pallamraju, and N. K. Bhatt	Interdisciplinary Research Scholars Meet, 3–4 march 2016, Sardar Patel University, Vallabh Vidyanagar	Oral Presentation
3.	Latitudinal distribution of mesospheric temperatures during stratospheric warming events <b>Singh, R. P.</b> , D. Pallamraju, and N. K. Bhatt	National Space Science Symposium, 9–12 February 2016, Space Physics Laboratory, VSSC, Thiruvananthapuram	Oral Presentation
4.	Investigation of upper atmospheric wave dynamics as inferred from optical nightglow observations <b>Singh, R. P.</b> , D. Pallamraju, and N. K. Bhatt	National Space Science Symposium, 9–12 February 2016, Space Physics Laboratory, VSSC, Thiruvananthapuram	Poster Presentation
5.	Influence of gravity waves and tidal variability on mesospheric temperatures over Mount Abu (24.6°N, 72.7°E) obtained using a high-resolution spectrograph <b>Singh, R. P.</b> , D. Pallamraju, R. Narayanan and K. A. Phadke	18 <sup>th</sup> National Space Science Symposium, 29 January–1 February, 2014, Dibrugarh University, Dibrugarh	Oral Presentation

Sr. No.	Paper title	Name of the Conference/Symposia/Meetings	Mode of presentation
6.	Recent advancements in the understanding of coupling of atmospheres Pallamraju, D., F. I. Laskar, <b>R. P. Singh</b> , et al.	51 <sup>st</sup> annual convention of Indian Geophysical Union, 19–21 November 2014, Kurukshetra University, Kurukshetra	Oral Presentation
7.	A CCD-based multiwavelength airglow photometer Narayanan, R., K. A. Phadke, <b>R. P. Singh</b> , S. Panchal, and D. Pallamraju	18 <sup>th</sup> National Space Science Symposium, 29 January–1 February, 2014, Dibrugarh University, Dibrugarh	Poster Presentation
8.	Daytime wave characteristics in the lower thermosphere as obtained from the Balloon-borne investigation of Regional Atmospheric Dynamics (BIRD) experiment Pallamraju, D., S. Chakrabarti, J. Baumgardner, <b>R. P. Singh</b> , et al.	18 <sup>th</sup> National Space Science Symposium, 29 January–1 February, 2014, Dibrugarh University, Dibrugarh	Oral Presentation (INVITED)
9.	Remote sensing of mesospheric temperatures using a grating spectrograph <b>Singh, R. P</b> and D. Pallamraju	Interdisciplinary perspectives: Defence studies, Earth system science & Bio-medical science (IPDEB-2013), November 15–17, 2013, Sardar Patel University, Vallabh Vidyanagar	Poster Presentation
10.	Development of automated digital optical imagers for photography of rocket released vapour clouds <b>Singh, R. P.</b> , D. Pallamraju, and R. Narayanan	National Space Science Symposium, 14–17 February 2012, Sri Venkateshwara University, Tirupati	Poster Presentation
11.	Multi-wavelength High-resolution optical technique for the investigations of daytime upper atmospheric processes Laskar, F. I., D. Pallamraju, <b>R. P. Singh</b> , R. Narayanan, and S. Chakrabarti	National Space Science Symposium, 14–17 February 2012, Sri Venkateshwara University, Tirupati	Oral Presentation

## **E. Participation in Advanced Course:**

1. 2012 International School on Atmosphere-Ionosphere Radar at National Central University, Taiwan (ISAR-NCU-2012), 12–17 November 2012, National Central University, Chung-Li, Taiwan.

## **F. Participation in National/ International Conferences/ Symposia/ Workshop:**

1. IAPSO-IAMAS-IAGA Joint Assembly 2017, 27 August–1 September 2017, Cape Town, South Africa.
2. 9<sup>th</sup> workshop on Long-Term Changes and Trends in the Atmosphere, 19–23 September 2016, Kühlungsborn, Germany.
3. Seminar on Space Qualified Processes, Space Application Centre, Ahmedabad, 8 April 2016.
4. UGC Sponsored National Level Interdisciplinary Research Scholars Meet, Sardar Patel University, Vallabh Vidyanagar, 3–4 March 2016.
5. National Space Science Symposium (NSSS–2016), Space Physics Laboratory, VSSC, Thiruvananthapuram, 9–12 February 2016.
6. 14<sup>th</sup> International Symposium on Equatorial Aeronomy (ISEA-14), Bahir Dar, Ethiopia, 19-23 October 2015.
7. National Space Science Symposium (NSSS–2014), Dibrugarh University, Dibrugarh, 29 January–1 February, 2014.
8. DST-PURSE Sponsored national conference on Interdisciplinary perspectives: Defence studies, Earth system science & Bio-medical science (IPDEB-2013), Sardar Patel University, Vallabh Vidyanagar, 15–17 November, 2013.
9. National Space Science Symposium (NSSS–2012), Sri Venkateshwara University, Tirupati, 14-17 February, 2012.



# Chapter 1

## Introduction

### 1.1 Background

The Earth's atmosphere is very important for the existence of life on Earth as it absorbs the high energy ultraviolet and x-ray solar radiation from entering the Earth's surface. The regions of the neutral atmosphere are named according to variation in temperature. The neutral atmosphere is generally divided into four regions, namely, *troposphere* (0-15 km), *stratosphere* (15-50 km), *mesosphere* (50-90 km) and the *thermosphere* (90-400 km). In this characterization the regions are separated by points of zero temperature gradients and are called 'pauses'. The *troposphere* is the region of negative lapse rate ( $\sim 10 \text{ K km}^{-1}$  or less) due to the decrease in the infrared radiation as one moves away from the Earth's surface. This region is generally unstable and is subject to active convection which gives rise to most of the variations in local weather. The height of the tropopause varies from 15-17 km at low latitudes ( $< 30^\circ$ ) and 8-10 km at high latitudes ( $> 60^\circ$ ). Above the tropopause the temperature increases with height from  $\sim 170 \text{ K}$  at the tropopause and attains a maximum value of  $\sim 260 \text{ K}$  near stratopause ( $\sim 50 \text{ km}$ ). The increase in temperature with altitude in the *stratosphere* is caused due to the absorption of solar ultraviolet radiation by ozone molecules. Stratosphere contains 90% of the atmospheric

ozone with a peak ozone density at  $\sim 25$  km. Due to the positive temperature gradient the stratosphere is highly stable. Above stratopause, the temperature again decreases with height and reaches a minimum value of  $\sim 180$  K near the mesopause at  $\sim 85$  km due to radiative cooling at infrared wavelengths. In the mesosphere, dynamical motions, such as waves and tidal forces become significant owing to the negative temperature gradient. Above the mesopause, the temperature increase rapidly with height, with a sharp gradient from 180 K at 85 km to  $> 1000$  K at 300 km. The peak temperature attained in the thermosphere is solar activity dependent and can vary from 600-2000 K. The high temperature of the thermosphere (90-400 km) is caused due to the absorption of solar EUV radiation by molecular oxygen at 100-150 km and the absorption of ionizing EUV radiation above 150 km. Most of the heat liberated in the thermosphere is removed by downward conduction, therefore temperature increases upward. The heat conductivity becomes so large that the heat flux due to conduction ( $\Phi = -AT^{1/2} dT/dz$ ) becomes negligible and the region of the upper atmosphere is maintained in a nearly isothermal condition at a relatively high temperature (1000-2000 K). Above thermosphere, there lies the *exosphere* where collisions between molecules are so infrequent that neutral particles move in ballistic orbits subject only to gravity.

The ionosphere (60-400 km) is the part of the thermosphere where the medium is partially ionized with sufficient plasma density to affect radio wave propagation. Above the ionosphere the region filled with the cold ( $< 1$  eV) ionospheric plasma (mostly  $H^+$ ) is called plasmasphere. The upper boundary of the plasmasphere is plasmopause which is situated at around 4-5  $R_E$ . Across the plasmasphere, the plasma density sharply falls (e.g., from  $10^3$   $cc^{-3}$  to  $1$   $cc^{-3}$ ). However, outside the plasmopause the plasmas are mostly hot and of solar wind origin especially during geomagnetically disturbed periods. Magnetosphere is the region where the concentration of the charged particles is more than that of the neutral species. The magnetosphere is filled with plasma of solar wind and ionospheric origin. Magnetosphere ends at magnetopause where the influence



of the geomagnetic field ends and the solar magnetic field become dominant. Magnetopause lies  $\sim 10 R_E$  ( $R_E$  is the radius of Earth) in the dayside and at much greater distance at nightside ( $\sim 100 R_E$ , the moon is at  $\sim 60 R_E$ ).

The atmosphere up to 100 km is well mixed due to convection and turbulence, the composition much like that at sea level and is known as ‘*turbosphere*’ or ‘*homosphere*’. Above turbopause the mixing is inhibited by the positive temperature gradient and is called ‘*heterosphere*’. Above the turbopause, the mean free path becomes large enough and the molecular diffusion process becomes dominant. The vertical distribution of the atmospheric species is governed by their individual molecular masses and their diffusion. Thus, due to the diffusive separation in the *heterosphere* the number densities of heavier constituents start decreasing faster with altitude than the lighter species.

The work presented in this thesis is mainly concentrated on understanding various processes that take place in the mesosphere lower thermosphere (MLT) region of the Earth’s upper atmosphere. In the following sections, some of these processes and their importance in the MLT region will be described. Further, various coupling mechanisms (altitudinal, longitudinal, and latitudinal), energy sources in MLT region, long- and short-term variations, and measurement techniques of MLT investigation, etc., will be described. Towards the end of this Chapter the objectives and scope of this thesis work is given.

## 1.2 The Mesosphere and Lower Thermosphere (MLT) Dynamics

The stratosphere and mesosphere in combination is often termed as the middle atmosphere (10-110 km). The mesosphere-lower thermosphere (MLT) constitutes the upper part of the middle atmosphere and is defined as the region of the atmosphere between about 60 and 110 km in altitude [[Andrews et al.](#)].

(1987); [Vincent \(2015\)](#)]. It is not quite long ago that the MLT region was used to be referred to as the ‘ignorosphere’ because its height region is too high for aircraft or balloon measurements and too low for satellite orbits for *in situ* measurements. Thus, owing to this lack of direct data the MLT region remained one of the least explored regions of the Earth’s atmosphere. Some limited *in situ* measurements of the mesosphere are possible by the method of chaff release on-board sounding rockets, however, they remain limited because these are location specific and only provide a snapshot of the atmospheric parameters. For continuous observations we have to rely on the ground- or space-based remote sensing techniques. The remote sensing techniques that have been used to study the MLT region include spectrographs, airglow photometers, all sky imaging cameras, lidars, meteor wind radars, medium frequency (MF) radars, incoherent scatter (IS) radars, mesosphere stratosphere troposphere (MST) radars, and satellite-based instruments. These remote sensing observations over past decade improved our understanding of the MLT region. This region is no more an ‘ignorosphere’ but it is now known that it is replete with several dynamical phenomena with significant consequences in the Earth’s atmospheric system. Recently, MLT dynamics have been reviewed by several authors with articles that describe some key phenomena in the MLT region [[Shepherd \(2000\)](#)], processes that control the mean circulation in the MLT region [[Becker \(2012\)](#)], and processes involved with the interaction between the lower middle and upper atmospheres [[Smith \(2012b\)](#)]. In addition to the effect on the neutral dynamics in the MLT region the waves that propagate upwards can contribute to the production of plasma irregularities in the night time ionosphere [[Kelley et al. \(1981\)](#); [Pallamraju et al. \(2014\)](#)] that adversely affect the radio communications.

Differential heating of the atmosphere, radiative transfer, and photochemistry, in general, mainly drives atmospheric dynamics. Figure 1.1 shows a schematic of the globally averaged lower- and middle-atmosphere thermal and dynamical structure for solstices [e.g., [Andrews et al. \(1987\)](#); [Meriwether and](#)

*Gerrard (2004)*].

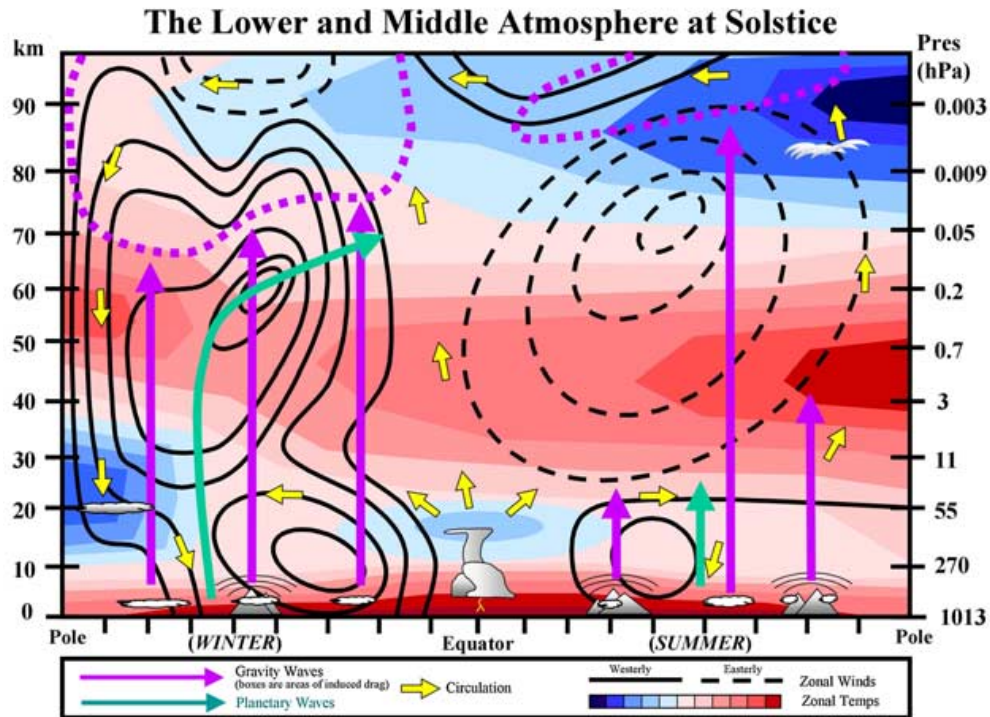


**Figure 1.1:** Schematic of lower and middle atmosphere showing thermal and dynamical structure. The relative temperatures are represented by colours, with red being warmer and dark blue being cooler. The wind directions are also shown with westerly (eastward) and easterly (westward) using solid and dashed lines, respectively. Ray path of gravity and planetary waves are also shown along with the circulation in the region [Adapted from *Meriwether and Gerrard (2004)*].

The altitudes below around 70 km are dominated by various neutral dynamics, e.g., Arctic polar vortex, planetary (Rossby) waves, and quasi-biennial oscillation. The higher altitudes contain a complex mixture of both seasonal neutral dynamics and electromagnetic effects, e.g., gravity wave breaking, polar mesospheric clouds (PMCs) or noctilucent clouds, polar mesospheric summer echoes (PMSEs), and sporadic layers. From Figure 1.1 one can note that the polar summer mesosphere is cold during the summer and warm in the winter. This departure of upper stratosphere and mesosphere from the radiative equilibrium is explained by the meridional circulation which is dominated by the motion of air mass from the summer pole to winter polar regions. This

is associated with upwelling of air over the summer polar region and downwelling over the winter polar region as shown by yellow arrows in Figure 1.1. The polar summer mesopause is the coldest location in the Earth's atmosphere (temperatures around 130 K) which results in the formation of PMCs at that height.

In addition to large scale winds that are shown in Figure 1.1 dynamics of the MLT region is also dominated by atmospheric waves (Gravity waves, tides, and planetary waves) that are generated in the lower atmosphere and propagate up. While propagating, these waves interact with background winds and other wave modes and dissipate their energy and momentum which contribute to the wind and temperature field variability in the region. Thus, these waves (under the influence of the background wind fields) create a greatly coupled system and act as a carrier for transporting energy, momentum, and chemical species from one part of the atmosphere to another [*Andrews et al. (1987)*; *Forbes (1995)*]. In order to keep the work presented in this thesis in perspective some background information on wind, temperature, and wave dynamics in the MLT region is provided in the following section.

### 1.3 Temperature and Wind Dynamics in MLT Region

From the tropopause to the mesopause, the net heating depends on the imbalance between local absorption of solar ultraviolet radiation and loss of infrared radiation. Figure 1.2 summarizes the heating/cooling rates calculated using radiative transfer equations considering major contributors to solar heating and terrestrial cooling [*London (1980)*]. As can be seen from Figure 1.2 on the average, the major contribution to solar heating is provided by the absorption of solar ultraviolet radiation by  $O_3$  in the stratosphere and the mesosphere and by  $O_2$  in the lower thermosphere. Terrestrial long wave thermal infrared

cooling is associated primarily with the presence of  $\text{CO}_2$ ,  $\text{O}_3$ , and  $\text{H}_2\text{O}$ , and is a strong function of temperature.

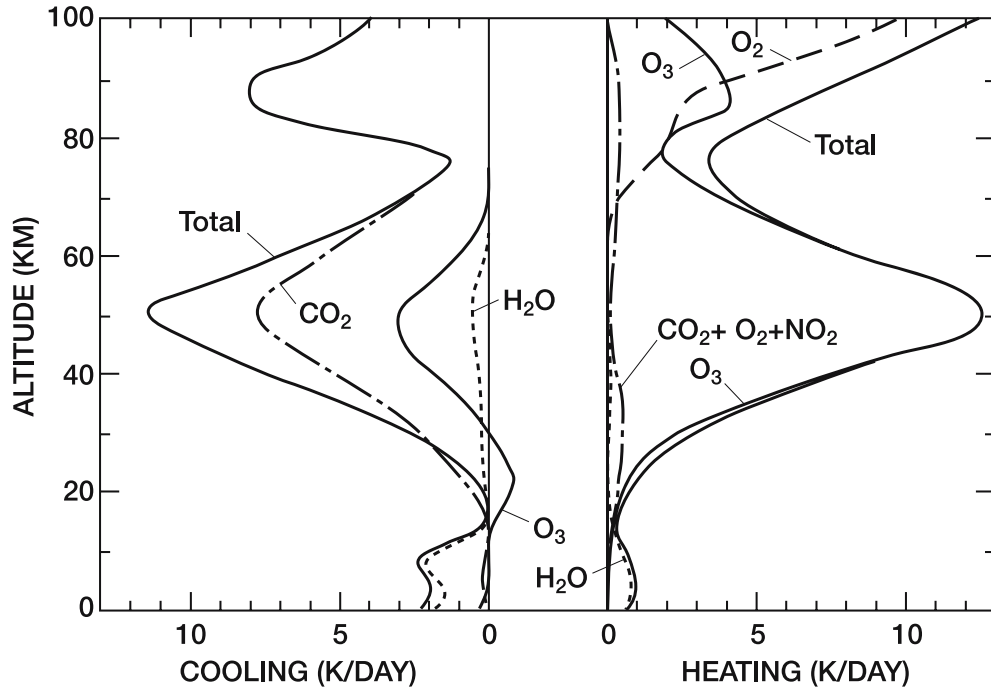


**Figure 1.2:** Vertical distribution of heating rates due to absorption of solar short wave radiation by  $\text{O}_3$ ,  $\text{O}_2$ ,  $\text{NO}_2$ ,  $\text{H}_2\text{O}$ ,  $\text{CO}_2$  (right), and of terrestrial long wave cooling rates by  $\text{CO}_2$ ,  $\text{O}_3$ , and  $\text{H}_2\text{O}$  (left) [Adapted from [London \(1980\)](#)].

When the atmosphere is in radiative equilibrium, which means that at all altitudes and latitudes the radiative heating and cooling rates must be in equilibrium. With the knowledge of heating and cooling rates (Figure 1.2) zonally averaged latitudinal temperature structure can be calculated [e.g., [Geller \(1983\)](#)]. From these calculations it is found that the temperature gradient in the stratosphere and mesosphere is from warm summer pole to the cold winter pole. This temperature gradient due to differential heating at the poles creates summer to winter pressure gradient which produces flow in the atmosphere towards winter pole. As the air parcel moves from summer to winter pole they will experience the Coriolis force which acts at right angle to the direction of the air parcel movement. A geostrophic wind arises when the pressure gradient force is balanced by the Coriolis force. Since the Coriolis

force pushes the flow to the right in the northern hemisphere and to the left in the southern hemisphere as a result westward/eastward geostrophic wind flows in the summer/winter hemisphere. By using the thermal wind equation and radiative equilibrium temperature structure (Figure 1.2) the geostrophic winds throughout the atmosphere can be calculated (and would be similar as shown in Figure 1.1).

The observed global circulation of the atmosphere is quite different and more complex calculations are required as compared to the simpler radiative equilibrium model as discussed above. In this section, a more realistic representation of the temperature and wind profile of the MLT region will be given based on the recent satellite-based measurements and one of the recent model results. The advanced middle atmospheric models provide better estimation of temperature and winds as a function of altitude, latitude, and longitude (local time). These models consider multidimensional transport of heat and the effect of various waves. In the lower atmosphere and mostly in MLT region (except for some very large amplitude waves- mainly diurnal tides), the basic dynamics varies more with latitude and altitude than with longitude. Thus, the 2-dimensional views (latitude  $\times$  altitude) averaged in longitude and local time is a useful framework to examine seasonal and inter-annual evolution of the MLT dynamics.

Figure 1.3 shows the mean temperature for 62-day periods centered on January and July obtained using SABER (SABER is described in Chapter 2) version 1.07 observations made between January 2002 and December 2011 [*Smith (2012a)*]. The lower panels in Figure 1.3 show the simulated average January and July temperatures from the Whole Atmosphere Community Climate Model (WACCM). WACCM is a comprehensive global climate model that extends from the Earth's surface into the lower thermosphere [*Garcia et al. (2007)*; *Richter et al. (2010)*; *Smith et al. (2011)*]. There are number of differences between the observed and model temperature the most noticeable is the temperature at the mesopause.

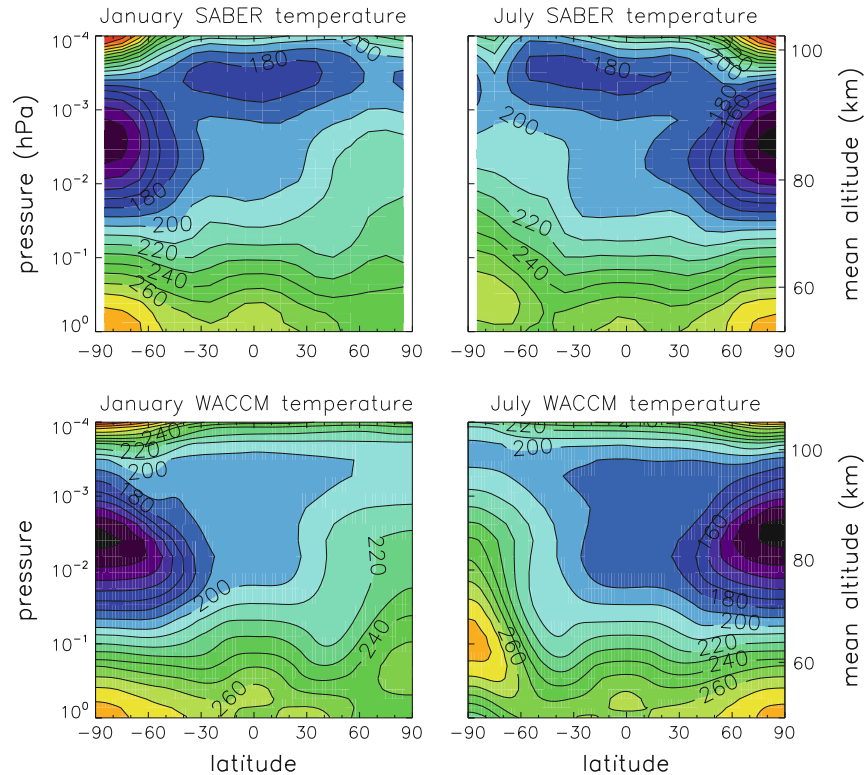


**Figure 1.3:** Zonal mean temperature from SABER retrievals averaged over the years 2002-2011 for 62-day periods centered on January and July (Top panels). Zonal mean temperature from WACCM averaged for a multiyear climatology 1960-2006 for January and July (Bottom panels). Contour interval is 10 K [Adapted from [Smith \(2012a\)](#)].

SABER observations show that there is a pole-to-pole extension of low temperature around 95-100 km that are seen at both solstices. The daily mean altitude of the mesopause is near 100 km in the winter hemisphere and in low latitude during all seasons. However, in the summer high latitudes, the mesopause temperature is much lower and its altitude is also lower (Figure 1.3). The global low temperature at 95-100 km is a result of the balance between the weak heating and the efficient radiation to space by  $\text{CO}_2$ . Another source of global heating and cooling is due to dissipating gravity waves and their interaction with the background atmosphere. This contribution is not clearly known because of the lack of comprehensive observations. However, the role of gravity wave propagation and dissipation has been accepted as the

dominant wave forcing in the MLT region [*Lindzen (1981); Holton (1983)*]. The work by *Levoy (1964)* showing cold summer mesopause must be maintained by dynamical motion is still accepted. The adiabatic cooling associated with strong rising motion is necessary to cool this region to temperatures well below the photochemical equilibrium conditions.

In the MLT region, the horizontal winds are highly variable, in which most of the observed variations are due to upward propagating waves. The High-Resolution Doppler Imager (HRDI) winds on-board the Upper Atmosphere Research Satellite (UARS) for the period 1991-1998 have been collected by the UARS Reference Atmospheric Project (URAP). Figure 1.4 shows zonal mean zonal winds for January and July months obtained from the URAP climatology (1992-1995) [*Smith (2012a)*]. URAP observations indicate that the summer zonal wind changes sign from westward to eastward at around 85 km. Whereas, the winter wind reversal from eastward to westward occurs at high altitude at about 95 km. WACCM simulations of zonal winds averaged for January and July are also shown in bottom panel of Figure 1.4 for comparison. The seasonal pattern for the solstice periods (westward in winter and eastward in summer) and the strengths of the jets are well represented in the model. Some aspects of the zonal mean winds simulated by WACCM differ from the observed winds e.g. WACCM show much lower altitude for the winter transition from eastward to westward wind. The climatological state of the MLT cannot be completely characterized due to the relatively short duration of most measurement records and to the large variability. As of now, there is not enough information to determine definitively how much of the variability is internal and how much is externally forced.

Thus, the observations in the MLT region improved our understanding about temperature structure and general circulation which is drastically different to that predicted by the radiative equilibrium. This indicated the existence of some other force acting on the atmosphere that needs to be properly taken into account. This external force acting in the middle atmosphere turns



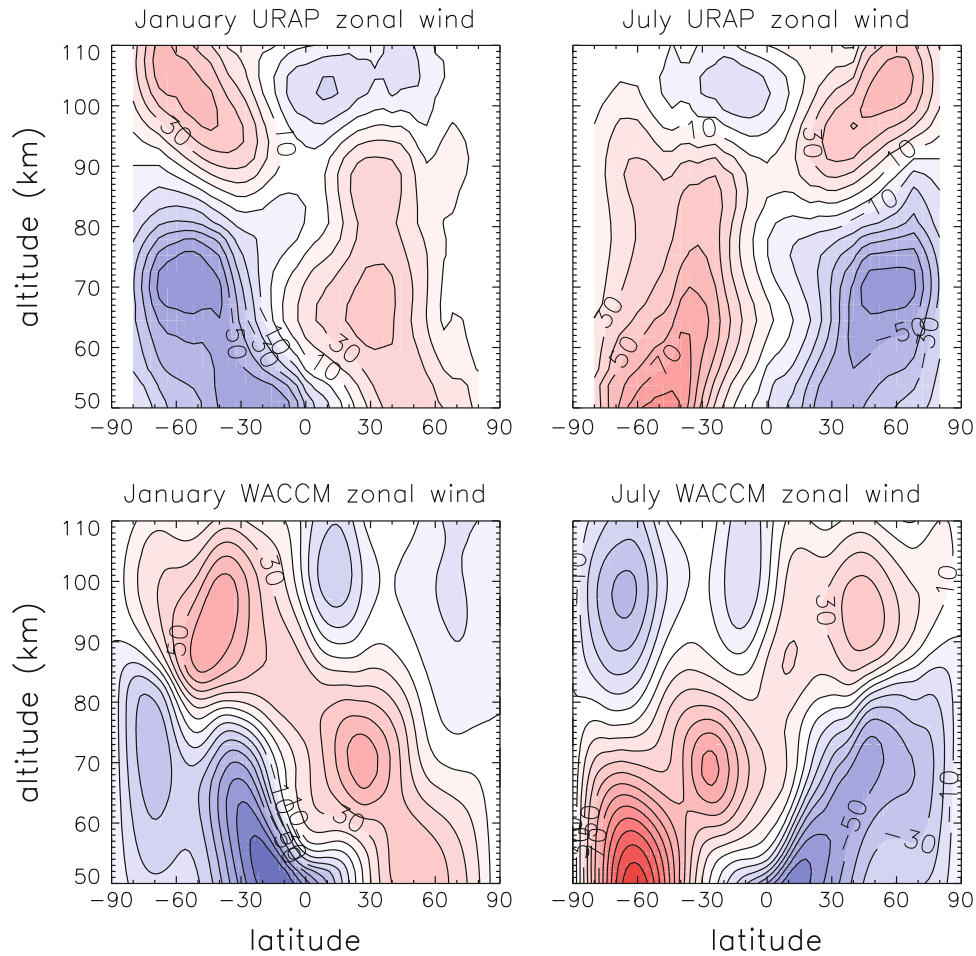


**Figure 1.4:** Zonal mean zonal wind from the URAP climatology (upper panels; 1992-1995) and simulated by WACCM (lower panels; multiyear climatology 1960–2006) for January and July. Contour interval is 10 m/s. Note that eastward is positive [Adapted from [Smith \(2012a\)](#)].

out to be some kind of dynamical forcing in the form of wave drag. This is believed that this external forcing comes from the breaking of the atmospheric gravity waves. As can be seen from Figure 1.4 this drag force has the effect of closing the jets and bringing in an eastward summer time jet in the lower thermosphere which in turn brings about pole-to-pole temperature gradient in the MLT region [[Andrews et al. \(1987\)](#)]. Therefore, it is apparent that the contribution of wave drag is accounted for obtaining the observed circulation and temperature structure in the middle atmosphere. Hence, it is vitally important to understand the role of wave dynamics in the middle atmosphere in

order to enhance our understanding of the processes involved in various regions of the atmosphere. The different waves which are pertinent in the MLT region are described in the next section.

## 1.4 Wave Dynamics

In general, the term wave is used for a disturbance that propagates in space and time which may be considered as a perturbation on the steady slowly changing background. Atmospheric waves are generated when air-parcel is displaced from its equilibrium position. These disturbances are opposed by the presence of one or more restoring forces present in the atmosphere and the balance between these two forces gives rise to wave motions. These waves are manifested in the spatial and temporal changes of the field variables such as concentration, pressure, temperature, and wind. The atmosphere is capable of sustaining a large number of wave phenomena. Atmospheric waves can be classified in various ways, according to their physical or geometrical properties [e.g., *Beer (1974)*; *Andrews et al. (1987)*]. Based on horizontal scales of fluid motion, the atmospheric waves may be classified as follows: sound (acoustic) waves, mesoscale waves, and (c) planetary (Rossby) waves. A more detailed classification of these waves and their probable restoring or wave generation forces are summarized in Figure 1.5. Each group of waves exhibits multiple flow regimes e.g., pure gravity waves may be further categorized as either vertically propagating waves or evanescent waves, depending upon whether the wave energy is free to propagate vertically.

The restoring forces for sound waves, pure gravity waves, inertia oscillations, and planetary waves are the compression force ( $C_s$ ), buoyancy force (N), Coriolis force (f), and meridional variation of the Coriolis force ( $\beta$ ), respectively. Restoring forces may also combine and work together to generate mixed waves, such as inertia-gravity waves, mixed acoustic-gravity waves, and mixed Rossby-gravity waves.

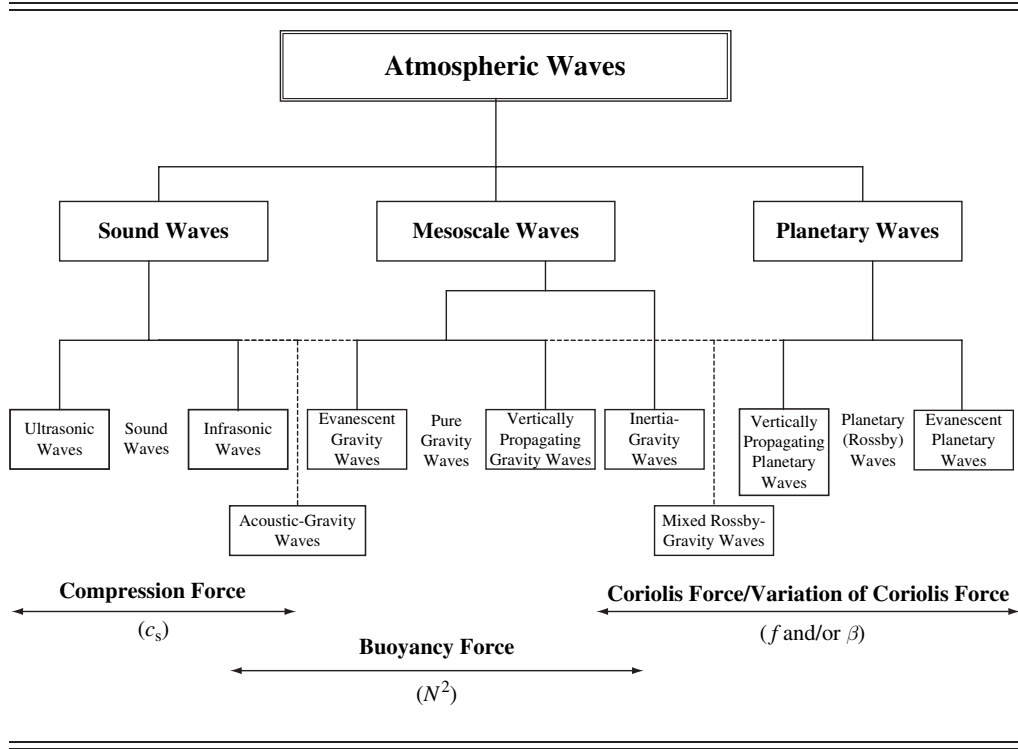


**Figure 1.5:** A Summary of atmospheric waves. [Adapted from [Lin \(2007\)](#)]

The oscillation period of the waves is determined by the strength of the restoring force and characteristics in the wave medium. These have a wide range of periods, ranging from a few minutes to a few years. The semi-annual oscillation (SAO) and quasi-biennial oscillation (QBO) are most significant features of the equatorial middle atmosphere dynamics. Table 1.1 summarizes the different waves and oscillations active in the equatorial middle atmosphere [e.g., [Reddi \(1998\)](#); [Murthy \(1998\)](#)].

Waves are characterized by their fundamental properties, such as, wave frequency ( $\omega = 2\pi/\tau$ ,  $\tau$  being period of oscillation), wave amplitude ( $A$ ), wave number ( $k=2\pi/\lambda_x$ ;  $l=2\pi/\lambda_y$ ;  $m=2\pi/\lambda_z$ , where  $\mathbf{k}=(k, l, m)$  is the wave vector and  $\lambda_x$ ,  $\lambda_y$ , and  $\lambda_z$  are the spatial scales in  $x$ ,  $y$ , and  $z$  directions), phase speed ( $c_p$ ), and group velocity ( $\mathbf{c}_g$ ). The phase speed of a wave is a scalar variable which is the speed at which lines of constant phase (such as wave crests, troughs, or any other part of the wave) propagate through the fluid

**Table 1.1:** Different types of oscillations/waves in the low-latitude middle atmosphere.

Oscillations /Waves	Period	Long. Scale size	Main Mechanism /Source of generation	Importance
11 year	~11 years		Solar	Met., UA
QBO	18-32 months	Global	WMFI involving Kelvin and Rossby GWs/GWs	Met.
AO	12 months	Global	Latitudinal differential solar heating	Met., UA
SAO	6 months	Global	WMFI involving Kelvin waves and GWs	Met., UA
Planetary waves	2-40 days	10,000-30,000 km	Spatially unequal (Orographic), Thermal forcing, land-ocean contrast	Met., UA
Tidal oscillations	24 h, 12 h, and 8 h.	Global	Thermal (due to heating of $O_3$ and water vapour)	Ionosphere, GM, UA
Gravity waves	BV to few hours	10-1000 km	Mountain waves, unsteady shear zone, deep convection	Ionosphere, UA
Acoustic	<270 sec	Meters to mm	Compression	speech

**QBO- Quasi-biennial oscillation, AO- Annual oscillation, SAO- Semi-annual oscillation, WMFI- Wave mean flow interactions, GM- Geomagnetism, UA- Upper atmosphere, BV- Brunt-Väisälä frequency**

medium in all of the three spatial dimensions and is given by:

$$c_{px} = \omega/k; c_{py} = \omega/l; c_{pz} = \omega/m \quad (1.1)$$

The phase speed of a wave may be estimated from the experimental data by determining and tracing the propagation of any given phase of the wave with time.

Since the phase speed is a function of wave frequency and wavenumber, and

therefore, for a given wave period,  $\tau$ , long waves will travel faster than short waves, and this leads to wave dispersion. The dispersion relation relates the wave frequency to the wave's spatial characteristics (wave number) and to the background atmospheric properties namely, Brunt-Väisälä (BV) frequency ( $N$ ) and zonal and meridional wind vectors ( $\mathbf{u}$ ,  $\mathbf{v}$ ). The group velocity is a vector quantity which is a measure of the rate at which the energy of the disturbance propagates or in the other words it represents the velocity at which the slowly-varying modulation of a wave propagates and is given by the relation:

$$\mathbf{c}_g = c_{gx}\mathbf{i} + c_{gy}\mathbf{j} + c_{gz}\mathbf{k} = \frac{\partial\omega}{\partial k}\mathbf{i} + \frac{\partial\omega}{\partial l}\mathbf{j} + \frac{\partial\omega}{\partial m}\mathbf{k} \quad (1.2)$$

As discussed above there are different kinds of waves present in the atmosphere, and three characteristic type of waves namely, gravity waves (GW), tides, and planetary waves, which are important in the MLT region will be introduced in the following section.

## 1.5 Short Time Scale Variations in MLT region

### 1.5.1 Gravity Waves (GWs)

The atmosphere is almost always stably stratified (fluid density increases with depth). A characteristic of a stably stratified fluid is the ability to support and propagate wave motions. Gravity waves are mesoscale oscillations that arise in a stably stratified fluid when air parcels are vertically displaced. Since they have the buoyancy force as the restoring force they are also referred to as buoyancy waves. The simplest example of GW occurs on the surface of an ocean, the restoring force is the action of gravity on a displaced body of fluid. Ocean waves can exist at the surface because of the abrupt change of density there and propagate primarily in the horizontal plane because vertically

propagating waves are reflected from the boundaries. On the other hand, atmospheric gravity waves propagate both horizontally and vertically from the source region. Figure 1.6 shows a surrealistic representation of atmospheric gravity waves given by *Hines* (1974).



**Figure 1.6:** A surrealistic representation of atmospheric gravity waves [Adapted from *Hines* (1974)].

Considerable progress has occurred in our understanding of gravity waves that exist in MLT region since the pioneering work by *Hines* (1960) who used gravity wave theory to explain the origins of turbulence observed in the ionosphere. A greater understanding of the gravity waves (both theoretical and experimental) can be found elsewhere [e.g., *Hines* (1960); *Hines* (1974); *Beer* (1974); *Fritts and Alexander* (2003); *Nappo* (2013)]. It is now widely accepted that gravity waves provide the bulk of the momentum forcing that drives the

circulation in the MLT region the effect of which can be seen in the observed temperatures (Figure 1.3). The generation, propagation, and dissipation of gravity waves depend on the winds and thermal structure of the surrounding environment.

Gravity waves can be generated through a variety of forcings. Mostly, these GWs are generated through tropospheric activities namely, air flow over mountains (orographic waves), convection (e.g., cyclones and thunderstorm), and wind shear. As the GWs propagate upward their amplitudes,  $A$ , grow non-linearly to compensate for the exponential decrease in,  $\rho$ , the atmospheric density ( $E = \frac{1}{2} \rho A^2$ ). The gravity wave propagation depends on the wind distribution and thermal structure, which varies markedly with season and the static stability [e.g., *Brasseur and Solomon (2006)*]. The spatial and temporal characteristics of GWs are different and are dependent on the generation mechanism(s). As discussed above, GWs affect the atmospheric dynamics and thermal/compositional structures ranging from mesoscales to global scales. Therefore, a thorough knowledge of gravity wave excitation, propagation, atmospheric coupling processes, and their breaking properties are required for their understanding.

Due to the multiscale nature of the gravity waves it is challenging to quantify these waves in both observations and numerical models. Incorporation of GW effects in climate models is a pressing problem [*Alexander et al. (2010)*]. The major challenges in the GW research in the MLT region is to trace the sources, derive the various wave characteristics, and to understand their effects in different part of the Earth's atmosphere. It is also equally important to understand and characterize the seasonal and solar cycle related effects in the GW wave parameters. However, these aspects are poorly understood. A significant part of thesis work deals with the derivation of GW parameters, their long term variations, excitation source(s), and the effect of GWs in the MLT region to address various poorly understood aspects of the MLT coupling through GWs. In the following section a brief review of the work related to

the GW studies are provided which is arranged according to the three main sources of the GW generation.

### 1.5.2 Topographic Generation

The gravity waves are generated when a vertical displacement of a stably stratified flow takes place, especially, when the flow is over terrain of obstacles such as ridges, hills, and mountains. However, terrain depressions such as canyons, basins, and valleys can also generate gravity waves [e.g, *Nappo (2013)*]. The amplitudes of terrain-generated gravity waves are proportional to the amplitudes of the wave-generating terrain. These waves are stationary relative to the ground surface (zero phase velocity), and they do not experience dispersion. When these waves propagate in the vertical direction the intrinsic speed of the waves becomes equal to the background wind speed but in the opposite direction. If the wind speed changes with height, then the wave also change and when wind speed becomes zero the wave is essentially absorbed into the mean flow [e.g, *Nappo (2013)*]. Under certain conditions, the amplitudes of terrain-generated waves can grow as they move upward and eventually break which results in outbreaks of turbulence, more commonly known as clear air turbulence [e.g, *Nappo (2013)*].

There are mainly two types of terrain-generated gravity waves and are named as lee waves and mountain waves. The lee waves are trapped between the ground surface and an upper level where wave reflection occurs and is characterized by a single horizontal wavenumber. Since lee waves are trapped in a layer their influence on the atmosphere above this layer is negligible. On the other hand, the mountain waves are found at higher heights in the atmosphere and generally have longer wavelengths and smaller amplitudes as compared to the lee waves. Mountain waves have been studied using theoretical, numerical, and observational methods more than any other kind of gravity wave. Horizontal wavelengths for vertically propagating waves are typically tens to



hundreds of kilometres, while amplitudes vary from small to breaking [e.g., *Fritts and Alexander (2003)* and references therein].

Statistical assessment of mountain waves over rough and smooth terrains and relative to other significant sources have been carried out. It has been shown that the horizontal velocity and temperature variances to be around 2–3 times higher over regions of significant topographical variations compared to plains and oceans, independent of other sources [e.g., *Nastrom et al. (1987)*; *Jasperson et al. (1990)*] and around 5 times higher than regions having no obvious meteorological sources [*Fritts and Nastrom (1992)*]. *Bacmeister et al. (1990)* showed that in the middle atmosphere mountain waves have dominant scales of around 10–100 km, phase speeds near zero, and vertical wavelengths dictated by the local static stability and mean wind in the plane of wave propagation. It was also argued that mountain waves likely account for a large fraction of zonally averaged wave-induced force (wave drag) in the mesosphere [*Bacmeister (1993)*].

### 1.5.3 Convective Activity Generation

One of the most important sources for the generation of gravity waves in the troposphere is convective activity. Understanding of the mechanisms responsible for the convective gravity waves (CGWs) and characterization of these waves is one of the important topics of research. Unlike topographically generated gravity waves CGWs are not characterized by a single prominent phase speed or frequency. However, CGWs have full range of phase speeds, wave frequencies, and vertical and horizontal scales. Convection involves a time-varying thermal forcing associated with latent heat release that can interact with overlying stable layers and shear in complex ways that are not yet fully understood.

Convective instability is the most important in the tropics because of strong solar heating, although, convection also occurs in the mid-latitudes, especially

over land surfaces during summer times. The occurrence of inertia-gravity waves in the tropics has been linked to convection as the source [e.g., *Pfister et al. (1986)*; *Tsuda et al. (1994)*; *Shimizu and Tsuda (1997)*; *Alexander and Vincent (2000)*]. The high-frequency gravity waves observed in the stratosphere have shown a close correspondence with deep convective clouds [e.g., *Sato (1992)*, *Sato (1993)*; *Alexander et al. (1995)*; *Dewan et al. (1998)*; *McLan-dress et al. (2000)*; *Alexander et al. (2000)*].

In the middle atmosphere, CGWs and their effects are studied using numerical simulations [e.g., *Piani et al. (2000)*; *Horinouchi et al. (2002)*; *Lane et al. (2003)*; *Vadas et al. (2012)*], airglow imagers [e.g., *Taylor and Hapgood (1988)*; *Taylor et al. (1997)*; *Swenson et al. (1999)*; *Wrasse et al. (2006)*; *Suzuki et al. (2007)*; *Yue et al. (2009)*; *Vadas et al. (2009)*; *Lakshmi Narayanan et al. (2010)*; *Vadas et al. (2012)*; *Yue et al. (2013)*; *Yue et al. (2014)*], and HF radars [*Vincent and Reid (1983)*; *Gavrilov et al. (1995)*].

In the real atmosphere there are different generation mechanisms which work in tandem to generate CGWs in the troposphere. While propagating in the middle atmosphere these waves are filtered through ambient winds. Due to this complexity, understanding of CGWs and their effects in the MLT region is far from complete which makes this field one of the active fields of research. Some part of this thesis work is related to the study of CGWs and characterization of these waves at the MLT altitudes. Over low-latitudes as will be described later in this thesis using spectrographic measurements the CGWs have been characterized [*Singh and Pallamraju (2016)*, *Singh and Pallamraju (2017b)*].

#### 1.5.4 Wind Shear Generation

Wind shear instability is also known as Kelvin-Helmholtz (KH) instability. Wind shears act as a potential source of gravity waves right from the troposphere to the thermosphere [e.g., *Fritts and Alexander (2003)*]. Shear instabil-

ity exists across an interface separating layers of fluid with different densities which can generate gravity waves when the vertical shear of horizontal velocity exceeds some critical value with respect to the vertical. Wind shear generated gravity waves has been studied for many years but remains one of the least quantified sources of gravity wave activity.

### 1.5.5 Atmospheric Tides

The sun and the moon exert periodic external forces on the Earth's atmosphere. In the case of moon these forces are mainly gravitational, however, sun exerts a strong thermal effect but a much weaker gravitational effect. Atmospheric tides are global-scale oscillations in the atmosphere which have periods that are submultiple of the solar or lunar day. Lunar (gravitational) tides are much weaker than solar (thermal) tides but are responsible for the periodic motion of the Earth's oceans. This effect of lunar tides on oceans is greater than the effect on the Earth's atmosphere. Solar tides are of two types: migrating and non-migrating. Migrating tides are sun synchronous, which means that they propagate westwards with the apparent motion of the sun as seen by a stationary observer on the ground. On the other hand, non-migrating tides do not follow the apparent motion of the sun. Non-migrating tides can propagate either eastwards or westwards or remain stationary and are mainly generated by differences in topography with longitude, land-sea contrast, surface interaction, wind shears, and convection in the tropics.

The large-scale dynamics in the MLT are dominated by the solar atmospheric tides. At any given height, the day-night variation in the absorbed radiation due to differential heating gives rise to periods which are integral subharmonics of a solar day: 24 hours, 12 hours, 8 hours, and are referred to as the diurnal tide, semidiurnal tide, terdiurnal tide, respectively. In the MLT region the tide is mainly semidiurnal whereas in the thermosphere it is diurnal [*Hargreaves (1992)*]. The solar atmospheric tides are excited by periodic

absorption of solar radiation of different spectral range at different altitudes e.g., near infrared by tropospheric water vapour, ultraviolet by stratospheric ozone, and extreme ultraviolet by the major constituents like O<sub>2</sub> and N<sub>2</sub> in the lower thermosphere [e.g., *Forbes and Groves (1987)*; *Forbes (1995)*]. They are also excited by large-scale latent heat release associated with deep convective activity in the troposphere, nonlinear interactions between global-scale waves [e.g., *Hagan et al. (2001)*; *McLandress et al. (2000)*], interactions between tides and gravity waves [e.g., *McLandress and Ward (1994)*], and to a lesser extent gravitational pull of the Sun.

Subsequent to the seminal work on the classical tidal theory by *Chapman and Lindzen (1970)* many researchers investigated the sources for tidal generation, propagation, its effect on middle atmospheric dynamics, and dissipation in the atmosphere through realistic models and observations. The effect of tides has been investigated using oscillations in density, temperature and horizontal winds from ground-based observations [e.g., *Fukao et al. (1980)*, *Vincent et al. (1998)*; *Sasi et al. (1998)*, *Sasi et al. (2001)*; *Deepa et al. (2006)*], satellite-based observations [e.g., *McLandress and Zhang (2007)*], and rocket-borne measurements [e.g., *Sasi and Krishna Murthy (1990)*].

These studies have contributed a lot to our understanding of tides and their effect in the upper atmosphere. However, due to complex nature of wave dynamical processes, coupling, and wave filtering due to ambient winds etc., a comprehensive understanding of tides especially at low latitudes is far from complete.

### 1.5.6 Planetary Waves (PWs)

Planetary waves (PWs) are large-scale oscillations in the atmosphere and are not tied to the location of sun and oscillate with a integral number of cycles wrapped around a circle of latitude. The horizontal propagation of PWs can either be traveling eastwards/westwards or remain stationary with re-

spect to the background zonal flow. Stationary PWs are forced modes, excited and maintained in the troposphere by topographic features such as mountain ranges and the differences in land/ocean heating. Traveling PWs are normal modes, generally have periods which are natural resonances of the atmosphere. The normal modes have periods which include quasi 2-day, 5, 10, and quasi 16-day waves [e.g., *Geisler and Dickinson (1976)*; *Wu et al. (1994)*; *Salby (1996)*; *Murphy et al. (2007)*]. PWs are often called as Rossby waves and are generated due to the latitudinal gradient of the Coriolis force that balances variations of the pressure gradient force. These waves show westward phase propagation and are strongly dispersive. Those waves which have faster speeds are usually trapped and do not propagate vertically. In contrast, the slowest planetary waves forced by surface inhomogeneities and/or surface temperature are locked to particular locations, are called quasi-stationary waves and have higher chances of propagating into the middle atmosphere [*Forbes (1995)*]. These wave are present mainly at middle- and high-latitudes, although sometimes they can move to lower latitudes. They control the dynamics at lower and middle atmospheres. At higher altitude the role of gravity waves become more important.

Kelvin waves (KW) are eastward propagating planetary scale waves and are generated due to the balancing of the Coriolis force against the waveguide at the equator. KWs are mainly trapped at low-latitudes, away from the equator, their wave amplitudes decay steeply, meridional velocity component vanishes, and zonal velocity fluctuates. These waves are non-dispersive which means that the phase speed of the wave crests is equal to the group velocity at all frequencies. KWs can be classified mainly into three types, namely, slow (periods of 10 to 20 days), fast (6 to 10 days), and ultra-fast (3 to 5 days). The vertical wavelengths of slow and fast KWs are small and are confined to the middle atmosphere below the stratopause [*Salby et al. (1984)*]. Slow KWs play an important role in the lower stratosphere dynamics, e.g., in forcing the quasi-biennial oscillation (QBO). Fast KWs are noticeable in the entire strato-

sphere. On the other hand, ultra-fast KWs play a major role in the vertical coupling of the atmospheres [e.g., *Forbes* (2000)]. Since ultra-fast KWs have very large vertical wavelengths these waves are capable of propagating upwards and reach in MLT region or higher (e.g, *Hirota* (1978), *Hirota* (1979); *Forbes et al.* (2009)] providing the coupling of the MLT region with the equatorial lower atmosphere.

In the MLT region, similar to gravity waves and tides, planetary waves can attain large amplitudes (of the order of tens of  $\text{ms}^{-1}$ ). The vertical propagation depends on zonal flow and is governed by wave/mean flow interactions. Majority of the traveling PWs are westward propagating, therefore they can propagate up through the eastward winds of the winter stratosphere and can ascend out of the troposphere and reach in MLT region. However, during summer their vertical propagation is restricted by westward winds of the summer stratosphere [e.g., *Charney and Drazin* (1961); *Salby* (1996)].

Owing to large horizontal wavelengths and amplitudes, PWs are an important feature in the atmosphere since they transport chemical species over long distances horizontally. Further, these waves are also known to modulate temperatures in the atmosphere and drive the poleward meridional flow in the lower stratosphere. As will be described later, PW activity acts to cause sudden stratospheric warmings (SSW) and breaks down the polar vortex at the end of winter in the northern hemisphere. The distribution of continents and topography of the northern hemisphere produces more PW activity as compared to that in the southern hemisphere. Some part of this thesis includes work related to the residual circulation in MLT region that exists during SSW events.

## 1.6 Long Time Scale Oscillations in the MLT region

As discussed earlier, winds are closely associated with the temperatures through the thermal wind balance. Long-term oscillations such as semiannual, annual, and quasi-biennial oscillations (SAO, AO, and QBO), are important features of the middle atmosphere and have been observed in both wind and temperature data. These oscillations primarily originate due to the interplay of planetary waves with the background wind and other waves. A brief description of these long-term oscillations in the middle atmosphere is given in following paragraphs.

SAO has periods of around 6 months and was first observed by *Reed (1966)* in the middle atmosphere using zonal wind data obtained by rocketsonde observations. Subsequent to this work using wind and temperature data it was shown that SAO is present throughout the mesosphere [e.g., *Groves (1972)*; *Hirota (1978)*; *Garcia et al. (1997)*]. In the tropical middle atmosphere, the mesospheric semiannual oscillation (MSAO) in the mean zonal winds is an important feature which is thought to be driven by the propagation of small-scale gravity waves through the wind system of the stratospheric semiannual oscillation (SSAO) [e.g., *Garcia et al. (1997)*; *Remsberg et al. (2002)*]. The MSAO is out of phase with the SSAO over the equatorial latitude [e.g., *Garcia et al. (1997)*]. This has been explained as follows: the eastward zonal mean wind in the stratosphere suppress waves which transport eastward momentum and allow propagation of those waves which transport westward momentum and vice versa. The forcing of the MSAO is not so well understood, but it is believed to be entirely wave driven. It is believed that the selective transmission of gravity and Kelvin waves by the SSAO is responsible for driving of the MSAO [*Dunkerton (1982)*]. However, due to sparse observations, there is scant evidence about the driving mechanism and the kind of waves that drive these oscillations are not completely understood. The Annual Oscillation (AO) is

also observed in middle atmosphere which have a period of around 12 months. The annual oscillation in the mean zonal wind is fundamentally driven by the annual cycle in solar insolation [*Andrews et al. (1987)*].

The quasi-biennial oscillation (QBO) is a tropical phenomenon of downward propagating westward and eastward winds in the equatorial stratosphere with a variable period from 22 to 34 months, with an average period of approximately 28 months [e.g., *Baldwin et al. (2001)*]. QBO is a fascinating example of a coherent, oscillating mean flow that is driven by propagating waves with periods unrelated to that of the resulting oscillation. Mesospheric variability is also affected by QBO by selectively filtering waves that propagate upward through the equatorial stratosphere. It is now believed that a combination of gravity, Kelvin, Rossby-gravity, inertia-gravity, and smaller-scale gravity waves provide most of the momentum flux needed to drive the QBO [*Dunkerton (1997)*]. In the tropical troposphere, these waves originate due to convection which are characterized by a variety of vertical and horizontal wavelengths and phase speeds, propagate into the stratosphere, transporting westward and eastward zonal momentum. Most of the zonal momentum is deposited at stratospheric altitudes which drives the zonal wind anomalies of the QBO. For each wave, the vertical profile of the zonal wind determines the critical level at or below which the momentum is deposited. Some gravity waves propagate through the stratosphere and produce a QBO near the mesopause known as the mesospheric QBO (MQBO). MQBO in the upper mesosphere is observed using satellite observations from the High Resolution Doppler Imager (HRDI) on-board Upper Atmosphere Research Satellite (UARS) [*Burrage et al. (1996)*].

Figure 1.7 summarizes the amplitude of the various equatorial oscillations in zonal wind as a function of height. The annual cycle (dotted curve) is relatively small in the stratosphere (around  $5 \text{ ms}^{-1}$ ). The stratospheric QBO is shown from 16 to 40 km, peaking near  $20 \text{ ms}^{-1}$  at about 25 km. The MQBO is based on UARS/HRDI observation [*Burrage et al. (1996)*], SAO is based on



rocket observation at Ascension Island [[Hirota \(1978\)](#)], and the AO is after COSPAR International Reference Atmosphere [1986].

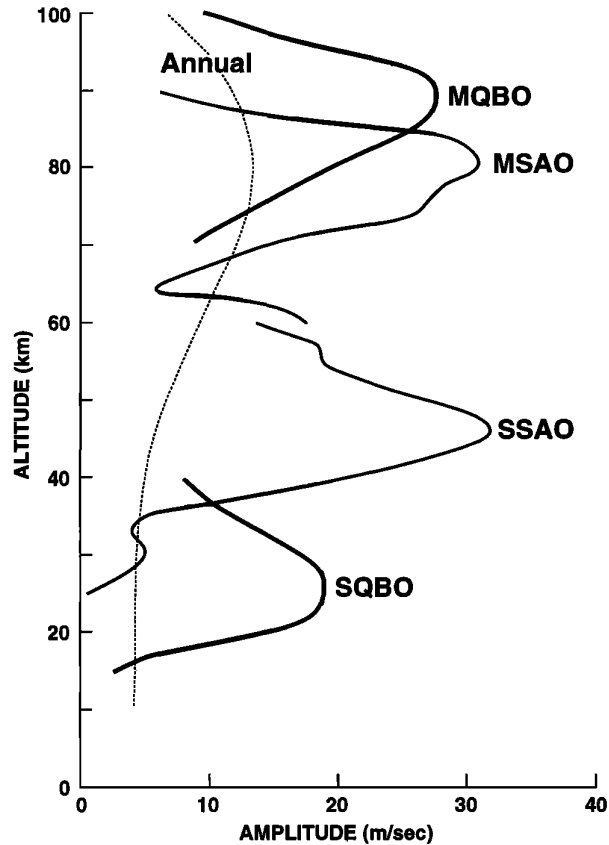


**Figure 1.7:** Vertical distribution of the amplitude of the MQBO, MSAO, SSAO, SQBO, and annual component at the equator [Adapted from [Baldwin et al. \(2001\)](#)].

In addition to these waves and oscillations, the MLT region is influenced by the cyclic variations in the sun. The MLT region is mainly affected by the extreme ultra-violet (EUV) solar energy input. There are some indices which are used for the measurement of activity level of the sun. In this work, solar 10.7 cm radio flux (F10.7) and sun spot number (SSN) is used for the proxy for the solar EUV and solar activity. It will be shown later in this thesis that the MLT parameters show the variations similar to those seen in F10.7 and SSN.

## 1.7 Sudden Stratospheric Warming (SSW)

As discussed above upward propagating waves of various timescale from the troposphere under the suitable zonal wind mean flow can cause dramatic events throughout the atmosphere starting from the lower to the upper atmospheric regions. The sudden stratospheric warming (SSW) is such a dynamic phenomenon which occurs mainly in the northern winter months as a result of the interaction between upward propagating planetary Rossby waves with the stratospheric zonal mean flow that can cause a reversal of the polar stratospheric zonal mean flow and even subsequent breakdown of the polar vortex [e.g., *Matsuno (1970)*]. The primary mechanism suggested by *Matsuno (1971)* is widely accepted mechanism of SSW which is shown to be induced by the interaction of planetary waves and the mean flow.

In general, the mean zonal wind is eastward and zonal mean temperature show a negative poleward gradient in the stratosphere during wintertime. However, during SSW events, westward forcing from upward propagating Rossby waves weaken the background mean winds and drives a poleward flow. The breaking of these waves in the stratopause forces adiabatic downwelling and warming over pole which makes positive poleward temperature gradient [*Matsuno (1971)*]. The two main defining characteristics of SSW events are reversal of the latitudinal temperature gradient and the zonal mean winds in the stratosphere [e.g., *Labitzke (1972)*, *Andrews et al. (1987)*]. An SSW event is called ‘minor’ if the mean temperature at or below the 10 hPa pressure level ( $\sim 32$  km) poleward of  $60^\circ$  rises by at least 25 K within a period of a week. An event is considered as ‘major’ if in addition to increased temperatures, zonal mean eastward winds reverse at these altitude and latitude region [*McInturff (1978)*; *Labitzke (1981)*]. However, due to less land-sea contrasts the planetary waves have smaller amplitudes in the southern hemisphere than in the northern hemisphere. Due to this dissimilarity the southern polar stratosphere is less disturbed and polar vortex is colder and more stable than the northern

polar stratosphere in winter months. This make SSW events mainly a northern hemispheric polar stratospheric phenomenon. Extensive observational and theoretical investigation of SSW events can be found in several review articles [e.g., *Matsuno (1971)*; *Holton (1980)*; *McIntyre (1982)*; *Andrews et al. (1987)*; *Labitzke and Van Loon (1999)*].

Figure 1.8 shows the temperature in the polar cap poleward of  $60^{\circ}\text{N}$  and longitudinally averaged zonal wind at  $60^{\circ}\text{N}$  from Modern Era Retrospective-analysis for Research and Application (MERRA) reanalysis data for the month of January 2013. It can be noted from Figure 1.8 that there is a significant enhancement in the temperature and reversal of zonal wind during January 2013 which shows that the 2013 event was a major SSW event.

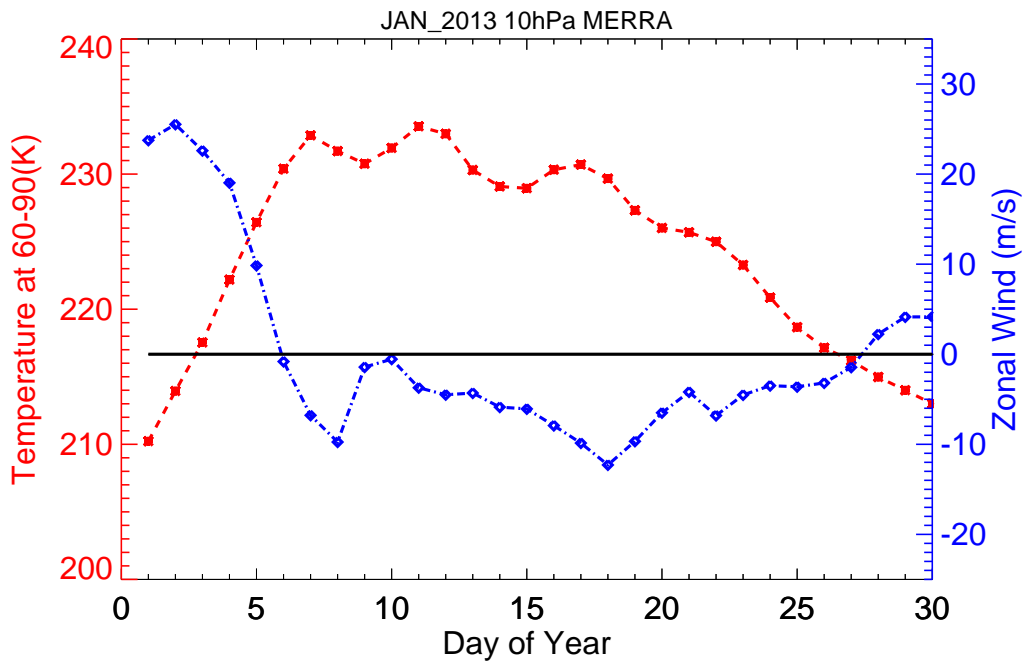


**Figure 1.8:** Temperatures in the polar cap poleward of  $60^{\circ}\text{N}$  and longitudinally averaged zonal wind at  $60^{\circ}\text{N}$  at 10 hPa pressure level ( $\sim 32$  km) obtained from MERRA dataset for the month was January 2013.

SSW can affect the vertical thermodynamical coupling in a large range of altitudes and latitudes in the middle atmosphere which causes significant variations in the MLT region. During SSW events, high-latitude stratosphere-

mesosphere system have been well researched. However, behaviour of tropical- and low-latitude middle atmosphere during SSW events are not well understood. Using Nimbus III satellite data *Fritz and Soules (1970)* showed an association between the high-latitude stratosphere warming and the tropical/equatorial summer hemisphere cooling. *Mukhtarov et al. (2007)* investigated the latitudinal structure of the stratospheric anomalies and showed that stratospheric warming at high-latitudes are associated with coolings at low-, mid-, and tropical-latitudes. They also found that deceleration/reversal of the eastward mean zonal winds at high-latitudes are associated with the amplification of the eastward flow at low-, mid-, and tropical-latitudes.

In the mesosphere, *Matsuno (1971)* modelling study show that there is a mesospheric cooling at high-latitude accompanying the SSW. Since then a number of observational and modelling studies describe the occurrence of a mesospheric cooling accompanied with SSWs [*Gregory and Manson (1975)*; *Myrabø et al. (1984)*; *Whiteway and Carswell (1994)*; *Walterscheid et al. (2000)*; *Liu and Roble (2002)*; *Hoffmann et al. (2007)*; *Siskind et al. (2010)*]. These studies indicated alternating regions of cooling and warming above the main warming in the lower stratosphere during SSW events at high-latitudes. The inter-hemispheric coupling and mesospheric temperatures in the summer hemisphere was also investigated during SSW events [e.g, *Karlsson et al. (2007)*, *Karlsson et al. (2009)*; *Körnich and Becker (2010)*]. They observed a decrease in the occurrence of polar mesospheric clouds due to the lowering of the residual circulation resulting in a positive temperature anomaly in the summer polar mesopause region. Due to paucity of datasets the low- and tropical-latitude MLT region is least explored especially during SSW events. In this work, an attempt has been made to understand latitudinal variations in MLT temperatures during SSW events which will be discussed in Chapter 5.

## 1.8 Mesospheric Inversion Layers (MILs)

The mesospheric inversion layers (MILs) also known as mesospheric temperatures inversions (MTIs) are the narrow thermal layers showing an inversion of the vertical temperature gradient from negative to positive which are formed in the middle atmosphere. The name of *inversion layers* was termed for these events since their appearance was very similar to that of *inversion layers* seen in tropospheric temperature profiles near the ground [e.g., [Meriwether and Gerrard \(2004\)](#)]. These MILs are seen in the MLT region at the low- and mid-latitudes at any time of the year. A typical structure of a MIL profile which might be observed with a Rayleigh/Na lidar system is depicted in Figure 1.9. MIL phenomenon was originally identified as a single layer near 70 km (lower MIL) with a typical thickness of 10–15 km and temperature enhancement of 20–100 K. The availability of more complete measurements of the temperature structure in the MLT region have indicated that multiple layers are more generally observed rather than a single layer near 70 km.

Reviews which deal with various aspects of MTIs can be found in the literature [e.g., [Meriwether and Gardner \(2000\)](#); [Meriwether and Gerrard \(2004\)](#)]. The formation mechanism for MTIs are quite complex and has been a subject of debate since their first detection. Till now it is very difficult to pin point the reason for the occurrence of MTIs. The causative mechanisms for the formation of MTIs are believed to be due to: nonlinear gravity wave-tidal interactions; dissipating planetary Rossby waves; chemical heating; and gravity wave breaking [e.g., [Meriwether and Mlynczak \(1995\)](#); [Meriwether and Gardner \(2000\)](#); [Meriwether and Gerrard \(2004\)](#); [Ramesh et al. \(2013\)](#); [Sharma et al. \(2016\)](#)]. Sometimes, more than one of the suggested process may also be operative.

In general, it is found that the upper MIL (found at higher altitudes between 85 and 100 km) is generated by gravity wave-tidal interactions since tidal amplitudes at these altitudes are much larger. However, the lower MIL

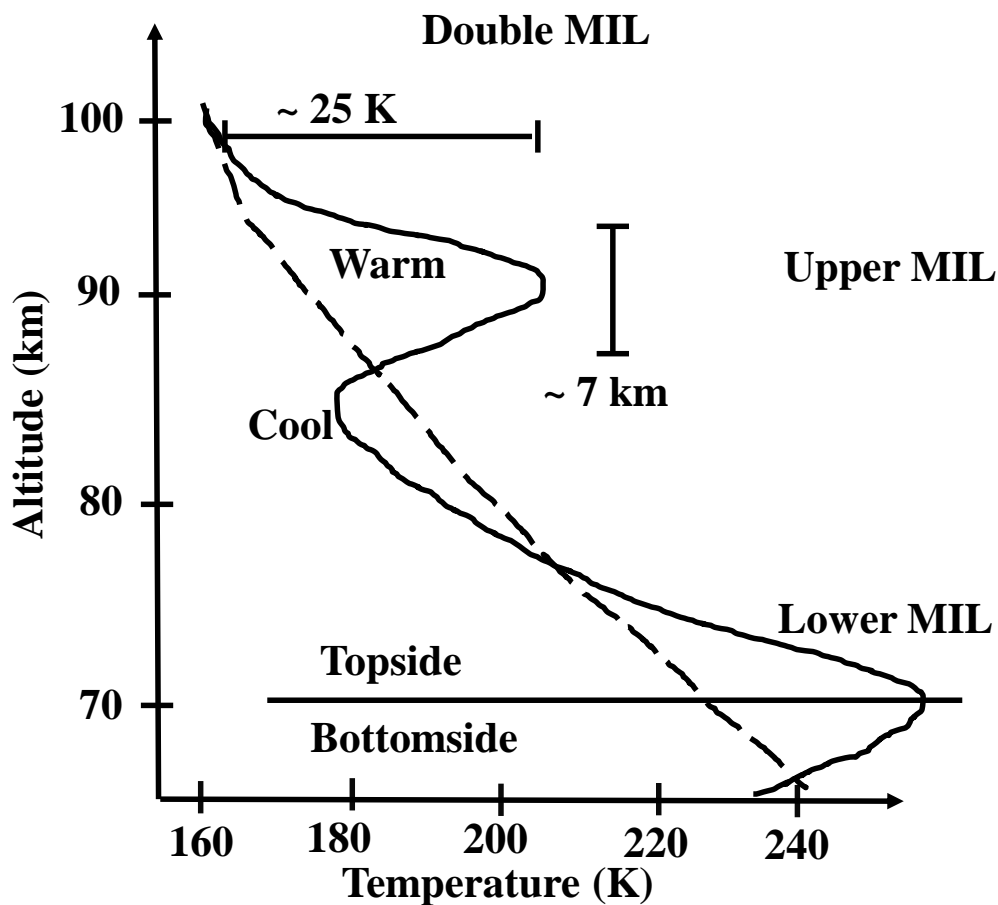


**Figure 1.9:** Schematic of upper and lower mesospheric inversion layers seen in the temperature profile for the MLT regions. Solid/dotted lines show with and without MILs [Adapted from *Meriwether and Gerrard (2004)*].

(found at lower altitudes between 65 and 80 km) is generated by planetary wave since at these altitudes planetary waves begin to break as the phase speed of the wave matches that of the zonal wind flow, thus forming a critical level. In addition to the dynamics, the energy budget of MLT region is also influenced by chemistry. For the formation of upper MILs chemical heating plays an important role and is a potential causative mechanism due to several exothermic chemical reactions. In this work, some effort has been made to understand the causative mechanism of MTIs based on our observation which will be discussed in one of the later Chapters.

## 1.9 Measurement Techniques for MLT investigation

The observables in the MLT region are kinetic temperatures, neutral density, horizontal winds, and airglow emission intensities. Measurement of these parameters have been carried out either by using remote sensing techniques (ground- and space-based) or *in situ* using rockets. However, each of these techniques have their own limitations e.g., ground-based/rocket-borne observations provide limited geographic coverage but high temporal/vertical resolution. Long-term high data cadence ground-based observations provide a great deal of information about local time variations of a given phenomenon. Satellite-based observations provide a global/near-global picture but suffer from poor time resolution.

There are two remote sensing techniques namely active and passive which have been widely used for the MLT investigations. In active remote sensing techniques, electromagnetic signals are transmitted into the atmosphere and the atmospheric parameters are retrieved from the return echoes. Whereas, in passive remote sensing techniques, atmospheric parameters are derived from the measurement of the naturally occurring radiations without disturbing the atmosphere. The various remote sensing techniques applied for the observations of MLT region are briefed below.

### 1.9.1 Ground-based Techniques

One of the widely used passive remote sensing techniques for the MLT investigations is observation of various airglow emissions which emanate from different altitudes. The various airglow emissions in the MLT region includes, OH Meinel band (around 87 km), sodium D line (around 92 km), O<sub>2</sub> atmospheric band emission (around 94 km), and oxygen green line (around 100 km). The details of these airglow processes will be discussed in subsequent

sections. The major source of database for present work is airglow emission intensities and derived temperatures from MLT region which is very useful mode of observing waves of various timescales. The derivation of temperatures from OH(6-2) band emissions and O<sub>2</sub>(0-1) atmospheric band emission is described in Chapter 3. A review of various techniques used to measure the airglow emission intensities and temperatures are also given in Chapter 3.

Radars and lidars are primarily used for the active ground-based observations of the MLT region. For the wind and temperature measurements in the MLT region two types of radars are commonly used, Meteor wind radar, which makes use of the reflection of radio wave pulses by meteor trails and provides observation of hourly zonal and meridional winds in the altitude range between 80 to 100 [e.g., [Kumar et al. \(2007\)](#)]. Meteor radars can also be used to estimate the temperature of the mesopause region by measuring the ambipolar diffusion of the meteor trails [e.g., [Hocking \(1999\)](#)]. Medium frequency (MF) radars use partial reflection that is caused by change in the refractive indices in the clear atmosphere and provide information on mesospheric winds in the altitude region of about 60 km to 100 km [e.g., [Vincent et al. \(1998\)](#); [Gurubaran and Rajaram \(1999\)](#)]. Most of the radars can operate in unattended mode round the clock and hence, they are able to provide information about the different wave dynamical features (gravity waves, tides, and planetary waves), other high-frequency variations, and long timescale oscillations. From lidars density variations as a function of altitude is measured from which vertical profile of the temperatures of stratosphere to lower mesosphere are obtained.

Over the years ground-based observations of MLT region have increased, but they are still not sufficient to provide a detailed global view. In order to understand MLT region in global perspective long-term systematic ground-based observations from different regions are required.



### 1.9.2 Rocket-borne Techniques

For *in situ* measurement of the MLT parameters, rocket sounding is the only technique with added advantage that it achieves very high vertical resolution. Rocket borne measurements includes measurement of neutral density fluctuations [e.g., [Lübken \(1992\)](#); [Lübken \(1997\)](#); [Rapp et al. \(2004\)](#)], ion density fluctuations [e.g., [Blix et al. \(1990\)](#)], electron density fluctuations [e.g., [Prakash et al. \(1972\)](#); [Sinha and Prakash \(1996\)](#); [Lehmacher et al. \(1997\)](#)], neutral wind measurements from vapour cloud release experiments [e.g., [Anandarao and Raghavarao \(1979\)](#); [Larsen \(2002\)](#)], and radar tracking of chaffs released by rockets [e.g., [Widdel \(1985\)](#)]. The rocket based experiments form various altitude regions provided a wealth of information of the MLT region. However, for the investigation of MLT region in recent decades the number of rocket borne experiments is reducing.

### 1.9.3 Satellite-based Techniques

Satellite-based observations mostly use passive remote sensing techniques and provide global coverage. Satellite-based instruments that are used for MLT investigations measure either emissions from the chemical species which are radiatively active or the occultation of solar (or stellar) radiation that reaches the satellite after passing through the Earth's atmosphere. Various satellite-based instruments have been used to probe the MLT region to obtain various atmospheric parameters e.g., airglow emission intensities, temperatures, line-of-sight horizontal winds. To obtain the vertical profile with good vertical resolution (a few km) limb scanning technique is used in many satellite-based observations. The satellites which have been extensively used for the MLT investigations are: Solar Mesosphere Explorer (SME; 1981-1989), Upper Atmosphere Research Satellite (UARS; 1991-2005), ODIN (2001-ongoing), Thermosphere Ionosphere Mesosphere Energetics and Dynamics satellite (TIMED; 2002–ongoing), and Envisat satellite (2002–2012). A lot of understanding of

the MLT dynamics is obtained by the analysis of the TIMED and Envisat satellite datasets which continue to function beyond their original design lifetime. In this work, to understand the MLT dynamics, mesospheric temperature data obtained from the TIMED and ODIN have been used. In addition, horizontal wind data is used which are obtained from the TIMED satellite.

## 1.10 Airglow emissions in MLT region

Airglow is a faint emission from upper atmospheric constituents i.e., atoms and molecules which are excited through photochemical or chemiluminescence processes. These atoms and molecules can be excited in direct (e.g., resonance emission) or indirect (e.g., chemical reactions) ways through the electromagnetic radiation coming from the sun. Chemical reactions due to interaction of incoming solar radiation with atoms and molecules present in the upper atmosphere produces chemiluminescence which in turn yields emissions at different wavelengths. Radiation emitted from airglow emissions are observed in infrared, visible, and ultraviolet wavelength regions. Majority of these airglow emissions emanate from the altitudes in the range of about 80 to 300 km with the brightest emission region concentrated at around 97 km altitude [*Chamberlain (1961)*]. A photograph of the nightglow emission in the visible part of the electromagnetic spectrum is shown in Figure 1.10. Aurora is mainly a high-latitude phenomenon observed as a consequence of solar disturbances such as the coronal mass ejection, wherein the energetic charged particles of solar origin enters the Earth's atmosphere due to magnetic reconnection. Aurora show structural features but airglow is uniform and is observed over all the latitudes. The spectral signatures of airglow and aurora consists of atomic lines and molecular bands of the neutral and ionized atmospheric constituents.

Airglow emissions take place when excited atmospheric species de-excite to their ground state by emission of photons. Many of these de-excitation processes are forbidden electric dipole transitions and therefore, the excited

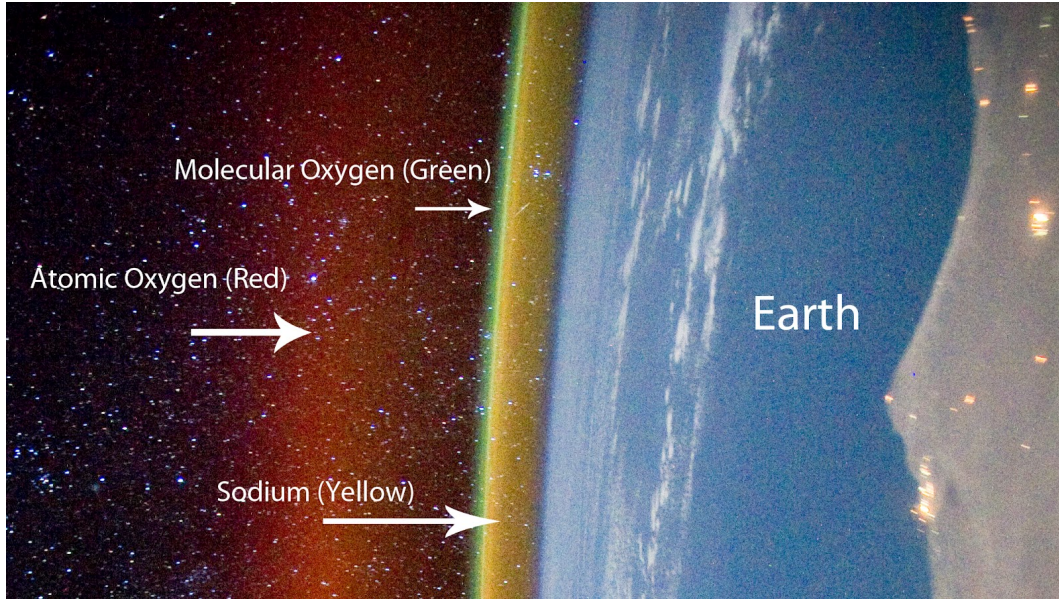


**Figure 1.10:** Red, green, and yellow airglow emission from the Earth's upper atmosphere photographed by the International Space Station. (<http://auroranightglow.blogspot.in/2012/05/night-glow.html>)

species return to their respective ground states via metastable transitions. Below certain heights in the Earth's atmosphere the energy of the excited state is lost due to the higher collision rate which is called quenching. Based on the time of occurrences, airglow is classified as dayglow, twilight glow, and nightglow. The various features of which are summarized in Table 1.2.

In this work, in order to understand coupling processes in the MLT region various nightglow emissions which emanate from this region have been

**Table 1.2:** Different types of airglow emissions

Type	Solar zenith angle	Excitation process	Intensities (Rayleigh)
Dayglow	$0^{\circ}$ - $90^{\circ}$	Photochemical reactions, Resonance, and fluorescence scattering	$\sim$ several $10^3$ R
Twilight glow	$90^{\circ}$ - $110^{\circ}$	Same as dayglow	$\sim$ several $10^2$ R
Nightglow	$>110^{\circ}$	Chemiluminescence	$\sim$ several 10's R

$$1 \text{ Rayleigh} = 10^6 \text{ photons.cm}^{-2}.\text{s}^{-1}$$

considered. Therefore, further discussion regarding airglow will be restricted to the nightglow in the MLT region. These nightglow emissions in the MLT region consists of several different atomic lines and molecular band emissions occurring at near infrared and visible wavelengths. The nightglow emission lines/bands which are pertinent to this work originates from OH, Na, O<sub>2</sub>, and OI (green line) emission layers in the MLT region. Based on the several sounding rocket and satellite-based observation Figure 1.11 shows the schematic of typical emission altitudes for these nightglow emissions in the MLT region.

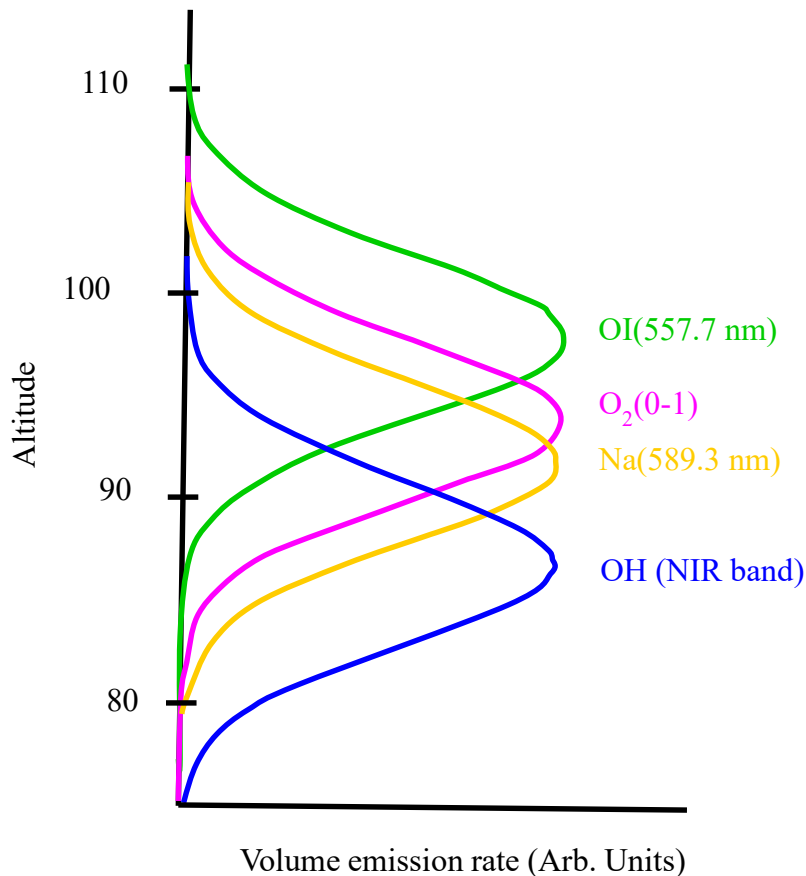


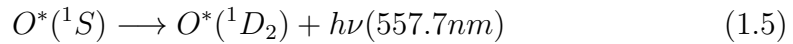
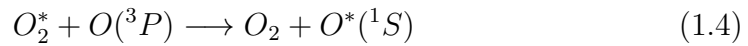
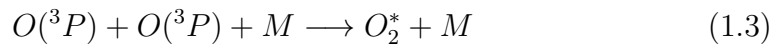
**Figure 1.11:** Schematic of the peak emission altitudes for the various nightglow emissions in the MLT region.

The mechanisms responsible for the generation of these nightglow emissions are described in the following section.

### 1.10.1 OI 557.7 nm Green Line Emission

The atomic oxygen green line nightglow emission (OI 557.7 nm) is the brightest line emission in the visible spectrum and was first to be observed among all airglow emissions in the atmosphere. This line was first identified by *McLennan and Shrum (1925)* to be due to the forbidden transition ( $^1S_0 \rightarrow ^1D_2$ ) of oxygen atom. This nightglow emission originates from two distinct layers, Mesopause region, around  $(97 \pm 10)$  km, and thermosphere, around 250 km which contributes around 20-30% of the total intensity, especially during space weather events over low- and equatorial-latitudes [e.g., *McDade (1998)*].

The excited state ( $^1S_0$ ) of the green line emission is produced by Barth mechanism which is a two-step process as given below [*Barth and Hildebrandt (1961)*; *Barth (1964)*; *Bates (1992)*]:



Where the third body M is  $O_2$  or  $N_2$  and \* is used to represent the excited state. OI 630.0 nm airglow emission can be produced by radiative transition of  $O(^1D_2)$  produced in reaction 1.5 to the ground state  $O(^3P)$ . But as shown in Figure 1.12 lifetime of  $O(^1D_2)$  state is quite large (110 sec.) hence, it loses its energy via collisions before it undergoes radiative transition at lower altitudes (below around 180 km). Therefore, at MLT altitudes OI 630.0 nm line is not observed since the neutral collision frequency is large enough for removal of  $O(^1D_2)$ .

### 1.10.2 O<sub>2</sub> (0–1) Atmospheric Band Emission

The peak of  $O_2(0-1)$  atmospheric band emission at 864.5 nm originates from a layer of  $(94 \pm 10)$  km altitude region [*Murtagh et al. (1990)*]. The  $O_2$  atmo-

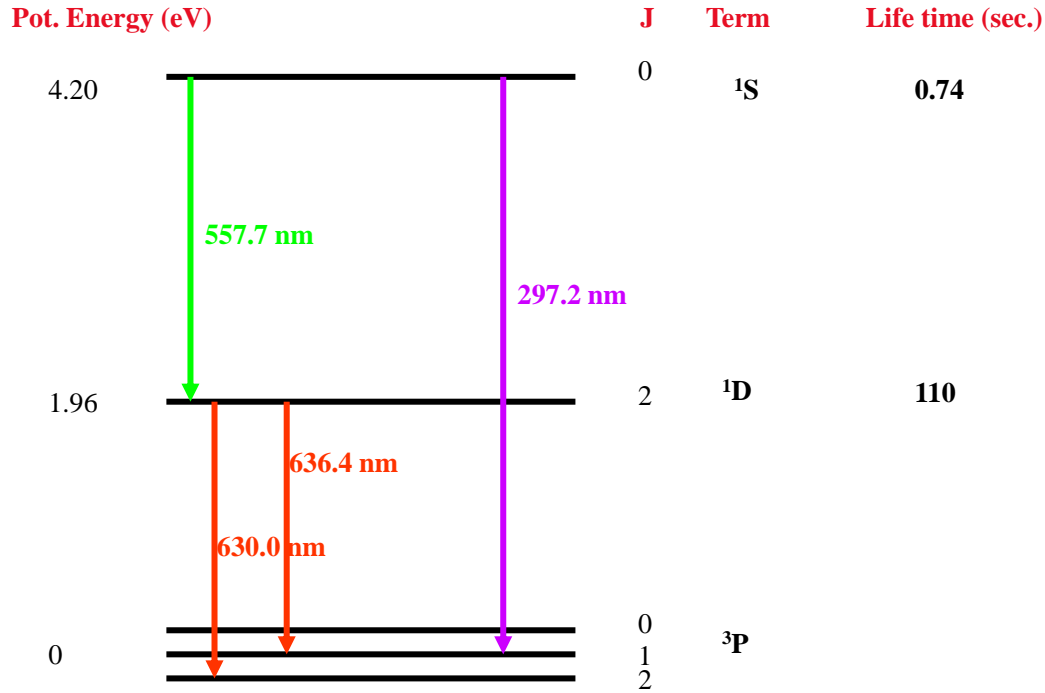
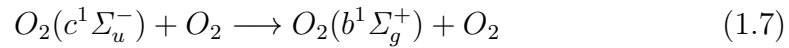
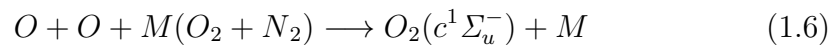
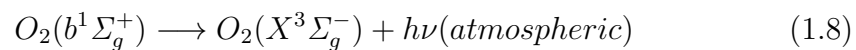


**Figure 1.12:** Schematic of the simplified energy level diagram along with various emissions of the atomic oxygen.

spheric band emission is a two-step process with a three body collision (Barth mechanism) required to place the  $O_2$  in an excited state [e.g., *Torr et al. (1985)*]:



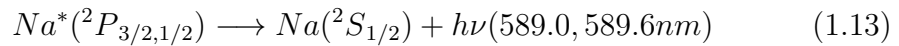
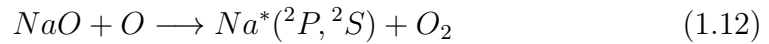
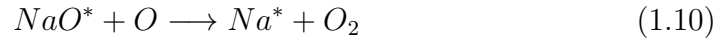
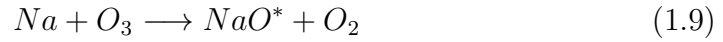
And the atmospheric  $O_2$  band emission results from de-excitation of the  $O_2(b^1\Sigma_g^+)$  state:



The lifetime of  $O_2(b^1\Sigma_g^+)$  state is about 12 sec. This ensures that the vibrational relaxation will be complete for the typical collision frequency in the mesopause region.

### 1.10.3 NaD Line Emission

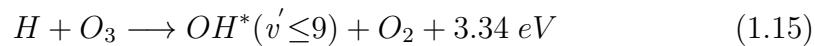
The yellow sodium doublet line (NaD) nightglow emission is a prominent emission in the MLT region. This nightglow originates at around 92 km altitude due to the presence of the neutral sodium which is believed to originate from meteor ablation in between 85 and 105 km altitude. The NaD emission arises from the atomic transition of Na which consists of two closely spaced lines, D1 and D2, at 589.0 nm and 589.6 nm wavelengths, respectively. The NaD nightglow emission is due to the following reactions which explains the conversion of neutral sodium to excited sodium atoms [*Chapman (1939)*; *Slanger et al. (2005)*]:



In this mechanism mesospheric ozone plays a major role which oxidises neutral sodium atom to produce NaO. NaO reacts with atomic oxygen to produce a mixture of excited and ground state of Na atom. Na emissions are the allowed transition with a lifetime of around  $2 \times 10^{-8}$  sec. The intermediary processes of 1.10 and 1.11 were introduced by *Slanger et al. (2005)* to explain the variations of the ratios of D1 and D2 line intensity. These processes were also found to be responsible for the night-to-night variations in the column integrated Na emission intensity [*Sarkhel et al. (2010)*]

### 1.10.4 OH Meinel Band Emission

The hydroxyl airglow was first identified by Meinel and is referred to as the Meinel bands of OH [*Meinel (1950)*]. The red and infrared emissions of Meinel bands are due to the vibrational-rotational transitions between the two levels of excited OH radicals in the ground electronic state of OH ( $X^2_{3/2,1/2}$ ). The production of OH\* ( $v' \leq 9$ ) at the mesopause altitudes is due to interaction of atomic hydrogen with ozone. The mechanism for OH Meinel band emission is given by [e.g., *Bates and Nicolet (1950)*; *Meriwether (1989)* and references therein]:



This OH\* de-excites to ground state at various vibrational levels. This reaction is the main cause for the destruction of ozone at night near the mesopause and the energy released is sufficient to excite the ground state OH to ninth vibrational state [*Bates and Nicolet (1950)*]. The hydroxyl emission layer is centered at  $86.8 \pm 2.6$  km with the thickness of the OH emission layer  $8.6 \pm 3.1$  km [*Baker and Stair Jr (1988)*].

## 1.11 Scientific Questions Addressed

The Earth's upper atmosphere, especially the Mesosphere Lower Thermosphere (MLT) from 60 to 110 km in altitude, is a region which is affected by complex interactions between photochemistry and dynamics. As mentioned in this Chapter MLT is probably the least explored regions of the Earth's atmosphere. In order to understand various processes in the MLT region such as, global- and residual- circulation, and energy budget, MLT dynamics plays



a very important role. MLT region provides a complex interface between the lower atmosphere and space environment. The interplay between these two inputs and processes that redistribute energy from the individual source region into the various atmospheric layers are not well understood. Therefore, it becomes important to quantify the influences from above (i.e., solar radiation) and from below (i.e., atmospheric waves) which affect the MLT region in various ways. In this thesis, efforts are made to understand following key scientific/technical issues pertaining to MLT region:

1. How large- and short-timescale waves and oscillations present in the MLT region can be quantified using airglow emission intensities and temperature measurements?
2. What are the solar influences on the MLT nightglow emission intensities and temperatures?
3. How are the lower and upper atmospheres coupled under varying background conditions?
4. What are the possible sources for the mesospheric temperature inversions?
5. What are the effects on the global mesospheric temperatures during sudden stratospheric warming (SSW) events?

## 1.12 Scope and Layout of the Thesis

In this thesis an attempt is made to primarily address the above mentioned five key questions. In order to do that the long-term ground-based observational database by couple of in-house built instruments is made use of. These instruments are being operated from PRL's optical aeronomy observatory at Gurushikhar in Mount Abu. In addition, supporting data from the satellite-based observations is made use of to obtain a broader context of our ground-

based measurements. This thesis consists of six Chapters, Chapter wise outline is given below.

**Chapter 1:** This thesis begins with a brief introduction of the various processes which are prevalent in the Earth's upper atmosphere with a greater emphasis on the mesosphere lower thermosphere (MLT) region. The various dynamical features in the MLT region e.g., temperature, wind, and wave dynamics are described. The importance of the MLT region in terms of its influence by both solar forcing from above and upward propagating waves from the lower regions of the atmosphere is highlighted. Different scale size waves (gravity waves, atmospheric tides, and planetary waves) are described in terms of their generation mechanisms and their influence in the MLT region. This is followed by a brief description of long-time scale oscillations in the MLT region. A brief overview of sudden stratospheric warming and their effect in the MLT region at different altitudes are described. The MTI phenomenon and its possible cause in the MLT region is discussed. Various remote sensing techniques that are available and commonly used for probing the MLT region have been briefly reviewed these includes observations from ground-based, rocket-borne, and satellite-based platforms. Information on the airglow processes focussed on the nightglow emissions in the MLT region is provided. Literature, both old and recent, has been surveyed so that one can appreciate the importance of results obtained in this thesis work. This Chapter, thus, gives a broad background of the work that has been carried out earlier to put into context the significance of the results from this thesis work.

**Chapter 2:** Investigations of the MLT region have been carried out by making use of passive remote sensing techniques. There are primarily three techniques namely, photometry, spectroscopy, and interferometry which are used for the passive remote sensing of the MLT region. The parameters which have been obtained using these techniques are nightglow emission intensities and temperatures. **Chapter 2** describes the development of two in-house built optical instruments namely, Near Infrared Imaging Spectrograph (NIRIS) and

CCD-based Multi-Wavelength Airglow Photometer (CMAP). Calibrations of the instruments have been carried out and data analysis methods to derive the desired parameters from these instruments are developed. Calculation of nightglow emission intensities from the raw data obtained from NIRIS and CMAP is discussed. Theory of mesospheric temperature determination and the derivation of mesospheric temperatures from the NIRIS obtained spectra are provided in this Chapter. Supplementary datasets used in this work, which are mainly from satellite-based observations, and from reanalysis dataset are described. Time series analyses methods namely Lomb-Scargle analysis and wavelet analysis that are used to derive the periodicities present in the time series data are also be discussed in this Chapter. The application of these spectral analysis methods is demonstrated by using sample data to obtain various wave parameters from the data.

**Chapter 3:** This Chapter deals with the results that are obtained from the NIRIS data from over three years (2013-2015) of observations from a low-latitude location, Gurushikhar, Mount Abu. NIRIS obtained mesospheric airglow intensities and corresponding rotational temperatures (obtained from O<sub>2</sub> and OH nightglow emission intensities) over this period have been utilized to derive the characteristics of large-time scale fluctuations at the mesospheric altitudes. The statistical analysis of short-time scale fluctuations is carried out by obtaining the periods that are present on each of the individual nights. Both, results that are obtained using long-term optical and radio data sets, and, those that are obtained by the analysis of data over short durations, are described in this Chapter. Appropriate background to appreciate the results arrived at in this study are also given.

**Chapter 4:** The processes of atmospheric coupling during cyclonic events are very important, and yet are poorly understood. Simultaneous ground-based observations of high data cadence from many emission wavelengths which emanate from different altitudes thus provide a means to understand such an event. An unambiguous signature of vertical coupling of the atmo-

sphere has been obtained during a cyclonic event which had developed in the Arabian Sea during 25-31 October 2014. For this event we have derived all gravity wave parameters based on the experimentally observed values. In addition to these experimentally derived GW parameters, we have also empirically calculated the vertical wavelength of the wave, by observing the downward phase propagation in the airglow emission intensities and by using linear gravity wave dispersion relation, which are found to be consistent with one another. Thus, **Chapter 4** will describe the results on atmospheric coupling during events with external sources of energy, such as cyclonic storms, in the troposphere.

**Chapter 5:** This Chapter describes the latitudinal distribution of the mesospheric temperature during sudden stratospheric warming (SSW) events which have been accomplished by using satellite-based observations in conjunction with ground-based observations. NIRIS derived mesospheric temperatures from Gurushikhar showed enhanced temperatures (compared to their monthly mean values) during the SSW event of January 2013. This led to a wider investigation to understand mesospheric temperature behaviour over different latitudes during SSW events. The “double-humped” structure in the mesospheric to stratospheric temperature ratios vs latitude is found with two crests over tropical- to mid-latitudes and a trough over the geographic equator and is very distinct during major SSW events. Mesospheric temperatures during minor events do not show formation of such “double-humped” structure. The results presented in this Chapter strongly support the interactions in stratospheric-mesospheric coupling and high- to low-latitude coupling of mesosphere lower thermosphere region, especially during SSW events.

**Chapter 6:** In **Chapter 6**, the summary of findings of this work and scope for the future is provided. The results reveal new information on the interaction within the mesosphere, the mesospheric effects due to tropospheric convective instabilities, and stratospheric energy sources. The results from this thesis provided new insights in terms of vertical coupling of atmospheres,

high- to low-latitude coupling and seasonal and solar activity dependence of the mesospheric dynamics. There is a large scope for both experimental and simulation/modelling studies. This Chapter will elicit some of these aspects.



# Chapter 2

## Instrumentation and Data Analysis

### 2.1 Introduction

Airglow intensity and temperature variations in time and space have a great potential in understanding the complex upper atmospheric dynamics at their altitudes of emissions. It is now understood that the waves of different scales, such as planetary, tidal, and gravity waves play an important role in the transfer of energy and momentum between various atmospheric layers and thereby modulate density and temperature while passing through the airglow emitting altitudes [e.g., *Krasovskij and Šefov (1965)*; *Hines (1974)*]. Various observations and models over the years have provided some information on the gravity waves, however, their effects at mesospheric altitudes over low-latitudes is yet to be understood comprehensively.

Various coupling processes, which are prevalent in the Earth's upper atmosphere, as discussed in Chapter 1 have been investigated and characterized by making use of nightglow emission intensities at multiple wavelengths and mesospheric temperatures derived from OH and O<sub>2</sub> band emissions. This Chapter deals with the measurements of these parameters from ground- and

space-based instruments, which have been used in this work. These parameters were obtained from ground-based observations which have been carried out using: (1) Near Infrared Imaging Spectrograph (NIRIS), and (2) CCD based Multi-Wavelength Airglow Photometer (CMAP). These two instruments were developed in-house at Physical Research Laboratory, and are being operated from PRL's optical astronomy observatory at Gurushikhar, Mount Abu (24.6°N, 72.8°E). These observations were supplemented by satellite-based observations in order to understand the global nature of some of the atmospheric phenomena. In this Chapter, details of NIRIS and CMAP are given, process followed for the determination of nightglow emission intensities, derivation of mesospheric temperatures, and data analysis methods are described. Also a brief description is given on the supplementary datasets used for the investigations described in this thesis.

## 2.2 Near InfraRed Imaging Spectrograph (NIRIS)

NIRIS is designed and developed at the Physical Research Laboratory for the measurement of mesospheric nightglow emission intensities and corresponding rotational temperatures using OH(6-2) Meinel and O<sub>2</sub>(0-1) atmospheric band spectra [*Singh and Pallamraju (2017a)*]. In this spectrographic technique rotational line ratios are obtained to derive temperatures corresponding to the emission altitudes of 87 and 94 km, respectively. Hence, simultaneous measurements of variations in these two emissions provide an opportunity to investigate the wave features corresponding to vertical propagation of gravity waves.

NIRIS is a grating spectrograph which uses 1200 lines mm<sup>-1</sup> grating as the dispersing element, a 1024×1024 pixels thermoelectrically cooled CCD camera, and has a large field-of-view (FOV) of 80° along the slit orientation. NIRIS



has a spectral resolution of 0.78 nm at 840 nm wavelength. Figures 2.1a and 2.1b show the optical layout of NIRIS and its photograph. The details of the optical components used in NIRIS are provided in Table 2.1. The details of the various components used in NIRIS are described in following section.

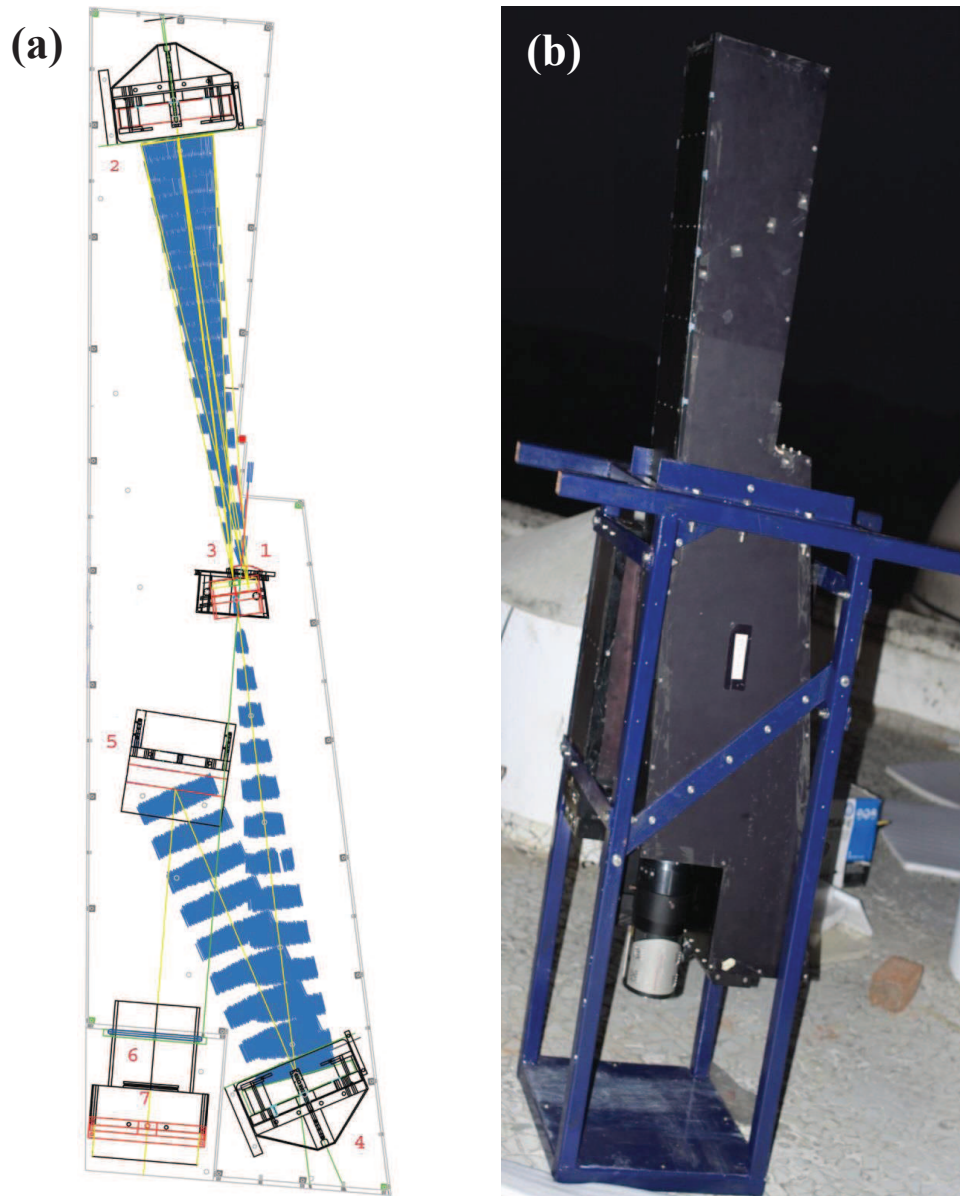


**Figure 2.1:** (a) Optical layout of Near InfraRed Imaging Spectrograph (NIRIS). Different components used in NIRIS are numbered, the details of which are given in Table 2.1. (b) Photograph of NIRIS on a mounting platform at the time of installation for the field operations.

### 2.2.1 Primary mirror

A convex spherical primary mirror (labelled 1 in the Figure 2.1a) in the front-end of NIRIS is used to reflect the incident beam of light onto a concave spherical secondary mirror (2). The radius of curvature of this mirror is 20 mm which allow the entry of incoming light from a large FOV.

**Table 2.1:** Characteristics of Near Infrared Imaging Spectrograph (NIRIS)

<b>1. Primary mirror</b>	Convex; r=20 mm
<b>2. Secondary Mirror</b>	Concave; f=600 mm, diameter=150 mm
<b>3. Slit</b>	45 mm×1 mm
<b>4. Collimator</b>	Off-axis paraboloid; f=600 mm, diameter=130 mm
<b>5. Diffraction Grating</b>	Plane; 120 mm x 100 mm; 1200 lines mm <sup>-1</sup>
<b>6. Converging Optics</b>	Schmidt telescope; f=139 mm, diameter= 100 mm
<b>7. CCD Detector</b>	1024×1024 pixels deep depleted; 13 μm pixel size, QE at 840 nm= 90%
<b>Resolution =0.78 nm at 840 nm wavelength</b>	

### 2.2.2 Secondary Mirror and slit assembly

The incoming light from a large FOV which is arriving from the convex primary mirror is allowed to fall on a concave spherical secondary mirror (2) which has a focal length of 600 mm. This secondary mirror focusses the light from a large FOV ( $\sim 80^\circ$ ) onto the slit of a size of 45 mm×1mm (3). This arrangement provides instrument's FOV of around  $80^\circ$  along the slit orientation for an all-reflecting optical design. Covering a large FOV in a grating spectrograph has a consequence of introducing deformation in terms of curvature in the image at the image plane. This curvature effect arises due to the differences in the angles of the rays between the center of the slit to those coming from locations away from the slit onto the grating facet. These angles of incidences form different angles on the grating, which results in deviations of the angles of diffraction that fall on the image plane. Therefore, to reduce this curvature effect, the slit is curved in opposite sense. This arrangement reduces curvature effect as incident on the detector to a large extent.

### 2.2.3 Off-axis Paraboloid

A 600 mm focal length off-axis paraboloid (4) is used as a collimator. The rays coming from the curved slit are allowed to fall on to this off-axis paraboloid which makes a parallel beam of light, which fall on the reflection grating (5).

### 2.2.4 Diffraction Grating

Diffraction grating works on a principle of spatial modulation of refractive index, thereby, separating polychromatic light into its monochromatic components. In NIRIS we have used reflection grating with a groove density of 1200 lines  $\text{mm}^{-1}$  which provides spectral image onto to the image plane. The geometry of a typical reflection grating and its various parameters are depicted in Figure 2.2.

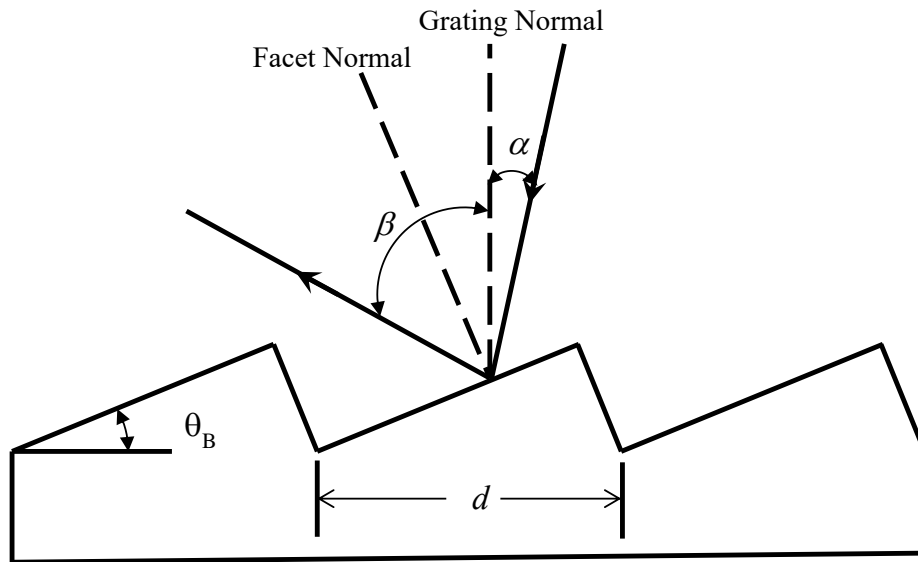


**Figure 2.2:** Schematic of a reflection grating.  $\alpha$  is the incident angle,  $\beta$  is the diffraction angle,  $\theta_B$  is blaze angle, and  $d$  is groove density. If two parallel rays are incident on the grating at the one groove spacing  $d$  apart then the diffracted beam has a difference in their path length equal to  $(d\sin\alpha + d\sin\beta)$  which leads to the grating equation.

From the principle of constructive interference, we get the following grating

equation:

$$m\lambda = d(\sin\alpha + \sin\beta) \quad (2.1)$$

where,  $\alpha$  and  $\beta$  are incident and diffraction angles,  $d$  is groove spacing,  $\lambda$  is the wavelength of incident light, and  $m$  is diffraction (or spectral) order which is an integer.

### 2.2.5 Converging Optics

To focus the diffracted light from the grating on to an array detector Schmidt telescope of a focal length of 139 mm is used. We have used all reflective optics in NIRIS except an aspherical correcting lens used in the Schmidt telescope. The idea to choose reflective optics over refractive optics in NIRIS is to make it operative over large wavelength ranges (from ultraviolet (UV) to infrared (IR)) by changing grating angle and detector. Lenses are known to absorb the incoming light in the UV and IR region. Schmidt camera also minimizes optical aberrations such as coma and astigmatism. Because of this design a variant of NIRIS was used to derive daytime wave characteristics in the mesosphere lower thermosphere (MLT) region wherein ultra-violet measurements of OI 297.2 nm dayglow emission have been obtained on-board a balloon in an earlier experiment [*Pallamraju et al. (2014)*].

### 2.2.6 Detector and Data Acquisition System

For imaging the near infrared spectra, a charge-coupled device (CCD) detector is used. The CCD detector used in NIRIS has  $1024 \times 1024$  pixels with a square pixel size of  $13 \mu\text{m}$ . This is a deep depleted thermoelectrically cooled CCD detector in which etaloning is suppressed and is sensitive in the near-infrared region with quantum efficiency (QE) more than 80% in the wavelength range 800-900 nm. This CCD is attached to the Schmidt telescope with sensor on the image plane of the spectrograph. The spectrograph is aligned in such a way that the dispersion and spatial directions correspond to the columns and

rows of the CCD detector. The CCD is cooled to  $-80^{\circ}\text{C}$  by a thermoelectric cooler to reduce thermal noise. The signal to noise ratio (SNR) is controlled by applying on-chip binning along the spatial direction (rows of the CCD). NIRIS obtains several spectral images on each night at pre-defined camera settings such as, exposure time, on-chip binning, and CCD temperature which are enabled through an in-house developed software. These spectral images are saved in Flexible Image Transport System (FITS) format. For the normal operations  $1 \times 32$  on-chip binning is done, CCD sensor temperature is set to be  $-80^{\circ}\text{C}$ , and exposure time is set to be 300 seconds. Hence, for moonless and cloud free nights the data cadence of NIRIS is 5 min which provides 120 spectral images per night for 10 hours of observations.

## 2.3 Calibration of NIRIS

We get two dimensional spectral images from NIRIS in which x- and y-axes correspond to wavelength and spatial direction of the sky. Therefore, calibration of NIRIS is performed to determine dispersion (wavelength calibration) and spatial location (view angle calibration). The methods used for these calibrations are described in detail in the following sections:

### 2.3.1 Wavelength Calibration

Wavelength calibration of NIRIS has been performed in the laboratory by using an argon spectral lamp (Newport model: 6030) as the source and a spectral image thus obtained is shown in Figure 2.3a.

Figure 2.3a shows that each spectral line is slightly curved as discussed above which is due to the differences in the incident angle to the grating at the edges of the slip. As we are using a curved input slit the effect of the curvature on the detector is considerably reduced. This curvature effect in the image is removed by shifting each pixel of raw data in x-direction by a quantity

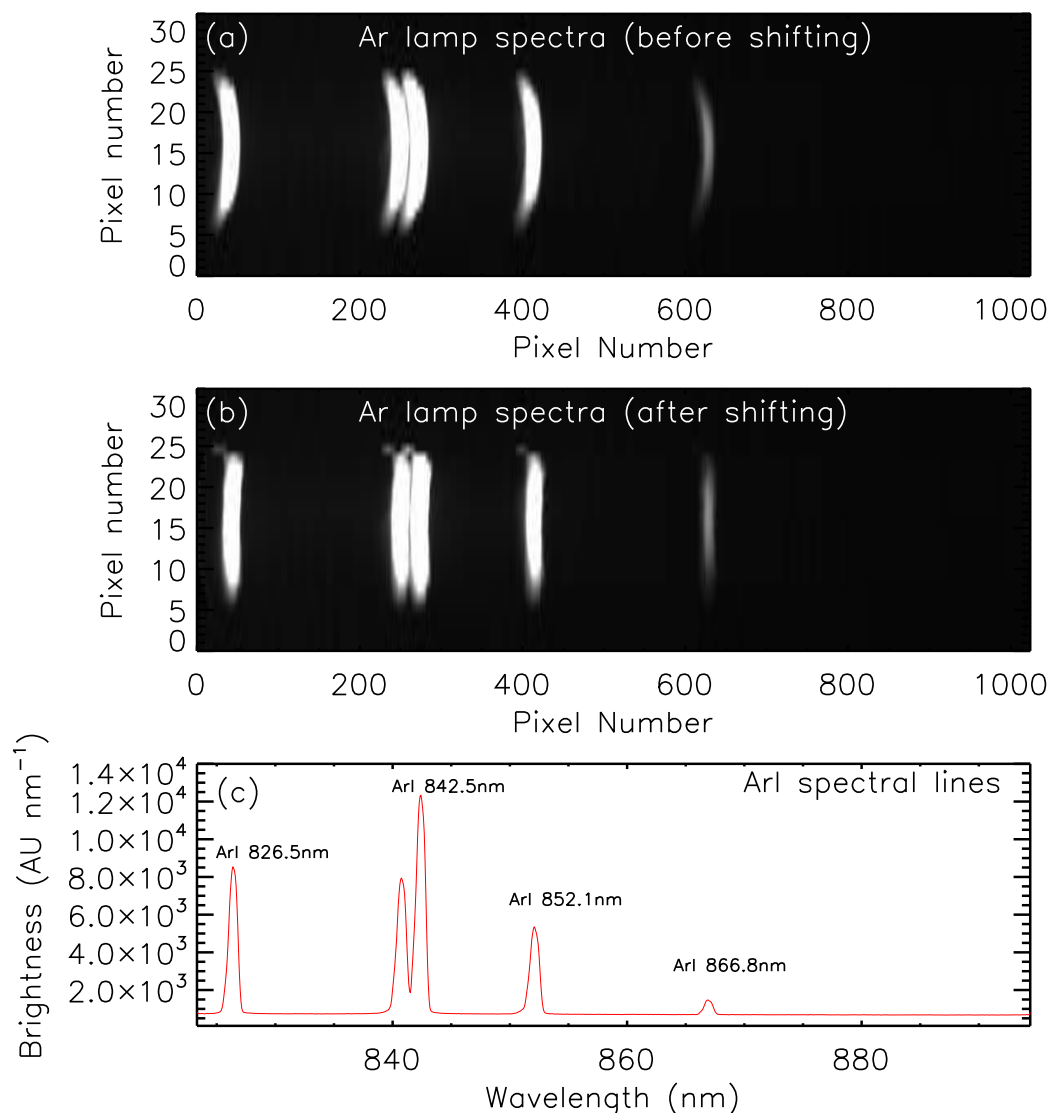


**Figure 2.3:** (a) NIRIS obtained spectral image using Argon lamp as the spectral calibration source. (b) Similar to the Figure 2.3a but after correcting for the image curvature. (c) Brightness of ArI spectral lines of the image shown in Figure 2.3a (represented in arbitrary units, AU). These show the emission lines at 826.5 nm, 842.5 nm, 852.1 nm, and 866.8 nm which are used for wavelength calibration of the spectrum obtained from NIRIS.

obtained by spline fitting of data at three locations along each spectral line. The image, thus corrected is shown in Figure 2.3b in which the x- and y-axes correspond to wavelength and spatial directions, respectively. The ArI spectral lines are obtained by taking a cut across the corrected spectral image. Some of the strong ArI emission lines which have been used for the spectral calibration

of the instrument are shown in Figure 2.3c. The dispersion achieved by NIRIS is  $0.07 \text{ nm pixel}^{-1}$  in the wavelength range of 823-894 nm. The resolution of the grating spectrograph is obtained by dispersion multiplied by full width at half maximum (FWHM) of the Ar spectral line. From Figure 2.3b, FWHM of each of the identified Ar spectral line is found, and average of which comes out to be 11.2 pixels. Therefore, the resolution of the NIRIS is  $(71/1024) \times 11.2 = 0.78 \text{ nm}$ .

### 2.3.2 Angle Calibration

As discussed earlier, NIRIS has FOV of around  $80^\circ$  in which y-axis of the image represents spatial coverage of the sky. The angle calibration is carried out to know the spatial location of the sky corresponding to the pixel number on the CCD chip. The angle calibration of NIRIS has been performed after mounting it for the field operations in which the slit is oriented along the N-S meridian. This is done by allowing diffused day light to fall onto the CCD chip only through a small portion along the slit orientation (by fully covering the light from rest of the directions). For the next image the light is allowed only through another small portion along the slit orientation. Using several of such images the angular coverage of each pixel has been obtained. It is found that the  $80^\circ$  FOV of the information from sky in the N-S direction is imaged onto fifteen vertical pixels (pixel number 8 to 22) onto the CCD chip with  $1 \times 32$  on-chip binning. Figure 2.4a shows a plot of pixel number vs view angle in which the dots and dashed lines show the observations and the best fit line. Similarly, Figure 2.4b shows a plot of pixel number vs distance which is obtained by converting the angle into distance assuming  $\text{O}_2$  and OH emission altitudes to be 94 and 87 km and are shown in magenta and blue coloured lines. The north and south direction is also marked in Figure 2.4 in which the horizontal line shows the zenith measurement which corresponds to pixel number 15 on the CCD chip.

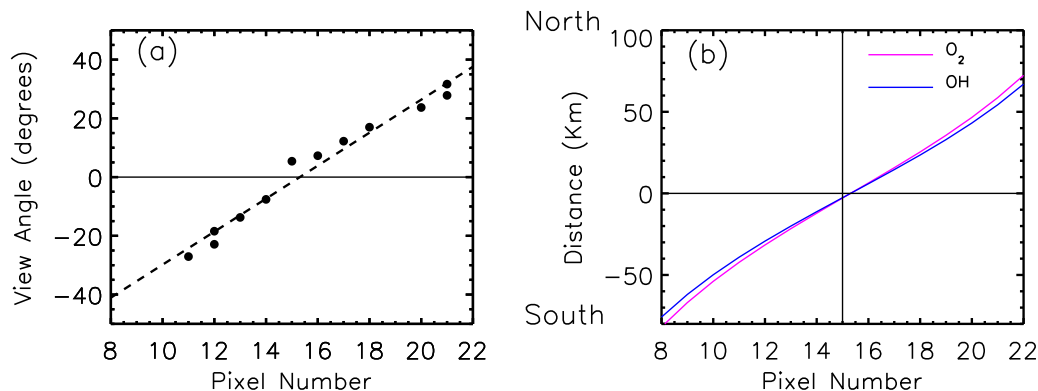


**Figure 2.4:** (a) View angles measured in degrees are shown with respect to the pixel position. (b) Distance covered on the CCD plane as a function of pixel numbers is shown for O<sub>2</sub> and OH emission altitudes in magenta and blue coloured lines which are 154 and 142 km, respectively. Horizontal lines show the measurement corresponding to zenith which is at pixel number 15.

## 2.4 Mesospheric Nightglow Intensity Determination

The nocturnal raw spectra (Figure 2.5a) obtained from NIRIS cannot be used directly as they are convolved with many artifacts, such as, incidences of cosmic rays, image curvature, vignetting etc., which need to be corrected before further analysis. Each of the spectral images are passed through a sigma filter to remove the contribution of the noise that arises from the hot pixels caused by the incident cosmic rays, if any, onto the CCD detector. The sigma filter used here replaces pixels with intensities more than a specified level from its neighbors. A 3×3 pixel sigma filter is used in the present case. The CCD uses thermoelectric air cooling technique which provides a typical sensor temperature of around -80°C. Even though the dark current generated at such low temperatures is very small, we do subtract this background. In order to do that, a dark frame is generated for every individual image by considering a portion of the image that is not illuminated by the incoming light. This dark frame is then subtracted from every spectral image to remove the contribution of dark current in it. Later, the images are corrected for flat-field in which



the effects on the images caused by pixel-to-pixel variability across the chip, vignetting, and features on the optical components, if any, are removed. For large FOV optical instruments it is a challenge to provide a Lambertian surface for equal intensity illumination across the field. However, diffused skylight during twilight is considered as a close approximation for this purpose [e.g., *Garcia et al. (1997)*] and has been implemented in this work.

As the method of determination of rotational temperature involves taking ratios of intensities it is important that the vignetting effect of transmission from one spectral region to the other in the spectral direction of the CCD is also required to be taken care of. This is achieved by using a non-spectral white light output from a low light level integrating sphere (Gooch & Housgo model: OL 426). The curvature effect in the image is also removed by the method as depicted in Figure 2.3 and discussed earlier. A typical nocturnal spectral image obtained by NIRIS for a 5-minute exposure and for an on-chip binning of  $1 \times 32$  is shown in Figure 2.5b which has been accomplished after performing all the treatments as discussed above. The Meinel OH(6-2), OH(7-3), and O<sub>2</sub>(0-1) atmospheric bands are identified based on the wavelength calibration described in Figure 2.3.

For the determination of nightglow emission wavelengths, calibration of the spectra was carried out using twelve known spectral lines located within the spectral region of 823–894 nm. The spectral scale for each of the spectra is obtained by fitting the line positions with the identified lines by using a 3rd-order polynomial fit. Also, the background level is determined by fitting a 3rd-order polynomial fit at twelve identified regions where there are no airglow emissions in the wavelength range of 823–894 nm. After performing the wavelength calibration and removing background level as discussed above the brightness of the resulting spectral lines over zenith are shown in Figure 2.5c which correspond to the spectral image shown in Figure 2.5b. In Figure 2.5c, emissions at five different wavelengths are obtained, whose centers are marked by I<sub>1</sub> to I<sub>5</sub>. These marked spectra show different regions of OH(6-2) Meinel and O<sub>2</sub>(0-1)

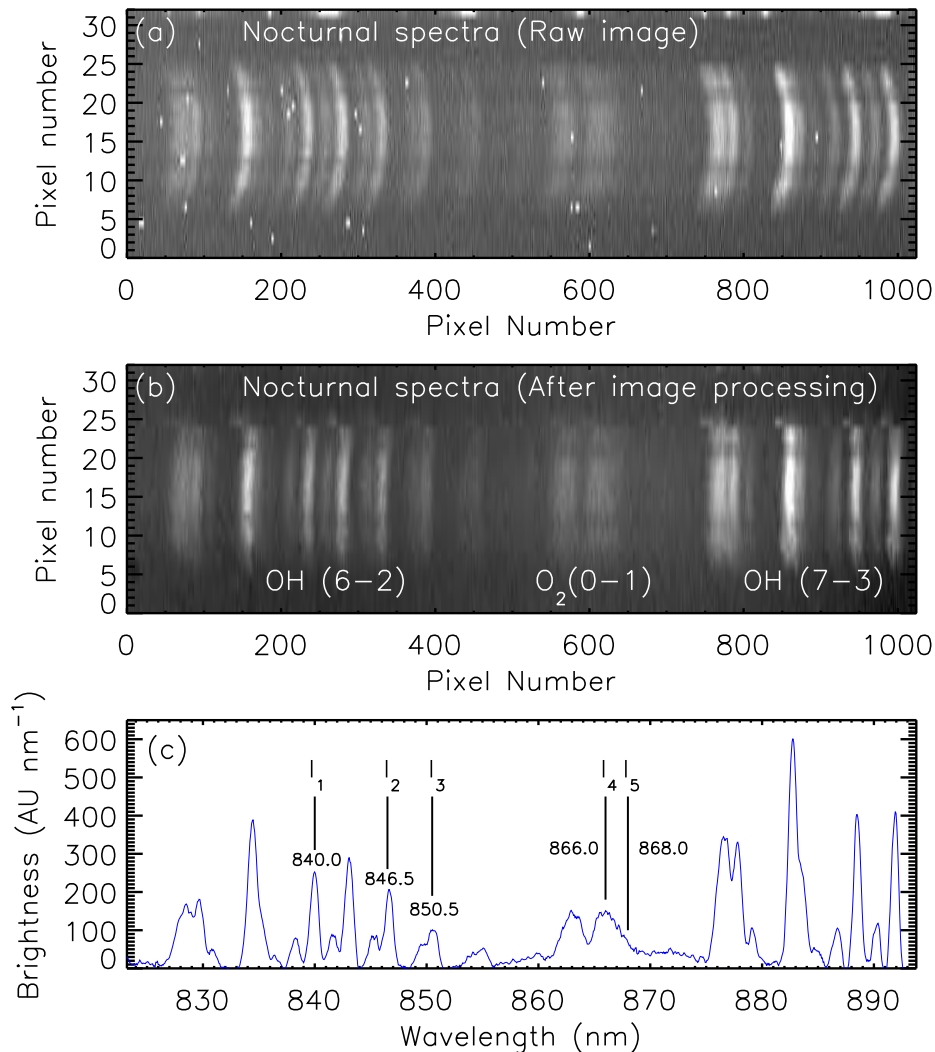


**Figure 2.5:** (a) A nocturnal raw spectral image obtained by NIRIS. (b) Same image as shown in Figure 2.5a but after correcting for all the issues as discussed in text. OH(6-2), O<sub>2</sub>(0-1), and OH(7-3) bands are identified based on the wavelength calibration of the instrument. The x- and y-axes represent spectral and spatial coverage of NIRIS. (c) Spectral lines are obtained by taking a cut across the spectral image of Figure 2.5b. The five different wavelength regions, which are used for the OH rotational temperature derivation are identified by I<sub>1</sub> to I<sub>5</sub>.

atmospheric bands that have been used for the determination of OH and O<sub>2</sub> emission intensities and derivation of corresponding rotational temperatures. These emission intensities are determined by integrating over 1.2 nm centered at each spectral line.

Nocturnal variation in three rotational lines of OH(6-2) band namely, P<sub>1</sub>(2)

at 840.0 nm,  $P_1(4)$  at 846.5 nm, and  $P_1(5)$  at 850.5 nm, respectively, are shown in Figure 2.6a on the night of 16 April 2013. Similarly, nocturnal variations for the two regions of  $O_2(0-1)$  atmospheric band centered at 866.0 nm and 868.0 nm on the same night are shown in Figure 2.6b. As will be seen later, these lines are used for the derivation of rotational temperatures corresponding to the  $O_2$  and OH emission altitudes which are considered to be 94 and 87 km, respectively.

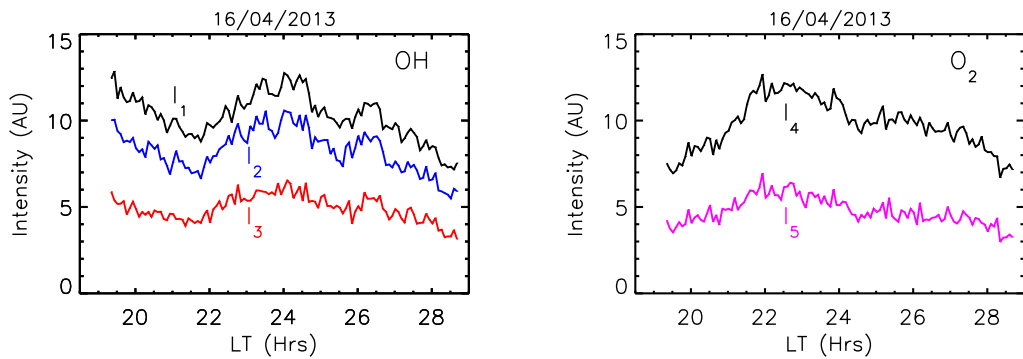


**Figure 2.6:** (a) Nocturnal variation of three different rotational lines of OH(6-2) Meinel band emission in which  $I_1$ ,  $I_2$ , and  $I_3$  correspond to the  $P_1(2)$  at 840.0 nm,  $P_1(4)$  at 846.5 nm, and  $P_1(5)$  at 850.5 nm, respectively. (b) Nocturnal variation of two regions of  $O_2(0-1)$  atmospheric band centered at 866.0 nm ( $I_4$ ) and 868.0 nm ( $I_5$ ), respectively.

## 2.5 Derivation of Mesospheric Temperatures

Mesospheric OH and  $O_2$  rotational temperature measurements using spectral line ratios is a well-established technique [e.g., *Meriwether Jr (1984)*; *Greet et al. (1997)*; *Taylor et al. (1999)*; *French et al. (2000)*; *Bittner et al. (2002)*; *Taori et al. (2005)*; *Shiokawa et al. (2007)*]. We have used this method to derive the mesospheric temperatures as discussed in the following sections. NIRIS is a large field-of-view imaging spectrograph which is sensitive to fluctuations in intensities of less than around two percent for a 5 min integration time. Due to a high spectral resolution (around 0.78 nm) and large spectral coverage,

rotational temperatures from the OH(6-2) Meinel and O<sub>2</sub>(0-1) atmospheric band emissions can be derived simultaneously.

Using photometric techniques [e.g., *Taylor et al. (1999)*; *Taori et al. (2011)*] temperature measurements have been carried out in which interference filters of different wavelengths are used in sequence to obtain the intensities of the desired rotational lines. In such methods, it is required that the filter bandwidths be narrow in order to discretely obtain the intensities of the two rotational lines. However, as the transmission from neighboring spectral regions through such filters is non-zero, it might not be possible to avoid contamination from the neighboring lines, which could lead to either over- or under-estimation of the mesospheric temperatures.

In the spectrographic technique, NIRIS, however, as the spectral resolution is high it is possible to obtain not only uncontaminated intensities from the desired rotational lines discretely, but also the night sky background contribution from around these wavelengths of interest. Therefore, background subtraction is enabled before proceeding further for obtaining ratios of rotational line intensities by this technique and therefore it reduces the errors in the measurements of intensities and temperatures. The derivation of mesospheric temperatures from OH(6-2) Meinel and O<sub>2</sub>(0-1) atmospheric band emissions is described in the following sections.

### 2.5.1 OH(6-2) Meinel Band Emission

The mechanism responsible for the production of the Meinel bands of OH is described in Chapter 1. The derivation of OH rotational temperatures through the spectral line ratio method assumes that the underlying gas is in Local Thermodynamic Equilibrium (LTE) [*Mies (1974)*; *Meriwether Jr (1984)*] which is valid for OH(6-2) vibrational band having rotational levels  $N' < 5$  [e.g., *Pendleton et al. (1993)*]. In this study as rotational levels corresponding to  $N'=1$  and  $N'=3$  are used, they satisfy the condition of LTE. The degree of thermalization

depends on the radiative lifetime of the excited OH\* molecule and the neutral collision frequency. For OH the radiative lifetimes for vibrational states of  $v=9, 6,$  and  $1,$  are  $3.62, 6.2,$  and  $44$  milliseconds, respectively [Turnbull and Lowe (1989)]. At  $87$  km altitude (for  $T \sim 200$  K and  $P \sim 3 \times 10^{-4}$  kPa) the neutral collision frequency is  $\sim 3 \times 10^4$  s $^{-1}$ . Therefore, depending on the vibrational state to which the OH molecule is excited, it would undergo  $110$  to  $1320$  number of collisions prior to radiative de-excitation, which is large enough to achieve thermalization. Therefore, population of the OH rotational states can be assumed to obey Boltzmann distribution and therefore the rotational temperatures determined by this spectrographic method can be taken to represent the ambient temperature of the region of emanation of airglow. Thus, the intensities of two OH lines from different rotational states of a single vibrational band are compared using the following equation [Mies (1974); Meriwether Jr (1984)] for estimating rotational temperatures:

$$T_{rot} = \frac{\frac{hc}{k} \times [F_{v'}(J_2) - F_{v'}(J_1)]}{\ln \left[ \frac{I_1(2J_2+1)A_2}{I_2(2J_1+1)A_1} \right]} \quad (2.2)$$

where,  $F(J_1)$  and  $F(J_2)$  are the energy levels of the initial rotational states;  $I_1$  and  $I_2$  are the emission intensities of the OH lines from different upper states;  $A_1$  and  $A_2$  are the transition probabilities;  $J_1$  and  $J_2$  are the upper state total angular momentum quantum numbers. The OH (6-2) band  $P_1(2), P_1(4),$  and  $P_1(5)$  rotational lines centered at  $840.0$  nm,  $846.5$  nm, and  $850.5$  nm, respectively, are used for the derivation of OH rotational temperatures. The values of Einstein coefficients A's are taken from Mies (1974) and those of  $F(J)$ 's from Coxon and Foster (1982). The rotational temperatures are calculated by taking two sets of rotational lines of OH(6-2) band emission. After putting the theoretical constants for  $P_1(2)$  and  $P_1(4)$  lines in equation 2.2 we get:

$$T(OH1) = \frac{228.59}{\ln [2.609 (I_1/I_2)]} \text{ K} \quad (2.3)$$

Similarly, After putting the theoretical constants for  $P_1(2)$  and  $P_1(5)$  lines in equation 2.2 we get:

$$T(OH_2) = \frac{401.10}{\ln [3.388 (I_1/I_3)]} \text{ K} \quad (2.4)$$

where  $I_1$  is the intensity of  $P_1(2)$  line at 840.0 nm,  $I_2$  is the intensity of  $P_1(4)$  line at 846.5 nm, and  $I_3$  is the intensity of  $P_1(5)$  line at 850.5 nm wavelengths which are obtained by integrating over 1.2 nm wide window centered at each spectral lines (Figure 2.5c), respectively.

## 2.5.2 $O_2(0-1)$ Atmospheric Band Emission

The mechanism responsible for the production of the  $O_2(0-1)$  atmospheric band emission is described in Chapter 1. To calculate the temperature using  $O_2(0-1)$  atmospheric band, similar procedure discussed above was applied in which PP and PQ pairs of rotational lines for  $K''=7$  and  $K''=15$  centered at 866.0 nm and 868.0 nm wavelengths, respectively, are considered. The spectroscopic constants and values of line strengths are taken from [Schlapp \(1937\)](#). The rotational temperature using  $O_2(0-1)$  atmospheric band is given by the following equation:

$$T(O_2) = [(248.88 \times (I_5/I_4)) + 77.7]K \quad (2.5)$$

where  $I_4$  and  $I_5$  are the intensities of the  $O_2(0-1)$  atmospheric band PP and PQ pairs of rotational lines obtained by integrating over each spectral line profile using a 1.2 nm wide window centered at 866.0 nm and 868.0 nm, respectively, as shown in Figure 2.5c.

### 2.5.3 Nocturnal Variation in OH(6-2) and O<sub>2</sub>(0-1) Band Intensities and Temperatures

NIRIS derived OH and O<sub>2</sub> nightglow emission intensities are calculated by taking averages of I<sub>1</sub> and I<sub>2</sub> and I<sub>4</sub> and I<sub>5</sub>, respectively. The variations in intensities over zenith for two representative nights of 16 April and 04 May 2013 are shown in Figures 2.7a and 2.7c along with the uncertainties in the measurements. On the night of 16 April 2013 the OH and O<sub>2</sub> intensities show out-of-phase variations from 19.5 hours (19:30 LT) to 25.5 hours (01:30 LT) and in-phase variation after that time until 28.6 hours (04:36 hrs). Whereas, on the night of 4 May 2013 no such relationship was observed except for initial couple of hours when out-of-phase variations were seen. Although OH and O<sub>2</sub> intensities on these two nights show both in-phase and out-of-phase variations with time, it is not necessary that the phase differences should always be either 0 or 180 degrees. Such kinds of variations in mesospheric airglow intensities are common and are due to the gravity wave effects.

The temperatures corresponding to an altitude of 87 km are derived by considering two different rotational line ratios which have been calculated using equations 2.3 and 2.4. For OH band emissions they are shown for two line ratios T(OH1) and T(OH2) (blue and green coloured lines) for these two nights in Figures 2.7b and 2.7d. The temperatures from O<sub>2</sub> emissions, T(O<sub>2</sub>), corresponding to an altitude of 94 km are calculated by using equation 2.5 and are also shown (magenta coloured lines) for these two nights in Figures 2.7b and 2.7d. The estimated uncertainty in the NIRIS derived mesospheric temperatures is approximately  $\pm 3\text{K}$ . The nocturnal mean values of T(OH1), T(OH2), and T(O<sub>2</sub>) are 194, 202, and 196 K, for the night of 16 April 2013 and are 193, 201, and 194 K, for the night of 4 May 2013, respectively. These are shown along with their standard deviations by square boxes (towards the left in each plot). As can be clearly seen, the variations in T(OH1) and T(OH2) are quite similar for both the nights and the nightly mean values are within the one-

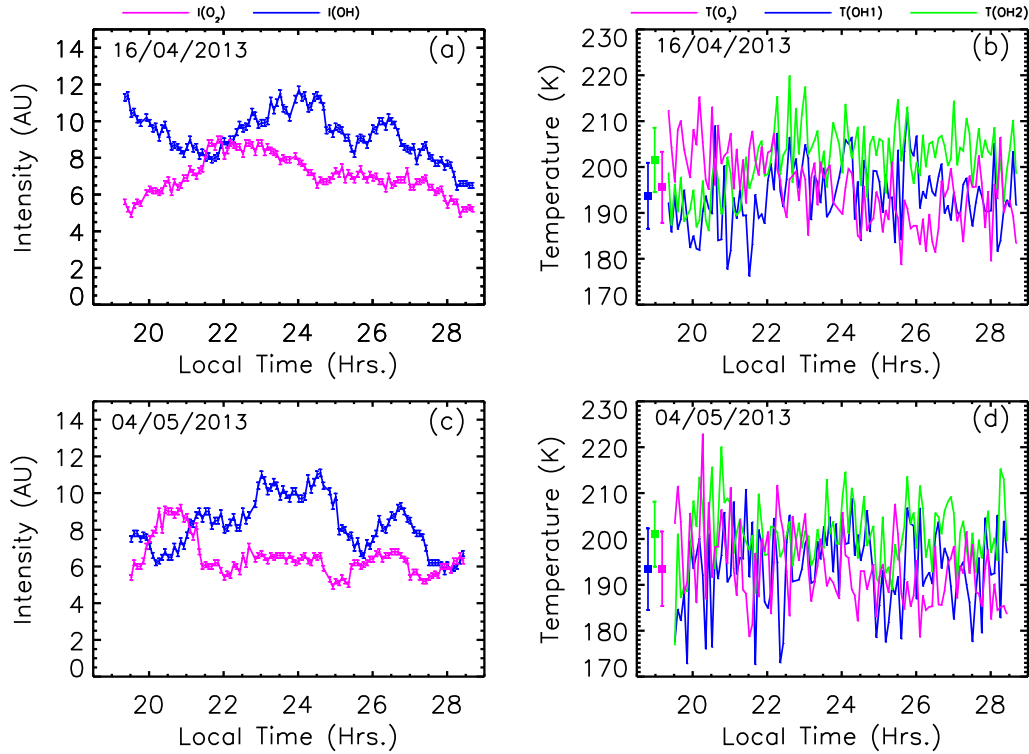


**Figure 2.7:** (a) Nocturnal variations in O<sub>2</sub> and OH intensities, (b) Rotational temperatures corresponding to O<sub>2</sub> and OH emissions on the night of 16 April 2013 in which the O<sub>2</sub> and OH intensities showed both in-phase and out-of-phase variations. (c and d) Similar to Figures 2.7a and 2.7b but for the night of 4 May 2013. It may be noted that O<sub>2</sub> and OH intensity variations do not show any phase relationship on this night.

sigma variation. This is an added advantage in the spectroscopic technique over the photometric ones in which simultaneous derivation of mesospheric temperatures can be achieved by using different sets of rotational lines without any need to change the filters and hence can also be used to cross-verify the accuracy of the temperature values arrived at. This also yields a better temporal cadence as no time is lost in the movement of filters from on-band to that of off-band.

Unlike the OH and O<sub>2</sub> emission intensities, the mesospheric temperatures, T(OH1), T(OH2), and T(O<sub>2</sub>), derived for the night of 16 April 2013 show out-of-phase variations for initial couple of hours and are in-phase for most of the time later. However, on the night of 4 May 2013 no such distinct



phase relationship has been noted in the temperatures. Therefore, nightglow emission intensities seem to be more sensitive to the fluctuations caused by the gravity wave propagations in comparison to the temperatures since the density fluctuations at these altitudes due to any perturbation in the medium are reflected in the intensities almost instantaneously.

## 2.6 NIRIS and SABER Temperatures Comparison

NIRIS derived mesospheric temperatures have been compared with independent satellite based observations. For that we have considered Level 2A data from the Sounding of the Atmosphere using Broadband Emission Radiometry (SABER) on-board Thermosphere, Ionosphere, Mesosphere Energetics and Dynamics (TIMED) satellite. SABER provides temperature profile with an estimated uncertainty of around  $\pm 4$  K in the altitude range of 80–100 km [[Mertens et al. \(2001\)](#)]. Figure 2.8 shows the vertical profile of SABER derived temperatures which is averaged over those obtained in the latitude and longitude range of 21.6°N–27.6°N and 69.8°E–75.8°E for the night of 4 May 2013.

The NIRIS derived mesospheric temperatures,  $T(\text{O}_2)$  and  $T(\text{OH1})$ , for the same night are also shown at their representative altitudes. The NIRIS data show large range in temperatures wherein  $T(\text{O}_2)$  and  $T(\text{OH1})$  vary from 179 to 223 K and 173 to 211 K with mean values of 193.5 K and 193.4 K on this night. The large nocturnal variations in the NIRIS derived temperatures are due to mesospheric dynamics due to GW propagations which are captured due to high temporal resolution measurement. On the other hand, the satellite-based observations have poor temporal resolution but provide information on spatial variations of a given parameter. Nevertheless, the temperature values from SABER (Figure 2.8) corresponding to the observational

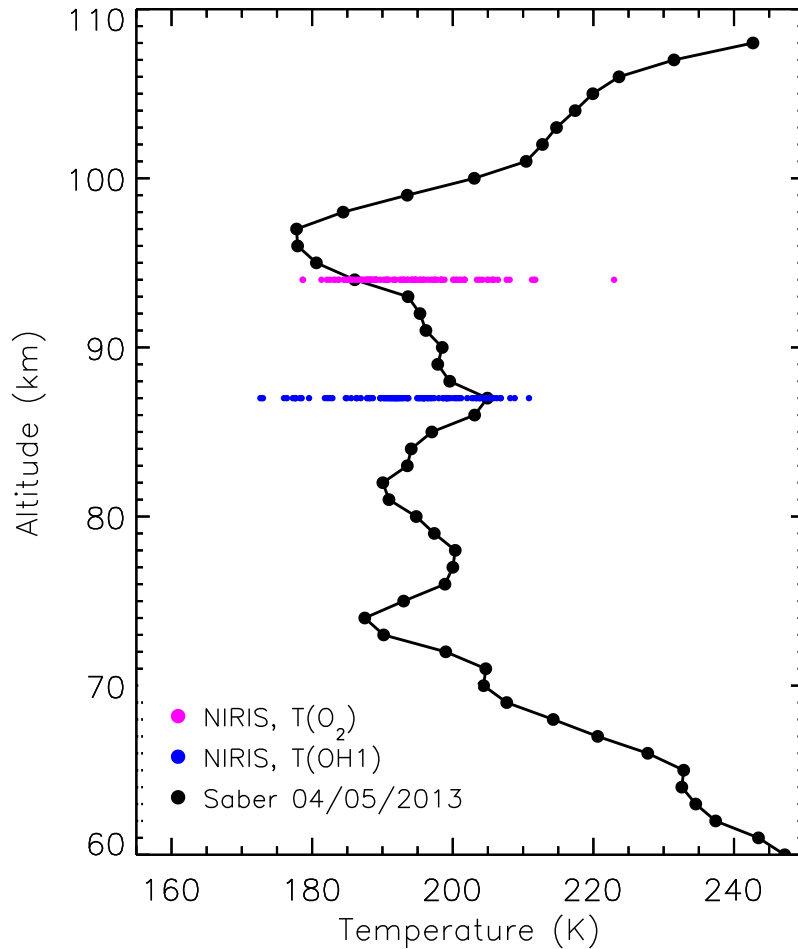


**Figure 2.8:** Vertical profile of SABER derived temperatures obtained by averaging over  $\pm 3^\circ$  latitude and longitude of the observational station for the night of 4 May 2013. The NIRIS derived temperatures for the same night are also shown at the respective altitudes which show large range in the nocturnal temperature variability at both the altitudes which are due to mesospheric dynamical variations.

station compare well with those of NIRIS observations. The combinations of ground- and satellite-based observations, thus, present complementary information on spatio-temporal variations in temperatures and provide an opportunity to study global phenomena. An example of such an investigation has been reported in an earlier study [*Singh and Pallamraju (2015)*] wherein mesospheric temperature enhancement over low-latitudes has been shown to be developed as a consequence of sudden stratospheric warming events over high-latitudes.

## 2.7 CCD-based Multi-wavelength Airglow Photometer (CMAP)

A CCD-based Multi-wavelength Airglow Photometer (CMAP) is developed in-house to study the nightglow emission intensities which emanate from MLT region of the Earth's upper atmosphere [*Phadke et al. (2014)*]. CMAP uses narrow bandwidth interference filters having full width at half maxima of 0.3 nm and these are mounted in a temperature stabilized filter wheel. Transmission of narrow bandwidth interference filters is prone to temperatures fluctuations. Therefore, to maintain the filter at the desired temperature level Peltier elements are used on the filter wheel, operation of which is controlled by a bipolar temperature controller. This bipolar temperature controller passes the current through Peltier elements in such a way that the Peltier element facing the filter chamber heats or cools the filter housing thereby maintaining the temperature of the filter. The filter temperature can be maintained to  $\pm 0.5^\circ$  C. The filter wheel can house five filters at a time enabling near-simultaneous measurements at five different airglow emissions. Software is developed in-house to control various operations of CMAP such as, data acquisition through CCD, filter wheel movement in a pre-defined and programmed modes, and monitoring of filter wheel temperature. CCD images are obtained in FITS format. The details of the various components used in CMAP and the derivation of nightglow emission intensities from the images obtained from CMAP are described in the following sections.

### 2.7.1 Optical Configuration of CMAP

The optical configuration of CMAP and its photograph after assembly of all the components for the field operation are shown in Figures 2.9a and 2.9b. As can be seen in Figure 2.9a, CMAP consists of fore optics, filter and imaging sections. The main objective of the front-end optics is to collimate the in-

coming light and make it into a parallel beam of light which is allowed to fall normally onto the interference filters. The filtered light is then made to fall on the imaging lens which focuses the photons from the interference filter onto the CCD chip. In CMAP we have used F/2 optical configuration throughout the optical path.

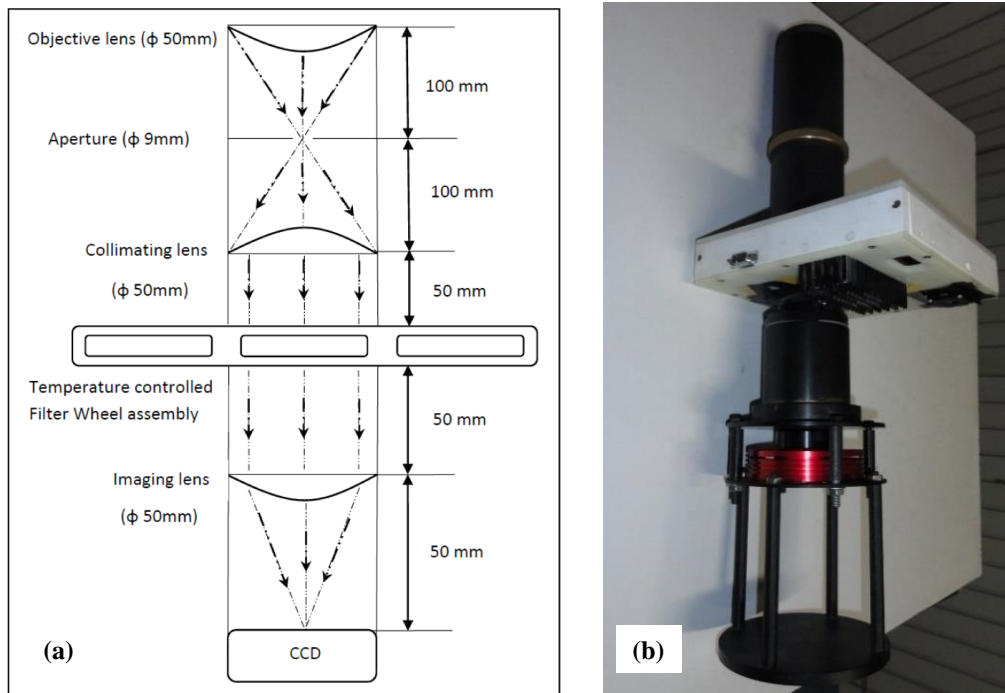


**Figure 2.9:** (a) Optical configuration of CMAP (b) Photograph of CMAP after assembling it for the field operations.

The combination of the field lens and the aperture decides the FOV of the system. The FOV of the system is given by  $\tan^{-1}(d/f)$ , where  $d$  is the diameter of the aperture and  $f$  is the focal length of the objective lens. For the optical configuration shown in Figure 2.9a the FOV turns out to be 5.1 degrees. Since, we are using a CCD detector, the chip size and the focal length of the imaging lens will decide the maximum FOV that can be imaged onto the detector.

In order to enable comparison with a PMT based system (FOV  $\sim 3^\circ$ ), in CMAP we have used 9 mm aperture size with 100 mm focal length objective lens (FOV  $\sim 5^\circ$ ), but appropriate region on the CCD chip was selected (2.5 mm diameter circle; which gives a FOV of  $\sim 3^\circ$ ) for integrating the counts to

compare with PMT based system.

Since the chip size of the CCD being used is  $8.98 \times 6.71$  mm, a shorter focal length of 50 mm imaging lens is used so that the photons from the whole aperture can be imaged onto the chip. The central area of the chip illuminated will be of a diameter of 4.5 mm. With this design, the aperture size can be increased even up to 11 mm without any loss of photons. The counts obtained from the pixels illuminated with photons of airglow origin are integrated during analysis and after subtracting the dark noise, information on the nightglow emission intensity is obtained as a function of time.

### 2.7.2 Filters and Filter Wheel Assembly

For the measurement of nightglow emission intensities at multiple wavelengths narrowband interference filters having full width at half maximum (FWHM) of 0.3 nm centred at the emission wavelength are used. The interference filters are also sometimes referred to as Fabry-Perot filters. The principle of operation of an interference filter is analogous to a lower order Fabry-Perot etalon and they are basically multiple cavity solid Fabry-Perot etalons [e.g., [Hernández \(1988\)](#); [Macleod \(2001\)](#); [Thorne et al. \(1999\)](#)]. These filters consist of multiple thin layers of alternative high and low refractive index materials which are arranged as a stack. The thickness of each layer is of the order of  $\lambda/4$ , where  $\lambda$  is the central wavelength. In these filters spectral rejection/selection is achieved by creating destructive/constructive interference conditions. A spacer layer is formed by depositing a half wavelength layer ( $\lambda/2$ ) or multiples thereof in between a systematic stack. A cavity is formed by a spacer layer and the immediate stack which decides the shape of the transmittance curve. The interference filters used in CMAP have 2-cavity design. The characteristic of an interference filter is given by following relation:

$$2\mu t \cos\theta = m\lambda \quad (2.6)$$

where  $\mu$  is the refractive index of the dielectric,  $t$  is the thickness of the layer,  $\theta$  is the angle of incidence, and  $m$  is the order of interference. These parameters decide the central wavelength,  $\lambda$ , of the filter. The filter temperature has a significant effect on the shift of the central wavelength by influencing the values of  $\mu$  and  $t$  in the equation 2.6.

The central wavelength at normal incidence,  $\lambda_i$ , shifts to  $\lambda_\theta$  at an angle of incidence  $\theta$  according to the following relation:

$$\lambda_\theta = \lambda_i \sqrt{1 - \frac{\text{Sin}^2 \theta}{n_e^2}} \quad (2.7)$$

where,  $n_e$  is the effective refractive index. The wavelength of peak transmittance of an interference filter depends on two parameters: (1) angle of incidence and (2) effective refractive index which in turn is a function of filter temperature. As can be seen from equation 2.7 the central passband wavelength of an interference filter shifts towards lower wavelength with an increase in the incident angle. Since we are using a collimating lens, the incident light will fall normally onto the filters thereby not changing the wavelength of peak transmittance. However, as increase in temperature of the filter increases thickness of the layer, the refractive index of the medium also changes. As a consequence, increase/decrease in temperature the wavelength of peak transmittance of the spectrum shifts slightly towards longer/shorter wavelengths.

The temperature coefficient of the filter used in CMAP is around 0.02 nm/ $^{\circ}$ C hence, the temperature of these filters has to be maintained, otherwise, it will allow light from the spectral regions other than that intended for use. For this purpose, a temperature controlled chamber using Peltier elements has been built in-house to augment with the commercially available filter wheel. A temperature monitoring system was developed to augment with a commercially available control system for this filter wheel assembly which can maintain temperature to an accuracy of  $\pm 0.5$   $^{\circ}$ C or better. To control the temperature for filter wheel chamber AD590 temperature sensor was used for

the temperature monitoring. The output of this temperature sensor was given as an input to the custom made bipolar temperature controller. The temperature controller (Figure 2.10b) with this given input calculates the amount of current and its polarity to be supplied to the Peltier elements for them to control the temperature of the filter wheel assembly. Four thermoelectric cooler (TEC) units of dimensions 40 mm×40 mm were attached to the filter wheel assembly (Figure 2.10a) and the assembly was insulated from ambient environment by using an additional insulating box made of Teflon as can be seen in Figure 2.9a and 2.10a. A software tool has been developed by which temperature values can be stored in a predefined format for monitoring the temperature.

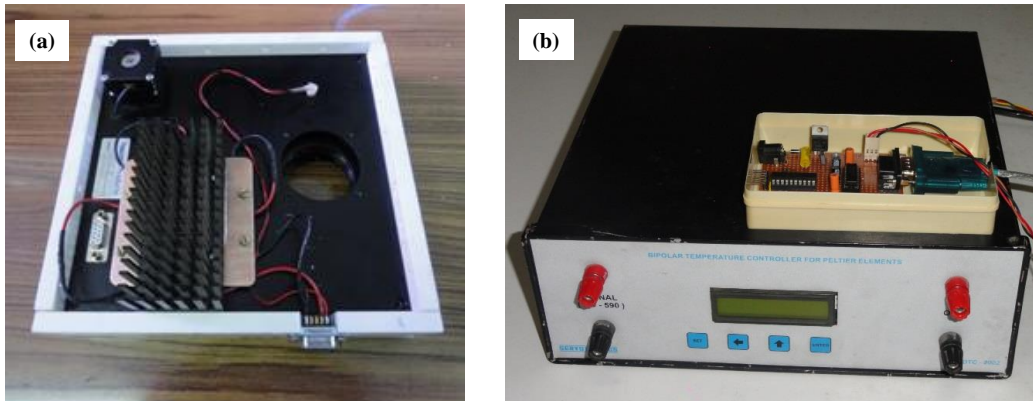


**Figure 2.10:** (a) The filter wheel assembly along with Peltier elements to control the temperature. (b) Bipolar temperature controller along with temperature logging unit which is used to regulate the current supplied to the Peltier elements attached to filter wheel.

Figure 2.11 shows nocturnal variation in temperature of the in-house built filter wheel assembly chamber on the night of 24 October 2014 when CMAP was commissioned for the field operations from our observatory at Gurushikhar, Mount Abu.

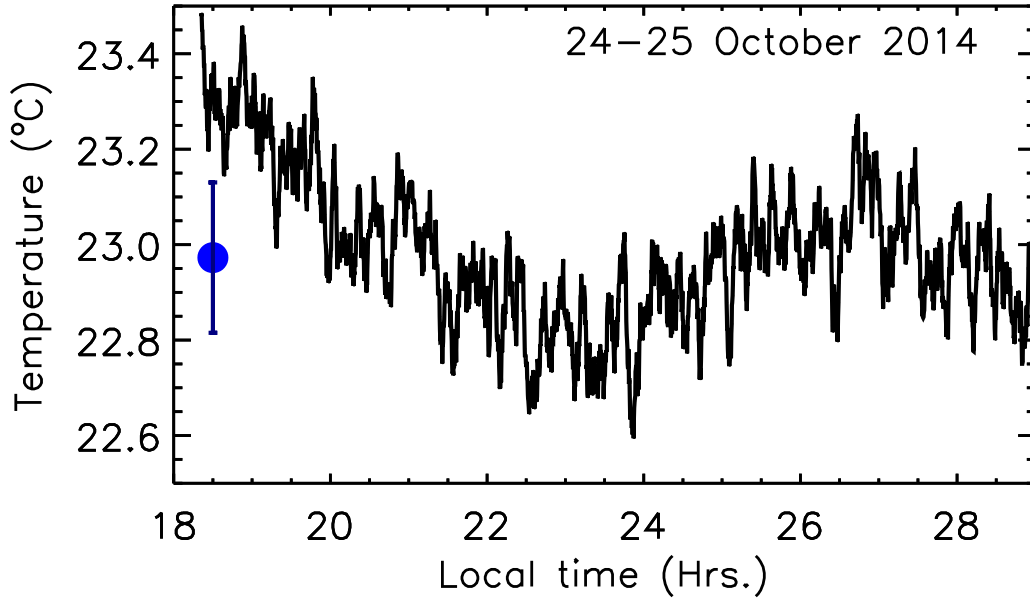


**Figure 2.11:** Shows nocturnal variation of temperature of the in-house built filter wheel assembly chamber on the night of 24 October 2014 when CMAP was commissioned for field operations from Gurushikhar, Mount Abu.

### 2.7.3 Detector and Data Acquisition System

In CMAP we have used CCD detector in contrast to conventional photomultiplier tube (PMT) as the detector. In CMAP a commercially available CCD (Atik 314L+) is chosen which uses Sony ICX285AL ExView  $1392 \times 1040$  sensor, having a pixel size of  $6.45 \mu\text{m}$  with the total size of the chip being  $8.98 \times 6.71 \text{ mm}$ . The QE of this detector is above 40% for wavelengths from 420 nm to 770 nm. Before commissioning CMAP for regular operations, its performance was inter-compared with a collocated PMT based photometer which showed one to one resemblance in the data obtained from two separate instruments.

The operation and monitoring of different subsystem of CMAP, such as, filter wheel, CCD, and temperature control unit is achieved by in-house developed software. Through this software we can control: (1) All the CCD parameters (temperature, on-chip binning, exposure time, and image acquisition), (2) Filter position, and (3) Temperature of filter wheel assembly. This software



also generates a catalogue file in which following eleven relevant parameters, namely, time (HHMMSS), month, date, year, day of the year, exposure time, x-binning, y-binning, CCD temperature, filter position, and filter temperature of the image being acquired are stored.

#### 2.7.4 Derivation of Nightglow Emission Intensities

In CMAP we have used four interference filters as per our scientific requirement which are (1) two sodium doublet lines (589.0 and 589.6 nm), (2) OI green line emission at 557.7 nm wavelength emission, and (3) OI red line emission at 630.0 nm wavelength. Sodium, OI green line, and OI red line emissions emanate from altitudes of 92 km, 100 km, and 250 km, respectively. Codes are developed to calculate the nightglow emission intensities from the FITS images obtained from the CMAP. Figure 2.12 show the nocturnal variation of the airglow emission intensities at the four wavelengths as given above.

## 2.8 Supplementary Datasets

The main datasets used in this thesis are nightglow emission intensities and temperatures obtained from ground-based observations using NIRIS and CMAP from Gurushikhar. In order to understand the global phenomena and long-term solar effect in the MLT region satellite-based datasets and solar parameters (SSN and F10.7) are used. These datasets are briefed in following section:

### 2.8.1 Sounding of the Atmosphere using Broadband Emission Radiometry (SABER)

SABER on-board Thermosphere, Ionosphere, Mesosphere Energetics and Dynamics (TIMED) satellite is a 10-channel broad-band limb viewing, infrared radiometer that measures daytime and night-time Earth limb emissions ( $\sim 20$ -450 km tangent height range) in the spectral range of 1.27  $\mu\text{m}$  to 17  $\mu\text{m}$

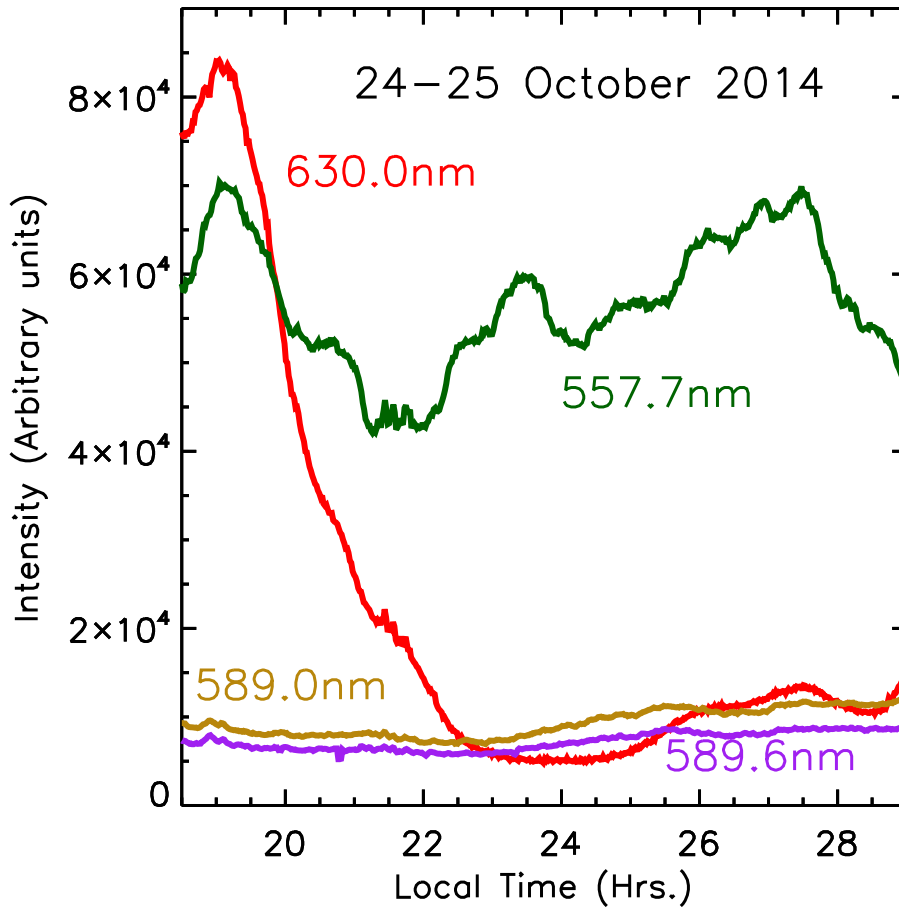


**Figure 2.12:** Nocturnal variations in the OI(630.0), OI(557.7 nm), and sodium (589.0 and 589.6nm) nightglow emission intensities as measured by CMAP at Gurushikhar, Mount Abu on the night of 24-25 October 2014. These emissions are considered to be originating from 250, 100, and 92 km altitudes, respectively.

[*Russell III et al. (1999)*]. TIMED was launched in December 2001 which orbits at around 625 km height with an inclination of  $74.1^\circ$  relative to the equatorial plane in a circular polar orbit which are approximately 15 orbits per day. SABER yields kinetic temperatures as a function of latitude and longitude in the altitude range of 20 to 140 km that are derived using the  $15 \mu\text{m}$   $\text{CO}_2$  emissions, which account for non-LTE conditions in the region. The view angle of SABER is oriented in the anti-Sunward direction of the spacecraft resulting in an asymmetric global coverage which is  $53^\circ$  in one hemisphere to  $83^\circ$  in the other hemisphere. This coverage alternates between both the hemispheres after approximately 60 days and is enabled by satellite yaw ma-

neuver. SABER temperature data used in this work has been obtained from [http://saber.gats-inc.com/browse\\_data.php](http://saber.gats-inc.com/browse_data.php). The retrieval uncertainty in the SABER temperatures as reported by *Mertens et al. (2001)* are 1.4 K at 80 km, 3.9 K at 88 km, 4.7 K at 94 km, and 22.5 K at 110 km. Using 1.07 version SABER temperatures *Remsberg et al. (2008)* compared it with ground-based observations which showed that the error in temperature was within  $\pm 5$  K in the MLT region. *García-Comas et al. (2008)* considered the errors in the non-LTE parameters and showed that the overall error in SABER temperatures are around  $\pm 1$ – $2$  K below 95 km and  $\pm 4$ – $5$  K at 100 km.

### 2.8.2 Optical Spectrograph and Infrared Imaging System (OSIRIS)

The OSIRIS instrument on-board Odin satellite is a limb-viewing instrument, which observes scattered solar radiation and airglow emissions in the wavelength range of 275–810 nm for tangent heights ranging from 10 to 100 km. The Odin satellite was launched into a sun-synchronous  $97.8^\circ$  inclination polar orbit in February 2001 [*Murtagh et al. (2002)*]. The latitude coverage of OSIRIS is  $82^\circ$  N and  $82^\circ$  S, however, daytime conditions are observed mainly in the summer hemisphere. The nominal Odin ascending/descending node is 06:00/18:00 LT. Retrieval algorithms have been developed to recover the stratosphere and MLT temperatures from limb radiances [*Haley and McDade (2002)*; *Sheese et al. (2010)*]. *Sheese et al. (2010)* derived MLT temperatures from the OSIRIS observations of O<sub>2</sub> A-band ( $\text{O}_2(\text{b}^1\Sigma_g^+) \rightarrow \text{O}_2(\text{X}^3\Sigma_g^-)$ ) emission spectra. The estimated accuracy of the retrieved temperatures is approximately  $\pm 2$  K near 90 km and less than  $\pm 6$  K at 105 km altitudes.

### 2.8.3 Solar Occultation For Ice Experiment (SOFIE)

SOFIE on-board the Aeronomy of Ice in the Mesosphere (AIM) satellite provides information on temperatures in the polar atmosphere with 15 sunset /

sunrise measurements at latitudes from  $65^{\circ}$ – $85^{\circ}$  S/ $65^{\circ}$ – $85^{\circ}$  N each day [*Gordley et al. (2009)*] with consecutive sunrises or sunsets separated by around 96 min ( $24^{\circ}$  in longitude). AIM satellite was launched on 25 April 2007 in 600 km circular polar orbit. SOFIE temperature retrievals above 50 km use broadband transmittance measurements in the  $4.3 \mu\text{m}$  absorption band of  $\text{CO}_2$  [*Marshall et al. (2011)*]. Level 2A data have been used to extract mesospheric temperatures at polar latitudes in both the hemispheres which are obtained from <http://sofie.gats-inc.com/sofie/index.php>.

#### 2.8.4 Kalpana-1

In this study Outgoing Longwave Radiation(OLR) level-2 data has been used which has been obtained from the Very High Resolution Radiometer (VHRR) on-board the Indian meteorological satellite Kalpana-1, which is in a geostationary orbit. OLR is the radiative flux emitted from the Earth-atmosphere system to the outer space in the wavelength range of  $3\text{--}100 \mu\text{m}$  and can be used as a proxy for assessing the strength of convective clouds, as they attenuate the OLR flux. VHRR provides observations from three bands namely, visible (VIS:  $0.55\text{--}0.75 \mu\text{m}$ ), Water vapour (WV:  $5.7\text{--}7.1 \mu\text{m}$ ), and thermal infrared (TIR:  $10.5\text{--}12.5 \mu\text{m}$ ) with round-the-clock coverage over Indian sub-continent ( $40^{\circ}\text{S--}40^{\circ}\text{N}$ ,  $25^{\circ}\text{--}125^{\circ}\text{E}$ ). OLR has been derived from the thermal infrared band data using radiative transfer algorithms [*Singh et al. (2007)*; *Mahakur et al. (2013)*]. The OLR values thus derived, have a spatial resolution of  $0.25^{\circ}\times 0.25^{\circ}$  and a 15-minute cadence.

#### 2.8.5 Modern Era Retrospective-analysis for Research and Application (MERRA)

MERRA has been developed by NASA's Global Modelling and Assimilation Office focusing on the satellite era (1979-present), the details of which are provided by *Rienecker et al. (2011)*. In this work, MERRA data have been used

to obtain the stratospheric temperatures poleward of 60°N and longitudinally averaged zonal wind at 60°N at 10 hPa pressure level ( $\sim 32$  km).

### 2.8.6 F10.7 cm Radio Flux and SSN Numbers

To understand solar effects on to the MLT region, two parameters, namely, solar radio flux at 10.7 cm (2800 MHz) and sunspot numbers (SSN) are used as a tracers. The F10.7 cm radio emission originates from the upper chromosphere and lower corona of the sun, magnitude of which is measured by integrating the radiation centered at 2800 MHz (a wavelength of 10.7 cm) with 100 MHz-wideband. One hourly averaged values are provided and are expressed in the solar flux units (1 solar flux unit (sfu) = 1sfu =  $1 \times 10^{-22}$  Wm<sup>-2</sup>Hz<sup>-1</sup>). The F10.7 cm flux correlates well with the extreme ultraviolet (EUV) emissions that impact and modify the Earth's upper atmosphere and ionosphere. The F10.7 cm flux index, which is also referred to as the F10.7 index data, were obtained from [ftp://ftp.ngdc.noaa.gov/STP/GEOMAGNETIC\\_DATA/INDICES/KP\\_AP/](ftp://ftp.ngdc.noaa.gov/STP/GEOMAGNETIC_DATA/INDICES/KP_AP/).

In addition to the F10.7 cm flux, sunspot number (SSN) data are also used (obtained from [ftp://ftp.swpc.noaa.gov/pub/indices/old\\_indices/](ftp://ftp.swpc.noaa.gov/pub/indices/old_indices/)). The SSN matches quite well with F10.7 cm radio flux and are extensively used as proxies for the magnetic flux activity in the solar active regions.

## 2.9 Time Series Analysis (TSA) Methods

In practice, almost all of the data obtained are in time domain, which means that we do measure signal as a function of time. Such measurement provides us time series. In many cases, it becomes inevitable to know as to what frequencies exist in a given signal, since most distinguished information is hidden in the frequency spectrum of a signal. In order to derive the wave characteristics at different altitude regions of the Earth's upper atmosphere, nightglow emission intensities at multiple wavelengths and corresponding mesospheric

temperatures have been used in the present work. There are several TSA methods that are used e.g., if the data are equally spaced in time, such as, discrete Fourier transform (DFT) techniques are used for finding periodicities. However, our measurements are unevenly sampled in time and at finite time intervals which are caused due to the changes in the phases of moon, seasons, and cloud cover, which make it difficult to derive frequency information using conventional spectral analysis techniques. Since the data discussed in this work is unevenly spaced, Lomb-Scargle periodogram analysis [*Lomb (1976)*; *Scargle (1982)*] have been used to obtain the periodicities that are present in the data. The duration of occurrence of a particular frequency is obtained using wavelet analysis [*Torrence and Compo (1998)*], however, this can only be used for continuous datasets. These two methods of analyses to obtain frequency components and time localization of these frequency components have been used in the work presented in this thesis and are explained in following sections.

### 2.9.1 Lomb-Scargle Analysis

Consider a given set of data values  $h_i$ ,  $i=1,2,\dots,N$  at respective observation times  $t_i$ . The Lomb-Scargle normalized periodograms (spectral power as a function of  $\omega$ ) is defined by [*Lomb (1976)*; *Scargle (1982)*; *Horne and Baliunas (1986)*; *Press and Rybicki (1989)*]:

$$P_N(\omega) \equiv \frac{1}{2\sigma^2} \left\{ \frac{\left[ \sum_j (h_j - \bar{h}) \cos\omega(t_j - \tau) \right]^2}{\sum_j \cos^2\omega(t_j - \tau)} + \frac{\left[ \sum_j (h_j - \bar{h}) \sin\omega(t_j - \tau) \right]^2}{\sum_j \sin^2\omega(t_j - \tau)} \right\} \quad (2.8)$$

where,  $\omega \equiv 2\pi f$  is the angular frequency,  $\bar{h}$  and  $\sigma^2$  are the data mean and variance. The time offset is given by:

$$\tau = \left(\frac{1}{2\omega}\right) \tan^{-1} \left[ \frac{\sum_j \sin 2\omega t_j}{\sum_j \cos 2\omega t_j} \right] \quad (2.9)$$

This constant  $\tau$  makes  $P_N(\omega)$  completely independent of shifting all the  $t_j$ 's by any constant. This particular choice of offset makes equation 2.8 identical to the equation that one would obtain if one estimated the harmonic content of a data set (at a given frequency  $\omega$ ) by linear least-square fitting to the model [*Lomb (1976)*]:

$$h(t) = A \cos \omega t + B \sin \omega t \quad (2.10)$$

This explains why this method gives superior results on unevenly spaced data as it weights the data on a “per point” instead of on a “per time interval” basis.

### 2.9.1.1 Fast Computation of Lomb-Scargle Periodogram

The spectral analysis method used throughout this thesis work to obtain the time periods from unequally spaced time series data is based on the fast Lomb-Scargle evaluation given by *Press and Rybicki (1989)*. The trigonometric sums that occur in equations 2.8 and 2.9 can be reduced to four simpler sums. If we define:

$$S_h \equiv \sum_{j=1}^N (h_j - \bar{h}) \sin(\omega t_j), C_h \equiv \sum_{j=1}^N (h_j - \bar{h}) \cos(\omega t_j) \quad (2.11)$$

and

$$S_2 \equiv \sum_{j=1}^N \sin(2\omega t_j), C_2 \equiv \sum_{j=1}^N \cos(2\omega t_j) \quad (2.12)$$

Then

$$\sum_{j=1}^N (h_j - \bar{h}) \cos \omega(t_j - \tau) = C_h \cos \omega \tau + S_h \sin \omega \tau \quad (2.13)$$

$$\sum_{j=1}^N (h_j - \bar{h}) \sin\omega(t_j - \tau) = S_h \cos\omega\tau - C_h \sin\omega\tau \quad (2.14)$$

and

$$\sum_{j=1}^N \cos^2\omega(t_j - \tau) = \frac{N}{2} + \frac{1}{2} C_2 \cos(2\omega\tau) + \frac{1}{2} S_2 \sin(2\omega\tau) \quad (2.15)$$

$$\sum_{j=1}^N \sin^2\omega(t_j - \tau) = \frac{N}{2} - \frac{1}{2} C_2 \cos(2\omega\tau) - \frac{1}{2} S_2 \sin(2\omega\tau) \quad (2.16)$$

It can be readily seen that if  $t_j$ 's were evenly spaced, then the four quantities,  $S_h$ ,  $C_h$ ,  $S_2$ , and  $C_2$  could be evaluated by two complex FFT's, and the results could then be substituted back through equations 2.13–2.16 to evaluate equations 2.8 and 2.9. The problem is therefore only to evaluate equations 2.11 and 2.12 for unevenly spaced data.

### 2.9.1.2 Phase and Amplitude Spectra

Phase and amplitude estimation of atmospheric data sets are of great interest e.g., in gravity wave studies. Commonly, phases and amplitudes of spectral components of unevenly sampled data are determined by least square fit procedures which are independently performed after calculation of the Lomb-Scargle normalized periodograms (Equation 2.8). [Hocke \(1998\)](#) showed that Lomb-Scargle periodograms method can be used for the estimation of the phase and amplitude of the spectra.

Sine wave of the form

$$h_f(t_i) = a \cos\omega(t_i - \tau) + b \sin\omega(t_i - \tau) \quad (2.17)$$

can be fitted to the time series data  $h_i$  (with zero mean) at times  $t_i$ ,  $i=1, \dots, n$ .



Equation 2.8 can be written as:

$$P_N(\omega) = \frac{1}{2\sigma^2} \frac{N}{2} (a^2 + b^2) \quad (2.18)$$

where,

$$a = \frac{\sqrt{\frac{2}{N}} \sum_{i=1}^N h_i \cos\omega(t_i - \tau)}{\sqrt{\left(\sum_{i=1}^N \cos^2\omega(t_i - \tau)\right)}} \quad (2.19)$$

and

$$b = \frac{\sqrt{\frac{2}{N}} \sum_{i=1}^N h_i \sin\omega(t_i - \tau)}{\sqrt{\left(\sum_{i=1}^N \sin^2\omega(t_i - \tau)\right)}} \quad (2.20)$$

Hence, the amplitude spectra,  $A(\omega)$ , is derived by:

$$A(\omega) = \sqrt{a^2 + b^2} = \sqrt{\frac{2}{N}} \sqrt{2\sigma^2 P_N(\omega)} \quad (2.21)$$

The fitted sine wave  $h_f(t_i)$  from equation 2.17 can also be expressed by:

$$h_f(t_i) = A(\omega) \cos[\omega(t_i - \tau) + \phi] \quad (2.22)$$

where,  $\phi = -\tan^{-1}(b/a)$ . Hence, the phase spectrum shall be defined by the cosine argument of  $h_f(t_i)$  at the time  $t_i = 0$ :

$$\varphi_j(\omega) = -\omega_j\tau + \phi = -\omega_j\tau - \tan^{-1}(b/a) \quad (2.23)$$

Thus, equations 2.21 and 2.23 provide amplitudes and phase spectra of the periodograms obtained using Lomb-Scargle method.

### 2.9.1.3 Uncertainty in the frequency

The uncertainty in frequency is calculated using the following relation [[Bretthorst \(2013\)](#)]:

$$\delta f = \frac{1.1\sigma}{A \cdot T_{total} \cdot \sqrt{N}} Hz \quad (2.24)$$

where,  $f$  is the wave frequency,  $T_{total}$  is the total duration of observation,  $A$  is the amplitude of the signal,  $N$  is the number of measurements, and  $\sigma$  is the standard deviation of the noise after the signal has been subtracted. The likelihood of the existence of a periodic signal can be established with the false alarm probability (FAP). False alarm level (FAL) is calculated according to the desired number of independent frequencies and FAP which is calculated using formula given by [Horne and Baliunas \(1986\)](#).

#### 2.9.1.4 REDFIT

Deriving accurate significance levels in the spectral analysis is very important. For this one has to choose an appropriate background spectrum. It is then assumed that different time series which are used to understand the geophysical process will be randomly distributed about this mean or expected background, and the actual spectrum can be compared against this random distribution. For many geophysical phenomena, an appropriate background spectrum is either white noise (with a flat Fourier spectrum) or red noise (increasing power with decreasing frequency). In the Lomb-Scargle periodograms the spectral power at the high-frequency end of a spectrum are often overestimated. A routine and the computational steps followed to obtain a red-noise spectrum of an unevenly spaced time series is provided in [Schulz and Mudelsee \(2002\)](#). This routine is used to derive the significant periodicities that are present in the data used in this work.

## 2.9.2 Wavelet Analysis

The Lomb-Scargle method described above provides only the frequency components that exist in the unevenly spaced time series. In practice, we deal with nonstationary signals which means that the frequency content of the sig-

nal changes with time. For the stationary signal whose frequency content do not change with time one does not need to know at what times a particular frequency component exists, since all frequency components exist at all times. In applications, wherein the time localization of the spectral components is needed, we need a transform which provides information on the time-frequency localization of the nonstationary signal. The wavelet transform is capable of providing such a representation simultaneously [*Daubechies* (1992); *Torrence and Compo* (1998)].

However, it should be kept in mind that the wavelet transform requires evenly sampled time series. The Heisenberg uncertainty principle, which states that the momentum and the position of a moving particle cannot be estimated simultaneously, can be applied to time-frequency localization as well. It means we cannot tell exactly what frequency exists at what time instance but we can only tell what frequency bands exist at what time intervals. In practice, we deal with a signal having high frequency components for short durations and low frequency components for long duration. The wavelet transform uses multi-resolution analysis which analyzes the signal at different frequencies with different resolutions. This approach provides good time resolution/poor frequency resolution at high frequencies and poor time resolution/good frequency resolution at low frequencies. The method to obtain the wavelet transform is adapted from *Torrence and Compo* (1998) and will be described in following section.

### 2.9.2.1 Continuous Wavelet Transform (CWT)

The continuous wavelet transform (CWT) of a function  $x(t)$  is defined as:

$$W_x^\psi(\tau, s) = \frac{1}{\sqrt{|s|}} \int x(t) * \psi^*\left(\frac{t-\tau}{s}\right) dt \quad (2.25)$$

As seen in the above equation, the transformed signal,  $W_x^\psi(\tau, s)$ , is a function of two variables, namely, translation,  $\tau$ , and a scale parameter,  $s$ .  $\psi\left(\frac{t-\tau}{s}\right)$

is called the mother wavelet and  $\psi^* \left( \frac{t-\tau}{s} \right)$  is its complex conjugate. The factor  $\frac{1}{\sqrt{|s|}}$  is used for energy normalization. Translation,  $\tau$ , corresponds to time information in the transform domain and related to the location of the window, as the window is shifted through the signal. High scales (low frequencies) correspond to global information of a signal that usually spans the entire signal. Whereas, low scales (high frequencies) correspond to detailed information of a hidden pattern in the signal that usually lasts for a relatively short time.

*Daubechies (1990)* showed that the wavelet transform can be used to analyse non-stationary time series. Consider a discrete equally spaced time series,  $x_n$ , where  $n = 0, 1, \dots, N-1$ , with equal time spacing,  $\delta t$ , then the CWT of  $x_n$  is defined as the convolution of  $x_n$  with a scaled and translated version of wavelet,  $\psi$ , [*Torrence and Compo (1998)*].

$$W_n(s) = \sum_{n'=1}^{N-1} x_{n'} \psi^* \left[ \frac{(n' - n)\delta t}{s} \right] \quad (2.26)$$

where,  $\psi^*$  indicates the complex conjugate and normalized wavelet function. By varying the wavelet scale,  $s$ , and translating along the localized time index,  $n$ , one can construct a picture that shows both the amplitude of any feature( $s$ ) versus the scale and how this amplitude varies with time.

### 2.9.2.2 Wavelet Functions

There are different wavelet functions such as Morlet, Paul, derivative of Gaussian (DOG), and Mexican hat (DOG,  $m=2$ ). However, in this work Morlet wavelet has been used which consists of a plane wave modulated by a Gaussian:

$$\psi_0(\eta) = \pi^{-1/4} e^{i\omega_0\eta} e^{-\eta^2/2} \quad (2.27)$$

where,  $\eta$  is the non-dimensional time parameter and  $\omega_0$  is the non-dimensional frequency, here taken to be 6 to satisfy the admissibility condition.

While choosing the wavelet function, there are several factors such as,

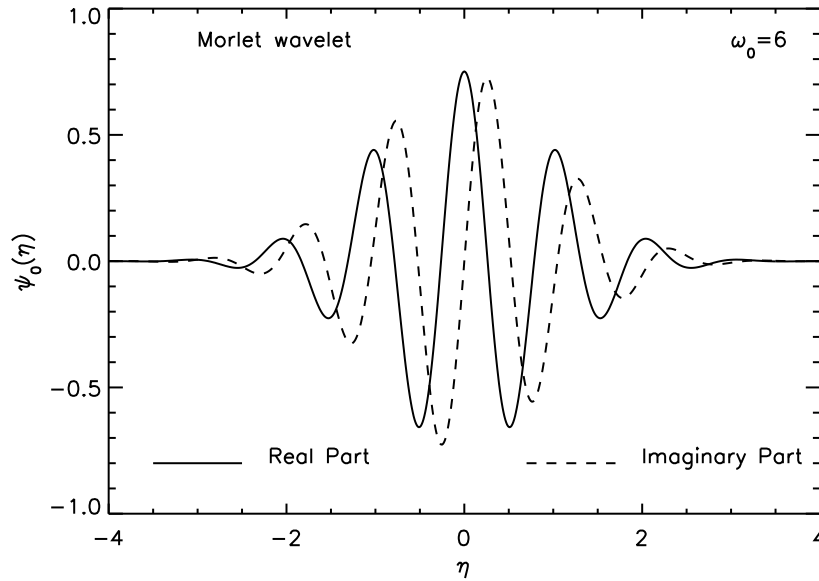


**Figure 2.13:** Real part (solid) and imaginary part (dashed) for the Morlet wavelet in the time domain.

orthogonal or nonorthogonal, complex or real, width, shape, and choice of scale ( $s$ ) which should be considered [e.g. [Farge \(1992\)](#); [Torrence and Compo \(1998\)](#)]. Figure 2.13 shows a Morlet wavelet in the time domain.

### 2.9.2.3 Wavelet Power Spectrum

The wavelet function  $\psi(\eta)$  is, in general, complex, the wavelet transform,  $W_n(s)$ , is also complex. The transform can then be divided into the real part,  $R\{W_n(s)\}$ , and imaginary part,  $I\{W_n(s)\}$ , or amplitude,  $|W_n(s)|$ , and phase,  $\tan^{-1} \left[ \frac{I\{W_n(s)\}}{R\{W_n(s)\}} \right]$ . The wavelet power spectrum is defined by  $|W_n(s)|^2$ .

### 2.9.2.4 Cone of Influence (COI)

As we are dealing with time series of finite length, errors are introduced at the beginning and towards the end of the wavelet power spectrum. This happens since the Fourier transform, which is used in deriving wavelet power spectrum, assumes that the data is cyclic. To circumvent this issue the time series is padded with sufficient zeros to bring the total data length  $N$  up to the next-

higher power of two thereby, limiting the edge effects and speed up the Fourier transform. As a result, padding discontinuities are introduced at the endpoints and, towards larger scales, amplitude decreases near the edges as more zeros enter the analysis. The cone of influence (COI) is the region of the wavelet spectrum in which the edge effects become important and is defined as the e-folding time for the autocorrelation of wavelet power at each scale. For a Morlet wavelet, the e-folding time ( $\tau_s$ ) is  $s\sqrt{2}$ . Since  $\tau_s$  is large at larger scales (larger periods) and forms the vertex of the cone and at smaller scales (smaller periods),  $\tau_s$  is small and forms the base of the cone. This e-folding time is chosen so that the wavelet power for a discontinuity at the edge drops by a factor  $e^{-2}$  and ensures that the edge effects are negligible beyond this point. For cyclic series there is no need to pad with zeroes, and there is no COI.

#### 2.9.2.5 Significance Levels

An appropriate background spectrum is defined which can be either white noise or red noise and if a peak in the wavelet power spectrum is significantly above this background spectrum, then it can be assumed to be a true feature with a certain percent confidence. It is defined, e.g., significant at the 5% level is equivalent to the 95% confidence level, and implies a test against a certain background level, while the 95% confidence interval refers to the range of confidence about a given value.

## 2.10 Wave Characteristics using NIRIS data

This section deals with the derivation of various parameters of mesospheric GW characteristics from O<sub>2</sub> and OH emission intensity variations. The use of time series analysis methods employed are demonstrated for a representative night of NIRIS observations on 4 May 2013 from Gurushikhar, Mount Abu.

### 2.10.1 Derivation of Wave Period ( $\tau$ )

To derive the wave periods, O<sub>2</sub> and OH nightglow emission intensities obtained from NIRIS, as shown in figure 2.7c is used. The large nocturnal variability in the NIRIS derived mesospheric intensities and corresponding temperatures show short period oscillations embedded in them (Figure 2.7). It is owing to high data cadence ground-based observations from NIRIS that these features could be obtained. As indicated before, the data cadence of NIRIS is 5 minutes and the duration of data available on this night is of around 9 hours (19:30 LT in the evening to 04:40 LT on the following morning). Therefore, it is possible to derive the periods between 10 minutes and 9 hours on these two nights. In general, the minimum frequency (maximum period) is given by total observational duration. However, we have put a more rigorous constraint in deriving the maximum periods in which we have considered that the data should contain at least two cycles.

The periodicities obtained using Lomb-Scargle analysis method in which Figure 2.14a and Figure 2.14b shows the periods that are obtained using method as described in *Horne and Baliunas (1986)* and *Schulz and Mudelsee (2002)*, respectively. All periods which are above FAL are statistically significant.

In order to derive the periodicities that are smaller than half of the observational duration (for the night of 4 May 2013 it is 4.5 hours), residuals have been obtained by subtracting 4.5-hour running average from the original data. The residuals so obtained are represented in the form of zero mean unit variances which were calculated by subtracting the mean value from the residuals and then dividing them by their standard deviation. This process normalizes the relative power in each period in a given dataset and thereby enables inter-comparison of the parameters on different nights [*Pallamraju et al. (2010)*; *Singh and Pallamraju (2017a)*].

In Figure 2.15a the solid lines show the nocturnal variation in O<sub>2</sub> and OH

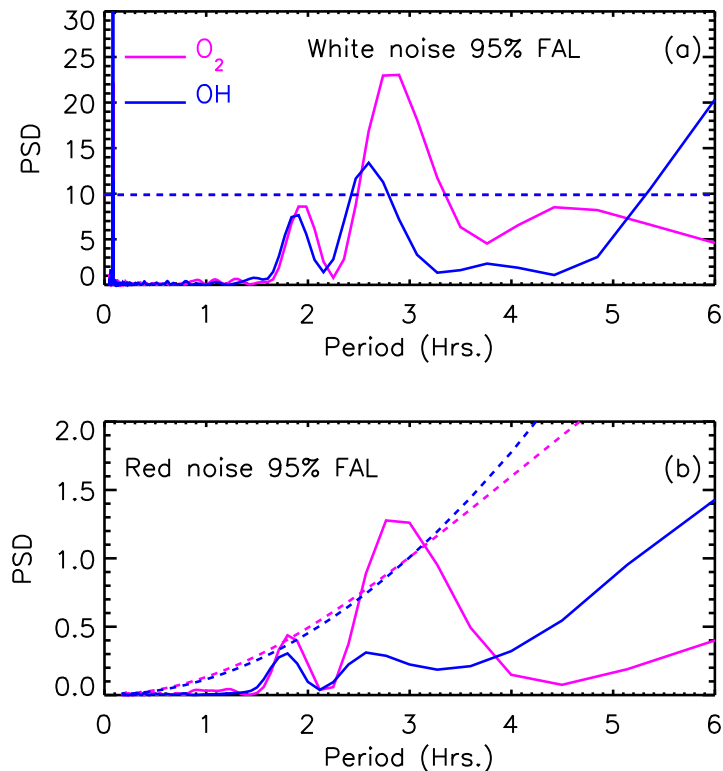


**Figure 2.14:** Periods that are present in nocturnal variation in  $O_2$  and  $OH$  emission intensities on the night of 4 May 2013 (shown in Figure 2.7c) obtained using methods described in: (a) Horne and Baliunas [1986] and (b) Schulz and Mudelsee [2002].

intensities,  $I(O_2)$  and  $I(OH)$  for 4 May 2013 (same data as shown in Figure 2.7c) and dashed lines are 4.5-hour running average of the intensity values. The residuals of these intensities are shown in Figure 2.15b which are represented in the form of zero mean unit variances.

These residuals have been subjected to spectral analyses which provide information on the GW periodicities that are smaller than 4.5-hour duration in the data. The result of this analysis is shown in Figures 2.15c and 2.15d and these periodograms are generated using the method described in *Horne and Baliunas* (1986) and *Schulz and Mudelsee* (2002), respectively. Statistically significant coherent periodicities (greater than FAL) of 1.8 hours can be clearly seen in  $I(O_2)$  and  $I(OH)$  obtained by both the techniques. As can be seen from Figure 2.15c around 2.7 hour periods is also seen in  $I(O_2)$  and  $I(OH)$ . However, 2.7 hour periods is seen in only  $I(O_2)$  and not in  $I(OH)$  by using the *Schulz and*



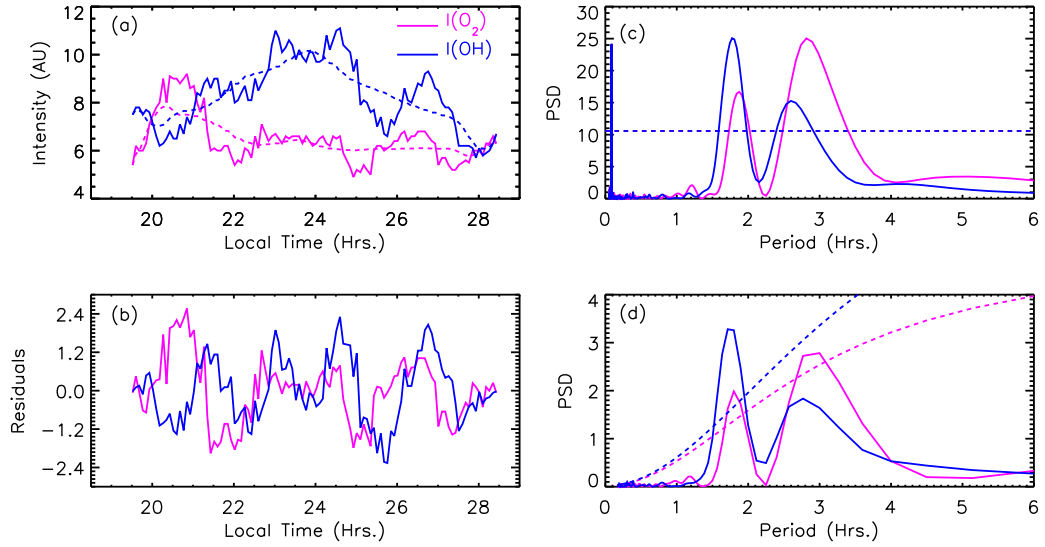


**Figure 2.15:** (a) Nocturnal variation in  $I(\text{O}_2)$  and  $I(\text{OH})$  on the night of 4/5/2013 (solid lines) and 4.5-hour running average (dashed lines). (b) Residuals obtained by subtracting the 4.5-hour running averaged values from the original data and are represented by zero mean and unit variances. (c) Lomb-Scargle periodograms of the residuals shown in Figure 2.15b adapting method described in *Horne and Baliunas (1986)*. (d) The periodograms obtained using method described in *Schulz and Mudelsee (2002)*.

*Mudelsee (2002)* method (Figure 2.15d). In general, in this work the method of *Horne and Baliunas (1986)* is used for deriving longer periodicities, and the method of *Schulz and Mudelsee (2002)* is used to derive shorter periodicities.

### 2.10.2 Derivation of vertical phase speed ( $c_z$ ) and vertical wavelength ( $\lambda_z$ )

Since the residuals of the  $I(\text{O}_2)$  and  $I(\text{OH})$  show a common periodicity and a downward phase propagation in the nightglow emission intensities on the night of 04 May 2013 (as can be seen in Figures 2.16a and 2.16b) it is apparent that the GW propagated upwards (*Hines (1960)*). These downward phase propagations seen in the residuals of the nightglow intensities are highlighted by green dashed lines in Figure 2.16.

By using cross correlation analysis between residuals of  $\text{O}_2$  and  $\text{OH}$  intensities seen in 2.16, we have calculated the phase offset times ( $\Delta t$ ) which are

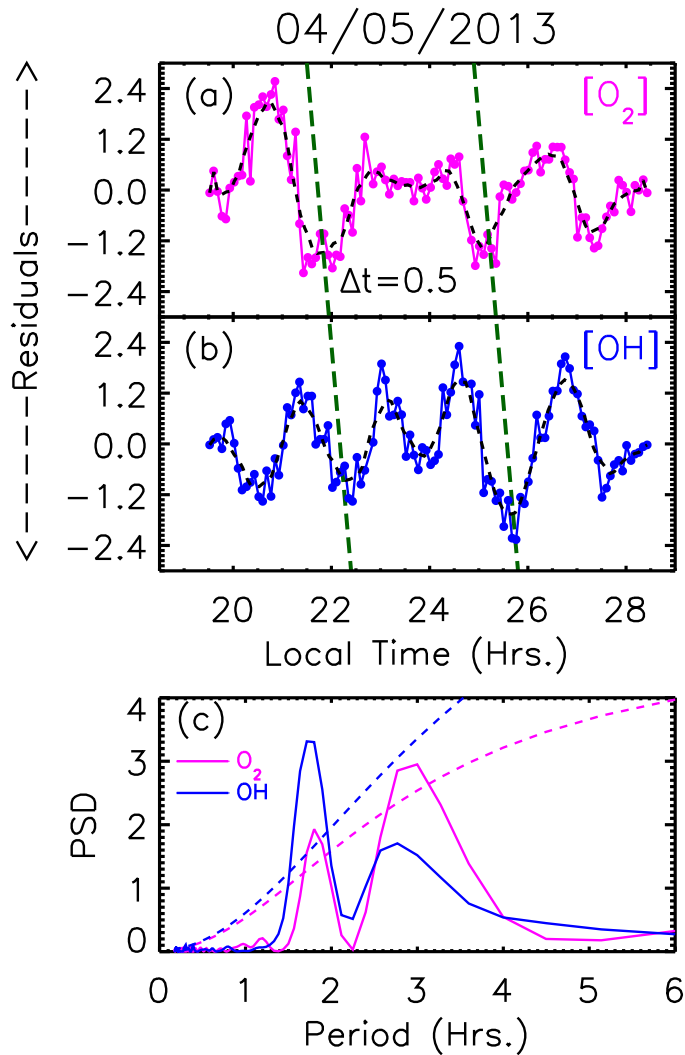


**Figure 2.16:** (a and b) Residuals obtained by subtracting the 4.5-hour running averaged data from the original nightglow intensities for both  $O_2$  and  $OH$  emissions as shown in Figure 2.7c and are represented by zero mean and unit variances on the night of 04 May 2013. (c) Lomb-Scargle periodograms of these residuals showing 1.85 hour common period in both the intensities that are greater than 95% false alarm level (FAL). As can be seen, the phase is propagating downwards indicating that there is an upward propagation of gravity waves.

found to be 0.5 hour for the nights 4 May 2013. With the knowledge that the waves show common periodicities in  $I(O_2)$  and  $I(OH)$  and the time offsets in the residual intensity variations ( $\Delta t$ ) the vertical phase speed,  $c_z$ , and vertical wavelength,  $\lambda_z$ , can be calculated using the following relations:

$$c_z = \frac{\Delta z}{\Delta t} \quad \text{and} \quad \lambda_z = \frac{\tau \cdot \Delta z}{\Delta t} \quad (2.28)$$

where  $\Delta z$  is the difference between the heights O<sub>2</sub> and OH emission layers (7 km). Thus, using  $\Delta t$  and  $\tau$  obtained experimentally as discussed above, the vertical phase speeds ( $c_z$ ) and the vertical wavelengths ( $\lambda_z$ ) are calculated using equation 2.28 which turn out to be 3.9 ms<sup>-1</sup> and 25.2 km on the night of 04 May 2013. It is important to note that the derivation of vertical wavelength can be done only if the GW period ‘ $\tau$ ’ is coherent at both the altitudes and wave shows vertical propagation (downward phase propagation). No coherency observed in  $\tau$  is an indication that the GWs at these two altitudes could be of different origin.

### 2.10.3 Derivation of Meridional Wavelength ( $\lambda_y$ )

As mentioned above, NIRIS has a large FOV of 80° and is presently being operated in north-south orientation. To increase the signal collection 1×32 on-chip binning has been carried out. The on-chip binning reduces the time taken to read-out the image thereby increasing the data cadence. A sample image so obtained is shown in Figure 2.5 in which the vertical axis represents the spatial coverage of the sky. Therefore, by using the airglow intensity variability from different directions along the meridian being imaged by NIRIS, it is possible to derive the neutral gravity wave scale sizes in the meridional direction ( $\lambda_y$ ). By operating NIRIS in the east-west orientation it is possible to obtain the gravity wave scale sizes in the zonal direction ( $\lambda_x$ ).

At the O<sub>2</sub> and OH emission altitudes (94 km and 87 km) the spatial extent being covered by NIRIS is 155 km and 145 km. Since a total of 15 pixels on the CCD (for 1×32 binning) cover 80° of the sky in the y-direction, the meridional scale sizes which are discernible at O<sub>2</sub> and OH emission altitudes are 20.6 to 155 km and 19.4 to 145 km. Meridional variations of O<sub>2</sub> and OH emission intensities for every individual observation (5 min cadence) throughout the

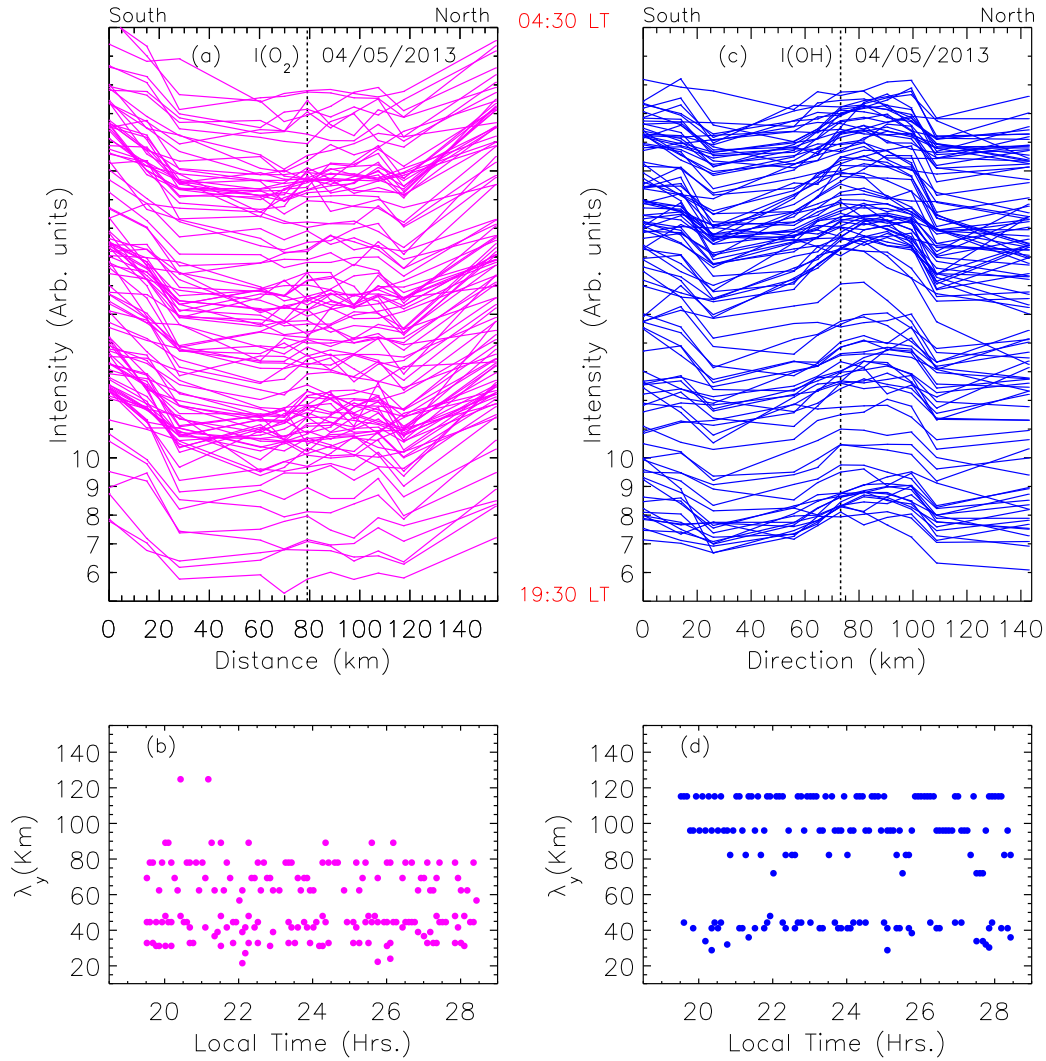


**Figure 2.17:** (a and c) Variations in the  $\text{O}_2$  and  $\text{OH}$  intensities along N-S meridian for the night of 4 May 2013 are shown. In both the figures the scales shown on the vertical axis is for the bottom-most intensity variations and the subsequent plots are shifted by 0.15 arbitrary units. The GW meridional scale lengths along the north-south meridian are obtained by carrying out wave number spectral analyses for each observation at a cadence of 5 minutes. (b and d) Statistically significant meridional wavelengths are shown for  $\text{O}_2$  and  $\text{OH}$  intensity variation throughout the night. A common 40 to 50 km meridional wavelength is observed at both altitudes for most of the duration on this night.

night are shown in Figures 2.17a and 2.17c for the night of 4 May 2013. Here, the vertical scale is for the bottom-most intensity variation and the subsequent plots are shifted by 0.15 arbitrary units (AU) for a better visualization. The start and end times of the observations (19.5 hours (19:30 LT) and 28.5 hours

(04:30 LT of 5 May) are marked on the right side of 2.17a. The horizontal axes in Figures 2.17a and 2.17c show the meridional coverage (from south to north) at the respective emission altitudes and the dashed vertical lines indicate the position of zenith. The large scale structures in the spatial intensity variations are evident throughout the night in both O<sub>2</sub> and OH intensities.

Wave number spectral analyses on these spatial intensity variations thus provide information on the GW scale sizes along the north-south meridian ( $\lambda_y$ ). Using Lomb-Scargle analyses statistically significant horizontal wavelengths are obtained which are above 90% FAL for every observation throughout the night. Nocturnal variations in  $\lambda_y$  for the night of 4 May 2013 obtained from O<sub>2</sub> and OH intensities are shown in Figures 2.17b and 2.17d. It can be noted that the meridional wavelengths,  $\lambda_y$ , of larger scale sizes (90 and 110 km) are present only at the OH emission altitudes in comparison with the 60-80 km meridional scale sizes observed at O<sub>2</sub> emission altitudes. The scale sizes of 30-50 km are more in number at O<sub>2</sub> emission altitudes as compared to the OH emission altitudes. The observation of larger scale sizes at the OH emission altitudes as compared to the O<sub>2</sub> emission altitudes seem most probably a signature of gravity wave breaking just above the OH emission altitude.

#### 2.10.4 Wavelet Spectrum

In order to investigate the duration of the occurrence of the periodicities present in the data, wavelet analyses have been performed (Morlet mother wavelet function was used [*Torrence and Compo (1998)*]). Figures 2.18(a-b) show the result of this analyses on the zero mean unit variances of the residual of the I(O<sub>2</sub>) and I(OH) (Figure 2.15b). The horizontal and vertical axes show local time and periods in hours. The normalized logarithmic power values are plotted and the scale is shown on the right. The cone of influence is also shown as a solid line. As can be seen from Figure 2.18, the duration of occurrence of the periodicities as seen in Lomb-Scargle periodograms are presented along

with their temporal occurrences.

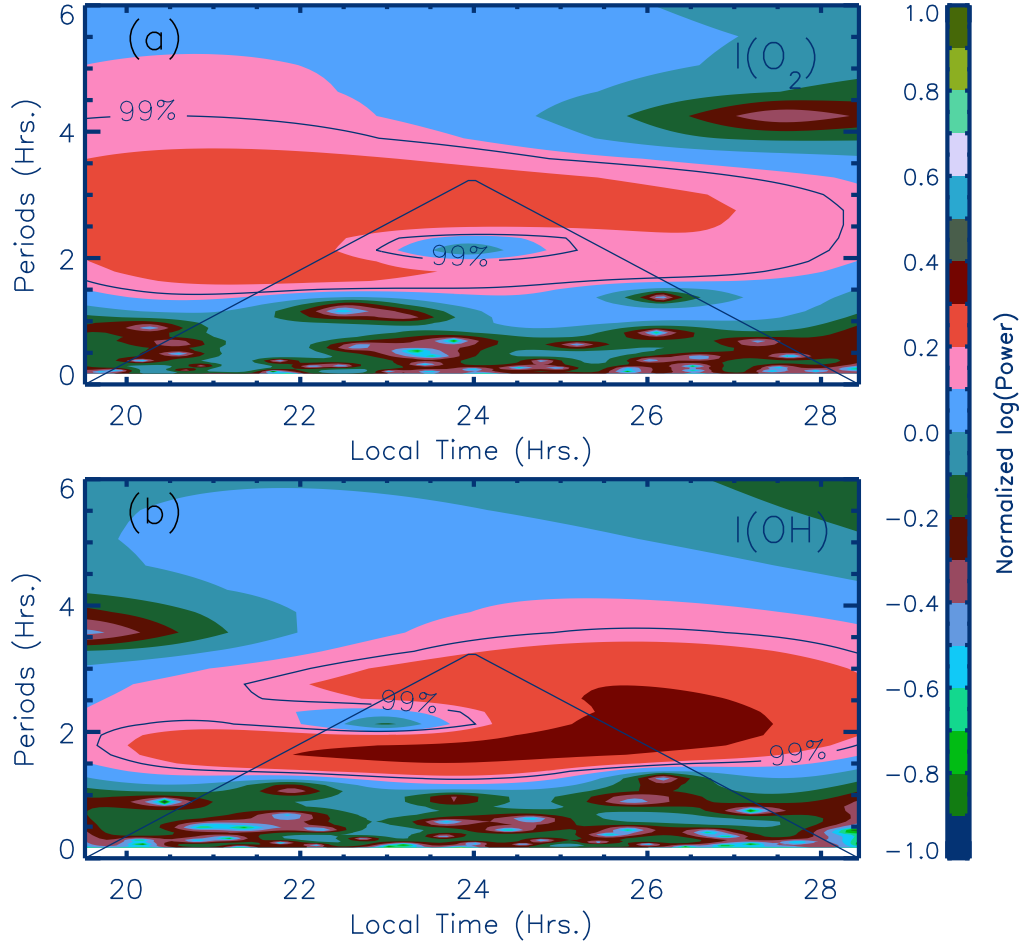


**Figure 2.18:** (a and b) The wavelet transform of the residuals of  $I(O_2)$  and  $I(OH)$  are shown. The cone of influence and significance levels are also shown. The occurrence of the same periodicities as seen from Lomb-Scargle method can be clearly seen along with their temporal duration of the occurrences of a given periodicity.

## 2.11 Schematic of the Wave Propagation

Figure 2.19a shows the schematic of a propagating gravity wave of horizontal wavelength,  $\lambda_h$ , and vertical wavelength,  $\lambda_z$ . Here, the wave fronts of the wave, both crests and troughs, are shown as filled and open loops (ellipses). The phase is shown to be progressing downwards (upward propagating wave). The magenta and blue coloured horizontal lines in Figure 2.19a represent the

altitudes of peak O<sub>2</sub> and OH emissions.

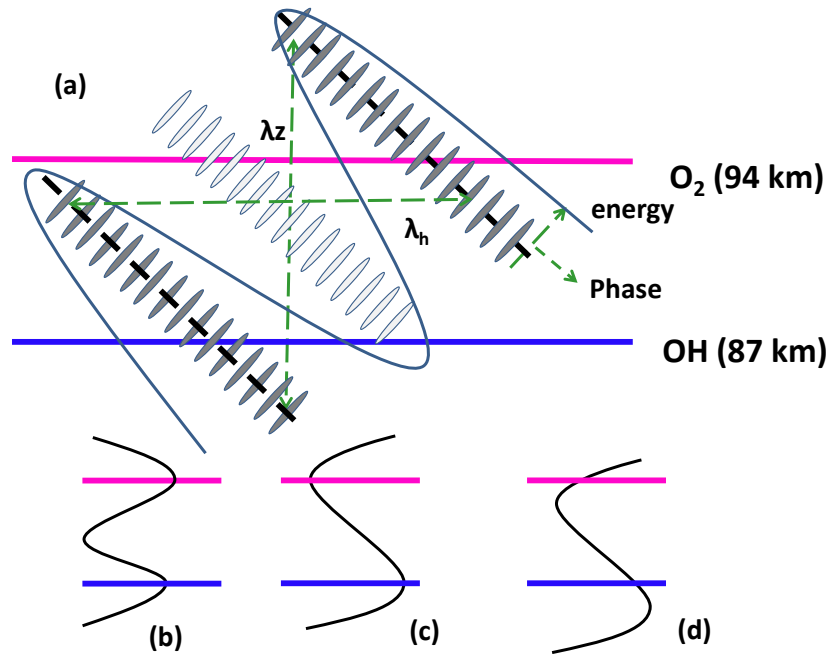


**Figure 2.19:** (a) A schematic of the propagation of gravity wave in which the phase is shown to be progressing downwards (upward propagating wave).  $\lambda_h$  and  $\lambda_z$  represent the horizontal and vertical wavelength of the gravity wave. (b-d) Possibilities for the nature of vertical wavelengths, which can show three different scenarios. Under these scenarios, the nocturnal variations in O<sub>2</sub> and OH intensities can show in phase, out of phase, and constant-phase variations.

The nocturnal variations in O<sub>2</sub> and OH emission intensities as seen in Figure 2.7 for both the nights are also due to convolution of the effect of wave propagation of similar kind as seen in Figure 2.19a from lower to higher altitudes. As can be seen in Figure 2.7 these variations in intensities and temperatures can have varying relationship (in-phase, out-of-phase or constant phase) depending on the GW vertical wavelengths and angles of propagation. Figures 2.19b, 2.19c, and 2.19d shown three representative possibilities. In the first scenario (Figure 2.19b) if the vertical wavelength of the upward propagating wave is such that the crests of the wave overlap with the peak altitudes of emission of O<sub>2</sub> and OH, then, both the intensities show in-phase variations.

In this case the vertical wavelength is equal to the distance between the altitudes of emission. The higher harmonics of this scale size will also give rise to in-phase variations, however, the lower scale sizes will be limited by kinematic viscosity. The second scenario (Figure 2.19c) could be when the crest/trough of the vertical wave falls at OH/O<sub>2</sub> emission altitudes or vice versa, then, both the intensities show out of phase variations. Thus, in this case the vertical wavelength will be equal to twice the difference in the emission altitudes of OH and O<sub>2</sub>. In the third scenario (Figure 2.19d) the crest/trough of the waves occur either lower or higher than the peak height of the OH and O<sub>2</sub> emissions. In such case, there could be in-phase/out-of-phase/constant-phase relationship between these two emissions. Also, depending on the vertical wavelength, angle of propagation, and the speed of propagation the in-phase relationship could change to out-of-phase with time. It should be noted that these three cases are not the only possibilities. There could be different harmonics of the wave that can show similar/dissimilar variations in the emission intensities at both the altitudes. This schematic is drawn to provide a visualization of the wave dynamical influence at altitudes of emissions so that the results pertaining to the MLT wave dynamics could be understood better.

## 2.12 Summary

This Chapter describes the details of the development of ground-based instruments and the satellite-based data sets that have been used in this thesis work. The main data sets used in this work are the nightglow emission intensities at multiple wavelengths (OI 557.7nm, O<sub>2</sub>(0-1) atmospheric band, Na 589.3 nm, and OH(6-2) band emission) and mesospheric temperatures derived from O<sub>2</sub>(0-1) and OH(6-2) band emissions. These parameters have been derived by using passive remote sensing techniques from in-house built spectrograph and photometer. NIRIS is based on spectrographic technique which provides nocturnal spectral images from which OH(6-2) Meinel and O<sub>2</sub>(0-1) atmospheric band



nightglow emission intensities and corresponding temperatures are obtained. The details of NIRIS, its calibration, derivation of nightglow emission intensities, and derivation of mesospheric temperatures are described. NIRIS derived mesospheric temperatures compare well with those derived from SABER observations. CMAP is used to obtain nightglow emission intensities at multiple wavelengths that emanate in the MLT region. The optical design, fabrication of different components, and derivation of nightglow emission intensities from CMAP are also discussed. The supplementary data sets that have been used in this work that include those obtained from SABER, OSIRIS, SOFIE, Kalpana-1, and MERRA are also discussed. Solar variability as seen in the F10.7 cm radio flux and sunspot numbers are also used in this work.

Time series analyses methods to derive the wave parameters from the time series are described. The mathematical background of Lomb-Scargle method which takes care of unequally spaced time series is discussed. The wavelet transform which is used for obtaining simultaneous time and frequency information from the time series is also discussed. The use of these analyses methods is demonstrated by applying it on the NIRIS data to derive different gravity wave characteristics on a particular night. A schematic is also drawn to suggest the possible vertical wavelength characteristics that can show the different kinds of observed variations in the MLT nightglow emission intensities. The codes used for implementing various analysis techniques are developed in Interactive Data Language (IDL). The IDL codes are also developed for the analysis of other supplementary data sets. Some other data analysis methods are also used in this work and are explained in the following Chapters which describe the science results on various aspects of variations in the intensities and temperatures in the MLT region.



# Chapter 3

## Large- and Small-Timescale Variations in the MLT region

### 3.1 Background

The motivation of present study is to understand the large- and short-timescale variations of the atmosphere in the MLT region and their variations with the solar activity. These results have been obtained using NIRIS derived mesospheric airglow emission intensities and corresponding rotational temperature data for over three years (2013-2015) of observations from a low-latitude location, Gurushikhar, Mount Abu. The statistical analysis of short-time scale fluctuations are carried out by obtaining the wave periods that are present on each individual night.

Airglow emissions are known to play an important role in the studies of the dynamical processes that occur in the Earth's atmosphere. This is because the changes in the photochemical processes that bring about the variations in the corresponding intensities is directly related to those in atmospheric temperature and density of the reactants. The large- and small-scale variations in the mesospheric intensities and temperatures can either be due to changes in the solar flux or due to atmospheric dynamical processes driven by gravity waves

(GWs), tides, and planetary waves, and therefore, the observed variability in mesospheric emissions is a resultant of the convolved behaviour between these two forcings. We have used O<sub>2</sub>(0-1) atmospheric and OH(6-2) band emission intensities that emanate from approximately 94 and 87 km, respectively, and corresponding temperatures, to understand the solar and dynamical effects on these parameters. In sections 3.3 and 3.4, large- and short-timescale waves which are of atmospheric origin and/or due to the solar effects are presented. The results are summarized in section 3.5.

## 3.2 Data set

The main data set which has been used in this study is the NIRIS measured O<sub>2</sub> and OH emission intensities and corresponding rotational temperatures from Gurushikhar, Mount Abu (24.6°N, 72.8°E) for over three years (2013-2015). Figure 3.1 shows total observational duration for a given night starting from 1 January 2013 to 21 November 2015 corresponding to day of the year (DOY) 1 to 1055.

The spectral images are checked visually for their quality. In addition, in this study we have considered only those nights for which the nightly observational duration is greater than 3 hours. After implementing these selection criteria conditions there exist a total of 437 nights of data available for detailed investigations. The average duration of the observation per night is  $8.4 \pm 2.3$  h which is based on more than 35000 clear spectra obtained from NIRIS. The variations in the data duration and data gaps seen in Figure 3.1 are due to the changes in phases of moon, seasons, and cloud cover. We get maximum durations of observation around the new moon phase for cloud free nights. These conditions prevail mostly during the winter season. There were two large data gaps during DOY 455 to 652 and 893 to 1003 caused due to technical difficulties with the data acquisition system of NIRIS.

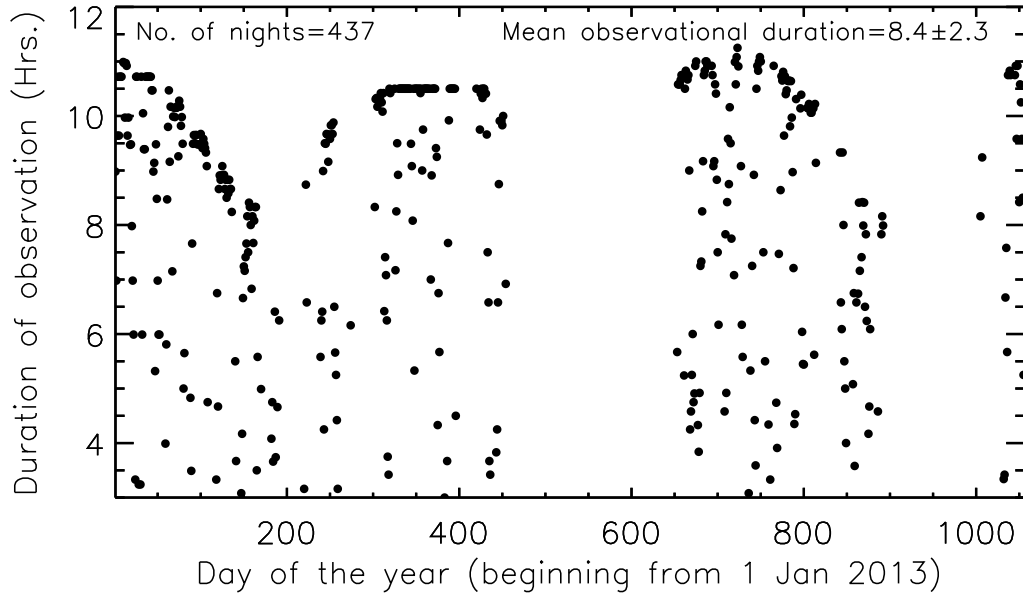


**Figure 3.1:** Details of the duration of observations obtained from the Near InfraRed Imaging Spectrograph (NIRIS) at Gurushikhar, Mount Abu (24.6°N, 72.8°E), in India. The durations of observations per night are shown as a function of day of the year (DOY); DOY 1 corresponds to 1 January 2013.

### 3.3 Large-time Scale Variations

In this section, the results that have been obtained pertaining to the large-time scale variations in the mesospheric nightglow emission intensities and temperatures will be discussed. The results obtained from the long-term NIRIS observations revealed that the solar effects and atmospheric wave dynamical processes were both present simultaneously in O<sub>2</sub> and OH emission intensities and temperatures.

#### 3.3.1 Introduction

The production mechanisms that give rise to the O<sub>2</sub> and OH band emissions in the mesosphere are described in Chapter 1. From those mechanisms it can be seen that the O<sub>2</sub> and OH nightglow emission intensities are related to the concentrations of atomic oxygen and ozone and hence, to the ultra-violet (UV) solar energy input that is responsible for their photochemical produc-

tion. Therefore, these emissions are expected to show variations with the UV solar energy input and hence, with solar activity. However, quantitative understanding of solar effects on mesospheric parameters is far from complete. The temporal variations of various time-scales can be investigated by carrying out high cadence and systematic long-term ground-based measurements of airglow emission intensities and temperatures.

In the mesopause region the response to solar activity is small in comparison to the upper thermosphere where strong absorption of solar UV causes significant solar forcing [e.g., *Laskar et al. (2015)*]. Solar effects on the variation of mesospheric emissions and temperatures have been studied by different investigators using ground-based data. For example, *Wiens and Weill (1973)* showed that OH(9-3) band nightglow intensity follows the variation in solar activity; *Batista et al. (1994)* showed that OH(9-4) band nightglow intensity had a positive correlation with the solar 10.7 cm radio flux index (F10.7). However, *Scheer et al. (2005)* showed that there was no correlation of OH(6-2) band nightglow intensities and temperatures with solar radio flux but they found a moderate positive correlation with O<sub>2</sub>(0-1) nightglow intensity and temperatures. *Pertsev and Perminov (2008)*, showed that the response of O<sub>2</sub> and OH nightglow intensity to solar 10.7 cm radio flux could reach to 40%/100 solar flux units (sfu), and 30%/100 sfu, respectively. The response of the mean annual OH temperature to solar activity is shown to be different in different works, for example, around 1 K/100 sfu [*Scheer et al. (2005)*], 4.5 K/100 sfu [*Pertsev and Perminov (2008)*], and 11 K/100 sfu [*Clemesha et al. (2005)*].

As discussed above, experimental results on solar cycle related effects on the magnitudes of intensity and temperature over low-latitude MLT region are ambiguous and continue to be a topic of investigation. In this study, we have made an attempt to carryout detailed investigations on this relationship by spectral analysis method. A clear imprint of solar effect in the mesospheric nightglow intensity and temperature variations is seen wherein significant periodicities in various parameters (nightglow intensities, temperatures, F10.7,

and SSN) are shown to be coherent.

### 3.3.2 Results and Discussion

Variation in the O<sub>2</sub> and OH emission intensities are presented in Figures 3.2a and 3.2b starting from 1 January 2013 (DOY1). The O<sub>2</sub>(0-1) atmospheric band and OH(6-2) Meinel band intensities are obtained by taking the mean of 866 nm and 868 nm emissions and mean of P<sub>1</sub>(2) and P<sub>1</sub>(4) rotational line intensities at 840.0 nm and 846.5 nm emissions. These two sets of intensities of the rotational lines of O<sub>2</sub> and OH band emissions are also used to derive the corresponding rotational temperatures at those altitudes [*Singh and Palle* (2017a)]. The nightly mean values for O<sub>2</sub> and OH emission intensities (IO<sub>2</sub> and IOH) are shown in magenta and blue colours and the spread in the nightly values are shown in pink and sky blue colours, respectively. As will be shown in the next section the large spreads in the nocturnal O<sub>2</sub> and OH emission intensity variations in a given night signify the presence of GWs type oscillations. These emissions also show large time period variations which seem to be due to the seasonal and solar cycle related effects.

In order to assess the effect of solar influence on the O<sub>2</sub> and OH intensities, the daily mean SSN and solar 10.7 cm radio flux are considered and are shown in Figure 3.2c. The temperatures derived using O<sub>2</sub>(0-1) and OH(6-2) band emission intensities (TO<sub>2</sub> and TOH) are shown in Figures 3.2d and 3.2e (wherein we have used the same colour codes as used for the intensities in Figures 3.2a and 3.2b). Similar to the variations in emission intensities, temperatures at both altitudes show both small- and large-time scale fluctuations.

A closer look at Figures 3.2a–3.2e shows that the response of solar effects is much more pronounced in intensities as compared to the temperatures. For example, the noticeable reductions in intensities seen during DOY 1-50 (January and February 2013) and in February and March 2015 (DOY 760-800) match quite well with those of the SSN and F10.7 cm radio flux. However, the

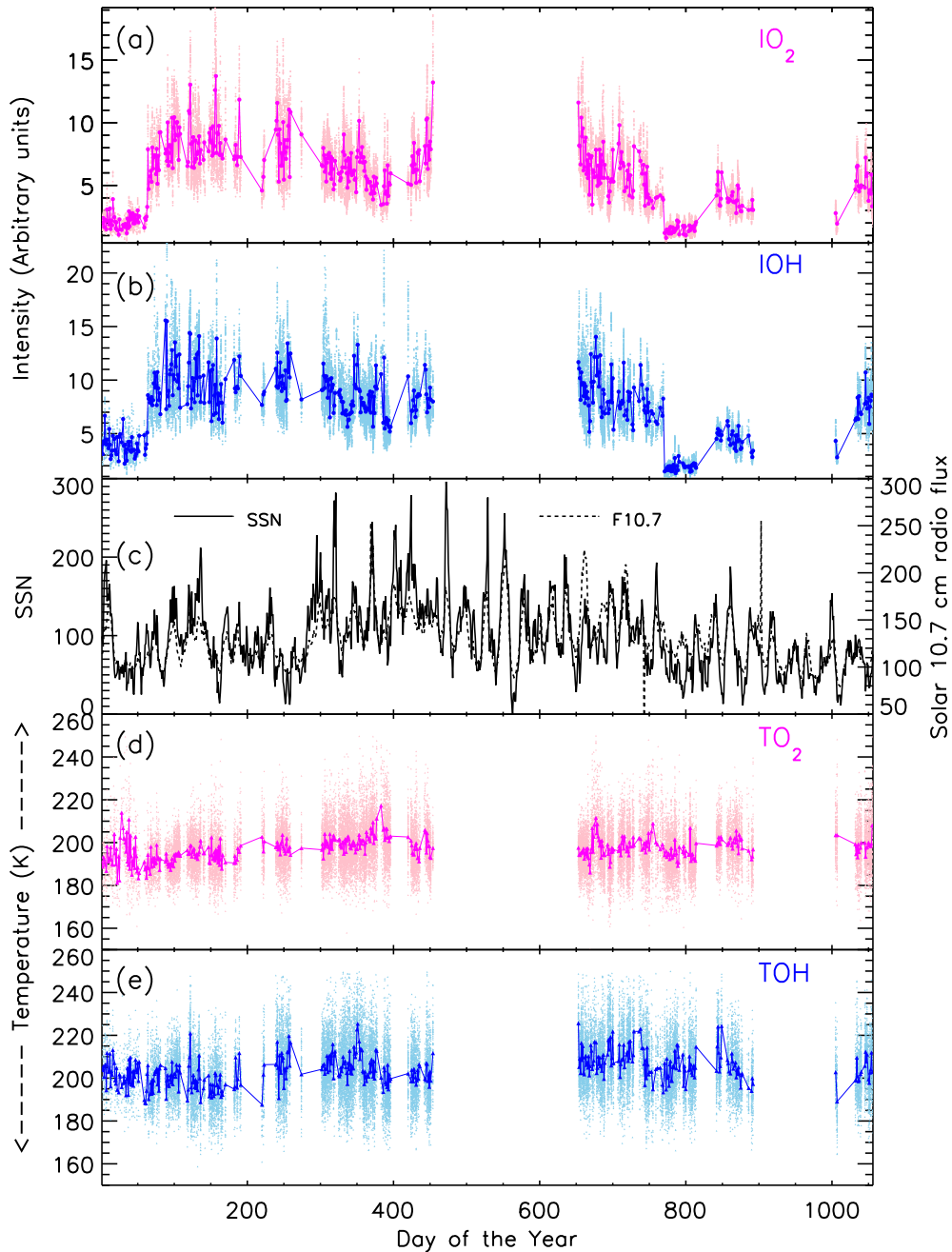


**Figure 3.2:** (a and b) Nightly mean  $O_2$  and OH intensity variations which originate from 94 and 87 km altitudes as measured by NIRIS at Mount Abu are shown. (c) Variations in daily mean sunspot numbers and F10.7 cm radio flux for all days (DOY 1 to 1055). (d and e) Nightly mean variations in the corresponding  $O_2$  and OH temperatures along with their nightly ranges.

variations in temperatures at both altitudes do not show any visible similarity during these periods in comparison to the nightglow emission intensities. We



have shown recently that the response to the tropical cyclone generated GWs in the mesospheric nightglow intensities were better than those in temperatures [*Singh and Pallamraju (2016)*].

All the six parameters shown in Figure 3.2 have been subjected to spectral analyses to obtain the periodicities that are present in the data. As discussed earlier in Chapter 2, the optical data obtained from the ground are not equally spaced in time, therefore, Lomb-Scargle periodogram analysis [*Lomb (1976)*; *Scargle (1982)*] have been carried out which takes care of unequal spacing in the data. As seen in Figure 3.2 there are two large data gaps in the ground-based observations. Therefore, we have considered two periods (DOY 1 to 454 and DOY 653 to 893), wherein we have continuous ground-based observations. In addition, we have also considered the total data from DOY 1 to 1055. It should be mentioned here that even though the ground-based observations suffer from gaps in the data, we have considered continuous data of solar parameters (SSN and F10.7), for obtaining information on the solar oscillations that exist in that duration.

The periodicities of the variations that are obtained from Lomb-Scargle periodogram analysis in the O<sub>2</sub> and OH intensities, their corresponding temperatures, SSN and F10.7 are all shown in Figure 3.3. The horizontal lines in all the panels in Figure 3.3 show the false-alarm level (FAL) related to the confidence level of 90% for the spectral analysis as obtained above. As can be seen from Figure 3.3a periodicities obtained from first 455 days of data (from DOY 1 to 454) in IO<sub>2</sub> are  $90 \pm 1.5$ ,  $120 \pm 2.5$ ,  $180 \pm 4.9$  days, in IOH are  $120 \pm 2.5$  and  $180 \pm 4.7$  days, and in TOH is  $120 \pm 2.4$  days. The uncertainty shown in the peak value of a given period is calculated using the method as described in Chapter 2.

For the same duration the periodicities in the solar parameters are found to be  $27 \pm 0.06$ ,  $58 \pm 0.3$ ,  $105 \pm 0.9$ ,  $150 \pm 1.9$  (in SSN) and  $27 \pm 0.06$ ,  $58 \pm 0.3$ ,  $105 \pm 0.9$  (in F10.7 cm flux) days (Figure 3.3a). The reason behind the presence of these periodicities in SSN and F10.7 cm solar flux is due to the internal magnetic

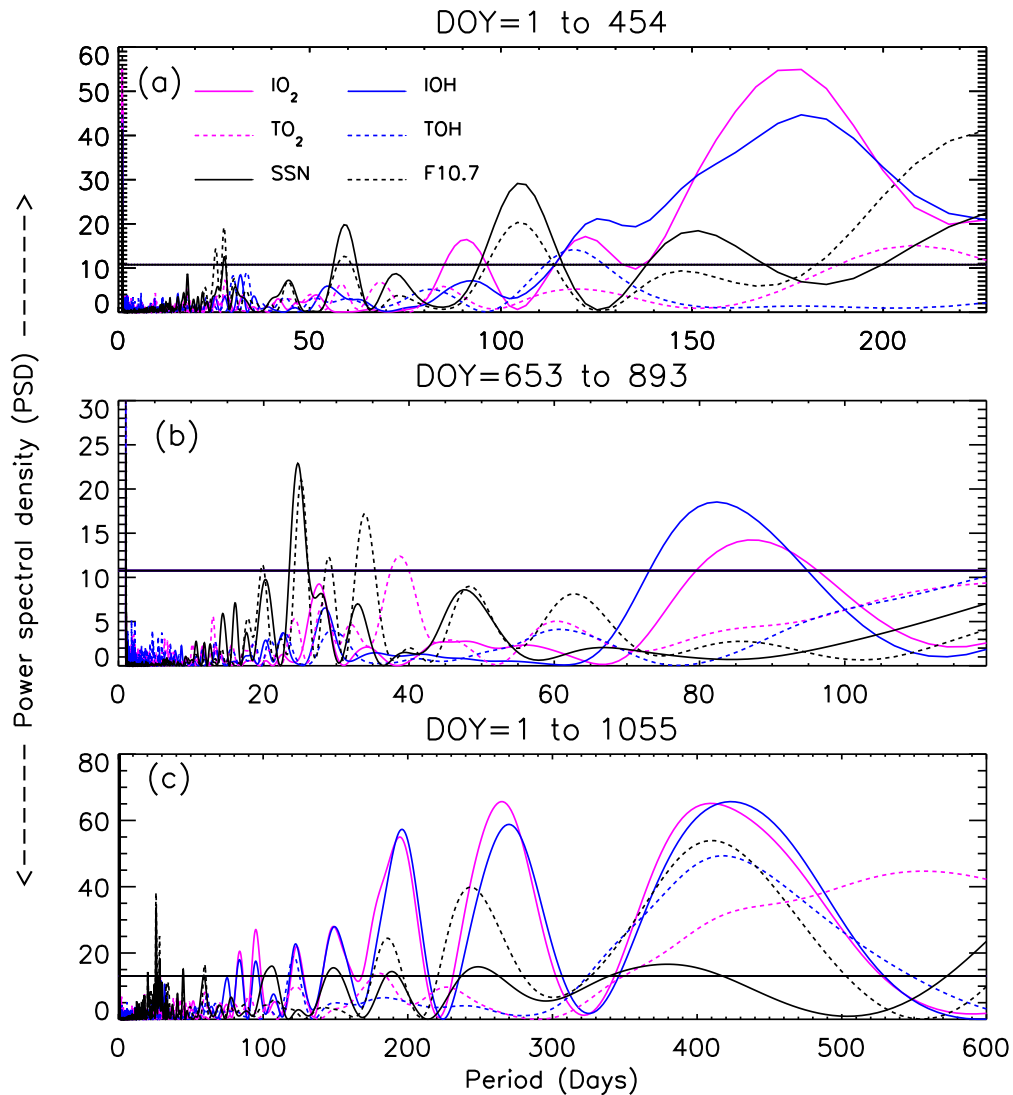


**Figure 3.3:** (a) Lomb-Scargle periodograms of the  $O_2$  and OH intensities and corresponding temperatures for the first 455 days of observations (DOY 1 to 454). Power spectral density (PSD) along with the 90% false alarm level (FAL) is shown for different periods of atmospheric nightglow and solar parameters. (b) Significant periodicities obtained using Lomb-Scargle periodogram analysis of 241 nights of data (DOY 653 to 893). (c) Similar to Figures 3.3a and 3.3b but for 1056 nights of optical observations (DOY 1 to 1055). It should be mentioned here that for solar parameters continuous data without any gaps is considered. It is striking to note that, in addition to atmospheric periodicities that are present in the mesospheric intensity and temperature variations, several coherent periods are present in the  $O_2$  and OH intensities and temperatures showing commonality with those obtained from SSN and F10.7 cm radio flux.

dynamo action in the solar interior. It has been shown that some of these periods are present in the solar magnetic flux variations during solar cycle 24 and may differ for year to year [*Chowdhury et al. (2015)*]. Hence, it can be seen from Figure 3.3a that the 90 and 120 days/180 days oscillations that are present in mesospheric intensity and temperature variations are of atmospheric (seasonal/semiannual) origin. Figure 3.3b shows the periodicities obtained from 241 days of data (DOY 653 to 893) in IO<sub>2</sub>, IOH, and TO<sub>2</sub> as  $85\pm 3.7$ ,  $85\pm 3.7$ , and  $38\pm 0.7$  days, respectively. Figure 3.3b also shows the presence of 27-day solar periods in SSN and F10.7. The 85-day period seen in IO<sub>2</sub> and IOH is due to seasonal variations.

Several significant periodicities in mesospheric intensities and temperatures that are present in 1056 days (DOY 1 to 1055) of data are shown in Figure 3.3c. IO<sub>2</sub> and IOH show presence of common periodicities of around  $84\pm 0.6$ ,  $95\pm 0.9$ ,  $122\pm 1.3$ ,  $150\pm 2.1$ ,  $195\pm 3.6$ ,  $270\pm 6.4$ , and  $420\pm 14.8$  days. In addition, TO<sub>2</sub> and TOH also show presence of periodicities of  $420\pm 14.8$  days and  $122\pm 1.4$  and  $420\pm 14.8$  days. Figure 3.3c also show the periodicities present in the solar variations which are,  $27\pm 0.02$ ,  $58\pm 0.08$ ,  $105\pm 0.3$ ,  $150\pm 0.5$ ,  $190\pm 0.9$ ,  $245\pm 1.4$ ,  $380\pm 3.3$ , and  $410\pm 3.9$  days. Results from spectral analyses of solar flux and SSN data showing the presence of periods around 150, 190, 245, and 410 days with significant power indicate that similar periods observed in optical emissions could be due to solar influences. There could be contributions from semi-annual oscillation (SAO) and annual oscillation (AO) as well that would be convolved with those of solar variations in the mesospheric intensities and temperatures, however, the relative contribution of these two may not be decipherable. It can also be seen from Figure 3.3c that the power spectral density (PSD) of optical emissions are maximum for the  $420\pm 14.8$  days followed by that for SAO (which showed two peaks at  $195\pm 3.6$  and  $150\pm 2.1$  days),  $95\pm 0.8$ , and  $84\pm 0.6$  days oscillations. *López-González et al. (2004)* presented results from 3 years of data of O<sub>2</sub> and OH emissions and temperatures wherein they showed a clear AO in temperatures and both AO and SAO of

similar magnitudes in the emission rates. Recently, *Reid et al. (2014)* showed using OH(8-3) nightglow emissions data that the amplitude of the AO dominates that of the SAO. Therefore, the results obtained in this study are in agreement with some of those reported in the literature from other latitudes.

As shown in Figure 3.2 and discussed earlier we have observed broad similarities in the variations of O<sub>2</sub> and OH emission intensities which vary with SSN and F10.7 flux. There are, however, occasions when both intensities do not show solar cycle related variations and these are most probably due to altitudinally varying wave activities in the mesosphere. In order to ascertain this, correlation analyses have been carried out between the mesospheric intensities and solar parameters over an interval of a few days.

Figure 3.4a shows 4-day running average of O<sub>2</sub> and OH intensities and SSN in magenta, blue, and green colours, which show a broad similarity with one another. The 4-day running average was taken to smooth out the night-to-night atmospheric fluctuations in the dataset so that the solar influences, if any, get highlighted. Figures 3.4b, 3.4c, and 3.4d, respectively show the correlation coefficients of the variability between O<sub>2</sub> intensities and SSN, OH intensities and SSN, and O<sub>2</sub> and OH intensities. These correlation coefficients are obtained by considering around 10 nights of continuous data of all the parameters that are shown in the Figure 3.4a. Thus, a total of 43 values of the correlation coefficients for 437 observational nights of existing data were obtained. The O<sub>2</sub> and OH emissions show positive correlation between them for most of the time during the reported observational period (Figure 3.4d).

It is also noteworthy to see that the O<sub>2</sub> and OH emissions show similar variations as in SSN and F10.7 cm flux in longer time periods (Figure 3.3c), however, as seen in Figures 3.4b and 3.4c their correlations with SSN are not always good for shorter time scales. From Figure 3.4d it may be noted that the duration when one of the mesospheric intensities (either O<sub>2</sub> or OH) shows poor or anti-correlation with SSN, the correlation between them is poor or opposite to one another. Whereas, it may be noted that the duration

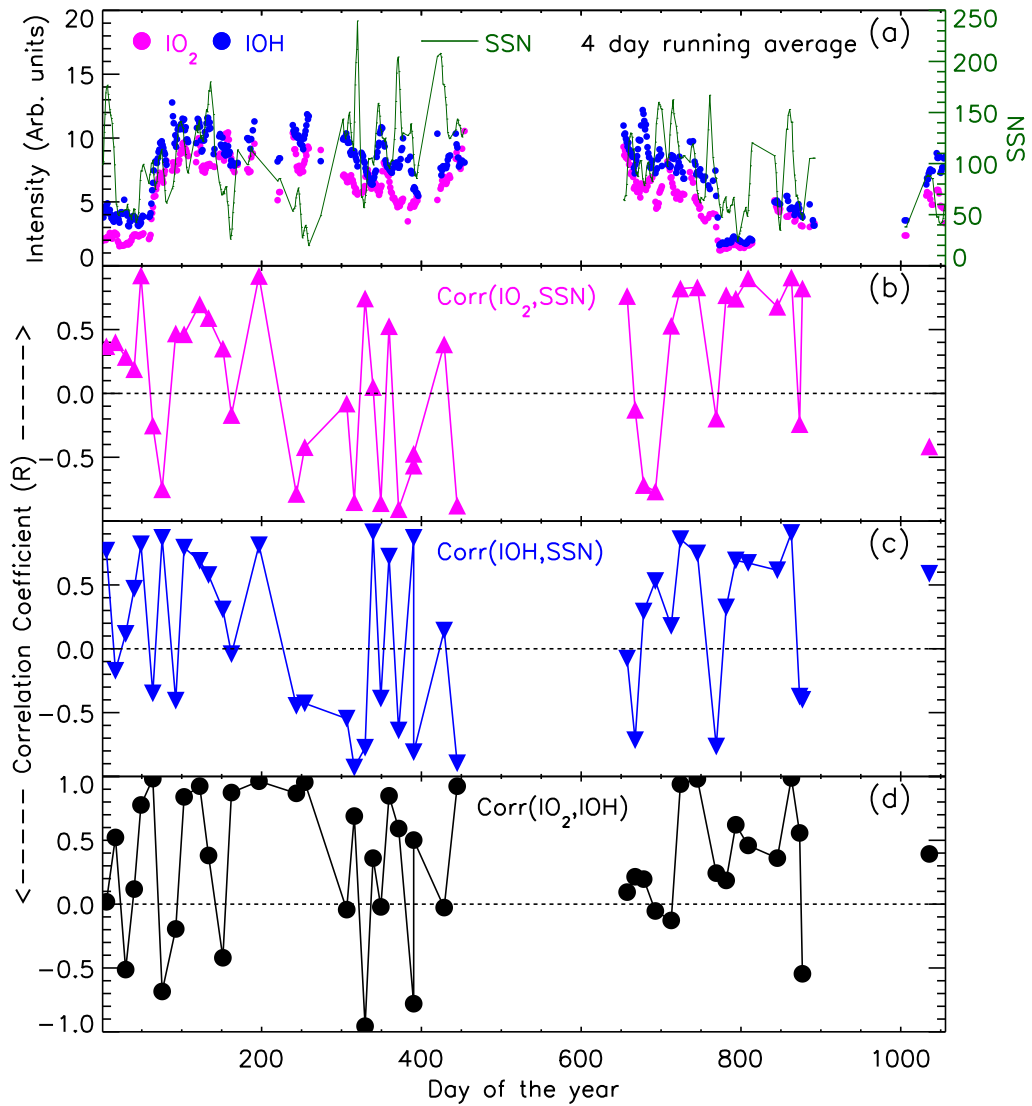


**Figure 3.4:** (a) Four-day running averages of O<sub>2</sub> and OH intensities and SSN. Correlation coefficients are shown for the variations obtained between: (b) O<sub>2</sub> intensities and SSN, (c) OH intensities and SSN, and (d) O<sub>2</sub> and OH intensities. These correlation coefficients are obtained by considering around 10 days of continuous data of all the parameters.

when O<sub>2</sub> and OH intensities show good correlations between them they also show better correlation with the SSN. These observations indicate that the altitudinal variations in mesospheric dynamics play a greater role than solar effects in those intervals. These altitudinal variations could be brought about due to dissimilar wave behaviour between 94 and 87 km altitudes, or presence

of wind shears in between these altitudes of nightglow emissions. No discernible seasonal effect was noted in the correlation coefficients.

### 3.3.3 Conclusion of Large-Time Scale Variations

We have presented the long-time scale variations in the nightglow emission intensities and corresponding rotational temperatures which have been measured from Gurushikhar, Mount Abu, in India using  $O_2(0-1)$  and  $OH(6-2)$  band nightglow emissions which emanate from 94 and 87 km altitudes, respectively. Spectral analyses on 437 nights of observations of  $O_2$  and  $OH$  intensities and the corresponding temperatures have been carried out for data during January 2013 to November 2015. Statistically significant periodicities of around 150, 195, 270, and 420 days were obtained. The solar variations in this duration also displayed some of the periodicities (150, 190, 245, 380, and 410 days) that are present in atmospheric oscillations as well, thereby, revealing a clear evidence of solar activity influencing the mesospheric airglow emissions and temperatures. In addition to these common periods, the  $O_2$  and  $OH$  intensities also showed periods around 84, 95, and 122 days which are due to the seasonal variations. Not all the periodicities which are present in  $O_2$  and  $OH$  intensities are present in temperatures and vice versa.

Although the dominant periods observed in the SSN are present in those of both  $O_2$  and  $OH$  emission intensities, in some durations the temporal variations in the intensities do not show similarity with that of the solar flux. Therefore, influence of solar variability on the behaviour of mesospheric intensity has been investigated in shorter durations. In order to do that correlation coefficients have been obtained by considering 10 days of continuous data of  $O_2$  and  $OH$  emission intensities and SSN. This analyses showed that  $O_2$  and  $OH$  intensity variations are correlated with each other for most of the nights. When they show better correlation between themselves their correlation with SSN variability is also good, which indicates that the variability in these in-

tensities is being affected by the solar effects. However, when  $O_2$  and OH intensities show poor- or anti-correlation between them, then in those periods one of these intensities does show poor or anti-correlation with SSN. This indicates that during these periods altitudinal dependent processes, which are due to atmospheric dynamics, play a greater role as compared to the solar forcings.

## 3.4 Short-Time Scale Variations

In this section, the results pertaining to the statistical study of the gravity wave (GW) characteristics in the MLT region will be discussed. This study was possible because of the availability of high data cadence long-term NIRIS observations. The GW time period for individual nights are obtained from the nocturnal variations in all the four parameters ( $IO_2$ , IOH,  $TO_2$ , and TOH). Statistical results obtained using these periodicities are described in the following sections.

### 3.4.1 Introduction

As discussed in Chapter 1, troposphere is the region where most of the waves are generated. These waves, under suitable conditions, can propagate in the upper atmosphere and affect the dynamics there. Therefore, in addition to the large scale effect on the mesospheric airglow intensities and temperatures which are discussed in section 3.3 above it is also important to understand the effect of oscillations of short scale waves (GW regime) on these parameters. The atmospheric dynamics varies with latitude, longitude, seasons, topography, etc., therefore, their effect on the mesospheric airglow intensities and temperatures are expected to be different at different locations. GWs play an important role in the MLT energetics and dynamics since they act as significant source of momentum and energy flux in this region. Therefore, gravity wave studies at various locations over different time durations have formed one of the impor-

tant topics of investigation [e.g., *Fritts and Alexander (2003)*]. Further, the GWs in the mesosphere are significantly affected by tropospheric cyclones, as shown in a recent study by *Singh and Pallamraju (2016)* wherein an unambiguous evidence was obtained for the propagation of waves from the troposphere to the mesosphere during cyclone Nilofar that occurred in October 2014 in the Arabian Sea westward of our optical observational location of Gurushikhar ( $24.6^{\circ}\text{N}$ ,  $72.8^{\circ}\text{E}$ ), in India.

Many ground-based techniques have been used to study GW activities in the MLT region, such as, photometers, spectrometers, imagers, radars, and lidars. A few of the results obtained by various techniques are described here to provide a broad context to understand the results reported in this section. *Taylor et al. (1997)* reported an anisotropic distribution in the directions of wave propagation during equinoxes over low-latitude from Alcantara, Brazil ( $2.3^{\circ}\text{S}$ ,  $44.5^{\circ}\text{W}$ ). *Nakamura et al. (1999)* reported that the GW propagations over mid-latitude (Shigaraki ( $35^{\circ}\text{N}$ ,  $136^{\circ}\text{E}$ ), Japan) showed seasonal variation with an eastward/westward preference in summer/winter. Similar behaviour was seen over another mid-latitude location (Mt. Bohyun,  $36.2^{\circ}\text{N}$ ,  $128.9^{\circ}\text{E}$ , Korea; *Kim et al. (2010)*) wherein it was found that GW tended to propagate westward during fall and winter, and eastward during spring and summer. In contrast, *Ejiri et al. (2003)* showed that GW propagated northward and northeastward in summers and westward at Rikubetsu ( $43.5^{\circ}\text{N}$ ,  $143.8^{\circ}\text{E}$ ) and southwestward at Shigaraki ( $34.9^{\circ}\text{N}$ ,  $136.1^{\circ}\text{E}$ ) in winters during a different epoch. Using OH airglow imager data from Tirunelveli ( $8.7^{\circ}\text{N}$ ,  $77.8^{\circ}\text{E}$ ) *Lakshmi Narayanan and Gurubaran (2013)* reported that nearly half of the high frequency GWs were evanescent with more occurrences in solstices as compared to equinoxes and showed a predominant meridional propagation throughout the year. *Sivakandan et al. (2016)* reported that GW propagates mostly northward of Gadanki ( $13.5^{\circ}\text{N}$ ,  $79.2^{\circ}\text{E}$ ). As can be noted most of the earlier works concentrated on the directions of propagations of gravity waves as seen in the imagers. The present work, in contrast, is focused on understanding the wave periodicities



and their variations over short-timescales.

### 3.4.2 Results and Discussion

The results discussed in section 3.3 clearly show that the mesospheric intensity variations are influenced either by solar effects or due to those of the local atmospheric dynamics depending on the time scales. In order to understand the fluctuations which are inherent in a given night in O<sub>2</sub> and OH emission intensities we have calculated the significant periods for each of the 437 nights of observations. In general, the minimum frequency (maximum period) is given by total observational duration. However, we have put a more rigorous constraint in deriving the maximum periods in which we have considered that the data should contain at least two cycles. Therefore, the periods considered are smaller than half of the observational duration. Also, Brunt-Väisälä period at these altitudes is around 5 min, which is equal to the data cadence of our measurement. Thus, the smallest periods of waves that are statistically discernible are  $\geq 10$  min.

The method we followed to derive the periodicities in the nocturnal variations of the data is depicted in Figure 3.5. The nocturnal variations in O<sub>2</sub> and OH intensities are shown by connected lines in Figures 3.5a and 3.5d and the dotted lines show 4.1 h running average of the data for a representative night of 10 June 2015 for which the total duration of data available is around 8.2 h. Therefore, the residuals obtained by subtracting the 4.1 h running average from the original data contain information on the periodicities that are smaller than 4.1 h duration. These are shown in the form of zero mean unit variances in Figures 3.5b and 3.5e for O<sub>2</sub> and OH intensities, respectively. This process normalizes the relative power in each period in a given dataset and enables inter-comparison of the periodogram of different parameters and of different days [*Pallamraju et al. (2010)*; *Singh and Pallamraju (2016)*].

We have used REDFIT spectral analyses [*Schulz and Mudelsee (2002)*] as

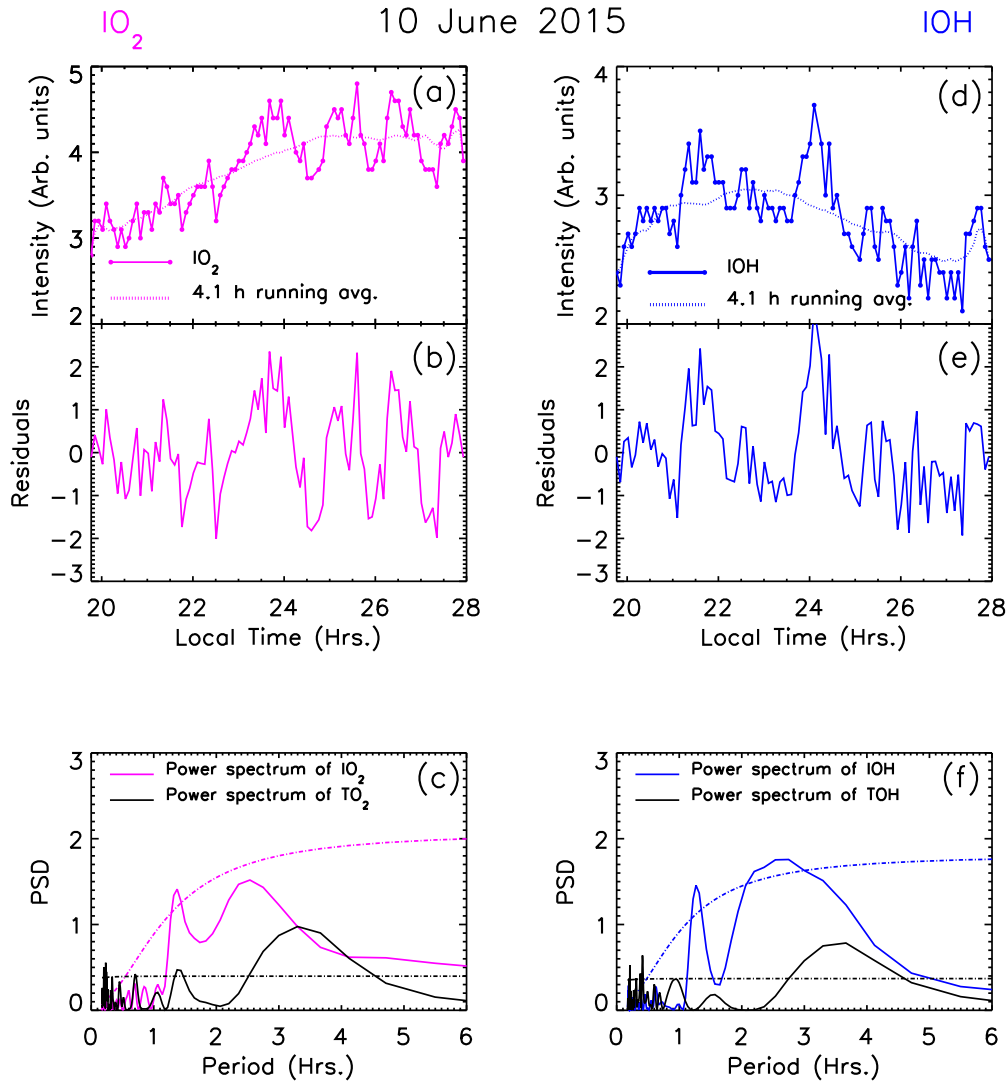


**Figure 3.5:** The procedure used to derive gravity wave periodicities from the nocturnal variations of the nightglow intensity data is shown for a sample night of 10 June 2015. (a and d) The nocturnal variation of the  $\text{O}_2$  and OH emission intensities are shown by the solid lines. Also shown are the corresponding 4.1 h running averages of these intensity variations by the dotted lines. (b and e) Residuals obtained by subtracting the 4.1 h running averaged signal from the original nightglow intensities for both  $\text{O}_2$  and OH emissions represented by zero mean and unit variances. (c and f) Lomb-Scargle periodograms of the residuals as shown in Figures 3.5b and 3.5e, and the residuals that are obtained using similar procedure but in  $\text{O}_2$  and OH temperature variations (not shown) along with 90% FAL (broken lines) are shown.

described in Chapter 2 which can be performed on unevenly spaced time series and computes a spectral estimate using Welch windowing coupled with the Lomb-Scargle periodogram [*Lomb* (1976); *Scargle* (1982)]. The power spec-

trum of  $O_2$  and OH intensities and corresponding temperatures are shown in magenta, blue, and black coloured lines in Figures 3.5c and 3.5f. The corresponding broken lines represent the FAL corresponding to the confidence level of 90%. It can be seen from Figures 3.5c that the significant period obtained from  $IO_2$  is of 1.4 h and those obtained from  $TO_2$  are of 1.4 h and 3.2 h duration. Similarly, Figure 3.5f shows the presence of periods of 1.3 h and 2.5 h in IOH and 0.9 h and 3.4 h in TOH on the night of 10 June 2015. Similar analyses as demonstrated here for one night have been performed to obtain the dominant periodicities in the  $O_2$  and OH intensities and corresponding temperatures for all the 437 nights of observations. Out of 437 nights of observations, GWs were found to be present on 379 (87%), 359 (82%), 412 (94%), and 401 (92%) nights in  $IO_2$ , IOH,  $TO_2$ , and TOH, respectively. Waves of periods (of GW regime) are known to play an important role in influencing the mesospheric dynamics [Fritts and Alexander (2003)].

Periods obtained from nocturnal  $O_2$  and OH intensity variations for all the 437 nights are shown in Figures 3.6a and 3.6d for the years 2013, 2014, and 2015 in red, green, and blue colours, respectively. As seen in Figure 3.5 the periodicities present in  $O_2$  and OH emission intensity variations and corresponding temperatures can be similar or different for the same night due to the presence of the altitudinal dependent processes at those altitudes. All the values shown in Figures 3.6a and 3.6d are independent and the periods shown are greater than or equal to 10 minutes and less than or equal to half of the observational duration. In order to note the broad variations in these GW periods a 30-day running average of these periodicities is performed and is shown in Figures 3.6b and 3.6e for all the three years using same colour codes as used in Figures 3.6a and 3.6d. It may be noted that the GW periods do not show any variation with year (solar cycle).

Estimation for the number of GW occurrences for all the 437 nights of observations have been carried out by summing up all the periods in different bins which are greater than 10 minutes (frequencies smaller than  $6 \text{ h}^{-1}$ ).

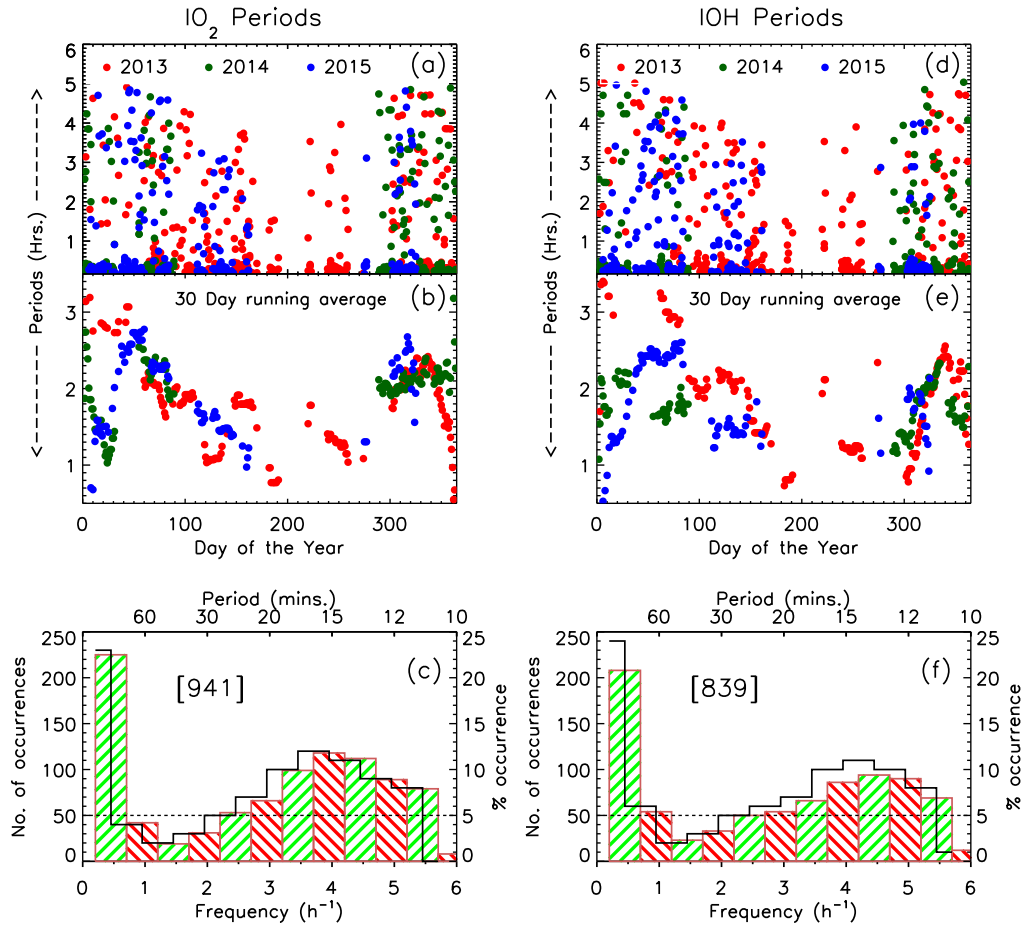


**Figure 3.6:** (a and d) Gravity wave periodicities obtained from the  $\text{O}_2$  and OH emission intensities for all the 437 nights of observations are shown which are folded into a one year interval. The periods for the year 2013, 2014, and 2015 are shown by red, green, and blue coloured dots, respectively. (b and e) 30-day running average of the periods shown in Figures 3.6a and 3.6d are shown for the year 2013, 2014, and 2015. (c and f) Histograms of different periodicities for all nights of observations obtained from the  $\text{O}_2$  and OH emission intensity variations as obtained by the method shown in Figure 3.5.

Figures 3.6c and 3.6f show histograms with number of occurrence of the GW periods as a function of frequency that have been obtained from the  $\text{O}_2$  and OH intensity variations, respectively. The temporal scale corresponding to the frequency values are also shown at the top of both Figures 3.6c and 3.6f. In order to carry out statistical study for percentage occurrence of fluctuations at any given frequency/time period the histograms have been generated consid-

ering a fixed bin size of  $0.5 \text{ h}^{-1}$  (i.e.,  $f \pm 0.25 \text{ h}^{-1}$ ) which will give rise to varying intervals in time domain. The histograms shown in black coloured solid line are the percentage number of nights in which waves in a particular frequency bin has occurred. The y-axis on the right shows the values corresponding to the percentage of occurrence. From the histograms shown in Figures 3.6c and 3.6f it can be seen that GW periods observed in both intensities with 11 to 24 min, and 2 h durations, occur more than 5% of the observational nights (shown as dotted horizontal line). More than 23% of nights show the presence of the 2 h followed by 12% of nights with 15 min of periodicities in both mesospheric intensities. It is encouraging to see from the statistics in Figures 3.6c and 3.6f that the GW periods obtained from the  $\text{O}_2$  and OH intensity variations show similar behaviour. The total number of periods (obtained by summing up the number of dots in Figure 3.6a and 3.6d) present in  $\text{O}_2$  and OH emission intensities for all the 437 nights are 941 and 839 (also shown in Figures 3.6c and 3.6f).

Similar to the intensities, the GW periodicities obtained from the nocturnal  $\text{O}_2$  and OH temperature variations are shown in Figures 3.7a and 3.7d. The same colour code as has been used for the periods obtained from the intensity data (in Figure 3.6) is used here as well. As seen from Figures 3.7b and 3.7e, similar to that of intensities, the temperatures too do not show significant variations in GW periods within the three years. The total number of GW periodicities (greater than Brunt-Väisälä period) which are present in  $\text{O}_2$  and OH temperatures for all the 437 nights of observations are 1266 and 1214, respectively, which are greater in numbers as compared to those observed in the intensity variations.

The histograms of the periodicities obtained in the  $\text{O}_2$  and OH temperatures are shown in Figures 3.7c and 3.7f, respectively. The GW periodicities obtained from the temperatures data also show the dominance of 2 h period similar to those observed in the intensities. From Figure 3.7 it can be seen that GW periods observed in both  $\text{O}_2$  and OH temperatures ranging from 15

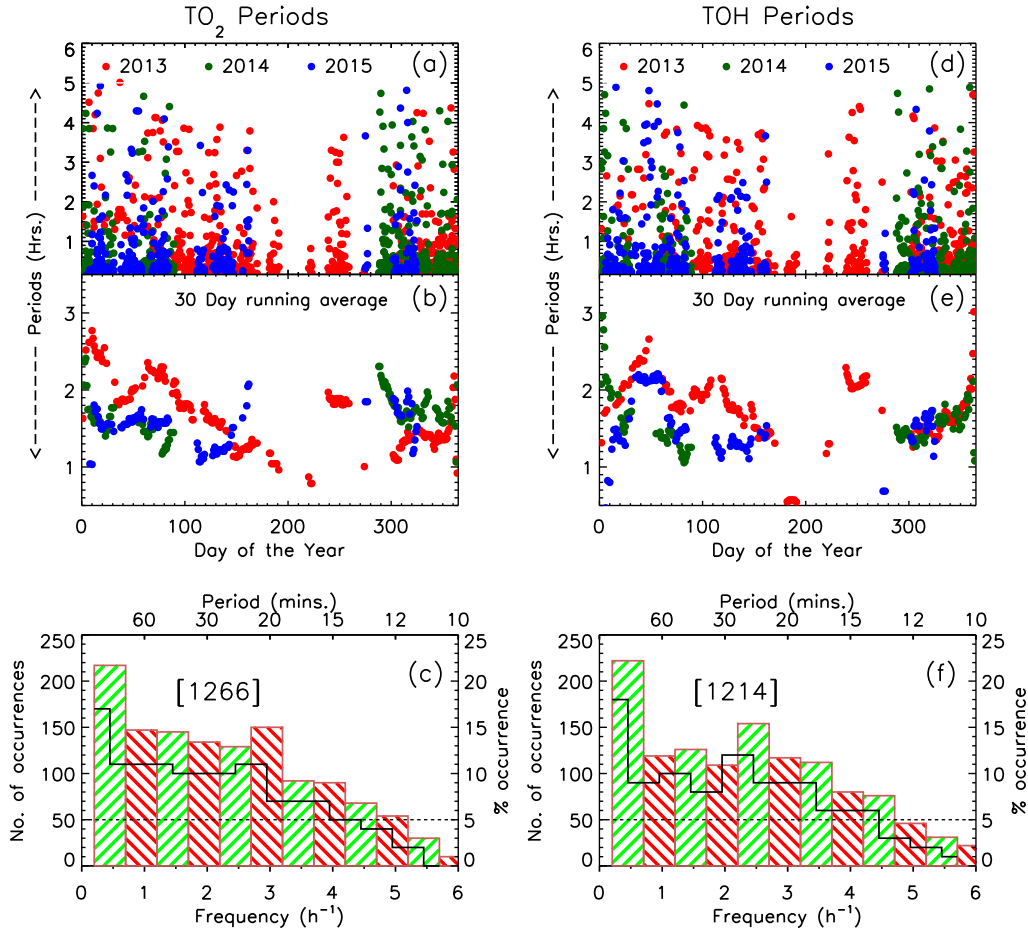


**Figure 3.7:** Same as in Figure 3.6 but for the temperatures obtained from the  $O_2(0-1)$  atmospheric and  $OH(6-2)$  band emissions intensities.

min to 2 h occur more than 5% of the observational nights. More than 18% of nights show the presence of the 2 h period and around 12% of nights show the periodicities with 20 to 60 min in both  $O_2$  and OH temperatures.

Hence, it is very clear that the total number of larger period gravity waves obtained from  $O_2$  and OH temperatures are greater than those observed in corresponding intensities. One of the findings of this statistical study is that the GW periods obtained using temperatures do not show significant number of shorter periodicities (of period less than 15 min) as observed in the intensities. Also, it is intriguing as to why the smaller timescales are seen less in number as compared to the longer ones in the temperatures. It should be ap-

preciated that intensity variations are due to changes in densities of reactants, temperature in the medium, or due to pressure waves. In this regard it has been shown that the shorter period waves are easily discernible in intensities as compared to the corresponding temperatures [*Singh and Pallamraju (2016)*] as also discussed in Chapter 4. The observations described above could be due to the fact that any fluctuations in the densities of reactants will directly affect the emission intensities and so readily respond to the smaller periods than those in the mesospheric temperatures. *Makhlouf et al. (1990)* showed that temperature variations induced in the nightglow emission intensity variability are directly proportional to the amplitude of the propagating wave. In the present work described above any wave with temperature fluctuation less than the uncertainty of  $\pm 3\text{K}$  will not be discernible.

However, some of the earlier experiments with simultaneous OH intensity and temperature measurements [e.g., *Tepley et al. (1981)*] also showed that on a given night not all the periods seen in temperatures be present in the intensities and vice-versa. Further, in another result when the periods in intensity and temperature were similar [*Taylor et al. (1991)*], it was shown that the intensity fluctuations lead those in the temperatures. In this background the circumstantial evidence points to large inertia of the system and/or small amplitude of the temperature that affects the response of smaller periodic fluctuations in temperature variations to be the cause. These factor(s) prevents them from being readily reflected in temperatures than those derived from the intensities. Further, the fact that longer periodicities in temperatures are seen in greater extent than the shorter ones confirms this proposition. It is akin to superposition of waves seen in intensities that form a longer time period wave in temperatures. Simulation studies will help in greater understanding and verifying this conjecture. For longer durations, the inertia of the system is not expected to have any effect, and so, similar to the variability in emission intensities, the temperature variations too show solar cycle related periods (Figure 3.3).

In an earlier study by *Wu and Killeen (1996)* using OH nightglow imager data from Peach Mountain Observatory, Michigan (42.3°N, 83.7°E) it was shown that the mesospheric gravity wave activity has a strong seasonal dependence with most of the GWs being observed during summer and almost nothing in winter. Figure 3.8a shows the number of hours of the clear sky (solid line), number of hours when gravity waves are present (dashed line), and number of night used (dotted line) on a monthly basis. The gravity wave occurrence frequency, which is the ratio of the number of hours with the presence of GW (defined by relative variation in OH brightness more than 7.5%) and the number of hours of the clear sky. As can be seen the majority of the observed GW activity occurred during the month of May, June, and July. However, it was later argued by *Li et al. (2011)* that this observation could be an artefact of counting the number of waves with certain amplitude (>7.5%). The amplitude of waves could be larger in summers as opposed to winters and this could lead to an erroneous conclusion on the GW activity itself.

It may be seen from Figures 3.6 and 3.7 that the longer periods exist during winter months and shorter ones in the summer/monsoon months. However, a closer inspection of Figures 3.6 and 3.7 along with Figure 3.1 indicates that this could be an artefact of the shorter observation duration in summer months. In summer nights there is a greater prevalence of clouds. Thus, in order to avoid any ambiguity in terms of data durations considered for analyses influencing the outcome and to make a fair judgement on seasonal changes in GW periods, we have to consider data of same duration all through the nights.

For this study we have chosen only those nights on which the observation duration is greater than 6 h and that number is 350 nights (among 437 nights as seen in the Figure 3.1). Since we have chosen the nights having more than 6 h of observations, therefore, in obtaining the statistics we have considered only those periods which are less than 3 hours (half of the observational duration), the procedure for this analysis is similar to that depicted in Figure 3.5. The periods so obtained in O<sub>2</sub> and OH intensities and corresponding temperatures



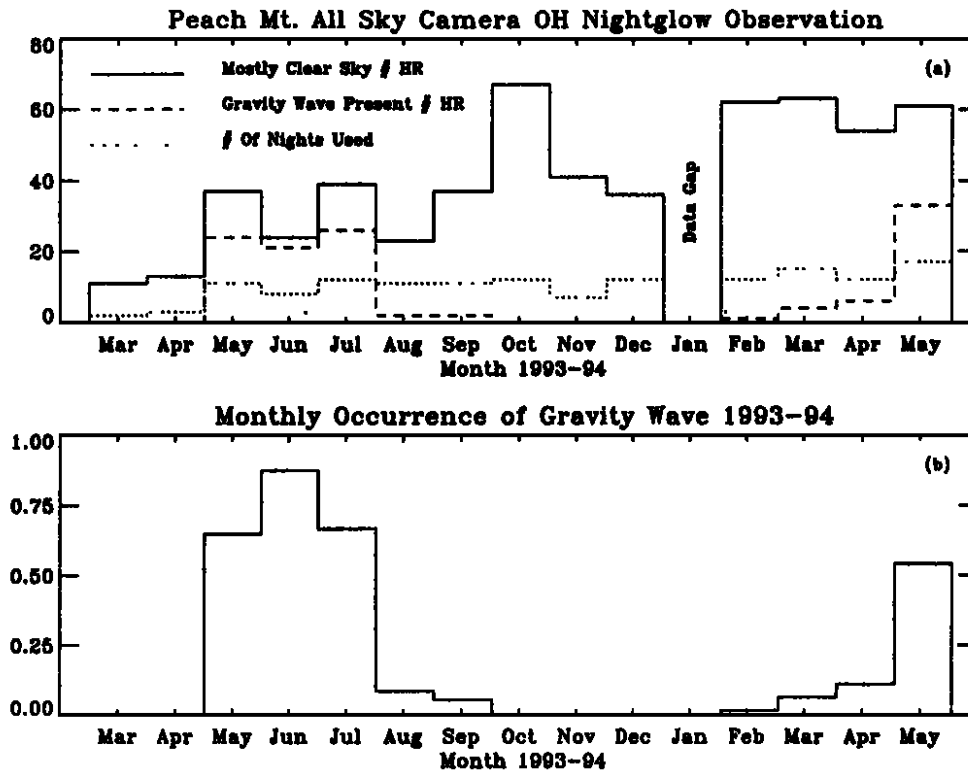


**Figure 3.8:** Statistical results of the GW occurrence frequency observed by all sky camera [Adapted from *Wu and Killeen (1996)*].

derived from them are shown in Figure 3.9 (colour codes are similar to those used in Figures 3.6 and 3.7). It can be seen that the GW periods do not show any seasonal variation. This is also confirmed in the 30 days running averages of the periods for all the three years of observation which do not show much variations in their values with respect to seasons. A few earlier studies which dealt with seasonal behaviour mainly concentrated on the number of wave occurrences and their propagation but not on the magnitudes of wave periodicities. The present study, thus, establishes that the wave periods (in GW regime) in the nighttime mesosphere do not show any seasonal variations.

### 3.4.3 Conclusion of Short-Time Scale Variations

For the study of short-timescale variations in the MLT region, GW periodicities have been obtained for all the individual nights using nocturnal variations in

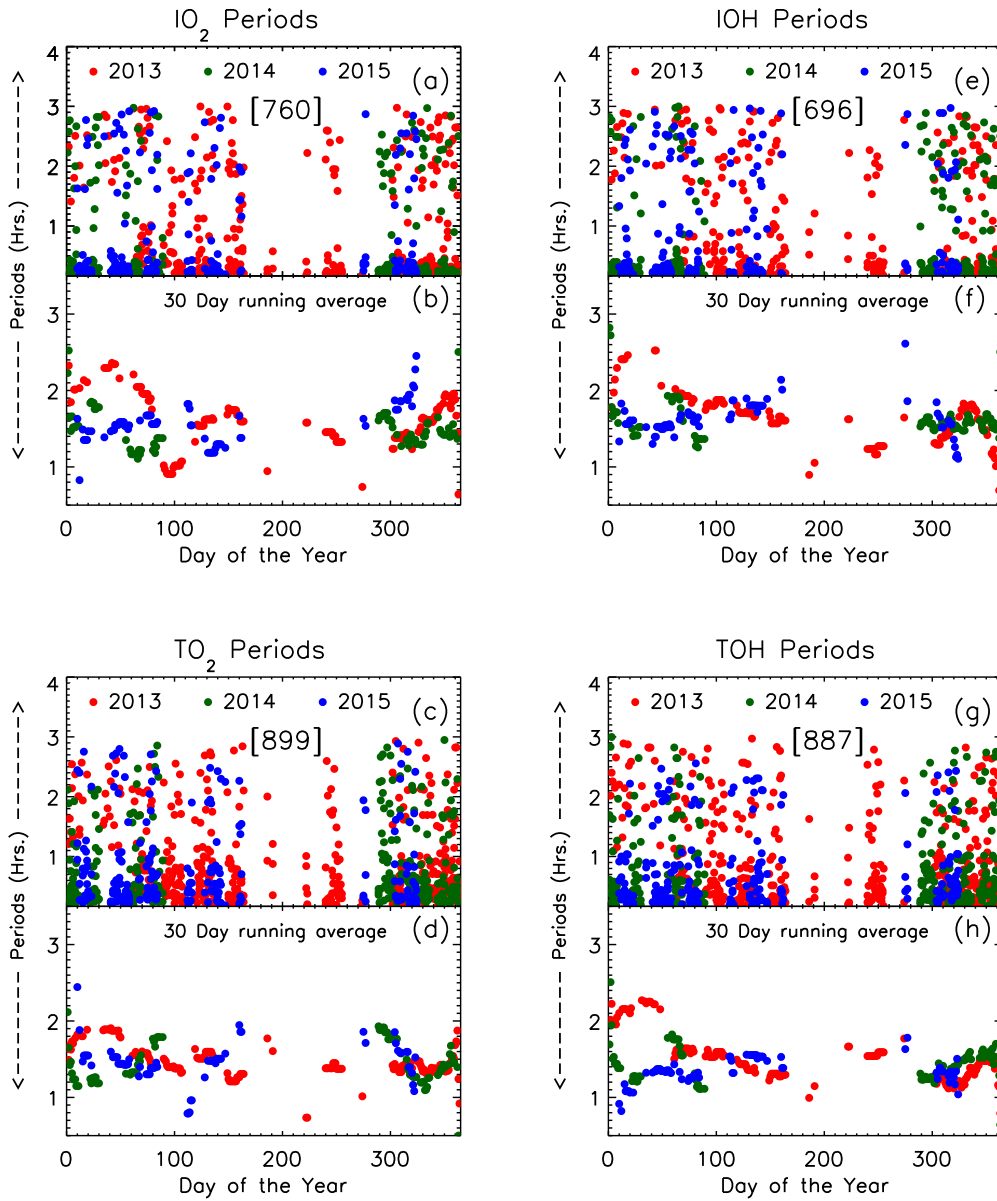


**Figure 3.9:** Same as in Figures 3.6 and 3.7 (a, b, d, e) but for the periods that have been derived from only those nights of observation for which the total duration of observation was greater than 6 h. The periods are obtained by using the same method as depicted in Figure 3.5. The residuals of  $O_2$  and OH intensities and temperatures correspond to the periods that are less than 3 h durations. As can be clearly seen the GW periods neither show any seasonal variations nor any solar activity dependence.

the  $O_2$  and OH intensities and corresponding temperatures. Statistical study of these periodicities obtained for all the 437 nights of observations reported

here show significantly different behaviour in intensities and temperatures. In intensities it has been observed that GWs show the presence of the 2 h and 15 to 20 min of periodicities in over 23% and 10% of nights, respectively. However, temperatures show 2 h and 20 to 60 min periodicities for over 18% and 12% of nights, and do not show significant number of periodicities smaller than 15 min. The smaller number of shorter periods seen in temperatures as compared to the intensities is attributed to the time taken for temperatures to respond to the dynamical processes, and/or the wave amplitudes, mainly in the smaller timescales range. The mesospheric GW periodicities neither show any seasonal dependence nor solar activity dependence in their occurrence rate or in the time periods. Thus, the results of the kind presented in this study provide us with a comprehensive picture of mesospheric wave dynamics in terms of characterizing their response to various sources that give rise to the variability in the mesospheric intensities and temperatures. In addition, these finding would help in modelling studies to characterize the mesospheric dynamics in large- and short-timescales better.

### 3.5 Summary

In this Chapter, large- and short- period waves which have been derived using  $O_2$  and OH emission intensities and corresponding rotational temperatures are discussed. It has been found that the longer periodicities observed in the mesosphere are resultant of the convolved behaviour between the solar forcing from above and atmospheric dynamics from below. With regard to the variability of the order of a few days,  $O_2$  and OH intensities were found to be correlated, in general, except when altitudinal dependent atmospheric processes were operative. From the statistical study of the mesospheric GWs over long term it was found that the major wave periodicity of around 2 h duration is present in all the four parameters ( $I(O_2)$ ,  $I(OH)$ ,  $T(O_2)$ , and  $T(OH)$ ). Our analyses also reveal that the range of periods in  $O_2$  and OH intensities and temperatures are

11 to 24 min and 20 to 60 min, respectively. Periods less than 15 min were not present in the temperatures, but were prevalent in both emission intensities. No seasonal dependence was found in either the wave periodicities or in the number of their occurrence.

This Chapter primarily concentrated on the large short-time period waves and oscillations in the MLT region. This study was made possible through high data cadence long-term systematic observations using NIRIS from Gurushikhar, Mount Abu. An attempt was also made to explain the cause and effect of these waves and oscillations in the mesosphere. This study shows that the MLT region is affected by solar forcing as well as atmospheric dynamics. In the next Chapter, we will continue with the discussion on the forcing in the MLT region, from below due to tropical convective activity as opposed to that from above (solar forcing) as discussed in this Chapter. The main focus in the next Chapter will be to understand vertical wave dynamical couplings during tropospheric convective activity. That result will also demonstrate on how different atmospheric layers respond to different types of external forcing.

# Chapter 4

## Vertical Coupling of the Atmospheres

### 4.1 Background

In this Chapter, the focus will be on understanding the vertical coupling of the atmospheres through gravity waves generated during a tropical cyclone. As has been discussed in Chapter 1 Earth's upper atmosphere is vertically coupled to the lower atmosphere through waves, which are generated mainly in the lower atmosphere. In Chapter 3, we have seen the presence of various long- and short-time period waves in the MLT region which are due to influences of solar origin and/or atmospheric processes. The propagation and dissipation of these atmospheric waves depend on the background conditions. Planetary waves and thermal tides combined with gravity waves generate most of the vertical coupling of the atmosphere and control significant portion of energy and momentum budget of the MLT region. This Chapter will be restricted mostly to understand vertical coupling of the atmospheres engendered due to gravity waves especially during cyclonic events. However, in order to appreciate the work presented in this Chapter a brief discussion on the vertical coupling of atmospheres due to planetary waves and tides is given below.

As introduced in Chapter 1 different waves generated in the lower-atmosphere are responsible for the dynamical coupling of the different regions of the atmospheres, as they propagate from the lower- to upper-atmospheric regions. Understanding the MLT dynamics is mostly concerned with the understanding the nature of wave motions responsible for the vertical coupling of atmospheres. Planetary-scale waves such as tides, Rossby waves, and Kelvin waves play an important role in controlling MLT dynamics at low-latitudes [e.g., [Vincent \(1993\)](#)]. As compared to the other part of the atmosphere, tropical atmosphere and its dynamics have distinctly different features, such as, small Coriolis parameter, strong latent heat release, deep convection, and large-scale oscillations (QBO, SAO). Therefore, tropics are the most important region of the atmosphere. The planetary waves with periodicities near 2, 5, 10, and 16 days are generated and present as westward propagating normal (Rossby) modes in the lower atmosphere and are observed in the MLT region [e.g., [Charney and Drazin \(1961\)](#); [Madden \(1979\)](#); [Salby \(1981\)](#)]. Another type of planetary waves, which are confined within the latitude of  $\pm 15^\circ$ , are called Kelvin waves. Propagation of these planetary waves in to the MLT region depends upon suitable background wind condition and play a major role in filtering these waves. The atmosphere behaves like a resonant waveguide and allows mainly the westward propagating Rossby modes to be sufficiently amplified outside tropical latitudes [e.g., [Andrews et al. \(1987\)](#)]. Hence, planetary waves are an important mode of coupling between different layers of the atmosphere. They can reach large amplitudes in the MLT region and are known to interact and modulate the amplitudes of atmospheric tides [e.g., [Teitelbaum and Vial \(1991\)](#)] and gravity waves [e.g., [Forbes et al. \(1991\)](#); [Manson et al. \(2003\)](#)]. The characteristics of these planetary waves in the MLT region have been reported by various researchers [e.g., [Forbes \(1995\)](#); [Dhaka et al. \(1995\)](#); [Gurubaran et al. \(2001\)](#); [Sasi et al. \(2005\)](#); [Pancheva et al. \(2008\)](#)]. The planetary wave influence on the upper atmosphere is shown to be solar activity dependent [[Laskar et al. \(2013\)](#); [Laskar et al. \(2015\)](#)] in which it was found

that vertical coupling is more efficient during low solar activity as compared with the high solar activity.

Atmospheric coupling during cyclonic events are very important, and yet it is poorly understood. Most of the understanding of the gravity waves effects in the upper atmosphere during cyclonic events have come from modelling and simulation studies. This is mostly because measurements are very difficult during such large convective activity since cloudy conditions prevent optical observations from ground-based instruments. In this Chapter, we will see the experimental derivation of gravity wave parameters during cyclone Nilofar which had developed in the Arabian Sea during 25–31 October 2014. An unambiguous signature of vertical coupling of atmospheres has been obtained during the cyclone Nilofar. These GW parameters were derived using high data cadence ground-based observations from NIRIS and CMAP from Gurushikhar, Mount Abu. In addition to that, one year of NIRIS data has been used to study the possible cause(s) for the occurrences of mesospheric temperature inversions (MTIs).

Thus, this Chapter will consist of results and discussion on atmospheric coupling during events with external sources of energy, such as tropical cyclone, in the troposphere and the experimental derivation of gravity wave parameters ( $\tau$ ,  $c_h$ ,  $c_z$ ,  $\lambda_h$  and  $\lambda_z$ ). This Chapter also includes results on the statistical study of MTIs that exists in the Earth's mesospheric altitudes.

## 4.2 Introduction

Three kinds of waves, namely, gravity waves (GW), thermal tides, and planetary waves that are generated in the troposphere have a significant impact in the Earth's MLT region. The type of waves which is pertinent to the study presented in this Chapter is gravity waves which are ubiquitous in the Earth's atmosphere and play a major role in the energetics and dynamics in the MLT region because of their ability to exchange energy over different atmospheric

layers [e.g., *Fritts and Alexander (2003)*]. As mentioned in Chapter 1, the major sources for GW generation in the troposphere include topography, convection, wind shear, and geostrophic adjustments which vary with geography, season, and local meteorology. GWs propagate away from the source region, both in the horizontal and vertical directions. Some of these waves dissipate in the MLT altitudes and thereby affect the atmospheric circulation at those altitudes. The GW breaking also contributes to the modulation of densities of the atmospheric species in the MLT region and their manifestation can be traced using airglow emission intensity variations. GWs can travel over large distances under favorable wind conditions with horizontal and vertical wavelengths in the range of 10-1000 and 1-100 km, respectively, and periods ranging from a few minutes to tens of hours in the MLT region [e.g., *Fritts and Alexander (2003)*; *Fritts et al. (2006)*, and references therein].

Tropical cyclones (TC) are among the most remarkable phenomena in the troposphere which are formed and developed over warm tropical oceans. They are known by different names in different locations e.g., hurricanes in the western hemisphere including North Atlantic and Eastern Pacific, typhoons in the Western Pacific, and tropical cyclones in Indian Ocean or the Southwestern Pacific. They are the important component of the Earth system since they transport huge amount of energy and moisture from the tropics towards the pole. The study of tropical cyclones with regards to their formation, intensification, decay characteristics under changing climate conditions is a very involved field of research of tropospheric and monsoon dynamics. However, the work presented in this Chapter deals with the vertical coupling of the atmospheres through GW generated during cyclone Nilofar and experimental derivation of various parameters using combination of ground- and satellite-based observations.

The main focus of the work presented in this Chapter is to investigate the effect of Tropical cyclone generated Gravity Waves (TGW) in the mesospheric altitudes which has been accomplished using, as tracers, the nightglow emission



intensities at multiple wavelengths that originate in the MLT region. As shown by observational and modelling studies [e.g., *Taylor and Hapgood (1988)*; *Fritts and Nastrom (1992)*; *Fovell et al. (1992)*; *Alexander et al. (1995)*] it is known that convection is a major source of GWs in the tropics. Unlike other sources, GWs generated through convection can have full range of phase speeds, periods, and vertical and horizontal scales [*Fritts and Alexander (2003)*]. By using a three-dimensional non-linear model, *Grimsdell et al. (2010)* have shown that thunderstorms can trigger a broad spectrum of GWs through latent heat release and interaction with the mean flow. However, in practice, not all waves succeed in moving to higher altitudes as they are filtered by winds which vary as a function of height. Occasionally, these waves and associated perturbations of mesospheric trace species such as OH and O<sub>2</sub> emission intensities appear in the form of horizontally propagating concentric circular rings as reported using ground-based airglow imagers [e.g., *Taylor and Hapgood (1988)*, *Yue et al. (2009)*].

Using all-sky OH imager at Yucca Field Station (40.7°N, 104.9°W) near Fort Collins, Colorado, *Yue et al. (2009)* observed concentric gravity waves (CGW). Figure 4.1 shows the sequence of the OH images recorded on the night of 11 May 2004 in which latitude and longitudes are shown on the vertical and horizontal axes, respectively. The gravity waves observed at OH emission altitude has two centers, which are denoted as red and blue solid dots in Figure 4.1. This implies that one convective plume is the source of the inner rings, while a second convective plume is the source of the outer ring. They showed that the centers of the concentric rings correspond nearly exactly to the location of two deep convective plumes which were active in the troposphere around 1 hour earlier.

A typhoon generated concentric GW has been reported by using a chain of three OH airglow imagers [*Suzuki et al. (2013)*]. They have estimated the horizontal wavelength, phase speed, and wave period to be 34.5 km, 50.2 ms<sup>-1</sup>, and 11.5 minutes, respectively.

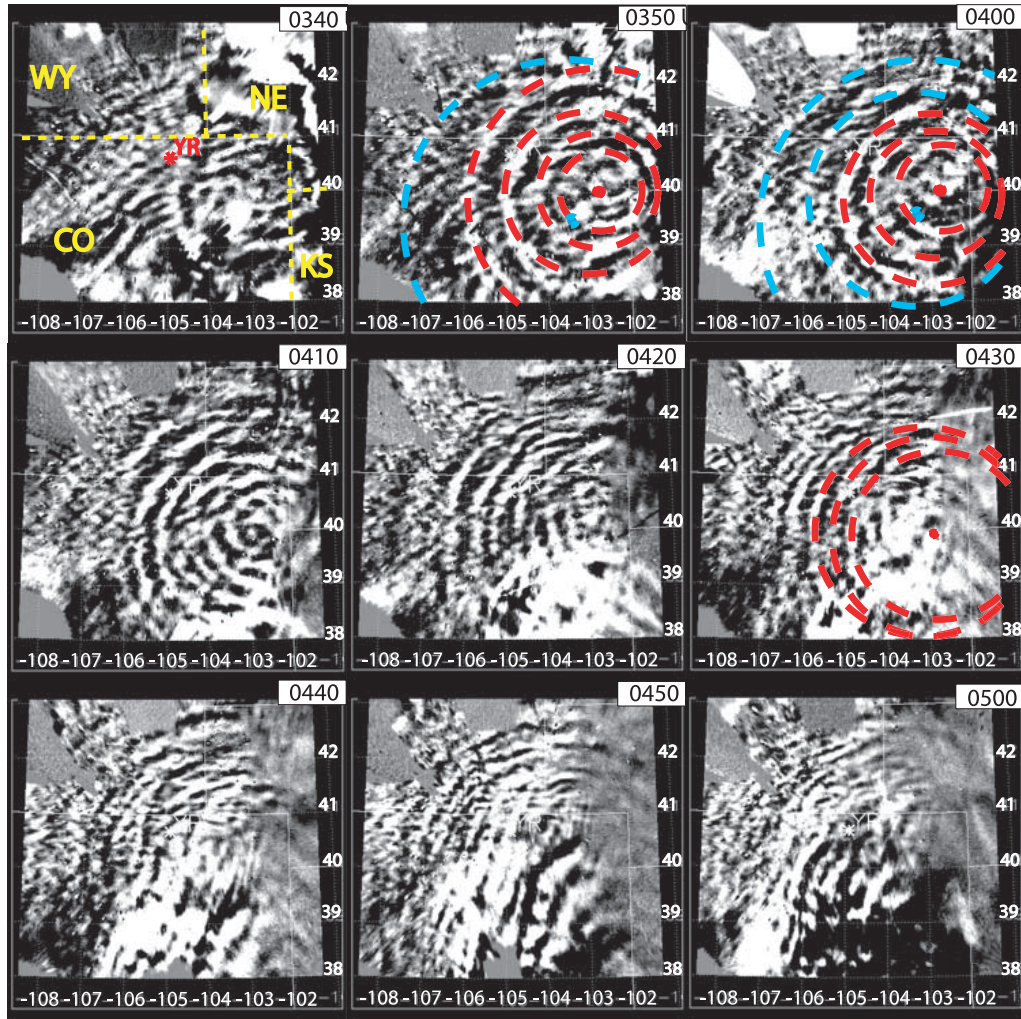


**Figure 4.1:** Time sequence of different OH images in geographic coordinates from 0340 to 0500 UT on 11 May 2004. The red and blue dashed circles denote CGW1 and CGW2 with estimated centers shown as red and blue solid dots [Adapted from [Yue et al. \(2009\)](#)].

In this Chapter, we present a TGW event that occurred on the night of 26 October 2014 induced by a tropical cyclone Nilofar which occurred during 25–31 October 2014 in the Arabian Sea. In contrast to the conventional methodology adopted using imagers, in our work, we have calculated the GW characteristics by using high data cadence ground-based photometric observations of nightglow emission intensities at multiple wavelengths obtained from Gurushikhar, Mount Abu (24.6°N, 72.8°E), in India, along with satellite-based OLR measurements during cyclone Nilofar. We have observed common wave

periodicities in all the three ( $O_2$ , Na, and OH) mesospheric nightglow emission intensities on the night of 26 October 2014. These wave characteristics observed on 26 October were different than those observed in other nights in the month of October 2014. This observation motivated us for further investigation with wider dataset to obtain the GW behavior at tropospheric altitudes. OLR flux data have been used as a tracer of tropospheric activity which revealed a clear signature on the night of 26 October 2014 that was consistent with those observed in the mesosphere. In addition to these GW parameters, we have also empirically calculated their vertical wavelengths, by observing the downward phase propagation in the airglow emission intensities and by using linear dispersion relation, which are found to be consistent with one another. This observation, thus, provides information on the GW propagation characteristics that existed during cyclone Nilofar on 26–27 October 2014.

### 4.3 Data set

To study the vertical coupling of atmosphere during cyclonic event Nilofar, measurements, which represent different altitudes of atmosphere, are considered. These include data from ground-based observations of nightglow emission intensities at OI 557.7 nm,  $O_2(0-1)$  atmospheric band, sodium 589.3 nm, and OH(6-2) Meinel band emissions obtained from Gurushikhar, Mount Abu using NIRIS and CMAP. As discussed in Chapter 1, different nightglow emissions emanate from different altitudes and hence, their intensity variations represent the atmospheric behaviour at the altitudes of their origin. The emissions namely, OI 557.7 nm,  $O_2(0-1)$ , sodium 589.3 nm, and OH(6-2) Meinel band emission are known to originate at altitudes of 100, 94, 92, and 87 km, respectively (Chapter 1). The OLR data measured on-board the Indian Geostationary satellite, Kalpana-1, have been used to investigate the convective activity and it represents the behaviour at top-of-the atmosphere in the troposphere. For the sake of completeness, the details of the data used in this

study are briefed in the following subsections.

### 4.3.1 Spectroscopic Observations

An in-house built Near InfraRed Imaging Spectrograph (NIRIS) has been used to carry out measurements of O<sub>2</sub>(0-1) and OH(6-2) band nightglow emission intensities which emanate at altitudes of 94 and 87 km, respectively. The details of NIRIS has been reported in Chapter 2, and the methodology adopted to derive mesospheric temperatures using rotational line intensity ratios of these band emissions from this instrument has been detailed in [Singh and Pallamraju \(2017a\)](#). The accuracy of temperatures derived by NIRIS is  $\pm 3\text{K}$  with a cadence of 5 minutes. NIRIS has a large field-of-view ( $80^\circ$ ), however, for the present study only zenith measurements have been considered.

### 4.3.2 Photometric Observations

Measurement of Na doublet (589.0 nm and 589.6 nm) and OI 557.7 nm nightglow emission intensities have been carried out using an in-house built CCD based Multi-wavelength Airglow Photometer (CMAP) [[Phadke et al. \(2014\)](#)] which is collocated with NIRIS. These emissions are known to originate at altitudes of 92 and 100 km, respectively. The details of the CMAP is described in Chapter 2, which is capable of carrying out near-simultaneous measurements at five different airglow emissions. In the work reported in this Chapter, Na airglow emission intensities at 589.0 and 589.6 nm have been averaged. Considering the data acquisition at these and other wavelengths in the filter wheel, the data cadence for Na and OI emissions turns out to be 1-minute.

### 4.3.3 Outgoing Longwave Radiation (OLR) Measurements

OLR is the radiative flux emitted from the Earth-atmosphere system to the outer space in the wavelength range of 3-100  $\mu\text{m}$  and can be used as a proxy for assessing the strength of convective clouds, as they attenuate the OLR flux. In this study OLR level-2 data has been obtained from the Very High Resolution Radiometer (VHRR) on-board the Indian meteorological satellite Kalpana-1 which is in a geostationary orbit. The OLR values thus derived, have a spatial resolution of  $0.25^\circ \times 0.25^\circ$  and a 15-minute cadence.

## 4.4 Observations

This section describes the two observations which led to investigation of the MLT coupling and experimental derivation of GW parameters. First, it was observed that NIRIS and CMAP measured nightglow emission intensities showed distinct behaviour on the night of 26 October 2014 as compared with other nights. This observation was followed by the investigation of the sources which can show such an effect at MLT altitudes. It was found that the effect seen in the MLT region from our ground-based observation was due to the tropical cyclone Nilofar. In the following subsections these observations are discussed in detail.

### 4.4.1 Tropospheric activity

Latent heat release in deep convections is the major source for the excitation of gravity waves in the tropics [*Fritts and Alexander (2003)*] along with orography and wind shears [*Pramitha et al. (2015)*]. OLR is considered to be a good tracer for convective activity as it is absorbed by clouds and water vapour in the atmosphere. Therefore, the variation in the OLR flux magnitudes can yield information on the behaviour of convective activity in the troposphere.

OLR values were averaged for 24 hours from 0450 LT on 26 October to 0450 LT on 27 October 2014 in the  $50^{\circ}$ – $80^{\circ}$ E longitude and  $0^{\circ}$ – $30^{\circ}$ N latitude ranges and the resultant values are shown as an image in Figure 4.2.

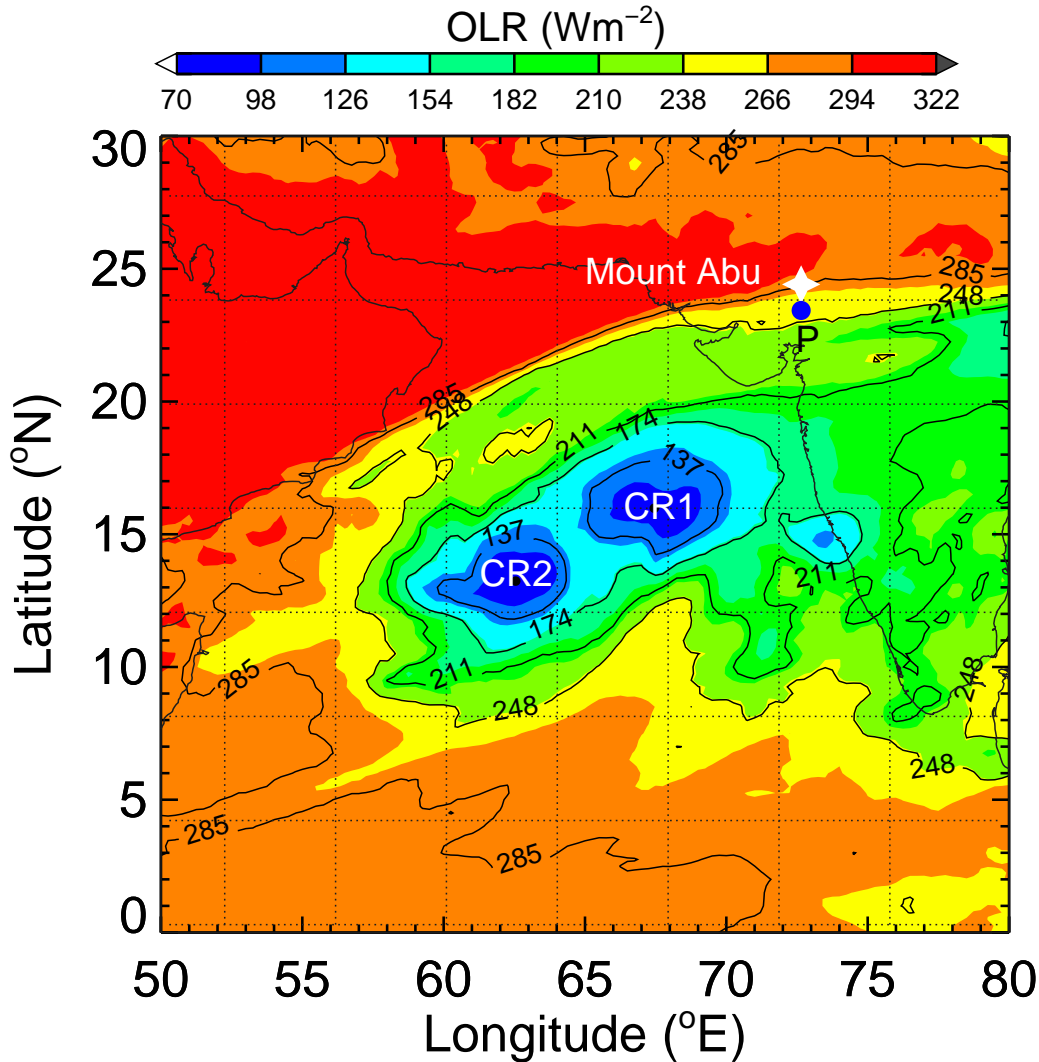


**Figure 4.2:** Outgoing longwave radiation (OLR) on 26 October 2014 as derived from VHRV on-board Indian meteorological satellite (Kalpana-1) shown over the Indian sub-continent in the longitude/latitude ranges of  $50^{\circ}$ E– $80^{\circ}$ E/ $0^{\circ}$ – $30^{\circ}$ N. A strong convective activity can be seen in the Arabian Sea which is due to the effect of cyclone Nilofar that occurred during 25–31 October 2014. The two centers of the cyclone Nilofar have been marked as CR1 ( $16^{\circ}$ N,  $67.5^{\circ}$ E) and CR2 ( $13.2^{\circ}$ N,  $62.5^{\circ}$ E). The observational site at Gurushikhar in Mount Abu ( $24.6^{\circ}$ N,  $72.8^{\circ}$ E, and altitude 1600 meters) is shown as a white star and the periphery point ‘P’ (shown by blue dot) is  $1^{\circ}$  south of the observational site has been considered in analysis to represent the cyclonic effect at the observational site.

A large convective activity in the Arabian Sea can be clearly seen with deep convections at two locations centered around  $16^{\circ}\text{N}$ ,  $67.5^{\circ}\text{E}$  referred to as convective region 1 (CR1) and  $13.2^{\circ}\text{N}$ ,  $62.5^{\circ}\text{E}$  convective region 2 (CR2) with a minimum OLR value of around  $100 \text{ Wm}^{-2}$  centered on CR1. As indicated above least values in OLR correspond to maximum magnitude of the convective activity. The optical observational site, shown with a white star symbol in Figure 4.2, is 1103 and 1665 km away in the northeast direction from CR1 and CR2, respectively. The effect of cyclonic activity can be clearly seen to be extended over a large spatial region in the western side of the Indian sub-continent. However, the optical observational site remained cloud free during 16 October 2014 to 27 October 2014 enabling uninterrupted optical ground-based measurements from Gurushikhar, Mount Abu.

The periphery of the observational site, identified as a point ‘P’ in Figure 4.2, is located approximately  $1^{\circ}$  south of our observatory. We have considered the OLR data at this point ‘P’ for our analysis as this location is in plains as opposed to the observational site, which is on the top of a mountain at a height of 1600 meters, thereby avoiding additional wave effects due to the mountains. The OLR values corresponding to this location have been considered to represent the lower atmospheric behaviour at the observational location, and have been used as the reference for comparison with the MLT emissions for the duration of the campaign (16–27 October 2014).

#### 4.4.2 Activity in MLT region

Figures 4.3(a-d) summarize the mesospheric nightglow emission intensity variations for OI, O<sub>2</sub>, Na, and OH airglow measured during the nights of 16–27 October 2014.

The continuous lines in Figure 4.3 show the variation of the emission intensities on the night of 26 October 2014 and the black dots show the variability in intensities on the nights of 16–27 October 2014. It can be noted that the

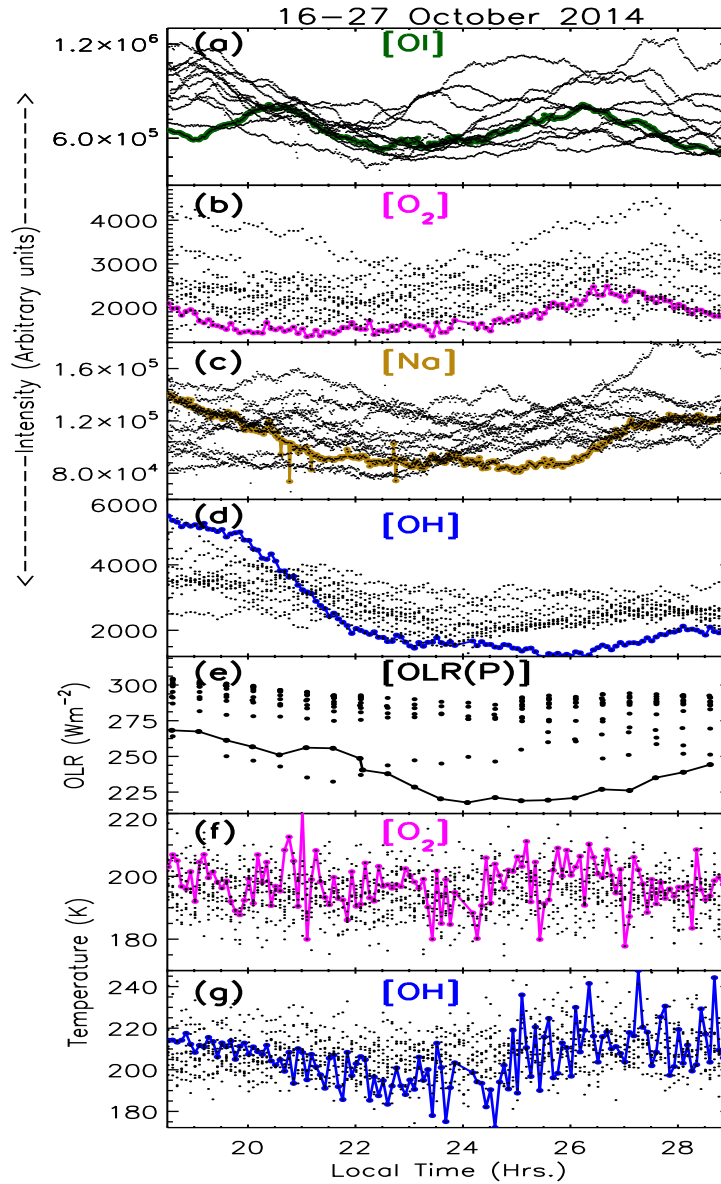


**Figure 4.3:** (a-d) Nocturnal variations in the OI (557.7 nm), O<sub>2</sub>(0-1) atmospheric band, Na (589.3 nm), and OH(6-2) Meinel band nightglow emission intensities as measured by CMAP and NIRIS at Gurushikhar, Mount Abu. These emissions are considered to be originating from 100, 94, 92, and 87 km altitudes, respectively. Figure 4.3e shows nocturnal variations in OLR data which are averaged over longitude/latitude ranges of 71.8°E–73.8°E/23.6°N–24.6°N. Figures 4.3f and 4.3g show the NIRIS derived mesospheric temperatures. The black dots in each of the subplots show the data for the duration of 16–27 October 2014 and the continuous lines are the variations in the respective parameters on the night of 26–27 October 2014. Distinct behaviour is seen in all the four nightglow emission intensities for 26 October 2014 when compared with the other nights of the month (16–27 October 2014).



variations in the mesospheric emission intensities on the night of 26 October were different as compared to those for all the other nights in several ways:

- O<sub>2</sub> intensities showed nearly the least values
- Na intensities decreased to nearly the lowest values after a couple of hours of sunset
- OH intensities showed a peak during evening hours and reduced thereafter

Such distinct differences in the emission intensity variability in O<sub>2</sub>, Na, and OH emissions on the night of 26 October 2014 in comparison to those in other nights during this month suggested a possible influence of some external source of energy at the mesospheric altitudes. As a major convective activity in terms of Nilofar occurred in the Arabian Sea west of Indian coast in that duration, an assessment was made to investigate its influence, if any, on the mesospheric nightglow emissions. In order to discern the effect due to the cyclone Nilofar on the observational site, it was decided to consider the OLR values as a proxy for the presence of the convective activity. However, as the presence of clouds in the field of view of NIRIS and CMAP will adversely affect the airglow measurements, a nearby location, P, in the neighborhood of observational site was considered to assess the strength of convective activity due to Nilofar. Wherein the OLR values at P (OLR(P)) were averaged over  $\pm 1^\circ$  in longitude and  $-1^\circ$  in latitude and are shown in Figure 4.3e. Similar to the convention followed for nightglow emission intensities, the OLR(P) data on the night of 26 October have been connected by a solid line, while those on other nights are shown as dots.

The effect of cyclone Nilofar can be seen in Figure 4.3e wherein a reduction had occurred in the values of OLR(P). It should be mentioned here that even though OLR(P) values show abnormal variation, the observational site which is around 100 km away towards northeast and on a mountain top was free of clouds (Figure 4.2) enabling the optical measurements until 27 October 2014.

However, from 28 October 2014 onwards the sky over the observational site became cloudy and moonlit thereafter and hence no data could be obtained after the night of 27 October 2014 for 15 nights. Variations in NIRIS derived mesospheric temperatures from O<sub>2</sub> and OH band emissions are shown in Figure 4.3f and 4.3g. Unlike nightglow emission intensities, significant deviations in temperatures were not noticeable on the night of 26 October 2014 as compared to other nights (16–27 October 2014). It can be appreciated from Figures 4.3 (a-d) and the discussion above that the variations in nightglow intensities on the night of 26 October were quite distinct compared to the other nights in the month of October 2014. These features motivated us to carry out investigations in further detail to study the possible linkage between the observed variations in the nightglow intensities (Figures 4.3(a-d)) and the cyclone Nilofar (Figure 4.2) on 26 October 2014.

## 4.5 Data Analyses and Results

The wave characteristics are obtained using the time series analysis methods discussed in Chapter 2. The following section deals with the derivation of various gravity wave parameters from the data shown in Figure 4.3.

### 4.5.1 Wave Period ( $\tau$ )

In order to understand the MLT dynamics spectral analysis have been performed on the high temporal resolution datasets obtained from the ground-based observations of NIRIS and CMAP. The data cadence of the optical data (O<sub>2</sub> and OH from NIRIS), (OI and Na from CMAP), and of OLR are 5, 1, and 15 minutes, respectively. The duration of the nightglow emission intensity data is approximately 10.5 hours (1830 LT in the evening to 0500 LT on the following morning) therefore, as discussed in Chapter 2 GWs having periods of less than 5.25 hours are reliable. Therefore, a 5-hour running average of

the data (dotted lines in Figure 4.4a-d) has been subtracted from the original data (solid lines in Figure 4.4a-d) on 26 October 2014 to obtain the residuals. These residuals will thus contain information on the periodicities that are smaller than 5-hours.

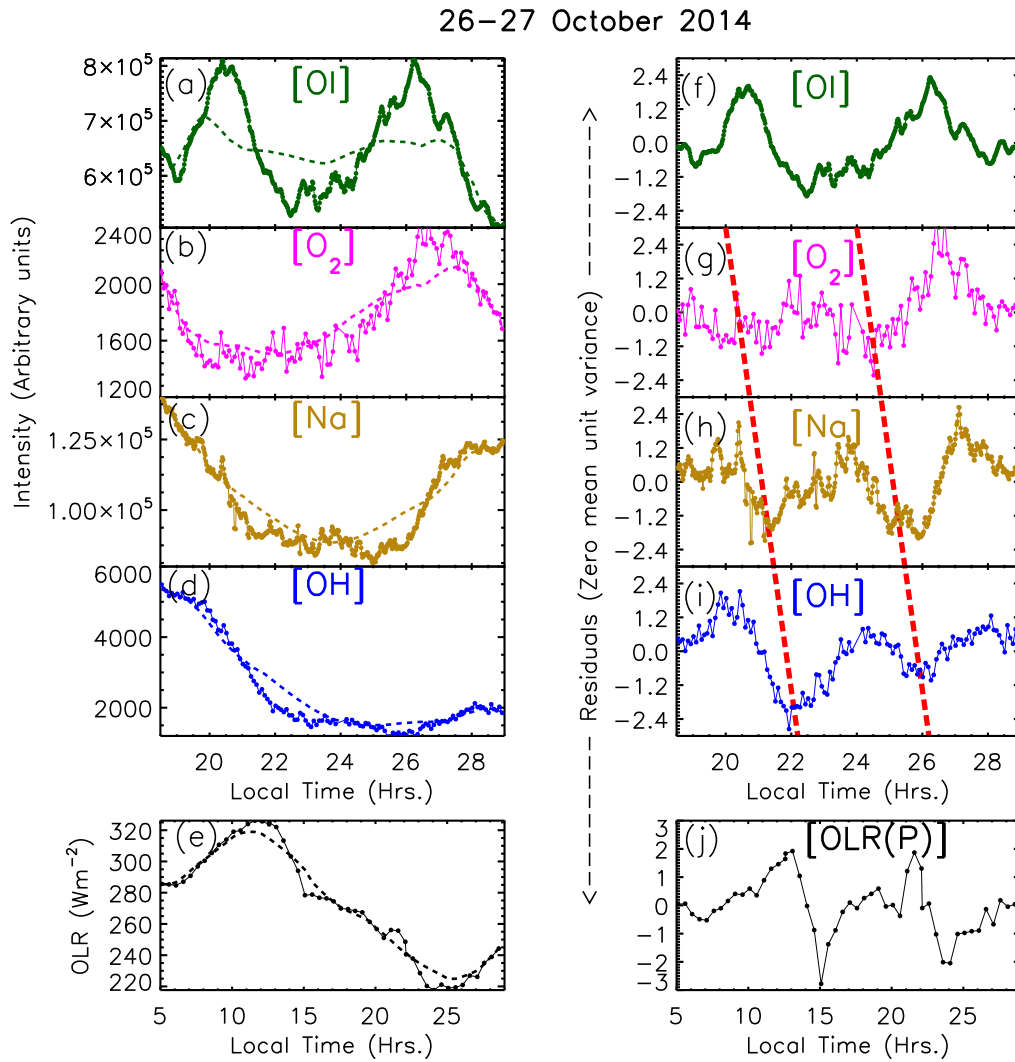


**Figure 4.4:** (a-d) Nocturnal variation in OI, O<sub>2</sub>, Na, and OH nightglow emission intensities on the night of 26 October 2014. (e) Variation of OLR values at the location ‘P’ for 24-hour duration during 26–27 October 2014 averaged over  $\pm 1^\circ$  in longitude and  $-1^\circ$  in latitude. The dotted lines in panels (a-e) show the 5-hour running average of the corresponding data. (f-j): Residuals obtained by subtracting the data with that of a 5-hour running average. Zero mean unit variances of the residuals corresponding to the data in panels a-e are shown. The red dashed line shows the downward phase propagation.

It is expected that the GW generated during cyclone Nilofar with centers in the Arabian Sea would take some time to propagate up to the mesospheric altitudes. Therefore, to obtain GW periods that existed in the troposphere even earlier in the day as seen in OLR(P), data for the whole day (24 hours) on 26–27 October 2014 have been considered and are shown in Figure 4.4e along with the 5-hour running average (dotted line). From the residuals of the data, zero mean unit variances have been calculated (shown in Figures 4.4f–j) by subtracting the mean value from the residuals and then dividing them by their standard deviation. As described in Chapter 2, this process normalizes the relative power in each period in a given dataset and thereby enables comparison of periodograms of different nights.

The residuals so obtained have been subjected to spectral analysis to obtain the GW periodicities that are smaller than 5-hour duration that may be present in the data. Further, as discussed in Chapter 2, the night time ground-based optical measurements are affected by moon light, clouds, and local light sources (occasionally). Care has been taken to remove such data from these measurements and as a consequence the data are not always equally spaced in time. Therefore, Lomb-Scargle periodogram analysis (described in Chapter 2), which takes care of unequal spacing of the data, has been carried out to investigate the periodicities of fluctuations present in the nightglow emission intensities and OLR datasets.

The OLR data are averaged in  $\pm 1^\circ \times 1^\circ$  (latitude  $\times$  longitude) at the two centers CR1 and CR2 and are represented by OLR(CR1) and OLR(CR2), respectively. Figures 4.5a and 4.5b depict periodograms obtained using zero mean unit variance of the residuals of the four airglow emission intensities, and OLR values at P, CR1, and CR2 for the night of 26–27 October 2014.

To derive the periodicities in the OLR at P, CR1, and CR2, 24-hour data have been used as shown in Figures 4.4e and 4.4j. The dashed curves shown in Figures 4.5a and 4.5b are the Red noise calculated using REDFIT (described in Chapter 2) [*Schulz and Mudelsee (2002)*] with 95% false alarm limit

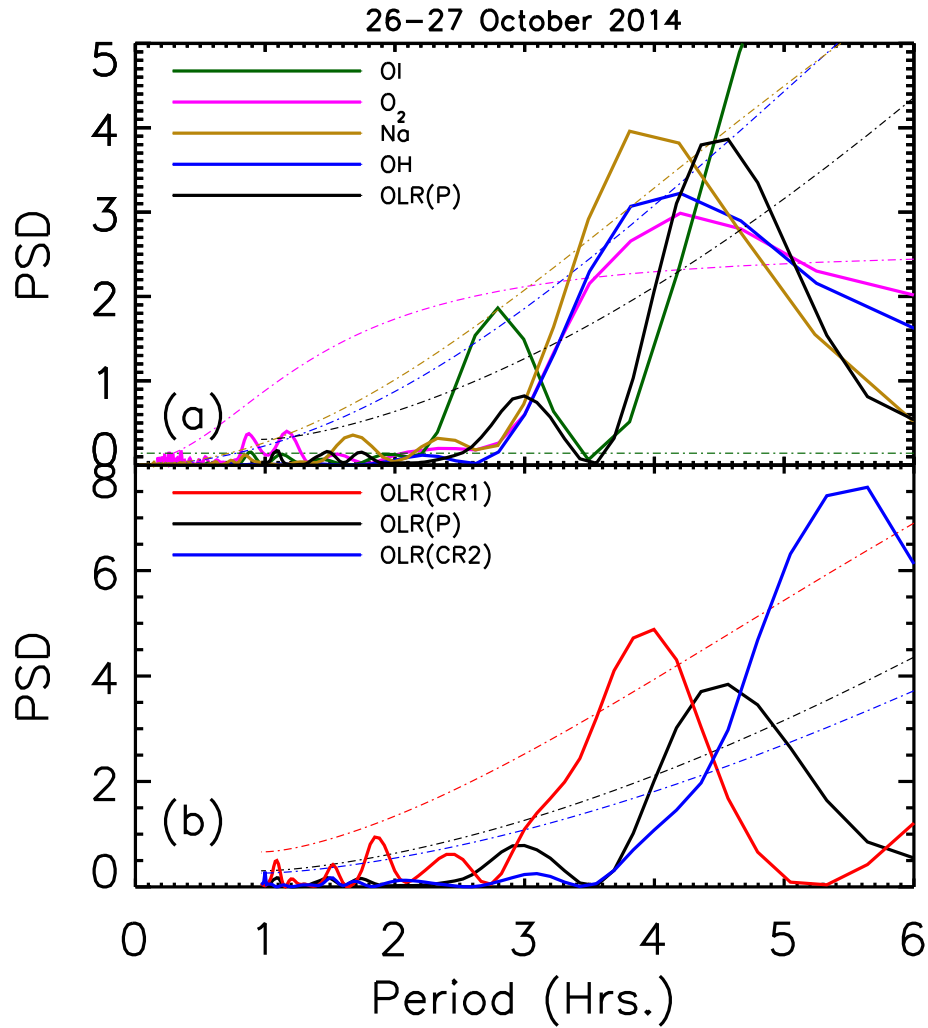


**Figure 4.5:** (a) Lomb-Scargle periodograms of the zero mean unit variance for the parameters shown in Figures 4.4(f-j) for the night of 26 October 2014 are shown. It is striking to note that a coherent period of around 4-hours is present in the three nightglow emission intensities (O<sub>2</sub>, Na, and OH) and in OLR(P) but not in the OI 557.7 nm emissions. (b) Results from similar analyses as shown for OLR(P) in Figures 4.4e and 4.4j as obtained for OLR at CR1 and CR2 (averaged over  $\pm 1^\circ$  longitude and latitude). The Lomb-Scargle periodograms of the OLR(P), OLR(CR1), and OLR(CR2) are shown by the black, red, and blue coloured lines, respectively. The dashed curves are the ambient (Red) noise in the data with 95% false alarm limit.

(FAL). It can be noted that statistically significant periodicities are present in the range of 3.99-4.45 hours in the O<sub>2</sub>, Na, OH nightglow intensities, and OLR(P). For OI emission intensities they are different at 2.78, 1.14, and 0.88

hours. The uncertainty in the determination of frequency  $\delta f$  in a periodogram is calculated using the relation given by equation 2.24 [*Bretthorst (2013)*]. Thus, the periodicities obtained in the O<sub>2</sub>, Na, OH nightglow intensities are  $4.20 \pm 0.14$ ,  $3.99 \pm 0.03$ , and  $4.00 \pm 0.10$  hours, respectively. It should be noted that coherent periodicities (in the range of 3.99 to 4.20 hours) were present in the mesospheric nightglow emission intensity fluctuations at three different altitudes (94, 92, and 87 km) on the night of 26 October 2014, which suggests that the dynamics at these three different altitudes were being affected by a common source.

It is plausible to assume that these common periodic oscillations seen in the mesosphere to have originated from the massive convective activity which occurred during cyclone Nilofar. However, to ascertain the effect of each of the convective centers in producing such common periods, Lomb-Scargle periodogram analysis on the zero mean unit variance of the residuals obtained from OLR(CR1) and OLR(CR2) have been performed and the results are shown in Figure 4.5b. Their dominant periods are found to be  $3.91 \pm 0.13$  and  $5.46 \pm 0.16$  hours, respectively. It is readily seen that the periodicity of OLR(CR1) is very similar to that of the mesospheric optical observations (around 3.99-4.20 hours), suggesting CR1 which is 1103 km away from the optical observational site to be source region for the observed effects in the mesosphere. The 5.46 hour period in the OLR(CR2) was not observed over Gurushikhar, presumably, as its center is further away at 1665 km and the wave that originated at CR2 could have propagated in different directions and/or weakened while propagating towards our optical observation station. The OI 557.7 nm green line emission does not show the presence of the 4-hour period as compared to the O<sub>2</sub>, Na, and OH emissions on this night and the possible reason will be discussed in the next section.

In order to ascertain if the observed features were due to any effect(s) other than that of cyclone Nilofar, similar analyses, as carried out for 26 October 2014, were also performed on all these parameters for all the data available

during 16–27 October 2014. As the convective region kept moving during this period from (12.5°N, 61.5°E) on 25 October 2014 to (20.7°N, 65°E) on 30 October 2014, we have considered the OLR values at a fixed location ‘P’ as the reference for comparison with our optical measurements during this extended period. The resulting periods along with the uncertainties obtained at all the four nightglow emission intensities and OLR(P) are shown in Figure 4.6.

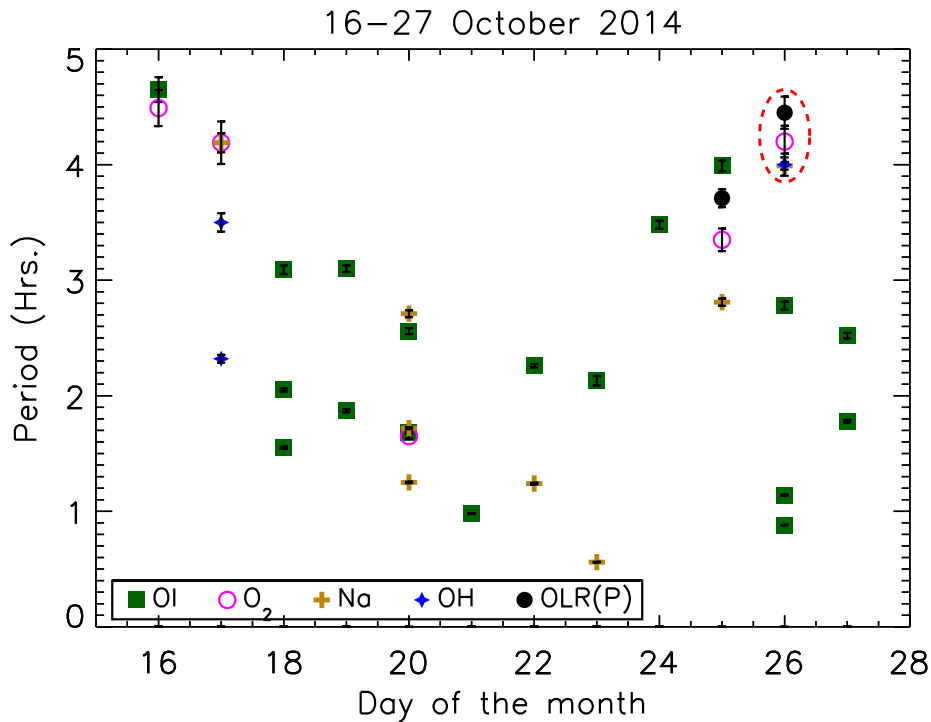


**Figure 4.6:** Periods obtained using Lomb-Scargle analyses for OI, O<sub>2</sub>, Na, and OH nightglow emission intensities for each night during 16–27 October 2014 are shown. Also shown are the periods in OLR(P) data obtained using similar procedure as adopted for nightglow emission intensities. It is striking to note that except for 26 October 2014 the GW periods obtained in three different nightglow emission intensities and in OLR(P) values are dissimilar for all other days.

It may be noted that on all other nights there were varying periods of GWs seen in different nightglow emission intensities and OLR(P). However, it is striking to note that on the night of 26 October, the three nightglow emission intensities (O<sub>2</sub>, Na, and OH) and OLR(P) show a common coherent period of around 4-hours (encircled by red dashed line). It is also striking to note that such kind of common periodicities as observed on 26 October

2014 were not present in any other nights during 16–27 October 2014. Thus, this observation provides an unambiguous evidence that the 4-hour common periodic oscillation seen in the mesospheric nightglow emission intensities over Gurushikhar and in OLR(P) on 26 October 2014 was indeed due to the strong convective activity due to cyclone Nilofar in the Arabian Sea. For the sake of completeness, we have also looked into other sources around the observational station that could have potentially been a cause for these waves, however, we could not find any.

### 4.5.2 Vertical Phase Speed ( $c_z$ ) and Vertical Wavelength ( $\lambda_z$ )

As the residual in the mesospheric emissions show a common periodicity and a downwards phase propagation in the nightglow emission intensities (as shown by red dashed line in Figure 4.4) it is apparent that the GW propagated upwards as presented in the GW dispersion relation [*Hines* (1960)]. An attempt has been made to obtain the signatures of propagation of waves through these heights. From cross correlation analysis between residuals of O<sub>2</sub> and OH emissions as seen in Figures 4.4g and 4.4i the phase offset time,  $\Delta t$ , is found to be 1.73 hours. The red dashed lines in Figure 4.4 clearly show the downward phase propagation in the intensity fluctuations of the nightglow emissions which confirms that the GW travelled upwards and adds credence to our conjecture on the effect of the tropospheric convective activity on the mesospheric wave dynamics. With the knowledge that the waves show common periodicities in I(O<sub>2</sub>) and I(OH) and the time offsets in the residual intensity variations ( $\Delta t$ ) the vertical phase speed,  $c_z$ , and vertical wavelength,  $\lambda_z$ , can be calculated using the following relations:

$$c_z = \frac{\Delta z}{\Delta t} \quad \text{and} \quad \lambda_z = \frac{\tau \cdot \Delta z}{\Delta t} \quad (4.1)$$

where,  $\Delta z$  is the difference between O<sub>2</sub> and OH emission layer heights (7



km). Thus, from Figure 4.4 the experimentally derived values of  $c_z$  and  $\lambda_z$  turn out to be  $1.13 \text{ ms}^{-1}$  and 16.47 km.

## 4.6 Discussion

We have seen in Figure 4.5b that the period of 4-hours in OLR(CR1) matches with the mesospheric optical emissions for the night of 26 October 2014 indicating it to be the source region for the wave activity. Therefore, for estimation of the horizontal wave characteristics (wavelength,  $\lambda_h$ , and phase speed,  $c_h$ ) for that night the position of CR1 was considered. As discussed in Chapter 2, it is to be remembered that although the Lomb-Scargle analysis yields information on the dominant periods, there is degeneracy in time frequency localization of the wave periodicities and therefore, it does not indicate the time duration at which a given period exists in a dataset. In order to investigate the duration of occurrence of the 4-hour period, wavelet analyses have been performed (as described in Chapter 2 in which Morlet mother wavelet function was used) on all the parameters.

Figures 4.7 (a-d) show the result of this analyses on the zero mean unit variances of the residual of the  $\text{O}_2$ , Na, and OH nightglow emission intensities and OLR(CR1) for 26 October 2014. The horizontal and vertical axes show LT and periods in hours. The normalized logarithmic power values are plotted and the scale is shown on the right.

As can be seen from Figure 4.7, the duration of occurrence of the gravity wave periods of around 4-hours in  $\text{O}_2$  (94 km), Na (92 km), and OH (87 km) nightglow intensity were centered around 2436 (0036 LT of 27 October 2014), 2348, and 2300 LT of 26 October 2014, respectively. Although the periods observed at three different altitudes in the nightglow intensities are similar, it is noteworthy that their occurrence peaks are delayed as we move towards higher altitudes suggesting propagation of the waves from below. This is consistent with the downward propagation in phase that was shown in Figure 4.4.

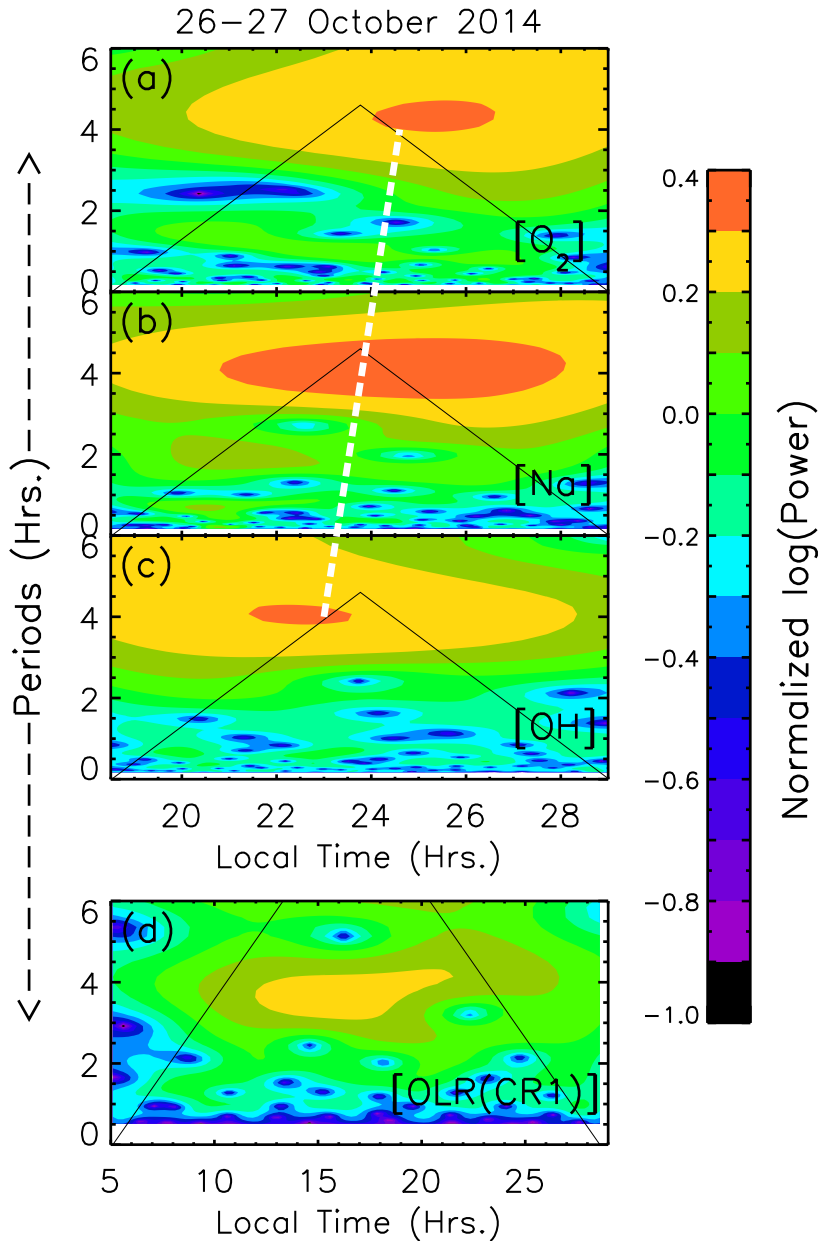


**Figure 4.7:** Normalized wavelet spectra of the corresponding zero mean unit variances of the  $O_2$ , Na, and OH nightglow emission intensities as shown in Figure 4.4(g-i) and OLR(CR1) showing temporal evolution of the periods seen in Figure 4.5. The peak power which are within the cone of influence in around 4-hour common GW period can be seen in  $O_2$ , Na, OH nightglow and OLR(CR1) datasets at around 2436 (0036 LT of 27 October), 2348, 2300 LT, and 1630 LT, respectively on the night of 26 October 2014. The white dashed line shows the shift in 4-hour period with respect to the altitude due to the vertical propagation of the wave generated in the troposphere.

Considering the 4-hour period and the cone of influence of the wavelet analyses for all these emission wavelengths a white dashed line is drawn (between O<sub>2</sub> and OH emission altitudes) in Figure 4.7 to indicate the time delay in the 4-hour period and hence the upward propagation of gravity waves due to cyclone effect below at tropospheric altitudes.

In estimating vertical wave characteristics we have considered OH and O<sub>2</sub> emission altitudes, and the vertical phase speed and wavelength turn out to be 1.22 ms<sup>-1</sup> and 17.76 km which are comparable to the downward phase propagation speed (Figure 4.4) and vertical wavelength obtained from the zenith intensity variations as discussed earlier. Further, the duration of occurrence of the 4-hour wave in troposphere as seen in the OLR(CR1) data was found to be centered around 1630 LT. Thus, the travel time of the TGW, which originated at CR1 of the cyclone Nilofar, to reach the highest of the mesospheric emissions at 94 km turns out to be 8.1 hours.

While the vertical phase speed and wavelength calculated here are consistent with the values obtained from the downward phase propagation (Figure 4.4) we have also carried out calculations to arrive at an independent estimate of vertical wavelength using the GW dispersion relation [*Hines (1960)*] with experimentally obtained values, as inputs, for this event. The observed evolution time of around 4-hours common wave period obtained using wavelet analyses have been used to calculate the horizontal phase speed of the wave.

Figure 4.8 shows a schematic of the geometry for a wave travelling from the source region, CR1, towards Gurushikhar (1103 km away in  $\sim 59^\circ$  from east). Let point A be the location of CR1 (16°N, 67.5°E) from where the gravity waves are set off. As described above, they are seen by our instruments located at Gurushikhar, Mount Abu (24.6°N, 72.8°E), identified as ‘C’ in this schematic. From a perpendicular line dropped from ‘C’ cuts the latitude of ‘A’ at point ‘B’ (16°N, 72.8°E). Assuming a planar geometry the distances AB and BC turns out to be 566 and 946 km for a given distance of 1103 km between AC, and the angle of propagation of waves is 59° towards north as measured from

east.

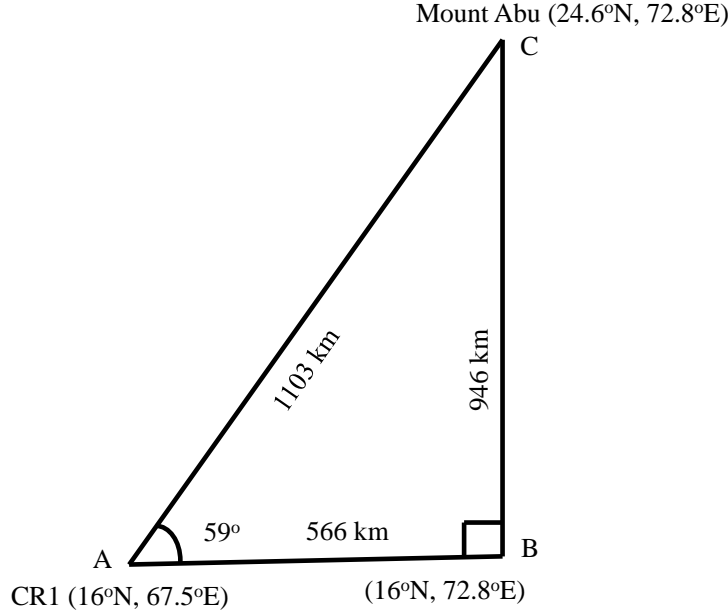


**Figure 4.8:** Schematic showing the wave propagation direction and distance from the source region to the observational location.

The horizontal phase speed,  $c_h$ , and horizontal wavelength,  $\lambda_h$ , can be calculated using the following relations:

$$c_h = \frac{d}{t} \quad \text{and} \quad \lambda_h = c_h \tau \quad (4.2)$$

where,  $d$  is the distance from CR1 to Gurushikhar and  $t$  is the time difference in the peak occurrences of the coherent period between OLR(CR1) and  $O_2$  intensities which is 8.1 hours. Hence, the horizontal phase speed ( $c_h$ ) is found to be  $37.8 \text{ ms}^{-1}$ . Considering this speed,  $c_h$ , and the measured wave period ( $\tau$ ) of 4.06 hours, the horizontal wavelength ( $\lambda_z$ ) turns out to be 553 km. As these are of gravity wave regime, it is expected that they would follow the linear dispersion relation of the GW given by *Hines (1960)*, which is:

$$k_z^2 = \frac{N^2}{(u - c)^2} - k_h^2 - \frac{1}{4H^2} \quad (4.3)$$

where,  $k_z (=2\pi/\lambda_z)$  is the vertical wave number, with  $\lambda_z$  being the vertical

wavelength,  $N$  is the Brunt-Väisälä frequency,  $u$  is the background wind velocity,  $c$  is the GW phase velocity,  $k_h (=2\pi/\lambda_h)$  is the horizontal wave number,  $\lambda_h$  is the horizontal wavelength, and  $H$  is the scale height.

This dispersion relationship is used to derive the vertical wave characteristics of the TGW using the horizontal characteristics, measured temperatures, and model winds as inputs for the night of 26 October 2014. On this night NIRIS measured nightly mean temperature of 197 K corresponding to 94 km, yield the value of the scale height ( $H=kT/mg$ ) to be 5.94 km, the Brunt-Väisälä frequency (which is given as  $N^2=2g/5H$ ) to be  $6.42 \times 10^{-4} \text{ rad}^2\text{sec}^{-2}$  (corresponding to a Brunt-Väisälä period of 4.14 minutes). The meridional and zonal components of the neutral winds as obtained from Horizontal Wind Model HWM14 [*Drob et al. (2015)*] at an altitude of 94 km at CR1 for the night of 26 October 2014 are shown in figure 4.9a.

The component of the resultant winds in the direction of Gurushikhar was calculated by using meridional and zonal winds obtained from HWM14. The vertical wave number,  $k_z$ , and thus, the vertical wavelength,  $\lambda_z$ , were calculated using equation 4.3 and the resulting values are shown in Figure 4.9b. As can be seen from Figure 4.9b the values of  $\lambda_z$  decreased from a peak of  $\sim 19$  km to 3 km by 0200 LT of 27 October 2014, which can be understood to be due to the changes in the direction and magnitude of the model winds. The vertical wavelength as calculated from equation 4.1, which is 16.47 km, is shown as a red dot in Figure 4.9b.

The time corresponding to the wave is taken as an average between its initiation (1630 LT) and time of observation at O<sub>2</sub> emission altitude (0036 LT of 27 October). Considering the uncertainties in determining the wave period (obtained using equation 2.24) and the minimum possible shift while deriving the time difference in cross correlation between residuals of O<sub>2</sub> and OH as seen in Figures 4.4g and 4.4i the minimum and maximum vertical wavelength values estimated are 15.09 and 18.51 km which is shown as a vertical error bar in Figure 4.9b. It is both striking and encouraging to note that the independently

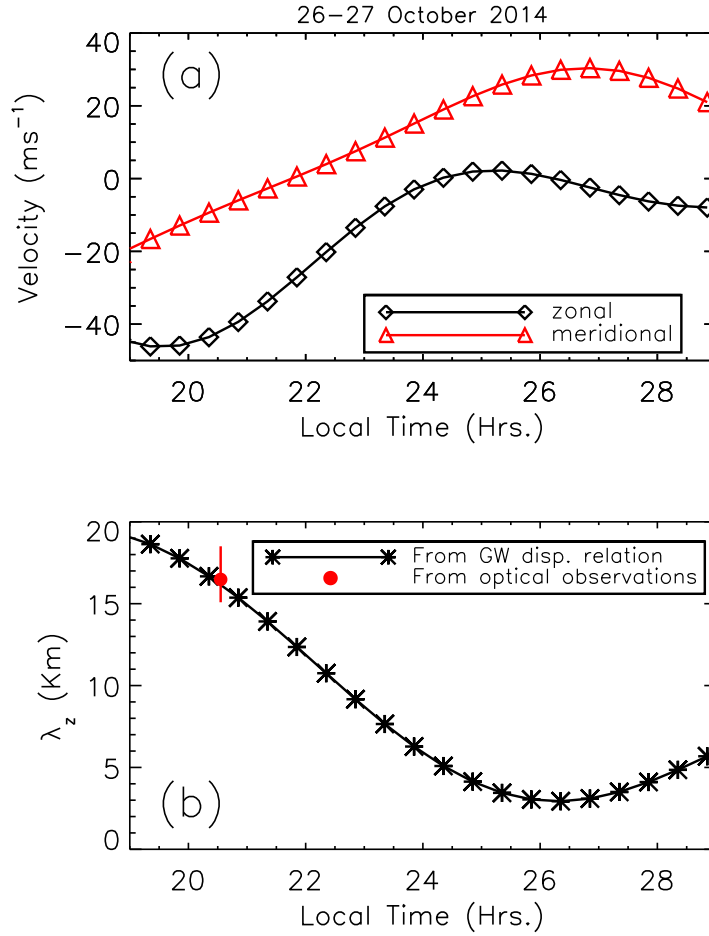


**Figure 4.9:** (a) Nocturnal variation in meridional and zonal wind at 94 km altitude as obtained from HWM14. (b) Nocturnal variation in vertical wavelength calculated using GW linear dispersion relation with the HWM14 winds (shown in panel (a)) and measured mesospheric temperature values from NIRIS as inputs. The red dot show the vertical wavelength derived from ground-based optical observations.

estimated values of  $\lambda_z$  and that obtained by observations show a very close match. Using the measured  $\lambda_h$  and  $\lambda_z$ , the vertical propagation angle,  $\theta_v$ , is found to be around  $88^\circ$  (as  $\theta_v = \tan^{-1}(k_z/k_h)$ ).

It is intriguing to note that the OI green line emission which emanates a few kilometers above the O<sub>2</sub> emission altitude did not show the common periodicity of around 4-hours as seen in O<sub>2</sub>, Na, and OH nightglow emissions. It is known that as the GW propagates up into the atmosphere its energy is dissipated primarily due to viscous drag and wind shears. In this regard, an estimate was made to understand the minimum requirements for the vertical

propagation of GWs. The minimum vertical wavelength,  $(\lambda_z)_{min}$ , required to propagate upwards overcoming the viscous drag is calculated using following relation [*Pitteway and Hines (1963); Beer (1974)*]:

$$(\lambda_z)_{min} = 25.386 \times \sqrt{\frac{\eta}{N}} \quad (4.4)$$

where,  $\eta$  is the coefficient of kinematic viscosity measured in  $\text{m}^2\text{s}^{-1}$  and  $N$  is the Brunt-Väisälä frequency.  $\eta$  has been estimated using the following relation [*Dalgarno and Smith (1962)*]:

$$\eta = \frac{3.34 \times 10^{-7} \times T^{0.71}}{\rho} \quad (4.5)$$

where,  $\rho$  is the mass density measured in  $\text{kgm}^{-3}$ . The mass densities ( $\rho$ ) at 94 and 100 km altitudes are calculated as  $1.831 \times 10^{-6}$  and  $6.917 \times 10^{-7} \text{ kgm}^{-3}$  using NRLMSIS-00 for the location of CR1 for the night of 26 October 2014 and therefore,  $\eta$  at these altitudes are estimated to be 7.76 and  $20.55 \text{ m}^2\text{s}^{-1}$ .  $N$  at these altitudes is calculated to be  $4.025 \times 10^{-3}$  and  $4.22 \times 10^{-3} \text{ sec}^{-1}$ . Therefore, from equation 4.5 the minimum vertical wavelength  $(\lambda_z)_{min}$  which can exist in the Earth's atmosphere at 94 and 100 km altitudes are 1.14 and 1.77 km, respectively. It is to be remembered that  $(\lambda_z)_{min}$  calculated using equation 4.5 considers only the static atmospheric conditions. Figure 4.9b shows the nocturnal variation in  $\lambda_z$ , all through the night on 26 October 2014, which were well above the minimum value of  $\lambda_z$  discussed above and therefore, it is unlikely that viscous drag would have caused its dissipation.

Thus, the absence of the signature of the 4-hour wave in OI emission is most likely due to wind shear mechanism in the heights below that of OI emissions. In this regard, TIDI (TIMED Doppler Interferometer) winds that were available on that night were looked into. The data available closest to the observational station were at  $30.6^\circ\text{N}$ ,  $55.1^\circ\text{E}$  and  $15.5^\circ\text{N}$ ,  $57.2^\circ\text{E}$  at 16.46 LT and 16.53 LT, respectively, which are shown in Figure 4.10. These passes do show presence of shears in the altitude range of 97 km to 102 km in the zonal

and meridional winds. Although, these measurements were not collocated with the optical observational site, it can be assumed that similar situation might have prevailed around the site and hence, most likely these shears prevented the waves from propagating upwards.

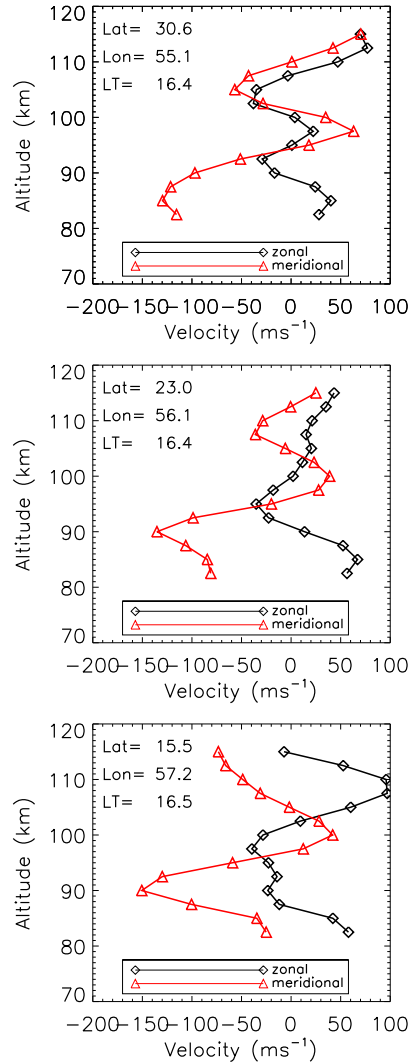


**Figure 4.10:** TIDI (TIMED Doppler Interferometer) winds at the Latitude/Longitude/LT shown in the panels. The presence of shear in the zonal/ meridional winds can be seen.

By using ray trace simulations of [Alexander \(1996\)](#) it was shown that the travel time of TGW for cyclone Mahasen from the tropospheric source to the OH airglow layer was in the range of 2-7 hours [[Yue et al. \(2014\)](#)]. It was also



shown that during favorable wind conditions these waves can propagate to large distances (1500 km away from the source) with horizontal phase speeds of  $75 \text{ ms}^{-1}$  in a travel time of around 5-hours. These wave characteristics derived from ray-trace simulation studies are broadly consistent with the parameters derived from the present measurements.

None of the earlier studies, however, presented the possible magnitudes of vertical wavelength of the GWs present during cyclonic activity. Majority of earlier studies estimated the GW characteristics through simulations, or ray-trace calculations, or by comparing with satellite- and ground-based measurements. It is known that parameters derived by such comparisons of measurements from satellite- and ground-based instrumentation are limited by assumptions in terms of geometric projections.

In the present work, however, we have experimentally obtained parameters of TGW in the mesosphere that existed during cyclone Nilofar using high cadence optical measurements from a single location, which is expected to minimize the uncertainties in the parameters derived. It is understood that derivation of these parameters experimentally using ground-based optical measurements are restricted to clear sky conditions, especially during large convective events. In that regard it was fortuitous that the ground-based optical observations from Gurushikhar were possible on the night of 26 October 2014 which provided the much needed information prevalent during such a convective activity.

## 4.7 Conclusion of Vertical Coupling of Atmospheres During Cyclone Nilofar

Spectroscopic measurement of nightglow emission intensities carried out from Gurushikhar, Mount Abu, in India using  $\text{O}_2(0-1)$  and  $\text{OH}(6-2)$  bands which emanate from 94 and 87 km altitudes were obtained from NIRIS showed un-

usual nocturnal variation on the night of 26 October 2014 compared to other nights during 16–27 October 2014. Concurrent measurements of sodium nightglow emission intensities (which emanate from 92 km) carried out using CMAP also showed a distinct nocturnal variation on that night which was different from those on other nights. To ascertain the reason for the observed unusual variations in these nightglow intensities we have performed Lomb-Scargle periodogram and wavelet analyses to investigate the periodicities present and their duration of occurrence in these datasets. On the night of 26 October 2014 a common wave period of around 4-hours was observed in mesospheric altitudes as derived from the O<sub>2</sub>, OH, and Na nightglow emission intensity variations.

The Kalpana-1 infrared images and the derived OLR fluxes (Figure 4.2) showed a strong convective activity in the Arabian Sea with two cyclonic centers at CR1 and CR2 and were 1103 km and 1665 km away from the optical observational location on 26 October 2014. Spectral analysis carried out on the OLR(P) values (averaged for  $\pm 1^\circ$  in longitude and  $-1^\circ$  in latitude) that were obtained at close proximity to the observing station showed a statistically significant  $4.45 \pm 0.14$  hour period. The periodicities in the OLR(CR1) and OLR(CR2) have been found to be  $3.91 \pm 0.13$  and  $5.46 \pm 0.12$  hours, respectively.

Spectral analysis performed on the O<sub>2</sub>, Na, and OH nightglow intensities and OLR(P) for each of the nights during 16–27 October 2014 showed varying periods of GWs. It is striking to note a common coherent period of approximately 4-hours in the three different mesospheric nightglow emission intensities and OLR(CR1) on the night of 26 October 2014 (Figure 4.5). These observations add credence to the inference that the TGW seen at the mesospheric heights must have originated from the strong convective source during cyclone Nilofar and propagated from the troposphere to the mesospheric heights. The residual of mesospheric intensities also showed a downward phase propagation which indicates that the GW was travelling upwards. Cross correlation analysis between the residuals of O<sub>2</sub> and OH revealed an offset in the phase by 1.73

hours. From these experimentally derived values the vertical phase speed ( $c_z$ ) and wavelength ( $\lambda_z$ ) is calculated to be  $1.13 \text{ ms}^{-1}$  and  $16.47 \text{ km}$ .

The duration of occurrence of the GW periods at these altitudes have been obtained using wavelet analysis and these times were found to be centered around 2436, 2348, 2300, and 1630 LT in O<sub>2</sub>, Na, OH airglow intensities and OLR(CR1), respectively. Using the parameters obtained in this study, horizontal phase speed ( $c_h$ ) and wavelength ( $\lambda_h$ ) of the TGW observed at the mesospheric height over Gurushikhar, Mount Abu were found to be  $37.8 \text{ ms}^{-1}$  and  $553 \text{ km}$ , respectively.

We have also calculated the vertical wavelength ( $\lambda_z$ ) using linear GW dispersion relationship which showed horizontal wind velocity dependent nocturnal variations with a peak to be around  $19 \text{ km}$  for an hour after sunset. It should also be noted here that the OI 557.7 nm green line nightglow emission intensity variability does not show the presence of around 4-hour periods on the night of 26 October 2014. This suggests that the wave observed at the O<sub>2</sub> emission altitude would have dissipated below OI 557.7 nm emission layer because its propagation was adversely affected by wind shears that were present at those altitudes. Thus in this work, we report on all the GW parameters ( $\tau$ ,  $c_h$ ,  $\lambda_h$ ,  $c_z$ ,  $\lambda_z$ , and  $\theta_v$ ) which were obtained experimentally from ground-based optical data that exist during a tropical cyclone. The study presented here provides an unambiguous signature of the propagation of tropical cyclone generated gravity wave up to the mesospheric heights during cyclone Nilofar.

## 4.8 Anomalous Increase in O<sub>2</sub> Temperatures

### 4.8.1 Introduction

From NIRIS observations of around one year it is seen that, in general,  $T(\text{O}_2)$  is lower than  $T(\text{OH})$  which is the synoptic picture of the mesospheric temperature structure. This also indicates that the height of mesopause is above that of

the O<sub>2</sub> emission layer (~94 km). However, it was also observed that there are several occasions when T(O<sub>2</sub>) is greater than T(OH) which can happen if:

1. The altitude of mesopause is below that of O<sub>2</sub> emission layer (~94 km) [e.g., *Venkat Ratnam et al. (2010)*].
2. Mesospheric temperature inversions (MTIs) [e.g., *Hauchecorne et al. (1987)*] also known as mesospheric inversion layers (MILs) [e.g., *Meriwether and Gardner (2000)*].
3. Large scale circulation in the MLT region [e.g., *Meriwether and Gerrard (2004)*].

One or more of these processes can act in tandem as well to enhance temperature at O<sub>2</sub> emission altitude regions in comparison with that of OH.

As discussed in Chapter 1, the mesospheric temperature inversions are the regions of enhanced temperatures above their normal values. They can have a thickness of several kilometres and appear in MLT region of the low- and mid-latitudes at any time of the year [e.g., *Meriwether and Gerrard (2004)*]. MTIs/MILs are mainly attributed to energy deposition of upward propagating tides and gravity waves [e.g., *Hauchecorne et al. (1987)*; *Meriwether and Gardner (2000)*] and chemical heat released *in-situ* by several exothermic reactions [e.g., *Meriwether and Mlynczak (1995)*; *Meriwether and Gardner (2000)*; *Meriwether and Gerrard (2004)*; *Ramesh et al. (2013)*]. The mean location of the mesopause over Gadanki (13.5°N, 79.2°E), in the Indian region is around 98 km (varying between 87 and 105 km) [*Venkat Ratnam et al. (2010)*]. That study also found that there is a secondary minimum in the temperature profile at 75–80 km. In between these two regions there is an increase in temperature (inversion) up to 85–90 km which are more prominent during equinoxes (March/April and September/October). These MTIs/MILs show small seasonal variation but they do show pronounced short-term variations. These satellite-based measurements present an average picture of the MLT region

but do not describe their dynamics in shorter time scales. In order to understand short-time fluctuation in the MLT temperatures high data cadence observations are required.

### 4.8.2 Observations

In order to investigate the MTIs observed using NIRIS derived temperatures from Gurushikhar, Mount Abu, the differences in T(O<sub>2</sub>) and T(OH) on the night of 16 April and 6 May 2013 are shown in Figure 4.11a and 4.11b.

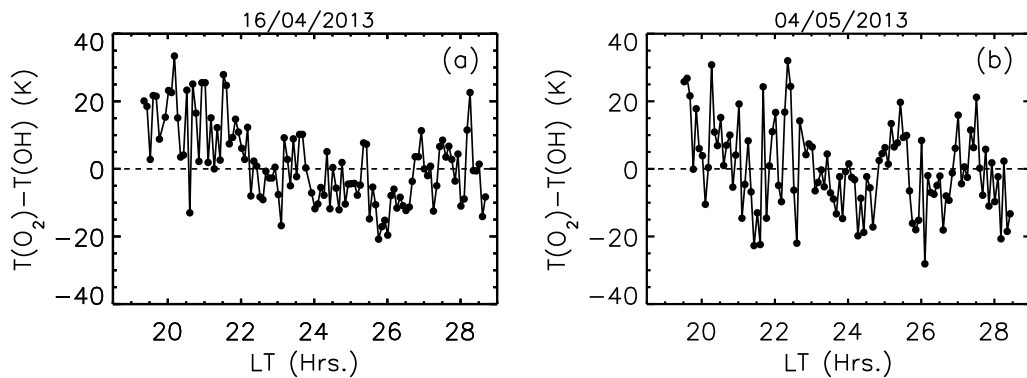


**Figure 4.11:** The difference in T(O<sub>2</sub>) and T(OH) on the night of (a) 16 April 2013, and (b) 6 May 2013. Temperature inversion on both nights can be noted mainly in the pre-midnight hours.

It can be seen that the difference in temperatures is positive for around 2.5 hours after the sunset (1930 to 2200 LT) on the night of 16 April 2013 and for around 3.5 hours (1930 to 2300 LT) on the night of 4 May 2013. The peak temperature difference observed on these two nights is around 30K. We have seen vertical propagation of waves on these two nights which is confirmed by the downward phase propagation in the residuals of O<sub>2</sub> and OH emission intensities (Figure 2.16). Hence, the cause for the observed temperatures inversions on these nights can be attributed to upward propagating gravity waves as discussed above.

### 4.8.3 Results

In order to assess the general behaviour of such temperature inversions in the mesosphere, we have considered all the data obtained in the year 2013 to characterize the different possibilities that exists. Some new developments in terms of mesospheric temperature dynamics have come to light owing to the high cadence simultaneous measurement of  $T(\text{O}_2)$  and  $T(\text{OH})$ . Different cases are made based on the mesospheric temperatures and nightglow intensities data obtained from NIRIS which are listed below. Based on the statistics of these cases an attempt is made to attribute the cause of observed enhancement in the  $\text{O}_2$  temperature as compared to OH temperatures.

Case 1: Difference between the temperatures at  $\text{O}_2$  and OH emission altitudes [ $T(\text{O}_2)-T(\text{OH})$ ] is positive and vertical propagation is seen in the  $\text{O}_2$  and OH emissions (as shown for the nights of 16/04/2013 and 04/05/2013). The source of such temperature enhancements (MTIs) could be attributed to vertical propagation of waves.

Case 2: Difference between the temperatures at  $\text{O}_2$  and OH emission altitudes [ $T(\text{O}_2)-T(\text{OH})$ ] is negative and vertical propagation not seen in the  $\text{O}_2$  and OH emissions (as seen for night of 15/04/2013; Figure 4.12 left column). This would be an ‘unperturbed’ quiet time synoptic mesospheric behaviour.

Case 3: Difference between the temperatures at  $\text{O}_2$  and OH emission altitudes [ $T(\text{O}_2)-T(\text{OH})$ ] is negative and vertical propagation seen in the  $\text{O}_2$  and OH emissions (as seen for night of 01/05/2013; Figure 4.12 middle column). Such type of cases would negate the argument (Case 1) of source for observed MTIs to be the vertically propagating gravity waves from below.

Case 4: Difference between the temperatures at  $\text{O}_2$  and OH emission altitudes [ $T(\text{O}_2)-T(\text{OH})$ ] is positive and vertical propagation not seen in the  $\text{O}_2$  and OH emissions (as seen for night of 03/05/2013; Figure 4.12 right column). Such behaviour has been considered as a signature of *in situ* chemical heating as the source for MTIs.

The mesospheric temperatures on the night of 04/05/2013 discussed in earlier paragraph and shown in Figures 4.11 represent the behaviour as in Case 1. The existence of vertical propagation on this night was shown in Chapter 2 (Figure 2.16).

In Figure 4.12 the other three cases as defined above have been shown in which the nights of 15/04/2013, 01/05/2013, and 03/05/2013 represent the Cases 2, 3, and 4, respectively, and are shown in three different columns. The subplots in rows of Figure 4.12 represent the differences in  $T(\text{O}_2)$  and  $T(\text{OH})$ , O<sub>2</sub> and OH emission intensities, residuals of O<sub>2</sub> and OH emissions (as obtained by similar method shown in Figure 4.4 and 4.5), and the periodicities in O<sub>2</sub> and OH emissions. As can be seen from Figure 4.12a  $T(\text{O}_2)$  is less than  $T(\text{OH})$  for most of the duration which means that no temperature inversion is seen on the night of 15 April 2013. Also, this night does not show common periods in  $I(\text{O}_2)$  and  $I(\text{OH})$  and hence, no vertical propagation seems to exist. Such scenario describes the quiet time synoptic mesospheric behaviour. However, on the night of 01/05/2013 no temperature inversion is seen but this night does show signatures of vertical propagation of GW as they show common wave periodicities of around 1.5 hours in O<sub>2</sub> and OH emissions and their residuals show downward phase propagation. Such observations indicate that vertical propagation in waves need not be responsible for MTIs.

The night of 03/05/2013 does show the temperature inversion wherein the difference between the temperatures [ $T(\text{O}_2) - T(\text{OH})$ ] is positive for around 3.5 hours (from 1930 to 2300 LT) with peak value of around 32 K. This night, however, does not show the common periods in O<sub>2</sub> and OH emissions and hence, no vertical propagation of wave seems to exist. Such cases have been interpreted as the signature of chemical heating to be the cause of observed MTI. These different cases shown above indicate that the temperature inversions in the O<sub>2</sub> emission altitude could be either due to the effect of upward propagating waves or due to chemical heating when the vertical propagation is not seen. It is also possible that even when vertical propagation is seen the

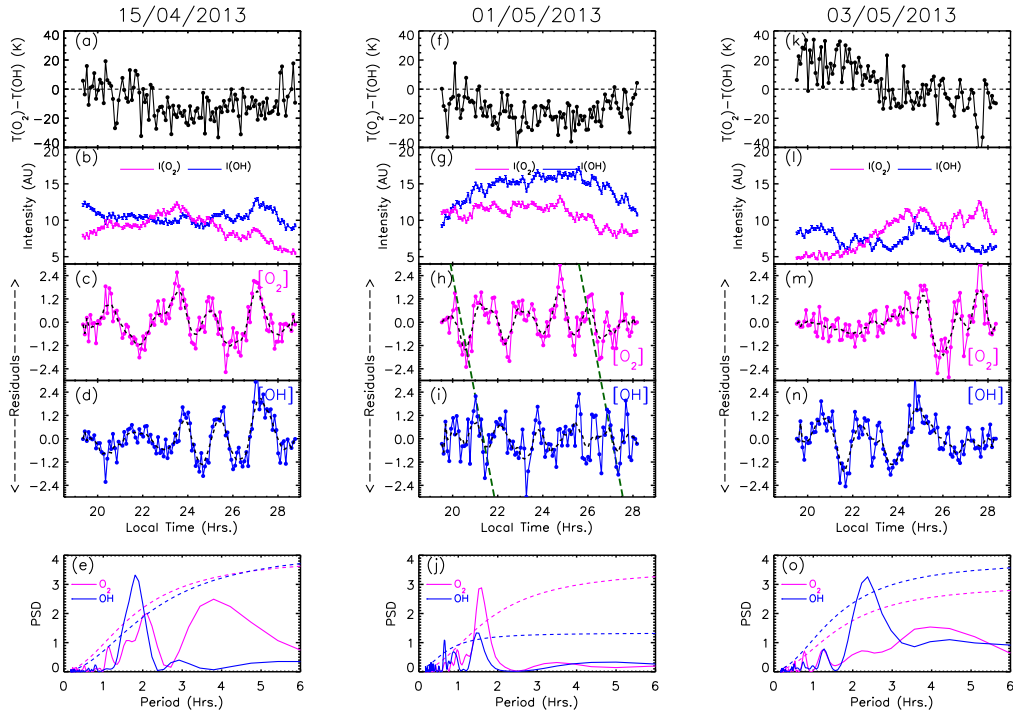


**Figure 4.12:** The five rows in the different subplots represent the difference in  $T(\text{O}_2)$  and  $T(\text{OH})$ ,  $I(\text{O}_2)$  and  $I(\text{OH})$ , residuals of  $\text{O}_2$  and  $\text{OH}$  emission intensities, and the periodicities present in the  $\text{O}_2$  and  $\text{OH}$  emission intensities, respectively. These nights are chosen to show three Cases (2, 3, and 4). (Left column) represents Case 2 in which observation on the night of 15/04/2013 are shown. On this night, both temperature inversion and vertical propagation are not seen. (Middle column) represents Case 3 in which temperature inversion is not seen but the vertical propagation is observed. (Right column) represents Case 4 in which temperature inversion is seen but the vertical propagation is not seen. It should be noted that to determine the periodicities that are present at  $\text{O}_2$  and  $\text{OH}$  emission altitudes we have used the same method as described in Chapter 2 (Figure 2.15 and Figure 2.16).

source of chemical heat might also be operative to form the MTIs.

NIRIS was running on a continuous mode from Gurushikhar throughout the year 2013 wherein a total of 234 nights of observations were possible excluding monsoon and moonlit periods. We have carried out statistical distribution of all four cases defined above. Similar plots as shown in Figure 4.12 were made for all nights of observations in the year of 2013. In this study it was found that:

1. Out of 234 nights of observations those nights which belong to Cases 1,



2, 3, and 4 are 17, 154, 23, and 40, respectively.

2. The nights on which the temperature inversion and the vertical propagation both are not seen are maximum in number (Case 2, 65.8%), followed by the nights in which temperature inversion is seen but not the vertical propagation (Case 4, 17.1%).
3. Those nights in which temperature inversion is not seen but vertical propagation is seen (Case 3) are around 9.8% followed by those nights in which both temperature inversion and vertical propagation are observed (Case 1, 7.3%).

Based on the present statistics it appears that chemical heating in the mesosphere could be a more probable cause for the observed MTIs in comparison to vertical propagation. Moreover, the cases for and against vertical propagation as the cause for MTI are nearly equal (Case 1 and Case 3). Therefore, at this stage it is difficult to ascertain if the excess energy carried upwards to the mesosphere is not deposited there but transported to altitudes higher above. This could explain the absence of MTIs on the night of the existence of vertical propagation. Answers to all these aspects require supporting simulation studies. These will be attempted in the future.

## 4.9 Summary

In this chapter, we have discussed that how various altitudes of the Earth's atmosphere are vertically coupled due to upward propagating waves of various time scales that are generated in the lower atmosphere. The vertical coupling of the atmospheres is shown to exist during cyclone Nilofar which occurred in Arabian Sea during 25–31 October 2014. The various gravity wave parameters are experimentally derived using simultaneous multi-wavelength ground-based and satellite-based observations. Experimentally derived vertical wavelength

of the GWs present during cyclone Nilofar was found to be in good agreement with independently estimated values based on the Hines dispersion relation.

Possible causes for the observed mesospheric temperature inversion from NIRIS data are discussed and different cases are made to carry out statistical study of the causes of the observed MTIs. Using a total of 234 nights of observations carried out in the year 2013 statistical distribution of all four cases which are defined based on the difference in O<sub>2</sub> and OH temperatures and the vertical propagation of the waves are investigated. The statistical result indicates that chemical heat release in the mesosphere on some nights to be a more probable cause for the MTIs.

In next Chapter, the results related to the latitudinal coupling of the mesospheric region during SSW events will be discussed. The results presented in the next Chapter are mainly based on the NIRIS observations, SABER derived mesospheric temperatures for over 10 years of observations, and few supplementary data sets.

# Chapter 5

## Mesospheric Temperature Variations During SSW Events

### 5.1 Background

The results discussed in earlier Chapters were mainly obtained from the ground-based observations which were related to the understanding of large- and short-timescale variations in the mesosphere, solar effects in the mesosphere, statistical characterization of gravity wave parameters, and vertical coupling of the atmospheres under varying atmospheric conditions.

In this Chapter, the focus is to understand the global nature of mesospheric temperature variability during SSW events. The phenomenon of sudden stratospheric warming (SSW) has been introduced in Chapter 1 wherein, we have briefly discussed its causative mechanism, and some of the effects in the MLT region. As briefed in Chapter 1, even though SSW is a northern hemisphere high-latitude phenomena, various altitudinal and latitudinal regions of the Earth's atmosphere can be affected during SSW events. In addition to NIRIS observations, the results presented in this Chapter are based on the data obtained from multiple satellite-based observations, and MERRA data sets. The results obtained on the nature of latitudinal variation of mesospheric tempera-

tures during SSW events which are based on 11 SSW events that occurred during 2004 to 2013 will be discussed. It has been found that during SSW events the well-known mesospheric cooling over the northern hemispheric high-latitudes turns to heating over mid-latitudes and then reverts to cooling closer to equatorial regions. This trend continues into the southern hemisphere as well. These variations in the mesospheric temperatures at different latitudes have been characterized based on northern hemispheric stratospheric temperature enhancements at high-latitudes during SSW periods. Such a characterization in mesospheric temperatures with respect to latitudes reveals an hitherto unknown intriguing nature of the latitudinal coupling in the mesosphere that gets set up during the SSW events.

## 5.2 Introduction

As discussed in Chapter 1, SSW is a large-scale phenomenon that occurs mostly in the northern hemispheric polar stratosphere during winter time, and is characterized by a drastic rise in temperature within a few days. An SSW event is called ‘minor’ if the mean temperature at or below the 10 hPa pressure level ( $\sim 32$  km) poleward of  $60^\circ$  rises by at least 25 K within a period of a week. An event is considered as ‘major’ if, in addition to increased temperature, zonal mean eastward winds reverse at these altitude and latitude region [*McInturff (1978)*; *Labitzke (1981)*]. SSW is attributed to the interaction of zonal winds with vertically propagating planetary waves (PWs) forced from the troposphere and their effect in terms of quasi-16-day waves have also been seen to be present over low- and equatorial-latitude E- and F-regions of the ionosphere [e.g., *Laskar et al. (2014)*].

It has also been shown that the westward acceleration of zonal winds over northern hemispheric high-latitudes occurs during SSW periods in the presence of PWs [*Matsuno (1971)*]. Further, it has been shown that during SSW events mesospheric cooling occurs at high-latitudes [*Labitzke (1972)*, *Labitzke (1981)*],

which has also been confirmed by the OH airglow temperature measurements over both northern and southern hemispheres (NH & SH) [e.g., [Walterscheid et al. \(2000\)](#); [Azeem et al. \(2005\)](#)]. In the NH observation from Eureka, Canada (80°N, 86°W) mesospheric cooling of  $\sim 25$  K was observed during 13 to 14 February 1993 [[Walterscheid et al. \(2000\)](#)] while, measurements over South Pole station in Antarctica showed a decrease in mesospheric temperatures of  $\sim 15$  K prior to the stratospheric warmings of May 1995 and July 2002 [[Azeem et al. \(2005\)](#)].

Moreover, by comparison of SABER temperatures at different pressure levels it was noted that while the stratospheric temperature at 10 hPa pressure level increased over several days, the mesospheric temperature (in the 0.3 to 0.01 hPa pressure range) decreased simultaneously during 2002 SSW period over SH at 80°S latitude [[Siskind et al. \(2005\)](#)]. Further, a new meridional circulation has been found to get set in the MLT region during SSW events owing to the concomitant increase in the lower thermospheric temperatures in the altitudes above cooler mesopause in high-latitudes [[Laskar and Pallamraju \(2014\)](#)]. Thus, it is imperative that a comprehensive investigation on latitudinal distribution of mesospheric temperatures be carried out, especially during SSW events.

Greater information on mesospheric temperatures and winds are available at high-latitudes compared with those at equatorial-, low- and mid-latitudes for the periods during SSW events. Lower mesospheric temperatures at equatorial-latitudes were first obtained using rocket-sondes from Thumba (8.5°N, 76°E), in India, wherein it was reported that occasional warmings occur in the upper stratosphere and lower mesosphere during SSW periods [[Mukherjee and Ramanamurty \(1972\)](#)]. Recently, for 2009 SSW event using Rayleigh lidar observations a warm mesospheric condition has been reported [[Sridharan et al. \(2010\)](#)] over Gadanki (13.5°N, 79.2°E), a low-latitude location in India. These observations were also found to be consistent with the SABER derived temperatures obtained over the same location. In all these studies the temperature

behaviour at altitudes below 80 km was investigated. Due to the paucity of continuous ground-based measurements of mesospheric temperatures over equatorial- to mid-latitudes, the behaviour of the mesosphere during SSW periods at these latitudes is not well-understood.

In this study, we have used high cadence NIRIS derived mesospheric temperatures from a low-latitude location (Gurushikhar), satellite derived global distribution of mesospheric temperatures from SABER, OSIRIS, and SOFIE, and stratospheric temperatures and zonal winds as derived from Modern Era Retrospective-analysis for Research and Applications (MERRA) datasets to characterize the behaviour of mesospheric temperatures along the North-South meridian in both the hemispheres. Stratospheric temperatures and winds at high-latitudes ( $>60^\circ\text{N}$ ) are considered as tracers of the stratospheric behaviour in the NH and hence the occurrence of SSW events. In that regard the observed stratospheric temperature enhancements and zonal wind reversals at NH high-latitudes during SSW periods would indicate the prevalent planetary wave activity.

### 5.3 Measurement Techniques

The results discussed in this Chapter are based on the NIRIS data, observations from multi-satellite platforms, and reanalysis data. The details of these data sets have been discussed in Chapter 2 and hence, are only listed below:

1. NIRIS derived mesospheric temperatures have been obtained from  $\text{O}_2(0-1)$  atmospheric and  $\text{OH}(6-2)$  vibrational band spectra which correspond to altitude regions of 94 and 87 km, respectively. These observations have been carried out from PRL's optical aeronomy observatory at Gurushikhar, Mount Abu ( $24.6^\circ\text{N}$ ,  $72.8^\circ\text{E}$ ) during January 2013. For the study reported in this Chapter zenith temperature measurements are used.

2. MERRA data have been used to obtain the stratospheric temperatures poleward of 60°N and longitudinally averaged zonal wind at 60°N at 10 hPa pressure level (~32 km).
3. SABER derived mesospheric temperatures for different latitudes obtained for 11 SSW events have been used. The SABER data products are briefed in Chapter 2. The estimated uncertainty in the SABER temperatures in the altitude range of 80-100 km is  $\pm 4$  K [*Mertens et al.* (2001)].
4. OSIRIS derived mesospheric temperatures during 2009 and 2010 major SSW events have been used.
5. SOFIE derived (level 2A) mesospheric temperatures in the polar latitudes (65°-85°S/65°-85°N) have been used.

## 5.4 Observations

In this section, it is described that how the observed features in the NIRIS derived temperatures in January 2013 provided motivation for a wider investigation to understand the behaviour of global large-scale mesospheric temperature distribution that exists during SSW events. In this study, SSW temperatures and winds at 10 hPa pressure level from MERRA and SABER derived mesospheric temperatures during eleven SSW events that occurred during the past ten years (2004-2013) in the months of January and February have been used. Of these eleven SSW events, six were major and five were minor in nature.

### 5.4.1 NIRIS Temperatures for January 2013

The mesospheric nocturnal temperatures derived from O<sub>2</sub> and OH using NIRIS in the month of January 2013 during day of the year (DOY) 7-21 are shown in Figures 5.1a and 5.1b, respectively. From Figure 5.1a it may be noted that

the mesospheric temperatures at 94 km show higher values for DOY 7, 8, 16, 18, and 19 before midnight and gradually reduce later.

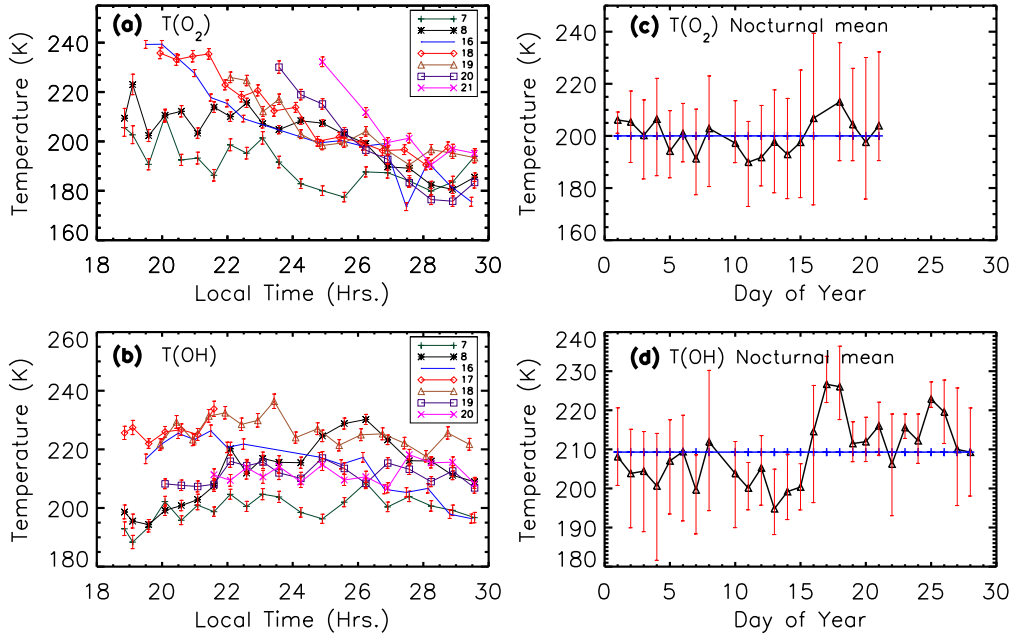


**Figure 5.1:** (a) NIRIS derived  $O_2$  rotational temperatures (at 94 km) over Gurushikhar, Mount Abu for a few selected nights during SSW period are shown along with the estimated uncertainty ( $\sim \pm 3K$ ) at each of the datum points. (b) Similar plot as in Figure 5.1a but for OH temperature (at 87 km). (c) Nocturnal mean mesospheric temperatures derived from  $O_2(0-1)$  atmospheric band for the month of January 2013 (black line) and monthly mean (blue line) are shown. The red vertical bar shows the range of the derived temperatures for a given night. (d) Similar plot as in Figure 5.1c but for OH derived temperatures. It may be noted that mesospheric temperatures are elevated throughout the night (as shown in the range of temperatures) during the SSW period.

From Figure 5.1b it can be seen that on 8 January 2013 the mesospheric temperature enhancement is in the post-midnight period. On 16 January 2013 OH temperature enhancements are seen during pre-midnight hours and seem to be reduced during post-midnight. All these observations show modulations due to the presence of gravity, tidal, and planetary waves in the mesospheric temperatures at these altitudes. On 17 and 18 January the OH mesospheric temperatures are elevated for the duration of the data available in comparison with the nocturnal mean temperature value for this month (discussed below).



The dissimilar behaviour in the temperatures at these two altitudes is a result of vertically propagating gravity waves as discussed in Chapter 4. The effects of PW type scale sizes on these altitudes are discussed here using these temperature values, while the characterization of temperatures at these two altitudes in the time scales of gravity and tidal wave regimes was discussed in Chapter 3.

Figures 5.1c and 5.1d show nocturnal mean O<sub>2</sub> and OH rotational temperatures during January 1-21 and January 1-29, respectively, together with the range of the temperature on a given night. From these figures it can be seen that mesospheric temperatures are elevated for several nights when compared with the monthly mean values. Especially, the nightly average together with the nightly range in the O<sub>2</sub> and OH temperatures are enhanced during January 16 to 19 and January 16 to 26, respectively, when compared with the monthly mean. This indicates to a significant additional source of energy to the low- and mid-latitudes spanning several days.

Interestingly, the enhancement in the mesospheric temperatures as seen from NIRIS data described here were found to be occurring during a major SSW event (January 7–27, 2013; Figure 5.2h) which occurs at polar latitudes. In this context, it is relevant to note that OH band emissions from higher vibrational levels peak at higher altitudes [Savigny *et al.* (2012)]. Using SCIAMACHY (SCanning Imaging Absorption spectroMeter for Atmospheric Cartography on Envisat) data it was shown that the OH (6-2) emission rate profile is typically vertically shifted upwards by 1-2 km relative to the OH (3-1) band, and the OH (8-3) band is generally found to peak about 1 km higher than the OH (6-2) band [Savigny *et al.* (2012)]. The O<sub>2</sub>(0-1) emission layer is considered to be located at 94 km altitude [Murtagh *et al.* (1990)] and the altitude of peak OH emission can be considered as  $86.8 \pm 2.6$  km [Baker and Stair Jr (1988)]. Further, using OSIRIS data it has been shown that ground-based OH temperatures can be affected by changes in the OH emission layer height [Sheese *et al.* (2014)] which could lead to an uncertainty in tempera-

tures of the order of  $\pm 2\text{--}4$  K (and up to  $\sim 7$  K in extreme cases as seen during 2009 major SSW event over high latitudes). However, as it can be seen from Figures 5.1c and 5.1d the enhancement in the NIRIS derived temperatures are much larger and therefore are believed to be due to SSW related effects and not by layer movement. This interpretation is confirmed by satellite-based measurements (as shown below in section 5.5).

#### 5.4.2 MERRA Temperatures and Winds for 2004-2013

In Figure 5.2, the stratospheric temperature ( $T_S$ ) in the polar cap region (poleward of  $60^\circ\text{N}$ ) and longitudinally averaged zonal wind ( $U_S$ ) at  $60^\circ\text{N}$  from MERRA are shown for the years 2004–2013 (from DOY 1 to 65). Six major warming events occurred during the years in 2004, 2006, 2008, 2009, 2010, and 2013 wherein the zonal mean zonal winds at  $60^\circ\text{N}$  at 10 hPa pressure level reversed from eastward to westward. Five minor events were observed in the years 2008 (three events), and one each in 2011 and 2012, wherein the temperature in the polar cap region at 10 hPa pressure level increased by more than 25 K without any reversal of zonal mean zonal winds. In Figure 5.2 the duration of all these events are marked by vertical dashed lines. A list of the duration together with the peak temperature and the minimum zonal wind during these periods is given in Table 5.1.

### 5.5 Results and Discussion

A description on the data analyses used, results obtained, and discussion on the global effects that seem to be occurring in the stratospheric-mesospheric system, especially during SSW times, will be presented in the following sections.

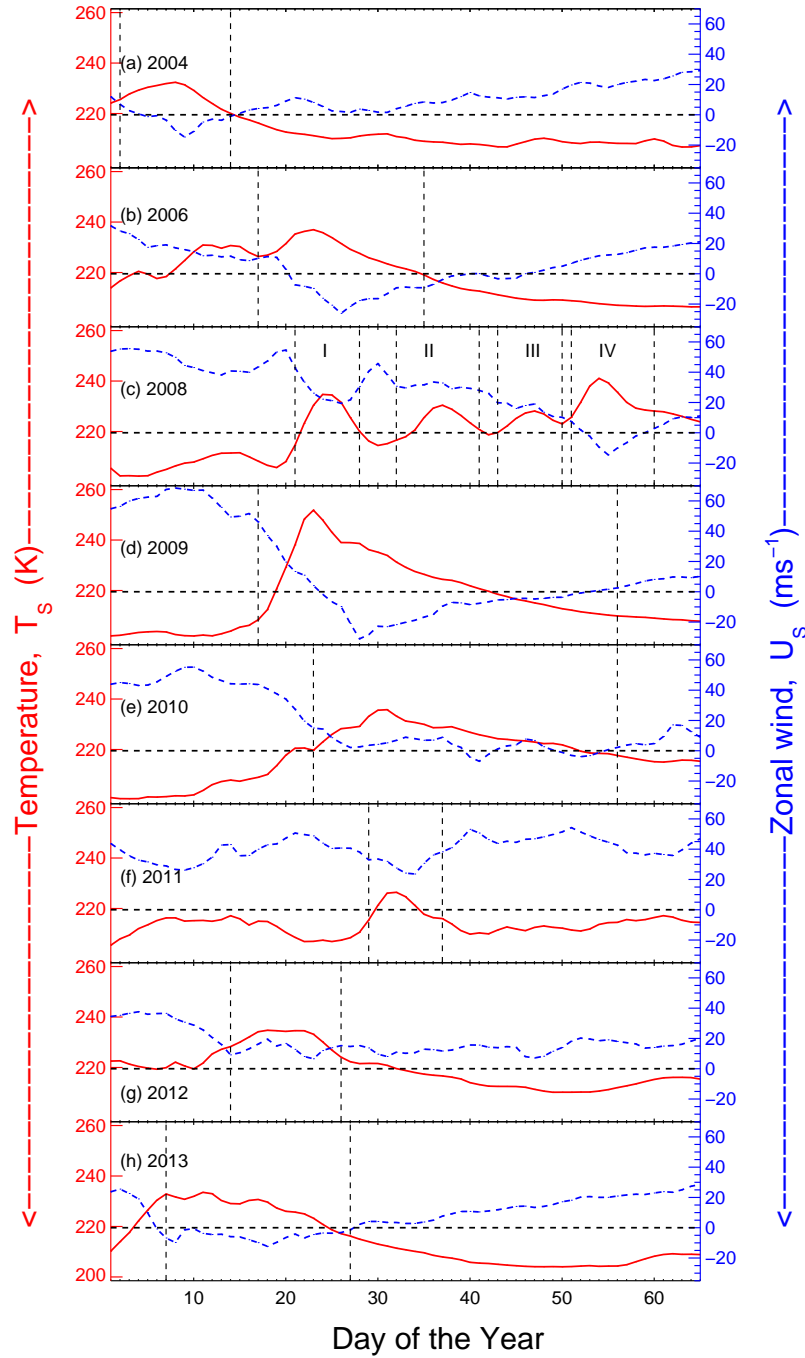


**Figure 5.2:** Temperatures in the polar cap poleward of  $60^\circ\text{N}$  ( $T_S$ ) and longitudinally averaged zonal wind at  $60^\circ\text{N}$  ( $U_S$ ) at 10 hPa pressure level ( $\sim 32$  km) obtained from MERRA dataset for eleven SSW events which occurred during 2004–2013 that are selected for present study. The first 65 days of data for each of the eight years are shown. The duration of the SSW events are marked by vertical dashed lines.

**Table 5.1:** List of SSW events considered for this study

Year	DOY Range	$T_{Smax}$ (K)	$U_{Smin}$ ( $\text{ms}^{-1}$ )
2004	2-14	232.37	-14.67
2006	17-35	236.96	-26.15
2008(I)	21-28	234.69	19.42
2008(II)	32-41	230.42	29.03
2008(III)	43-50	228.12	10.77
2008(IV)	51-60	241.06	-14.58
2009	17-56	251.83	-31.08
2010	23-56	235.77	-6.92
2011	29-37	226.41	23.61
2012	14-26	234.77	6.57
2013	7-27	233.53	-12.29

### 5.5.1 SABER, OSIRIS, and SOFIE Temperatures for 2009 and 2013 SSW Events

The latitudinal coverage of the TIMED satellite is  $135^\circ$ , ( $83^\circ$  and  $52^\circ$  in opposite hemispheres). Every 60 days the latitudinal coverage reverses due to periodic yaw manoeuvre of the satellite [*Russell III et al. (1999)*]. The latitudinal coverage of the SABER derived temperature data is approximately from  $55^\circ\text{S}$  to  $85^\circ\text{N}$  for the eleven SSW events considered in this study. Thus, the data are organized into a total of 15 ranges of  $10^\circ$  latitude from  $80^\circ$ – $90^\circ\text{N}$  to  $60^\circ$ – $50^\circ\text{S}$  in the NH and SH. The SABER mean mesospheric temperatures (longitudinally averaged in the range of  $2^\circ$ – $142^\circ$  and in the altitude range of 85–89 km) are obtained at each of the  $10^\circ$  latitudinal intervals for all the SSW events considered in this study.

Similarly, OSIRIS derived mean mesospheric temperatures (with similar longitudinal averaging as for the SABER data, but in the altitude range of 86–89 km) are obtained at each of the  $10^\circ$  latitudinal intervals for all major SSW events. For all the given latitudinal ranges the daily mean mesospheric temperature from OSIRIS is derived wherever the number of data points is more than 10 for a given DOY.

The zonal mean mesospheric temperatures from SOFIE dataset are derived

with the latitude ranges poleward of  $65^\circ$  in both hemispheres for all the major SSW events considered here.

In Figures 5.3a and 5.3b the blue coloured lines show SABER derived daily mean mesospheric temperature values at all the 15 latitude ranges as a function of DOY for the year 2013 and 2009, respectively, while the purple coloured lines show the SOFIE derived mean mesospheric temperatures over polar latitudes in both hemispheres. The dashed vertical lines in Figures 5.3a and 5.3b show the duration of the SSW events (DOY 7–27 in 2013 and DOY 17–56 in 2009). The dashed horizontal lines in Figures 5.3a and 5.3b show the mean mesospheric temperature (for a given latitude range) during the DOY ranges as indicated above for the 2013 and 2009 SSW events. From Figure 5.3a mesospheric cooling at high-latitudes ( $>60^\circ$ ) over the NH is clearly seen during the SSW period especially during DOY 9–20 in both SABER and SOFIE data. As one moves from high- to low-latitudes the mesospheric cooling turn into mesospheric heating around mid-latitudes (during DOY 7–25 in  $10^\circ$ – $50^\circ$ N latitude range) before turning again to cooling over equatorial latitudes (during DOY 7–15).

The red coloured line in Figure 5.3a shows the NIRIS derived nocturnal mean OH temperatures obtained at Gurushikhar, Mount Abu, which is overlaid on the longitudinal mean mesospheric temperatures obtained from SABER datasets for the latitude range of  $20^\circ$ – $30^\circ$ N. From Figure 5.3a the NIRIS derived mesospheric temperatures are seen to be higher. This is not unexpected as the temperatures obtained by NIRIS are over a small FOV (zenith) and at a high data cadence as opposed to the SABER temperatures that are obtained by averaging a large longitude range ( $2^\circ$ – $142^\circ$ ). An enhancement in temperature is also noticed in the SH during DOY 10–23 (depending on the latitude).

In Figure 5.3b similar behaviour in the SABER and SOFIE derived mesospheric temperatures is seen for the major SSW events of 2009. The mesospheric cooling at higher latitudes ( $>50^\circ$ N) is clearly observed in both SABER

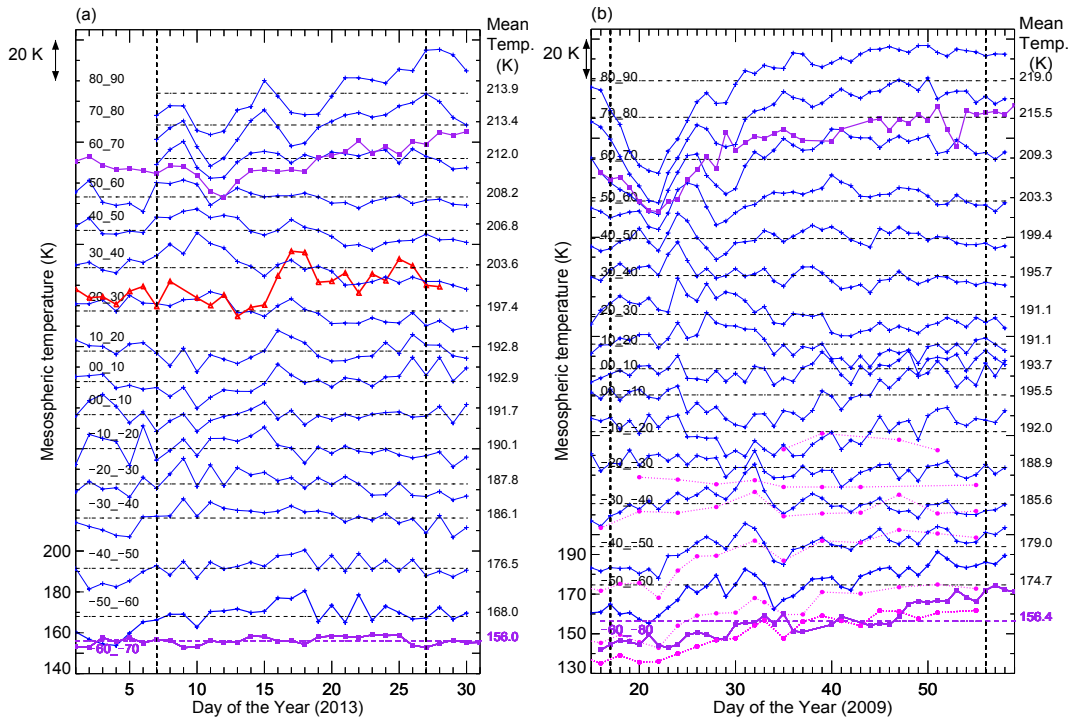


**Figure 5.3:** (a) Longitudinally ( $2^{\circ}$ - $142^{\circ}$ ) averaged mesospheric temperatures (averaged in the height range 85-89 km) derived from the SABER dataset at  $10^{\circ}$  latitude interval (indicated in the top left of each sub panel) for both the hemispheres over 30 days (during DOY 1-30, 2013) are shown in blue coloured lines. NIRIS derived OH temperatures from Gurushikhar are overlaid in red colour. Vertical scale is for the bottom-most temperature variability, and the subsequent plots are shifted by 15 K. The horizontal dashed lines show the mean temperature values (for the DOY ranges indicated in the Table 5.1) which are shown on the right side. SOFIE derived zonal mean mesospheric temperatures at polar latitudes in NH and SH are shown by purple coloured lines. (b) Similar plot as shown in Figure 5.3a but for 2009 major SSW event in which in addition to SABER and SOFIE, OSIRIS derived mesospheric temperatures are also shown by magenta coloured lines at different latitudes.

and SOFIE derived mesospheric temperatures. The OSIRIS derived mesospheric temperatures are shown by magenta coloured lines in Figure 5.3b for the 2009 major SSW event since OSIRIS data are not available for 2013. For 2009 SSW event the OSIRIS temperatures are available in the SH from  $10^{\circ}$  S to  $90^{\circ}$  S for the altitude, latitude, and longitude ranges as discussed above. As can be seen from Figure 5.3b, the OSIRIS temperature trends for the given latitudinal range matches well with the SABER and SOFIE data with some differences in the absolute values.

### 5.5.2 SABER Temperatures for 2006 and 2010 Major SSW Events

Similar to Figure 5.3 the latitudinal variations of mesospheric temperatures for 2006 and 2010 major SSW events are shown in Figures 5.4 and 5.5, respectively. As can be seen from both the Figures the mesospheric cooling at high-latitudes are quite evident for both major SSW events. The mesospheric warmings at mid-latitudes are also seen during both major SSW events.

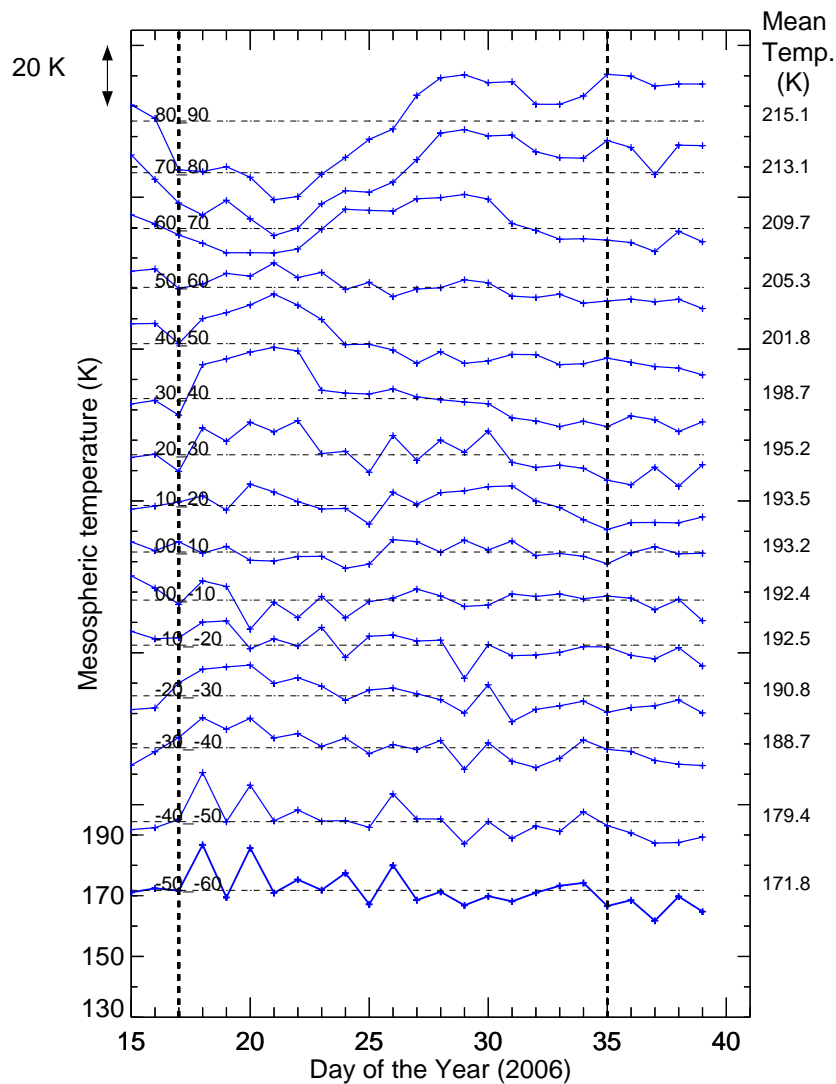
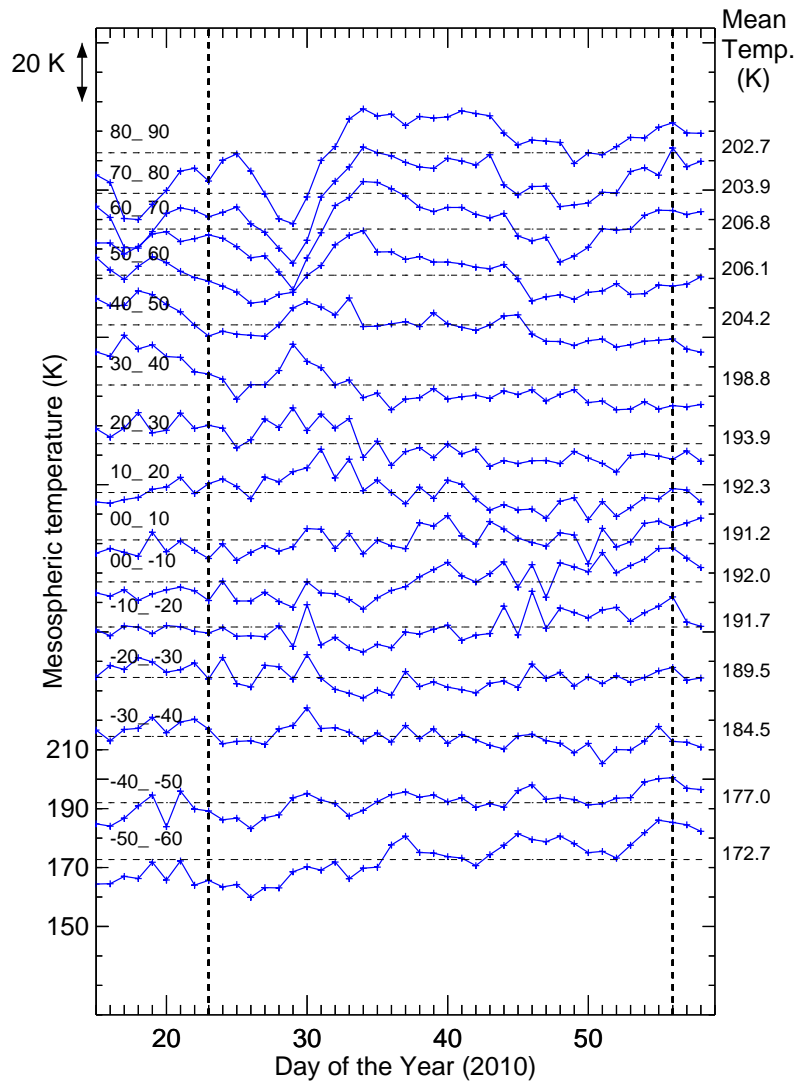


Figure 5.4: Similar to Figure 5.3 but for 2006 major SSW event.



**Figure 5.5:** Similar to Figure 5.3 but for 2010 major SSW event.

### 5.5.3 SABER Temperatures for 2011 and 2012 Minor SSW Events

Similar to Figure 5.3 the latitudinal variations of mesospheric temperatures for two minor SSW events of 2011 and 2012 are shown in Figures 5.6 and 5.7, respectively. As can be seen from Figures 5.6 and 5.7 the mesospheric coolings at high-latitudes are not as evident as seen during the major SSW events.



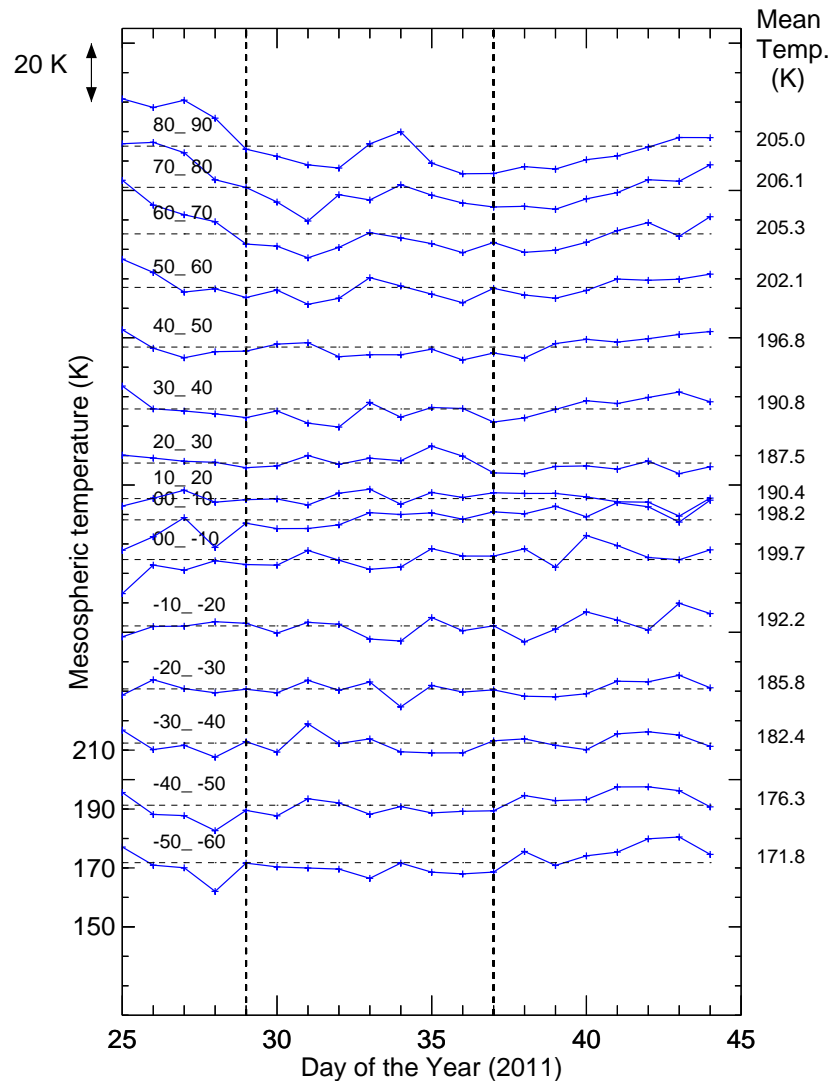


**Figure 5.6:** Similar to Figure 5.3 but for 2011 minor SSW event.

#### 5.5.4 SABER Temperatures for 2008 SSW Events

Similar to Figure 5.3 the latitudinal variations of mesospheric temperatures for 2008 SSW event are shown in Figure 5.8. As can be seen from Figure 5.2, 2008 SSW event consists of three minor and one major SSW events. Since 2008 SSW event is a prolonged one mesospheric cooling at high-latitudes even during minor events of 2008(I) and 2008(II) can be seen clearly.

It may be noted that the transitions from cooling to warming from high- to low-latitudes in the NH and SH occur with some finite time delay indicat-

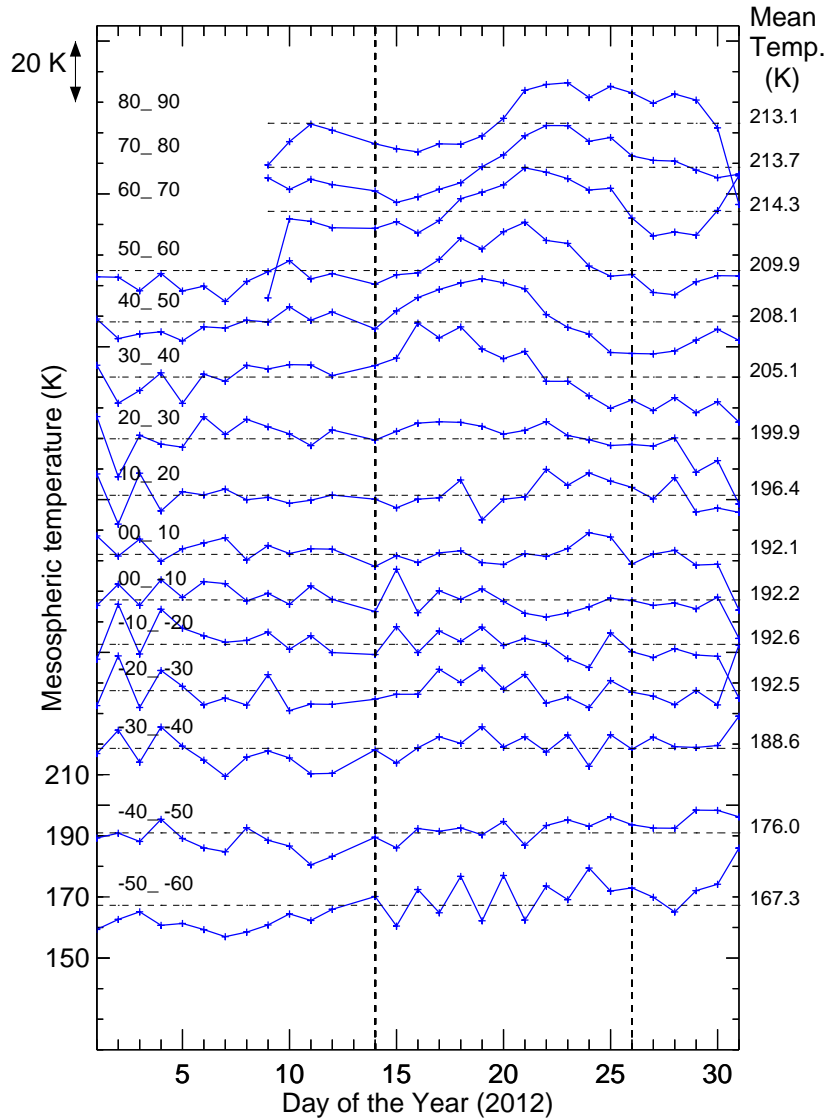


**Figure 5.7:** Similar to Figure 5.3 but for 2012 minor SSW event.

ing a physical transport of energy from high-latitudes in the NH to different latitudes extending to even those in the SH. Since the OSIRIS mesospheric temperatures are only available every other day and the data cadence for the SABER derived mesospheric temperatures are better. Therefore, further analysis has been carried out using SABER derived mesospheric temperatures. The observed latitudinal behaviour of the variability in the mesospheric temperatures has been characterized with respect to stratospheric temperatures poleward of  $60^{\circ}\text{N}$  at 10 hPa pressure level during SSW events and is explained

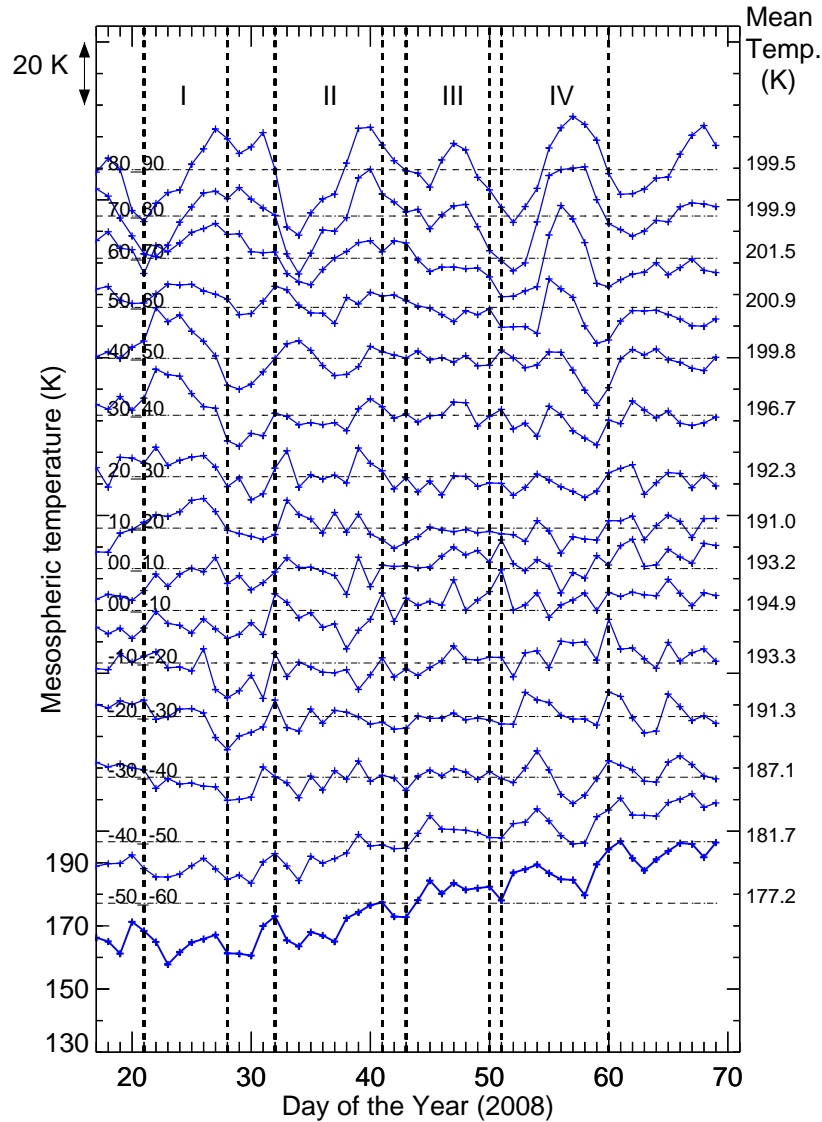


Figure 5.8: Similar to Figure 5.3 but for 2008 SSW event.

below.

### 5.5.5 Difference in Stratospheric vs Mesospheric Temperatures for 2009 and 2013 SSW Events

The mean mesospheric temperature for a given latitude range was obtained by averaging the temperature values over that latitude range for a week before and after the SSW period. The differences in mesospheric temperatures at

a given latitude range from the mean mesospheric temperatures ( $\Delta T_M$ ) are calculated for all the 15 latitude ranges for a given SSW duration. Similarly, the deviations in stratospheric temperatures ( $\Delta T_S$ ) from the mean value (calculated by averaging  $T_S$  over  $60^\circ$ – $90^\circ$ N for one week before and after the SSW event) are obtained using the MERRA dataset. As discussed earlier, there is a time delay in mesospheric response to the SSW events at high-latitudes that is different at different latitudes. Therefore, we have defined the post-SSW period as the one when the longitudinally averaged zonal wind at  $60^\circ$ N at 10 hPa pressure level for the major SSW events becomes close to zero. The SSW periods are summarized in Table 5.1 and are also shown by vertical dashed lines in Figure 5.2 for all the eleven SSW events considered in this study.

As seen in Figures 5.3a and 5.3b the mesospheric temperatures at NH high-latitudes show cooling up to  $60^\circ$ – $70^\circ$ N during the SSW event with different behaviour at other latitudes. Correlation analyses have been performed between  $\Delta T_S$  at high-latitude and  $\Delta T_M$  obtained at different latitudes to investigate their interrelationships, if any. Figures 5.9a and 5.9b show the result of such analyses for some chosen latitude ranges for the 2013 and 2009 major SSW events, respectively.

In Figure 5.9, the horizontal and vertical axes represent stratospheric temperature deviation,  $\Delta T_S$ , at high-latitude and mesospheric temperature difference,  $\Delta T_M$ , at different latitudes as discussed above, and each “+” symbol represents a day during the SSW period. The slopes and the correlation coefficient for each of the latitude ranges are also shown in the respective panels. The high-latitudes (panels (i) and (ii) of Figures 5.9a and 5.9b) show a negative slope which indicates that increase in stratospheric temperatures,  $\Delta T_S$ , is correlated with a decrease in mesospheric temperature,  $\Delta T_M$ , which is consistent with general understanding. It is clearly seen (panels (iii)) that for  $20^\circ$ – $30^\circ$ N latitude range  $\Delta T_M$  increases with increase in  $\Delta T_S$ , indicating a mesospheric heating with respect to stratospheric warming. For the  $0^\circ$ – $10^\circ$ N latitude range  $\Delta T_M$  decreases with increasing values of  $\Delta T_S$  (panels (iv)). These observa-

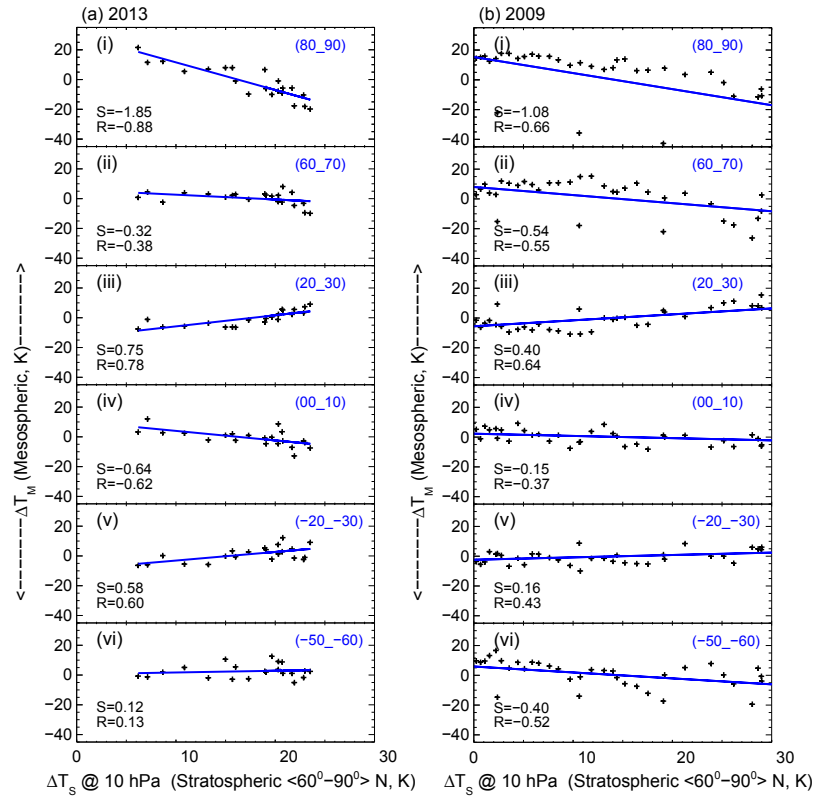


**Figure 5.9:** (a) Differences in SSW temperatures ( $\Delta T_S$ ) over  $60^\circ$ – $90^\circ$ N at 10 hPa pressure level vs difference in mesospheric temperatures ( $\Delta T_M$ ) for six selected latitude ranges for 2013 SSW event as derived from SABER datasets. (b) Similar plot as shown in Figure 5.9a but for 2009 SSW event.

tions show similar trends for all the major SSW events with different values of the slope for individual major SSW events. While the mesospheric cooling over high-latitudes during SSW has been reported in the literature, the excursions in the mesospheric temperatures over other latitudes as detailed here have not been reported before.

### 5.5.6 $\Delta T_S$ vs $\Delta T_M$ for Major and Minor SSW Events from SABER Data

The analyses relating the observed  $\Delta T_M$  at different latitudes with  $\Delta T_S$  at high-latitude as shown in Figure 5.9 for a few latitude ranges have been extended to all the 15 latitude ranges in Figure 5.10a. This Figure 5.10a includes

the three major SSW events of 2009, 2010, and 2013 as these were stronger and extended over a longer duration among the six major events considered in this study. Similarly, in Figure 5.10b the combined behaviour of  $\Delta T_M$  with respect to  $\Delta T_S$  for all five minor events at different latitude range is shown.

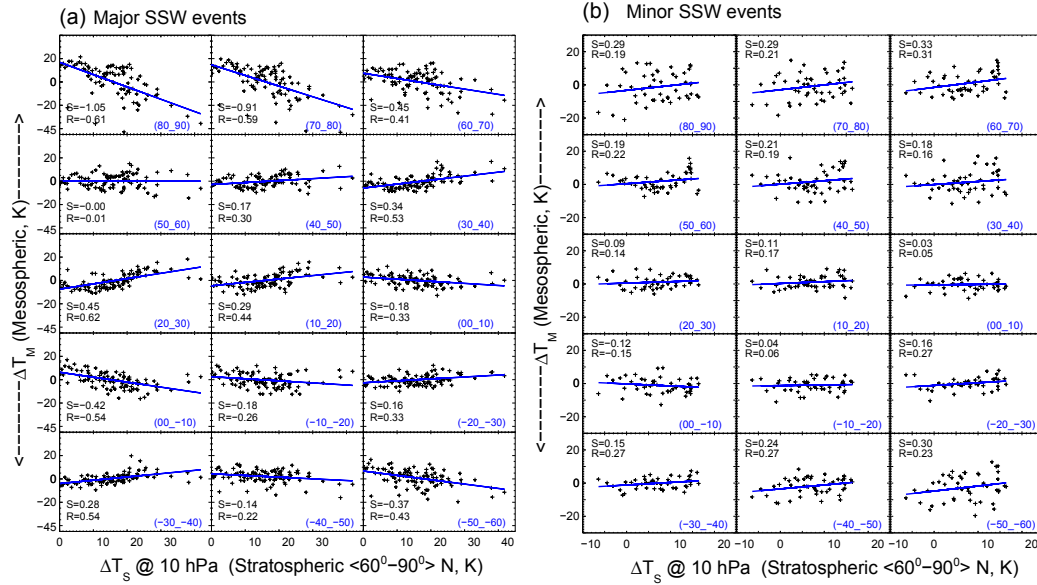


**Figure 5.10:** (a) Difference in SSW temperatures ( $\Delta T_S$ ) over  $60^{\circ}$ – $90^{\circ}$ N at 10 hPa pressure level vs difference in mesospheric temperatures ( $\Delta T_M$ ) at  $10^{\circ}$  latitude intervals as derived from SABER dataset from both the hemispheres for three major SSW events of 2009, 2010, and 2013 for the durations as shown in Table 5.1. The latitudinal coverage to derive  $\Delta T_M$  is shown in each plot in blue colour. The correlation coefficients (R) and the slopes (S) of the line are also shown in each sub-plot. A negative/positive slope with respect to an increase in  $\Delta T_S$  indicates mesospheric cooling/warming at that latitude range. (b) Similar plot as shown in Figure 5.10a but for all five minor SSW events as shown in Figure 5.2. A better correlation is noted for major SSW events as compared to the minor ones.

Each “+” symbol in Figures 5.10a and 5.10b corresponds to a day during SSW period. From these scatterplots, correlation analyses have been performed and the slopes of the best fit lines obtained. The correlation coefficients (R) between  $\Delta T_S$  and  $\Delta T_M$  together with the slope of the best fit lines (S) are shown in each of the subplots in Figures 5.10a and 5.10b. It is apparent from the mesospheric temperature behaviour as shown in Figures 5.3 to 5.8 that the transitions in temperature from high- to low-latitudes occur during

different days (DOY's as discussed above) and is a non-linear phenomenon. Therefore, the linear fits shown in Figure 5.10 are a first order approximation of the variability between  $\Delta T_S$  and  $\Delta T_M$ , and hence, show smaller 'R' values than expected for a linearly varying phenomena.

Nevertheless, the slopes obtained by these linear fits do provide a broad 'visual' picture of the mesospheric temperature variability at different latitudes with respect to the stratospheric temperature changes at high-latitudes during SSW events. The slope (S) is positive if R is positive and vice-versa. Thus, the slopes of the best fit lines indicate the effect of the stratospheric temperatures enhancement ( $\Delta T_S$ ) on the mesospheric temperature differences ( $\Delta T_M$ ) at different latitudes. As mentioned above, a negative/positive slope indicates that there is a cooling/warming in the mesosphere in that latitude region. It is seen from Figure 5.10a that the slope is negative to begin with in the NH high-latitude (mesospheric cooling) and gradually turns positive (mesospheric heating) in mid- to tropical-latitudes. At latitudes closer to the equator we see a small negative slope, which, after crossing the equatorial-latitudes, turns positive before again turning negative over SH high-latitudes. The change of slopes from -1.05 at 85°N farther away from equator as compared to -0.37 at 55°S, indicates that the latitudinal temperature behaviour is asymmetric, with respect to the equator. For major events (Figure 5.10a) it is seen that in the NH, mesospheric cooling is seen up to 65°N, and the peak in mesospheric heating occurs at 25°N. In the SH, the mesospheric warmings peak at ~35°S and change to mesospheric cooling at ~45°S. It may be noted that for major warming events (Figures 5.10a) there are stronger and systematic variations in the slopes as compared to the minor events (Figures 5.10b). For minor events the excursions of the slopes are in-and-around zero and the mesospheric cooling at the higher latitudes is not apparent. For both major and minor events, the SH mesospheric temperatures show smaller changes as compared to those in the NH.

### 5.5.7 $\Delta T_S$ vs $\Delta T_M$ for Major SSW events from SOFIE and OSIRIS Data

Using SOFIE data  $\Delta T_M$  was calculated in a similar way as was done for SABER data discussed in the previous section. Figure 5.11a shows  $\Delta T_S$  vs  $\Delta T_M$  scatterplot using SOFIE data, which includes all three major SSW events of 2009, 2010, and 2013. As can be seen in this Figure the mesosphere in the  $60^\circ$ – $80^\circ$  latitude range for both NH and SH shows mesospheric cooling during major SSW events, which is in accordance with the trends observed using SABER data (Figure 5.10a for the NH). The data from SOFIE extends the coverage by  $20^\circ$  latitude in the SH when compared with SABER.

As discussed earlier OSIRIS derived mesospheric temperatures are available from  $20^\circ$ – $85^\circ$ S.  $\Delta T_M$  values have been calculated for every  $10^\circ$  latitudinal intervals from  $80^\circ$ – $90^\circ$ S to  $20^\circ$ – $30^\circ$ S for 2009 and 2010 major SSW events and are shown in Figure 5.11b with respect to  $\Delta T_S$ . The trends at different latitudinal coverage are similar to those estimated by SABER (Figure 5.10a). However, there are minor differences in the values of slopes which could be due to the fact that the OSIRIS data are available for alternate days and data for 2013 SSW event are not included in Figure 5.11b. Nevertheless, OSIRIS provides data polewards of  $55^\circ$ S latitude which are not available from SABER and the values of slope show a somewhat constant behaviour polewards of  $55^\circ$ S. This is in contrast to the steep slopes in the NH and is understood to be a consequence of SSW being a NH phenomenon.

It is important to note that independently obtained mesospheric temperatures from satellites do show an increase in mesospheric temperatures over tropical- to mid- latitudes during several major SSW events. These add credence to the ground-based NIRIS measurements that first indicated the existence of such a feature during the major SSW event of 2013.



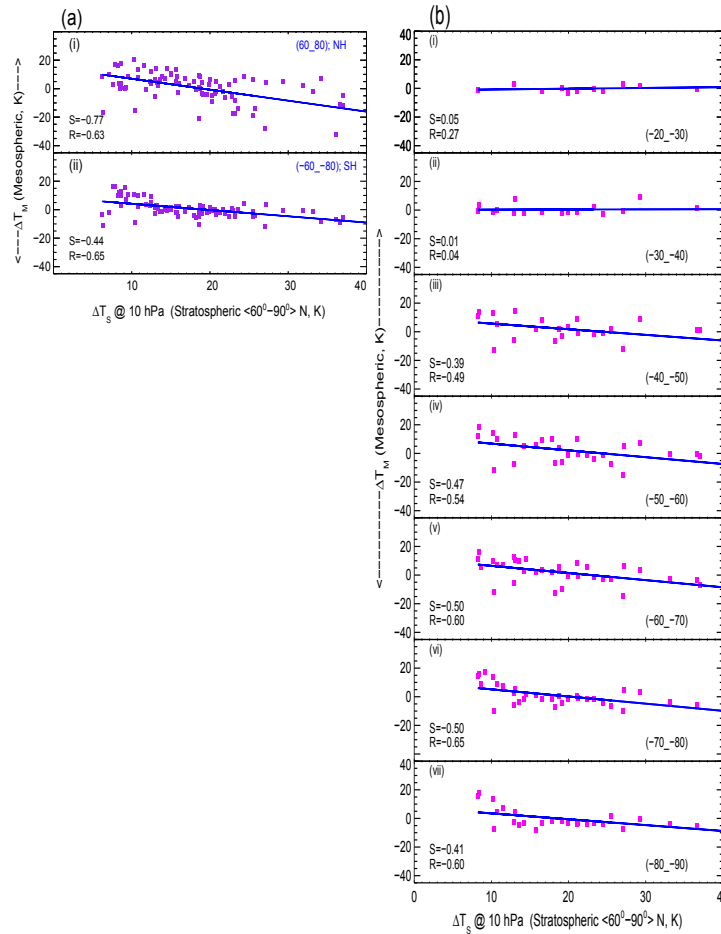


**Figure 5.11:** (a) Same as in Figure 5.9 but for SOFIE data at two latitudinal ranges in NH and SH for three major SSW events of 2009, 2010, and 2013 for the durations as shown in Table 5.1 combined together. The trends seen in this figure is in accordance with the one observed with the SABER data (Figure 5.10a). (b) Same as in Figure 5.9 but for OSIRIS data for two major SSW events of 2009 and 2010 for the durations as shown in Table 5.1. In spite of lower data cadence as seen in this figure compared to that as shown in Figure 5.10 from SABER data it is interesting to note that the trends are similar at different latitudinal ranges. As one move towards equator from SH polar latitudes the number of data points reduces. Also, OSIRIS data shows that the slopes remain constant poleward of  $55^\circ\text{S}$  during major SSW events.

### 5.5.8 Slope ( $\Delta T_M/\Delta T_S$ ) vs Geographic Latitude for Major and Minor SSW Events

To investigate the characteristic behaviour of individual events, plots such as those shown in Figure 5.10, have been made for each of the eleven events

considered in this study (plots not shown here) and the variations in their slopes with respect to latitude are plotted in Figures 5.12a and 5.12b for major and minor events, respectively.

The geographic latitudes marked in Figure 5.12 are the midpoints of the 15 latitude ranges. The values of the slopes as obtained from Figures 5.10a and 5.10b are also shown as green coloured lines in Figures 5.12a and 5.12b respectively, to indicate the typical behaviour for major and minor SSW events. From Figure 5.12a it is clear that the NH polar mesosphere shows a cooling trend during major SSW events and this can even extend to  $50^{\circ}\text{N}$  (as seen for the 2009 SSW event). However, as one moves equatorwards the mid-latitude mesospheric temperature shows warming effects. Closer to the equator, the mesospheric temperatures again indicate cooling. This trend is similar for all the major SSW events studied. Away from the equator towards mid-latitudes in the SH, the mesospheric temperatures again start increasing. A transition from mesospheric warming to mesospheric cooling is observed beyond the mid-latitudes in the SH as well, similar to the NH.

SABER measured mesospheric temperature data in the SH are available only up to  $55^{\circ}\text{S}$  but, from OSIRIS data (Figure 5.6b) it can be seen that the mesospheric cooling further poleward of  $55^{\circ}\text{S}$  is constant. The mesospheric warmings in the NH seem to be greater and distributed over a larger spatial extent when compared with the SH. This is seen in the characteristic “double-humped” structure in the slopes ( $\Delta T_M/\Delta T_S$ ) with respect to the latitude during major SSW events. During minor SSW events (Figure 5.12b) no significant trend is noticed in the slopes derived for different geographic latitudes. During one of the minor SSW events of 2008 (marked as 2008\_III in Figure 5.12b) the high-latitudes show warming, which turns to a cooling in the mid-latitude in NH, whereas, high-latitude over SH shows warmings. During the 2012 minor event the mid-latitude NH shows significant mesospheric warming. These two seem anomalous and at present, the reason for which is unknown.

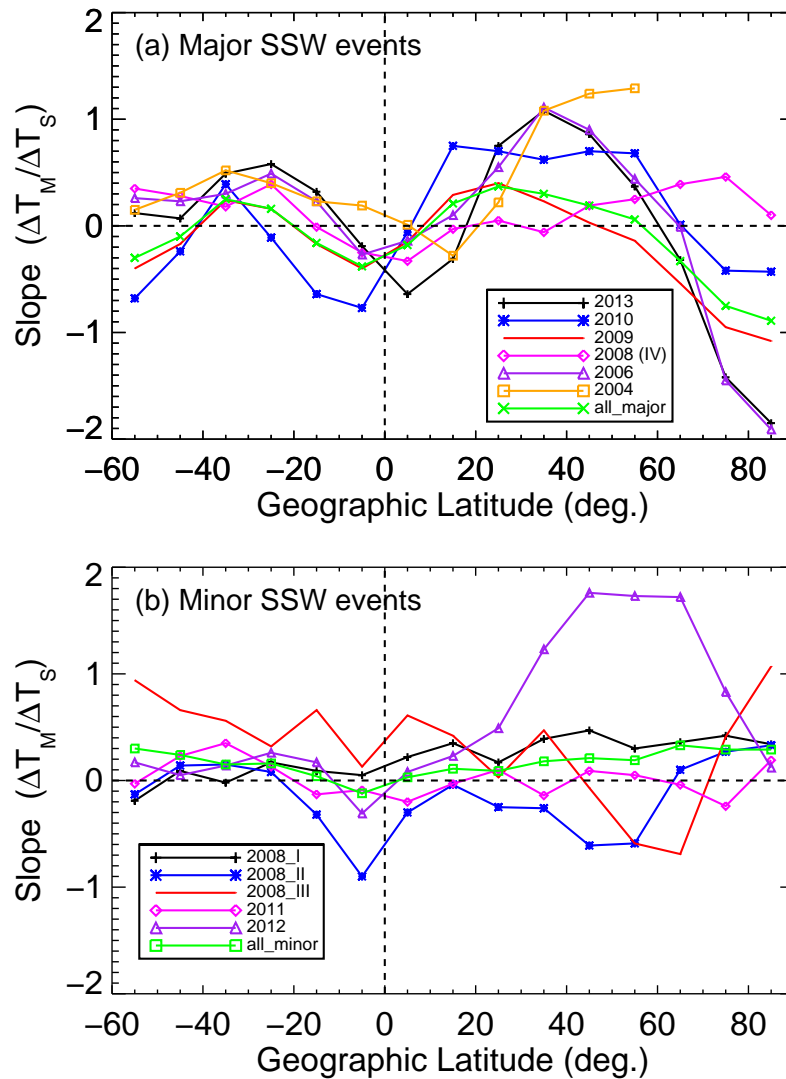


**Figure 5.12:** (a) Slopes ( $\Delta T_M / \Delta T_S$ ) derived from analyses for each individual major SSW event using SABER data with respect to the geographic latitude (Figure 5.10 shows the slopes obtained for three major events combined together). Six major SSW events occurred during northern hemisphere winter months during 2004, 2006, 2008, 2009, 2010, and 2013. For the 2004 SSW period, the SABER derived mesospheric temperature data are available only up to  $60^\circ\text{N}$  latitude. (b) Similar plots as in Figure 5.12a but for the minor SSW events, which occurred during northern hemisphere winter months for the three minor events of 2008, 2011, and 2012. The green curves in Figures 5.12a and 5.12b show the slope values as obtained from Figures 5.10a and 5.10b. One may note the “double-humped” structure in temperature ratios with respect to the geographic equator during major SSW events. For minor events, on an average, the slopes are in-and-around-zero.

### 5.5.9 Relationship between SRL with $T_{Smax}$ and D with $T_{Smax}$

As can be seen from Figure 5.12, the variation in slopes at different latitudes for different SSW events are organized in a similar fashion. However, to investigate if there is any order in this behaviour with respect to the strength of SSW events, the latitudes of slope reversals from negative to positive values in both hemispheres as a function of peak stratospheric (at 10 hPa pressure level) temperature ( $T_{Smax}$ ) poleward of  $60^\circ\text{N}$  are shown in Figure 5.13a. The slope reversal latitudes (SRL) from positive to negative or vice-versa are very distinct during major SSW events (as shown in Figure 5.12a). However, slope reversals are not so evident during minor SSW events (Figure 5.12b). For the minor SSW events the latitudes of slope reversals are found by considering either the latitudes at which the slope is zero, or latitudes of trend reversals, if the slope does not cross the zero level. The result of correlation between the peak SSW temperatures ( $T_{Smax}$ ) and the latitudes of slope reversals in both hemispheres in the poleward directions are plotted in Figure 5.13a.

Red/blue colour shows the best fit plots for NH/SH together with the R values. From Figure 5.13a we find a linear relationship ( $R=-0.66$ ) between  $T_{Smax}$  and the SRL in the poleward side of NH. It indicates that when  $T_{Smax}$  is large, the mesospheric cooling over high-latitudes in the NH extends further towards mid-latitudes. From the same figure we find a linear relationship ( $R=-0.45$ ) between  $T_{Smax}$  and the SRL in the poleward side of SH. The R values are better in the NH as compared to the SH, possibly due to the fact that the SSW events are NH phenomena. The relationship between SRL in term of SSW strengths,  $T_{Smax}$ , in the poleward direction in both NH and SH considering all the eleven SSW events (including major and minor) are given below:

$$SRL_{NH} = -1.3 \times T_{Smax} + 380.67 \quad (5.1)$$

$$SRL_{SH} = -0.44 \times T_{Smax} + 151.25 \quad (5.2)$$

where  $T_{Smax}$  and SRL are measured in K and degrees, respectively. Equatorward transition latitudes have not been considered as they are not structured as that of poleward transitions.

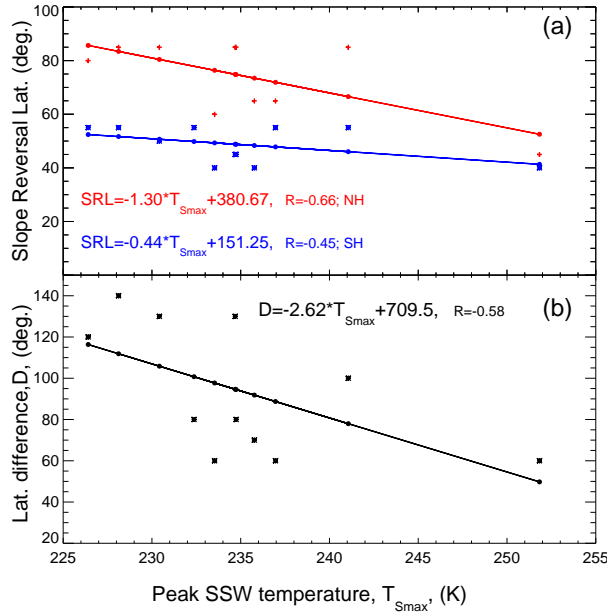


**Figure 5.13:** (a) Peak stratospheric temperature achieved over  $60^{\circ}$ – $90^{\circ}$ N latitude at 10 hPa pressure level for all the eleven selected SSW events are plotted with slope reversal latitudes in the poleward direction in both hemispheres. (b) Latitudinal difference in peak slopes of the “double-humped” structure as obtained from Figure 5.12 with respect to the peak stratospheric temperatures for all eleven SSW events are shown, which indicate an inverse relationship between them.

From Figure 5.12 it is seen that the latitudes of peak positive slopes in both the hemispheres are different for all the SSW events considered as the strengths of each event differs from the other.  $T_{Smax}$  during an SSW event and the difference,  $D$ , between the latitudes of peak positive slopes in the NH and SH (of the “double-humped structure”) are plotted in Figure 5.13b for all the eleven SSW events. It is interesting to note that when  $T_{Smax}$  is greater, the latitudinal difference between NH and SH maxima in mesospheric warming at mid-latitudes decreases and vice versa.  $T_{Smax}$  and  $D$  are related linearly as:

$$D = -2.62 \times T_{Smax} + 709.5 \quad (5.3)$$

where  $T_{Smax}$  and  $D$  are measured in K and degrees, respectively.

Thus, through the characterization in this work, it can be appreciated that just by the knowledge of  $T_{Smax}$  (which is available in the public domain) a first order approximation on the behaviour of latitudinal mesospheric temperature structure can be made. From equations 5.1 and 5.2 the poleward transition latitudes of mesospheric temperature (from cooling to heating) can be obtained in both the hemispheres. From equation 5.3 the latitudinal difference,  $D$ , between the peak positive slopes can be obtained for any SSW event. It is known that the mesospheric temperature behaviour and its variation with respect to latitudes (and altitude) is a non-linear process. In all the characterizations attempted in this study, the behaviour of mesospheric temperature has been made considering only a linear approximation. Nevertheless, this empirical characterization is an attempt to obtain a broad picture of mesospheric temperature variation with respect to latitudes during SSW events.

### 5.5.10 SABER vs CIRA Temperatures Comparison During SSW Events

Figure 5.14a shows SABER derived mean mesospheric temperature during the periods shown in Table 5.1 for all the eleven SSW events as a function of geographic latitudes and are compared with the COSPAR International Reference Atmosphere (CIRA-86) model [*Fleming et al. (1990)*]. CIRA model outputs provide an estimation of temperature, zonal wind, and geopotential/geometric height as a function of altitude from 0–120 km altitudes in the latitudinal range of 80°S to 80°N.

The CIRA zonal mean temperatures have been averaged for the altitude range from 84.8 to 89.2 km and over 10° latitudes for the months of January and February and are shown as the red dashed line in Figure 5.14a together

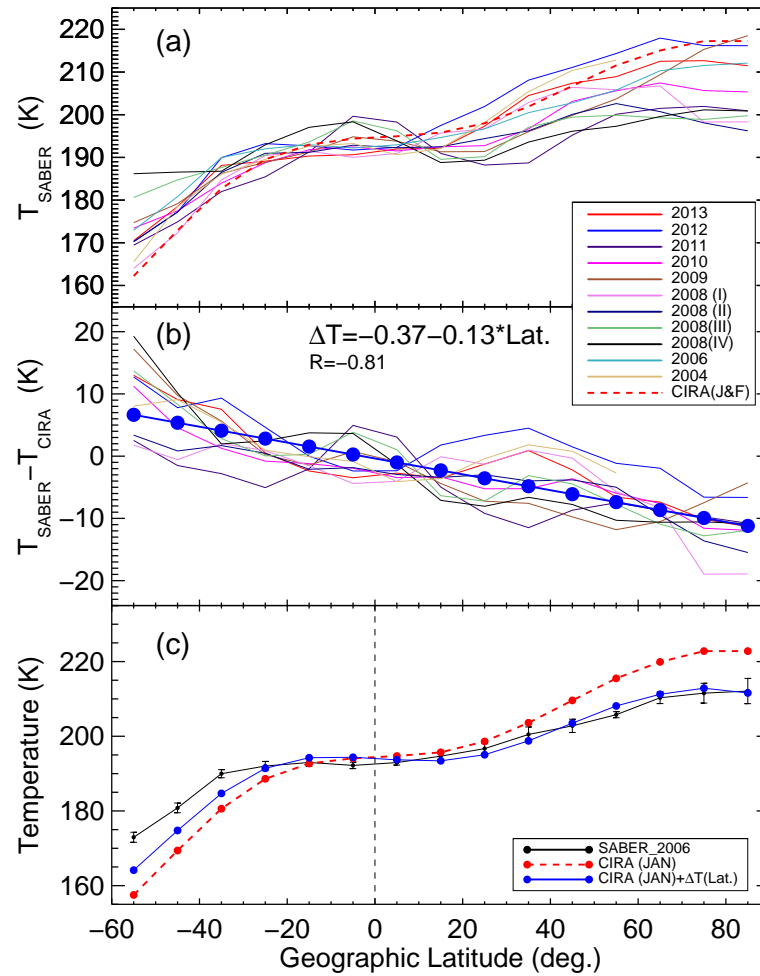


**Figure 5.14:** (a) Daily mean mesospheric temperatures derived from SABER data during SSW periods for all the eleven SSW events considered in this study with respect to geographic equator are shown. CIRA-86 derived temperature values averaged for the month of January and February are also shown in dashed red line. The CIRA-86 temperatures seem to overestimate/underestimate the values in the NH/SH. (b) The differences in the SABER measured and CIRA-86 estimated mesospheric temperature for the month in which the SSW event occurred (except for the 2006 event which is used for validation as shown in panel c) are shown. A linear relationship is also seen between  $T$  and geographic latitude. (c) SABER measured mesospheric temperatures (black) for the event of January 2006 (see Table 5.1) together with the standard error, CIRA-86 derived mesospheric temperatures (dashed red) for the month of January are shown. It may be noted that the CIRA estimated temperature values are higher/lower in the NH/SH high-latitude than the SABER measured value. The blue line shows the temperature values after accounting for the corrections as arrived at in equation 5.4 (shown in Figure 5.14b) in the CIRA derived values, which shows a better agreement with the SABER measured values.

with all the eleven SSW events that occurred during these two months. The temperature difference ( $\Delta T$ ) between the observed (SABER) and the modelled (CIRA-86) values for the months in which SSW events occurred have been obtained and are shown in Figure 5.14b as a function of geographic latitude. As seen from Figures 5.14a and 5.14b the CIRA-86 seems to overestimate the mesospheric temperatures in the NH and underestimate them in the SH, especially over high-latitudes. As it can be seen from Figure 5.14b, extreme  $\Delta T$  values can be up to +20 K in the SH and -20 K in the NH showing a large range, which is due to the fact that different SSW events have different background conditions. A linear relationship has been obtained between the correction to be applied,  $\Delta T$  (in K) and geographic latitudes (in degrees) as shown below:

$$\Delta T = -0.13 \times Lat - 0.37 \quad (5.4)$$

It should be mentioned here that in obtaining the equation 5.4 we have not considered the 2006 event as that event is used to validate this relationship. In Figure 5.14c the SABER derived mesospheric temperature values for the year 2006 are shown as a black curve together with the standard error. As it can be seen, the standard error is larger at NH polar latitudes showing large range of variations in mesospheric temperatures during SSW period. The red dashed curve shows the zonal mean mesospheric temperatures as obtained from CIRA model for the month of January (averaged for the altitude range from 84.8 to 89.2 km and over  $10^\circ$  latitudes). To these CIRA values, the latitude dependent correction shown by equation 5.4 has been applied and the resulting values are shown by the blue coloured line. It can be seen that the correction shown by equation 5.4 brings the CIRA modelled mesospheric temperature values closer to the SABER measured values.



## 5.6 Summary and Conclusion

Ground-based spectroscopic measurement of mesospheric rotational temperatures from O<sub>2</sub> and OH bands originating at 94 km and 87 km altitudes as obtained from NIRIS from Gurushikhar (24.6°N, 72.8°E), a low-latitude location in India, showed enhanced temperatures (compared to their monthly mean values) during the SSW event of January 2013. This led to a wider investigation to understand mesospheric temperature changes over low-latitudes and to characterize the behaviour of mesospheric temperature variation as a function of geographic latitude during an SSW period with respect to the stratospheric (at 10 hPa pressure level) temperatures over high-latitude (60°–90°N). In this regard, SABER derived mesospheric temperatures for eleven SSW events which occurred during 2004–2013 have been considered. OSIRIS and SOFIE measured mesospheric temperatures are also considered, when available, and both showed broad similarity in their behaviour with SABER data. A detailed analyses of all of these independent measurements has revealed that there is a mesospheric heating over tropical- to mid- latitudes, more so in the NH, during major SSW events. All the major SSW events studied showed well-known mesospheric cooling over NH high-latitudes. Closer to the equatorial-latitudes the mesospheric heating turns into cooling and again turns to heating over mid-latitudes in the SH before turning to cooling over the SH high-latitude regions.

The “double-humped” structure in the mesospheric to stratospheric temperature ratios ( $\Delta T_M/\Delta T_S$ ) vs latitude is very clear during major SSW events with two crests over tropical- to mid-latitudes and a trough over the geographic equator. Mesospheric temperatures during minor events do not show formation of such “double-humped” structure. A relationship between slope reversal latitudes (SRL) towards poleward side in terms of the peak SSW temperature,  $T_{Smax}$ , is obtained for both hemispheres [ $SRL_{NH} = -1.3 \times T_{Smax} + 380.67$  and  $SRL_{SH} = -0.44 \times T_{Smax} + 151.25$ ]. Further, it is found that the latitu-

dinal difference (D) between the two crests in the observed “double-humped” structure is related linearly with  $T_{Smax}$  as:  $D = -2.62 \times T_{Smax} + 709.5$ .

It is also found that the CIRA-86 derived mesospheric temperatures overestimate the values in the NH and underestimate them in the SH as compared to the SABER measured temperatures, which is more prominent at the higher latitudes. A linear relationship has been obtained between the differences in SABER and CIRA derived mesospheric temperatures ( $\Delta T$ ) as a function of latitude  $\Delta T = -0.13 \times \text{Lat} - 0.37$ ; wherein ten SSW events have been considered. Thus, with just the knowledge of the peak SSW temperatures,  $T_{Smax}$ , the mesospheric temperature behaviour with respect to latitude can be determined and their magnitudes with respect to latitudes can be found by applying the above mentioned correction to the CIRA model temperatures. Moreover, from the results presented in this study, a hitherto unknown aspect of the relationship between stratospheric temperature at high-latitude and mesospheric temperatures at different latitudes has been brought to light. These results strongly support the interactions in stratospheric-mesospheric coupling and high- to low-latitude coupling of mesosphere lower thermosphere region, especially during SSW events.

# Chapter 6

## Summary and Scope for Future Work

### 6.1 Summary and Conclusions

The major objectives of this thesis were to investigate various interactions of the Earth's upper atmosphere using ground- and satellite-based observations to understand the scientific objective that were set in Chapter 1. These goals were accomplished by studying the waves and oscillations present in the MLT region, solar and atmospheric influences in the MLT region, wave dynamical coupling of atmospheres, mesospheric wave dynamics during cyclones, mesospheric temperature inversion and their possible causes, and latitudinal coupling of the atmosphere during SSW events. Nightglow emission intensities at multiple wavelengths, which emanate from different altitudes of the Earth's upper atmosphere and OH and O<sub>2</sub> derived mesospheric temperatures along with some supplementary data have been used to address the scientific objectives used in this thesis.

As discussed in Chapter 1, the Earth's atmosphere is capable of sustaining various timescales atmospheric waves. These atmospheric waves are generated through disturbances in the lower atmosphere e.g., convection, orography, or

thunderstorm and while propagating upwards to the upper atmosphere they carry energy with them. They mostly break in the MLT region, deposit their momentum, which causes changes in the winds and temperatures that can induce large-scale circulations at those altitudes. Measurement of airglow emission intensities is an important tool to understand the dynamical process in the Earth's atmosphere since they respond to the density of the reactants involved in the photochemical processes which in turn is affected by these atmospheric waves. In addition to these waves, the Earth's upper atmosphere is also influenced by the incoming solar radiation. In this thesis, the effect of these two forcing on the upper atmosphere, in general, and MLT region, in particular has been studied under varying geophysical conditions. This Chapter summarizes the main findings of the present thesis work that has been achieved using ground- and satellite-based observations.

The present work has added new long-term and high cadence measurements on the multi-wavelength nightglow emission intensities and temperatures using in-house built spectrograph (NIRIS) and photometer (CMAP). NIRIS provides spectral images of OH(6-2) Meinel and O<sub>2</sub> atmospheric bands simultaneously, from which nocturnal variation in nightglow emission intensities and temperatures corresponding to 87 and 94 km altitudes are derived. CMAP provides nocturnal variation of nightglow emission intensities of Na (589.0 and 589.6 nm), OI 557.7 nm, and OI 630.0 nm emission emanating from peak altitudes of about 92, 100, and 250 km. The details of NIRIS and CMAP and procedure for retrieval of nightglow emission intensities and temperatures are described in Chapter 2. In addition to these ground-based measurements, mesospheric temperatures from SABER, SOFIE, and OSIRIS, OLR from Kalpana-1, and stratospheric temperatures and winds from MERRA have been used in this study.

The important findings that have emerged based on the scientific objectives set in Chapter 1 (section 1.11) is summarized below:

### 6.1.1 Atmospheric Waves and Coupling in the Earths Upper Atmosphere

The results dealing with the vertical coupling of the atmospheres are discussed in Chapter 3 and Chapter 4. Some of the main results that emerged from these studies are:

1. In Chapter 3, we have seen that OH(6-2) and O<sub>2</sub>(0-1) band intensities and corresponding temperatures shows presence of short-timescale (of gravity wave regime) variations. These GW periodicities have been obtained from the nocturnal variations of these parameters for all the individual nights for three years (2013-2015) of NIRIS observations from Gurushikhar, Mount Abu. There are total of 437 nights of observation from which GW periods ranging from 10 min to 3 hours are obtained. These periods showed significantly different behaviour in intensities and temperatures. In intensities it has been observed that GWs show the presence of the 2 h and 15 to 20 min of periodicities in over 23% and 10% of nights, respectively. However, temperatures show 2 h and 20 to 60 min periodicities for over 18% and 12% of nights, and do not show significant number of periodicities smaller than 15 min. These GW periodicities neither show any seasonal dependence nor any solar activity dependence in their occurrence rate or in the time periods [*Singh and Pallamraju (2017b)*].
2. In Chapter 4, we have addressed the question related to the vertical coupling of the atmosphere during cyclone Nilofar which developed in the Arabian sea during 25–31 October 2014. In this study, data obtained from NIRIS, CMAP, and Kalpana-1 satellite have been used. Using these multiple data sets obtained for 26 October 2014, not only was it demonstrated that the Earths atmosphere is coupled through gravity waves that were generated due to the cyclone Nilofar but also different

gravity wave parameters that can be present during cyclonic storms ( $\tau$ ,  $c_h$ ,  $\lambda_h$ ,  $c_z$ ,  $\lambda_z$ , and  $\theta_v$ ) were derived [*Singh and Pallamraju (2016)*].

### 6.1.2 Solar Influences in the MLT Nightglow Emissions and Temperatures

From the production mechanisms that give rise to the O<sub>2</sub> and OH band emissions in the mesosphere (Chapter 1) it was reported that the O<sub>2</sub> and OH nightglow emission intensities are related to the concentrations of atomic oxygen and ozone and hence, to the ultra-violet (UV) solar energy input that is responsible for their photochemical production. Therefore, these emissions are expected to show variations with the UV solar energy input and hence, with solar activity. From the NIRIS derived nightglow emission intensities and temperatures from over three years (2013-2015) of observations we have seen presence of waves and oscillations of both the origins i.e., atmospheric and solar. Spectral analyses of these O<sub>2</sub> and OH intensities and the corresponding temperatures showed statistically significant periodicities of around 150, 195, 270, and 420 days. The solar variations in this duration (F10.7 cm solar flux and SSN) also displayed some of the periodicities (150, 190, 245, 380, and 410 days) that are present in atmospheric oscillations as well thereby revealing a clear evidence of influence of solar activity on the mesospheric airglow emissions and temperatures. In addition to these common periods, the O<sub>2</sub> and OH intensities also showed periods around 84, 95, and 122 days which are due to the seasonal variations [*Singh and Pallamraju (2017b)*].

### 6.1.3 Mesospheric Temperature Inversions and their Possible Sources

NIRIS observations of around one year (2013) show that, in general, T(O<sub>2</sub>) is lower than T(OH) which is the synoptic behaviour of Earth's atmospheric mesospheric temperature structure. However, it was also observed that there

are several occasions when  $T(\text{O}_2)$  is greater than  $T(\text{OH})$  indicating the formation of mesospheric temperature inversion layers. Based on the statistical study, some preliminary results were discussed in Chapter 4, which indicate that such formation of MTIs could be more probable due to chemical heating in the mesosphere [*Singh and Pallamraju (2017a)*].

#### 6.1.4 Global Mesospheric Temperatures During SSW Events

In Chapter 5, we have shown how mesospheric temperatures varies latitudinally during SSW events. NIRIS derived mesospheric temperatures from Gurushikhar showed enhanced temperatures (compared to their monthly mean values) during the SSW event of January 2013. This led to a wider investigation to understand mesospheric temperature changes over various latitudes and to characterize the behaviour of mesospheric temperature variation as a function of geographic latitude during SSW periods with respect to the stratospheric (at 10 hPa pressure level) temperatures over high-latitude ( $60^\circ$ – $90^\circ\text{N}$ ). In this work, SABER, SOFIE, and OSIRIS derived mesospheric temperatures have been considered. Detailed analyses revealed that there exists mesospheric heating over tropical- to mid- latitudes, more so in the NH, during major SSW events. All the major SSW events studied showed well-known mesospheric cooling over NH high-latitudes. Closer to the equatorial-latitudes the mesospheric heating turns into cooling and again turns to heating over mid-latitudes in the SH before turning to cooling over the SH high-latitude regions. The “double-humped” structure in the mesospheric to stratospheric temperature ratios ( $\Delta T_M/\Delta T_S$ ) vs latitude is very clear during major SSW events with two crests over tropical- to mid-latitudes and a trough over the geographic equator. Mesospheric temperatures during minor events do not show formation of such “double-humped” structure. It is also found that the CIRA-86 derived mesospheric temperatures overestimate the values in the NH and underestimate

them in the SH as compared to the SABER measured temperatures, which is more prominent at the higher latitudes. These results strongly support the existence of stratospheric-mesospheric coupling and high- to low-latitude coupling of mesosphere lower thermosphere region, especially during SSW events [*Singh and Pallamraju (2015)*].

### 6.1.5 Techniques to Measure MLT Nightglow Emission Intensities and Temperatures

1. **NIRIS:** In order to derive nocturnal variations in nightglow emission intensities and corresponding temperatures representing the emission altitudes of 87 and 94 km, spectrographic technique is used. Using this technique a grating spectrograph called NIRIS, Near InfraRed Imaging Spectrograph, is developed which uses  $1200 \text{ lines mm}^{-1}$  grating as the dispersing element, a  $1024 \times 1024$  pixels thermoelectrically cooled CCD camera and has a large field-of-view (FOV) of  $80^\circ$  along the slit orientation [*Singh and Pallamraju (2017a)*]. The details of NIRIS are given in Chapter 2. Most of the results obtained in this thesis work have been obtained using data obtained from NIRIS that has been operating since 2013 in an automated mode from PRL's optical aeronomy observatory at Gurushikhar, Mount Abu.
2. **CMAF:** A CCD-based Multi-wavelength Airglow Photometer (CMAF) is developed in-house to study the nightglow emission intensities which emanate from mesosphere lower thermosphere (MLT) region of the Earth's upper atmosphere. In contrast to NIRIS, CMAF works on the photometric technique, which uses narrow bandwidth interference filters having full width at half maxima of 0.3 nm and these are mounted in a temperature stabilized filter wheel. The temperature controlled filter wheel can house five filters at a time enabling near-simultaneous measurements at five different airglow emissions. A Software is developed in-house to control



various operations of CMAP such as, CCD and filter wheel operations in a pre-defined mode, filter wheel temperature monitoring, which is programmed in such a way to provide CCD images in FITS format [*Phadke et al. (2014)*]. The details of CMAP which deals with the optical design, fabrication of different components, and derivation of nightglow emission intensities from CMAP is discussed in Chapter 2.

## 6.2 Scope for Future Work

This work provided significant contribution in the understanding of the vertical and latitudinal couplings in the MLT region under varying atmospheric conditions. The results presented in this thesis have underlined some promising areas especially those related to the MLT region and raised the numerous issues for further investigations. This opens up further scope for interesting scientific and technical studies some of them are ongoing and some can be followed in the future.

1. Understanding the mesospheric temperature inversions and their possible causes is very important in order to comprehensively model the atmospheric dynamics. From the existing NIRIS data, work is ongoing to understand these aspects.
2. We have described in Chapter 2 that how by making use of large FOV information of NIRIS the meridional scale sizes are derived. Similar method can be adopted to derive the zonal scale sizes by orienting NIRIS in the east-west direction. From the existing data, studies are ongoing to understand the observed variations in the scale sizes at two altitudes and to understand their behaviour in different seasons and solar activity levels.
3. The characteristics of vertical wave propagation during strong convective storms has been presented in this thesis. However, the vertical propa-

gation characteristics of waves during normal conditions is still not well known experimentally. These kind of continuous observations with good temporal and spatial resolution as presented in this thesis will help to address these scientific issues.

4. A detailed investigation of tidal and planetary waves in the MLT region is being studied, which will enhance our understanding of the coupling processes in those time scales.
5. NIRIS provides simultaneous measurement of nightglow emission intensities and temperatures using OH(6-2) Meinel and O<sub>2</sub>(0-1) atmospheric band spectra. The brightest emission of OH nightglow occurring in between 1.4  $\mu\text{m}$  to 1.8  $\mu\text{m}$  which includes OH(2-0), OH(3-1), and OH(4-2) vibrational rotational transitions. Historically the observation of these brighter emissions are sparse and more difficult since they require the use of InGaAs photodiode arrays. However, with the commercially available InGaAs arrays now it is becoming possible to make instruments which can provide observation of these vibrational bands with required resolution and efficiency. We are in the process to develop such an instrument which will provide OH(3-1) rotational line spectra to derive nightglow emission intensities and temperatures. The OH(3-1) band is around 70 times brighter than the OH(6-2) band and is less affected by the water vapour absorption. Also at these longer wavelengths as the scattering is less in comparison to near infrared with such an instrument it should also be possible to obtain data during even full-moon nights (when the moon is not directly in the instruments FOV).
6. Since OH rotational temperatures can be derived using different methods. Different simulation exercises are planned to assess the differences between various methods of mesospheric temperature determination.
7. Although the mesospheric emission intensities show a clear solar activity

dependence, the effect of solar activity on to the mesospheric temperatures are ambiguous on short time scales. This needs further investigation with respect to the wave amplitudes versus viscous drag effects that may prevent its presence in temperatures.

===== end =====



# Bibliography

- Alexander, M., J. R. Holton, and D. R. Durran (1995), The gravity wave response above deep convection in a squall line simulation, *J. Atmos. Sci.*, *52*(12), 2212–2226. [20](#), [131](#)
- Alexander, M., et al. (2010), Recent developments in gravity-wave effects in climate models and the global distribution of gravity-wave momentum flux from observations and models, *Q. J. R. Meteorol. Soc.*, *136*(650), 1103–1124. [17](#)
- Alexander, M. J. (1996), A simulated spectrum of convectively generated gravity waves: Propagation from the tropopause to the mesopause and effects on the middle atmosphere, *J. Geophys. Res.*, *101*(D1), 1571–1588. [154](#)
- Alexander, M. J., and R. A. Vincent (2000), Gravity waves in the tropical lower stratosphere: A model study of seasonal and interannual variability, *J. Geophys. Res.*, *105*(D14), 17,983–17,993. [20](#)
- Alexander, M. J., J. H. Beres, and L. Pfister (2000), Tropical stratospheric gravity wave activity and relationships to clouds, *J. Geophys. Res.*, *105*(D17), 22,299–22,309. [20](#)
- Anandarao, B., and R. Raghavarao (1979), Gravity waves and tidal winds in the equatorial thermosphere, in *Space Research XIX*, pp. 263–266. [35](#)
- Andrews, D. G., J. R. Holton, and C. B. Leovy (1987), *Middle atmosphere dynamics*, 40, Academic press, London. [3](#), [4](#), [6](#), [11](#), [12](#), [26](#), [28](#), [29](#), [128](#)

- Azeem, S., E. Talaat, G. Sivjee, H.-L. Liu, and R. Roble (2005), Observational study of the 4-day wave in the mesosphere preceding the sudden stratospheric warming events during 1995 and 2002, *Geophys. Res. Lett.*, *32*(15). [167](#)
- Bacmeister, J. T. (1993), Mountain-wave drag in the stratosphere and mesosphere inferred from observed winds and a simple mountain-wave parameterization scheme, *J. Atmos. Sci.*, *50*(3), 377–399. [19](#)
- Bacmeister, J. T., M. R. Schoeberl, L. R. Lait, P. A. Newman, and B. Gary (1990), Small-scale waves encountered during AASE, *Geophys. Res. Lett.*, *17*(4), 349–352. [19](#)
- Baker, D. J., and A. Stair Jr (1988), Rocket measurements of the altitude distributions of the hydroxyl airglow, *Physica Scripta*, *37*(4), 611–622. [42](#), [171](#)
- Baldwin, M., et al. (2001), The quasi-biennial oscillation, *Rev. Geophys.*, *39*(2), 179–229. [xv](#), [26](#), [27](#)
- Barth, C. A. (1964), Three-body reactions., *Ann. Geophys.*, *20*, 182–196. [39](#)
- Barth, C. A., and A. F. Hildebrandt (1961), The 5577 Å airglow emission mechanism, *J. Geophys. Res.*, *66*(3), 985–986. [39](#)
- Bates, D. (1992), Nightglow emissions from oxygen in the lower thermosphere, *Planet. Space Sci.*, *40*(2-3), 211–221. [39](#)
- Bates, D. R., and M. Nicolet (1950), The photochemistry of atmospheric water vapor, *J. Geophys. Res.*, *55*(3), 301–327. [42](#)
- Batista, P., H. Takahashi, and B. Clemesha (1994), Solar cycle and the QBO effect on the mesospheric temperature and nightglow emissions at a low latitude station, *Adv. Space Res.*, *14*(9), 221–224. [104](#)

- Becker, E. (2012), Dynamical control of the middle atmosphere, *Space Sci. Rev.*, 168(1-4), 283–314. [4](#)
- Beer, T. (1974), Atmospheric waves, *New York, Halsted Press; London, Adam Hilger, Ltd., 1974. 315 p.* [12](#), [16](#), [153](#)
- Bittner, M., D. Offermann, H.-H. Graef, M. Donner, and K. Hamilton (2002), An 18-year time series of OH rotational temperatures and middle atmosphere decadal variations, *J. Atmos. Solar Terr. Phys.*, 64(8), 1147–1166. [61](#)
- Blix, T., E. Thrane, and Ø. Andreassen (1990), In situ measurements of the fine-scale structure and turbulence in the mesosphere and lower thermosphere by means of electrostatic positive ion probes, *J. Geophys. Res.*, 95(D5), 5533–5548. [35](#)
- Brasseur, G. P., and S. Solomon (2006), *Aeronomy of the middle atmosphere: chemistry and physics of the stratosphere and mesosphere, 3rd ed.*, vol. 32, Dordrecht, Netherlands. [17](#)
- Bretthorst, G. L. (2013), *Bayesian spectrum analysis and parameter estimation, in Lecture Notes in Statistics*, vol. 48, Springer, New York. [83](#), [144](#)
- Burrage, M., R. Vincent, H. Mayr, W. Skinner, N. Arnold, and P. Hays (1996), Long-term variability in the equatorial middle atmosphere zonal wind, *J. Geophys. Res.*, 101(D8), 12,847–12,854. [26](#)
- Chamberlain, J. W. (1961), *Physics of the Aurora and Airglow: International Geophysics Series*, vol. 2, Academic Press, New York. [36](#)
- Chapman, S. (1939), Notes on Atmospheric Sodium., *Astrophys. J.*, 90, 309–316. [41](#)
- Chapman, S., and R. S. Lindzen (1970), *Atmospheric tides: thermal and gravitational*, D. Reidel, Dordrecht, Holland. [22](#)

- Charney, J. G., and P. G. Drazin (1961), Propagation of planetary-scale disturbances from the lower into the upper atmosphere, *J. Geophys. Res.*, *66*(1), 83–109. [24](#), [128](#)
- Chowdhury, P., D. Choudhary, S. Gosain, and Y.-J. Moon (2015), Short-term periodicities in interplanetary, geomagnetic and solar phenomena during solar cycle 24, *Astrophysics and Space Science*, *356*(1), 7–18. [109](#)
- Clemesha, B., H. Takahashi, D. Simonich, D. Gobbi, and P. Batista (2005), Experimental evidence for solar cycle and long-term change in the low-latitude MLT region, *J. Atmos. Solar Terr. Phys.*, *67*(1), 191–196. [104](#)
- Coxon, J., and S. Foster (1982), Rotational analysis of hydroxyl vibration-rotation emission bands: Molecular constants for OH, *Can. J. Phys.*, *60*(1), 41–48. [63](#)
- Dalgarno, A., and F. Smith (1962), The thermal conductivity and viscosity of atomic oxygen, *Planet. Space Sci.*, *9*(1-2), 1–2. [153](#)
- Daubechies, I. (1990), The wavelet transform, time-frequency localization and signal analysis, *IEEE Trans. Inform. Theory*, *36*(5), 961–1005. [86](#)
- Daubechies, I. (1992), *Ten lectures on wavelets*, Society for Industrial and Applied Mathematics. [85](#)
- Deepa, V., G. Ramkumar, M. Antonita, K. Kumar, and M. Sasi (2006), Vertical propagation characteristics and seasonal variability of tidal wind oscillations in the MLT region over Trivandrum (8.5°N, 77°E): First results from SKiYMET meteor radar, *Ann. Geophys.*, *24*(11), 2877–2889. [22](#)
- Dewan, E., R. Picard, R. O’Neil, H. Gardiner, J. Gibson, J. Mill, E. Richards, M. Kendra, and W. Gallery (1998), MSX satellite observations of thunderstorm-generated gravity waves in mid-wave infrared images of the upper stratosphere, *Geophys. Res. Lett.*, *25*(7), 939–942. [20](#)



- Dhaka, S., B. K. Murthy, O. Nagpal, R. R. Rao, M. Sasi, and S. Sundaresan (1995), A study of equatorial waves in the Indian zone, *J. Atmos. Solar Terr. Phys.*, *57*(11), 1189–1202. [128](#)
- Drob, D. P., et al. (2015), An update to the Horizontal Wind Model (HWM): The quiet time thermosphere, *Earth and Space Science*, *2*(7), 301–319. [151](#)
- Dunkerton, T. J. (1982), Theory of the mesopause semiannual oscillation, *J. Atmos. Sci.*, *39*(12), 2681–2690. [25](#)
- Dunkerton, T. J. (1997), The role of gravity waves in the quasi-biennial oscillation, *J. Geophys. Res.*, *102*(D22), 26,053–26,076. [26](#)
- Ejiri, M., K. Shiokawa, T. Ogawa, K. Igarashi, T. Nakamura, and T. Tsuda (2003), Statistical study of short-period gravity waves in OH and OI nightglow images at two separated sites, *J. Geophys. Res.*, *108*(D21). [114](#)
- Farge, M. (1992), Wavelet transforms and their applications to turbulence, *Annu. Rev. Fluid Mech.*, *24*(1), 395–458. [87](#)
- Fleming, E. L., S. Chandra, J. Barnett, and M. Corney (1990), Zonal mean temperature, pressure, zonal wind and geopotential height as functions of latitude, *Adv. Space Res.*, *10*(12), 11–59, doi:10.1016/0273-1177(90)90386-E. [192](#)
- Forbes, J. M. (1995), Tidal and planetary waves, in the upper mesosphere and lower thermosphere: A review of experiment and theory, edited by R.M. Johnson and T.L. Killeen, *Geophys. Monogr. Ser.*, *87*, 67–87. [6](#), [22](#), [23](#), [128](#)
- Forbes, J. M. (2000), Wave coupling between the lower and upper atmosphere: case study of an ultra-fast Kelvin Wave, *J. Atmos. Solar Terr. Phys.*, *62*(17), 1603–1621. [24](#)

- Forbes, J. M., and G. V. Groves (1987), Diurnal propagating tides in the low-latitude middle atmosphere, *J. Atmos. Solar Terr. Phys.*, *49*(2), 153–164. [22](#)
- Forbes, J. M., G. Jun, and M. Saburo (1991), On the interactions between gravity waves and the diurnal propagating tide, *Planet. Space Sci.*, *39*(9), 1249–1257. [128](#)
- Forbes, J. M., X. Zhang, S. E. Palo, J. Russell, C. J. Mertens, and M. Mlynczak (2009), Kelvin waves in stratosphere, mesosphere and lower thermosphere temperatures as observed by TIMED/SABER during 2002–2006, *Earth, planets and space*, *61*(4), 447–453. [24](#)
- Fovell, R., D. Durran, and J. Holton (1992), Numerical simulations of convectively generated stratospheric gravity waves, *J. Atmos. Sci.*, *49*(16), 1427–1442. [131](#)
- French, W., G. Burns, K. Finlayson, P. Greet, R. Lowe, and P. Williams (2000), Hydroxyl (6/2) airglow emission intensity ratios for rotational temperature determination, *Ann. Geophys.*, *18*(10), 1293–1303. [61](#)
- Fritts, D. C., and M. J. Alexander (2003), Gravity wave dynamics and effects in the middle atmosphere, *Rev. Geophys.*, *41*(1), doi:10.1029/2001RG000106. [16](#), [19](#), [20](#), [114](#), [117](#), [130](#), [131](#), [135](#)
- Fritts, D. C., and G. D. Nastrom (1992), Sources of mesoscale variability of gravity waves. Part II: Frontal, convective, and jet stream excitation, *J. Atmos. Sci.*, *49*(2), 111–127. [19](#), [131](#)
- Fritts, D. C., S. L. Vadas, K. Wan, and J. A. Werne (2006), Mean and variable forcing of the middle atmosphere by gravity waves, *J. Atmos. Solar Terr. Phys.*, *68*(3), 247–265. [130](#)
- Fritz, S., and S. Soules (1970), Large-scale temperature changes in the stratosphere observed from Nimbus III, *J. Atmos. Sci.*, *27*(7), 1091–1097. [30](#)

- Fukao, S., T. Sato, N. Yamasaki, R. M. Harper, and S. Kato (1980), Radar measurement of tidal winds at stratospheric heights over Arecibo, *J. Atmos. Sci.*, *37*(11), 2540–2544. [22](#)
- Garcia, R., D. Marsh, D. Kinnison, B. Boville, and F. Sassi (2007), Simulation of secular trends in the middle atmosphere, 1950–2003, *J. Geophys. Res.*, *112*(D9), 1950–2003, doi:10.1029/2006JD007485. [8](#)
- Garcia, R. R., T. J. Dunkerton, R. S. Lieberman, and R. A. Vincent (1997), Climatology of the semiannual oscillation of the tropical middle atmosphere, *J. Geophys. Res.*, *102*(D22), 26,019–26,032. [25](#), [59](#)
- García-Comas, M., et al. (2008), Errors in Sounding of the Atmosphere using Broadband Emission Radiometry (SABER) kinetic temperature caused by non-local-thermodynamic-equilibrium model parameters, *J. Geophys. Res.*, *113*(D24), doi:10.1029/2008JD010105. [77](#)
- Gavrilov, N., A. Manson, and C. Meek (1995), Climatological monthly characteristics of middle atmosphere gravity waves (10 min–10 h) during 1979–1993 at Saskatoon, *Ann. Geophys.*, *13*(3), 285–295. [20](#)
- Geisler, J., and R. E. Dickinson (1976), The five-day wave on a sphere with realistic zonal winds, *J. Atmos. Sci.*, *33*(4), 632–641. [23](#)
- Geller, M. A. (1983), Dynamics of the middle atmosphere, *Space Sci. Rev.*, *34*(4), 359–375. [7](#)
- Gordley, L. L., et al. (2009), The solar occultation for ice experiment, *J. Atmos. Solar Terr. Phys.*, *71*(3), 300–315, doi:10.1016/j.jastp.2008.07.012. [78](#)
- Greet, P., W. French, G. Burns, P. Williams, R. Lowe, and K. Finlayson (1997), OH (6–2) spectra and rotational temperature measurements at Davis, Antarctica, *Ann. Geophys.*, *16*(1), 77–89. [61](#)

- Gregory, J., and A. Manson (1975), Winds and wave motions to 110 km at mid-latitudes, III, Response of mesospheric and thermospheric winds to major stratospheric warmings, *J. Atmos. Sci.*, *32*, 1676-1681. [30](#)
- Grimsdell, A. W., M. J. Alexander, P. T. May, and L. Hoffmann (2010), Model study of waves generated by convection with direct validation via satellite, *J. Atmos. Sci.*, *67*(5), 1617–1631. [131](#)
- Groves, G. (1972), Annual and semi-annual zonal wind components and corresponding temperature and density variations, 60–130 km, *Planet. Space Sci.*, *20*(12), 2099–2112. [25](#)
- Gurubaran, S., and R. Rajaram (1999), Long-term variability in the mesospheric tidal winds observed by MF Radar over Tirunelveli (8.7°N, 77.8°E), *Geophys. Res. Lett.*, *26*(8), 1113–1116. [34](#)
- Gurubaran, S., S. Sridharan, T. Ramkumar, and R. Rajaram (2001), The mesospheric quasi-2-day wave over Tirunelveli (8.7°N), *J. Atmos. Solar Terr. Phys.*, *63*(10), 975–985. [128](#)
- Hagan, M., R. Roble, and J. Hackney (2001), Migrating thermospheric tides, *J. Geophys. Res.*, *106*(A7), 12,739–12,752. [22](#)
- Haley, C. S., and I. C. McDade (2002), Procedures for recovering mesospheric and stratospheric temperatures from OSIRIS scattered-sunlight measurements, *Can. J. Phys.*, *80*(4), 435–442. [77](#)
- Hargreaves, J. K. (1992), *The solar-terrestrial environment: an introduction to geospace-the science of the terrestrial upper atmosphere, ionosphere, and magnetosphere*, Cambridge University Press. [21](#)
- Hauchecorne, A., M. L. Chanin, and R. Wilson (1987), Mesospheric temperature inversion and gravity wave breaking, *Geophys. Res. Lett.*, *14*(9), 933–936. [158](#)

- Hernández, G. (1988), *Fabry-perot interferometers*, 3, Cambridge University Press. [71](#)
- Hines, C. O. (1960), Internal atmospheric gravity waves at ionospheric heights, *Can. J. Phys.*, *38*(11), 1441–1481. [16](#), [91](#), [146](#), [149](#), [150](#)
- Hines, C. O. (1974), *The upper atmosphere in motion*, Am. Geophys. Union, Washington, DC. [xv](#), [16](#), [49](#)
- Hirota, I. (1978), Equatorial waves in the upper stratosphere and mesosphere in relation to the semiannual oscillation of the zonal wind, *J. Atmos. Sci.*, *35*(4), 714–722. [24](#), [25](#), [27](#)
- Hirota, I. (1979), Kelvin waves in the equatorial middle atmosphere observed by the Nimbus 5. SCR, *J. Atmos. Sci.*, *36*(2), 217–222. [24](#)
- Hocke, K. (1998), Phase estimation with the Lomb-Scargle periodogram method, *Ann. Geophys.*, *16*(3), 356–358. [82](#)
- Hocking, W. (1999), Temperatures Using radar-meteor decay times, *Geophys. Res. Lett.*, *26*(21), 3297–3300. [34](#)
- Hoffmann, P., W. Singer, D. Keuer, W. Hocking, M. Kunze, and Y. Murayama (2007), Latitudinal and longitudinal variability of mesospheric winds and temperatures during stratospheric warming events, *J. Atmos. Solar Terr. Phys.*, *69*(17), 2355–2366. [30](#)
- Holton, J. R. (1980), The dynamics of sudden stratospheric warmings, *Annu. Rev. Earth Planet. Sci.*, *8*(1), 169–190. [29](#)
- Holton, J. R. (1983), The influence of gravity wave breaking on the general circulation of the middle atmosphere, *J. Atmos. Sci.*, *40*(10), 2497–2507. [10](#)

- Horinouchi, T., T. Nakamura, and J.-i. Kosaka (2002), Convectively generated mesoscale gravity waves simulated throughout the middle atmosphere, *Geophys. Res. Lett.*, *29*(21), doi:10.1029/2002GL016069. [20](#)
- Horne, J. H., and S. L. Baliunas (1986), A prescription for period analysis of unevenly sampled time series, *Astrophys. J.*, *302*, 757–763. [80](#), [84](#), [89](#), [90](#), [91](#)
- Jasperson, W., G. Nastrom, and D. Fritts (1990), Further study of terrain effects on the mesoscale spectrum of atmospheric motions, *J. Atmos. Sci.*, *47*(8), 979–987. [19](#)
- Karlsson, B., H. Kőrnic, and J. Gumbel (2007), Evidence for interhemispheric stratosphere-mesosphere coupling derived from noctilucent cloud properties, *Geophys. Res. Lett.*, *34*(16), doi:10.1029/2007GL030282. [30](#)
- Karlsson, B., C. McLandress, and T. G. Shepherd (2009), Inter-hemispheric mesospheric coupling in a comprehensive middle atmosphere model, *J. Atmos. Solar Terr. Phys.*, *71*(3), 518–530. [30](#)
- Kelley, M., M. Larsen, C. LaHoz, and J. McClure (1981), Gravity wave initiation of equatorial spread F: A case study, *J. Geophys. Res.*, *86*(A11), 9087–9100. [4](#)
- Kim, Y. H., C. Lee, J.-K. Chung, J.-H. Kim, and H.-Y. Chun (2010), Seasonal variations of mesospheric gravity waves observed with an airglow all-sky camera at Mt. Bohyun, Korea (36°N), *J. Astron. Sp. Sci.*, *27*(3), 181–188, doi:10.5140/JASS.2010.27.3.181. [114](#)
- Kőrnic, H., and E. Becker (2010), A simple model for the interhemispheric coupling of the middle atmosphere circulation, *Adv. Space Res.*, *45*(5), 661–668. [30](#)
- Krasovskij, V., and N. Šefov (1965), Airglow, *Space Sci. Rev.*, *4*(2), 176–198. [49](#)

- Kumar, K. K., G. Ramkumar, and S. Shelbi (2007), Initial results from SKiYMET meteor radar at Thumba (8.5°N, 77°E): 1. Comparison of wind measurements with MF spaced antenna radar system, *Radio Sci.*, *42*(6), doi:10.1029/2006RS003551. [34](#)
- Labitzke, K. (1972), Temperature changes in the mesosphere and stratosphere connected with circulation changes in winter, *J. Atmos. Sci.*, *29*(4), 756–766. [28](#), [166](#)
- Labitzke, K. (1981), Stratospheric-mesospheric midwinter disturbances: A summary of observed characteristics, *J. Geophys. Res.*, *86*(C10), 9665–9678. [28](#), [166](#)
- Labitzke, K. G., and H. Van Loon (1999), *The stratosphere: phenomena, history, and relevance*, Springer-Verlag, New York. [29](#)
- Lakshmi Narayanan, V., and S. Gurubaran (2013), Statistical characteristics of high frequency gravity waves observed by OH airglow imaging from Tirunelveli (8.7°N), *J. Atmos. Sci.*, *92*, 43–50, doi:10.1016/j.jastp.2012.09.002. [114](#)
- Lakshmi Narayanan, V., S. Gurubaran, and K. Emperumal (2010), Airglow imaging observations of small-scale structures driven by convective instability in the upper mesosphere over Tirunelveli (8.7 °N), *J. Geophys. Res.*, *115*(D19). [20](#)
- Lane, T. P., R. D. Sharman, T. L. Clark, and H.-M. Hsu (2003), An investigation of turbulence generation mechanisms above deep convection, *J. Atmos. Sci.*, *60*(10), 1297–1321, doi:10.1175/1520-0469(2003)60<1297:AIOTGM>2.0.CO;2. [20](#)
- Larsen, M. (2002), Winds and shears in the mesosphere and lower thermosphere: Results from four decades of chemical release wind measurements, *J. Geophys. Res.*, *107*(A8), doi:10.1029/2001JA000218. [35](#)

- Laskar, F. I., and D. Pallamraju (2014), Does sudden stratospheric warming induce meridional circulation in the mesosphere thermosphere system?, *J. Geophys. Res.*, *119*(12), 10,133–10,143, doi:10.1002/2014JA020086. [167](#)
- Laskar, F. I., D. Pallamraju, T. V. Lakshmi, M. A. Reddy, B. Pathan, and S. Chakrabarti (2013), Investigations on vertical coupling of atmospheric regions using combined multiwavelength optical dayglow, magnetic, and radio measurements, *J. Geophys. Res.*, *118*(7), 4618–4627. [128](#)
- Laskar, F. I., D. Pallamraju, and B. Veenadhari (2014), Vertical coupling of atmospheres: dependence on strength of sudden stratospheric warming and solar activity, *Earth, Planets and Space*, *66*(1), 94, doi:10.1186/1880-5981-66-94. [166](#)
- Laskar, F. I., D. Pallamraju, B. Veenadhari, T. V. Lakshmi, M. A. Reddy, and S. Chakrabarti (2015), Gravity waves in the thermosphere: Solar activity dependence, *Adv. Space Res.*, *55*(6), 1651–1659. [104](#), [128](#)
- Lehmacher, G., R. Goldberg, F. Schmidlin, C. Croskey, J. Mitchell, and W. Swartz (1997), Electron density fluctuations in the equatorial mesosphere: Neutral Turbulence or plasma instabilities?, *Geophys. Res. Lett.*, *24*(13), 1715–1718. [35](#)
- Levoy, C. (1964), Simple models of thermally driven mesospheric circulation, *J. Atmos. Sci.*, *21*, 327–341. [10](#)
- Li, Q., J. Xu, J. Yue, W. Yuan, and X. Liu (2011), Statistical characteristics of gravity wave activities observed by an OH airglow imager at Xinglong, in northern China, *Ann. Geophys.*, *29*(8), 1401–1410. [122](#)
- Lin, Y.-L. (2007), *Mesoscale dynamics*, Cambridge University Press, Cambridge. [xv](#), [13](#)
- Lindzen, R. S. (1981), Turbulence and stress owing to gravity wave and tidal breakdown, *J. Geophys. Res.*, *86*(C10), 9707–9714. [10](#)



- Liu, H.-L., and R. Roble (2002), A study of a self-generated stratospheric sudden warming and its mesospheric–lower thermospheric impacts using the coupled TIME-GCM/CCM3, *J. Geophys. Res.*, 107(D23). 30
- Lomb, N. R. (1976), Least-squares frequency analysis of unequally spaced data, *Astrophys. Space Sci.*, 39(2), 447–462. 80, 81, 107, 116
- London, J. (1980), *Radiative energy sources and sinks in the stratosphere and mesosphere*, 703 pp., Proc of the NATO Advanced Institute on Atmospheric Ozone, A.C. Aikin, ed., U.S. Dept. of Transportation, FAAEE8020, FAA, Washington, D.C., USA. xv, 6, 7
- López-González, M., et al. (2004), Seasonal variations of  $O_2$  atmospheric and  $OH(6-2)$  airglow and temperature at mid-latitudes from SATI observations, *Ann. Geophys.*, 22(3), 819–828. 109
- Lübken, F.-J. (1992), On the extraction of turbulent parameters from atmospheric density fluctuations, *J. Geophys. Res.*, 97(D18), 20,385–20,395. 35
- Lübken, F.-J. (1997), Seasonal variation of turbulent energy dissipation rates at high latitudes as determined by in situ measurements of neutral density fluctuations, *J. Geophys. Res.*, 102(D12), 13,441–13,456. 35
- Macleod, H. (2001), Thin Film Optical Filters, *Institute of Physics Publishing*, 3rd edition. 71
- Madden, R. A. (1979), Observations of large-scale traveling Rossby waves, *Rev. Geophys.*, 17(8), 1935–1949, doi:10.1029/RG017i008p01935. 128
- Mahakur, M., A. Prabhu, A. Sharma, V. Rao, S. Senroy, R. Singh, and B. Goswami (2013), A high-resolution outgoing longwave radiation dataset from Kalpana-1 satellite during 2004–2012, *Curr. Sci.*, pp. 1124–1133. 78
- Makhlouf, U., E. Dewan, J. Isler, and T. Tuan (1990), On the importance of the purely gravitationally induced density, pressure, and temperature variations

- in gravity waves: Their application to airglow observations, *J. Geophys. Res.*, *95*(A4), 4103–4111. [121](#)
- Manson, A., C. Meek, Y. Luo, W. Hocking, J. MacDougall, D. Riggin, D. Fritts, and R. Vincent (2003), Modulation of gravity waves by planetary waves (2 and 16 d): observations with the North American-Pacific MLT-MFR radar network, *J. Atmos. Solar Terr. Phys.*, *65*(1), 85–104. [128](#)
- Marshall, B., L. Deaver, R. Thompson, L. Gordley, M. McHugh, M. Hervig, and J. Russell III (2011), Retrieval of temperature and pressure using broadband solar occultation: SOFIE approach and results, *Atmos. Meas. Tech.*, *4*(5), 893–907, doi:10.5194/amt-4-893-2011. [78](#)
- Matsuno, T. (1970), Vertical propagation of stationary planetary waves in the winter Northern Hemisphere, *J. Atmos. Sci.*, *27*(6), 871–883. [28](#)
- Matsuno, T. (1971), A dynamical model of the stratospheric sudden warming, *J. Atmos. Sci.*, *28*(8), 1479–1494. [28](#), [29](#), [30](#), [166](#)
- McDade, I. (1998), The photochemistry of the MLT oxygen airglow emissions and the expected influences of tidal perturbations, *Adv. Space Res.*, *21*(6), 787–794. [39](#)
- McInturff, R. M. (1978), Stratospheric warmings: Synoptic, dynamic and general-circulation aspects, *NASA Ref. Publ.*, p. 1017. [28](#), [166](#)
- McIntyre, M. E. (1982), How well do we understand the dynamics of stratospheric warmings?, *J. Meteorol. Soc. Jpn.*, *60*(1), 37–65. [29](#)
- McLandress, C., and W. Ward (1994), Tidal/gravity wave interactions and their influence on the large-scale dynamics of the middle atmosphere: Model results, *J. Geophys. Res.*, *99*(D4), 8139–8155. [22](#)
- McLandress, C., and S. P. Zhang (2007), Satellite observations of mean winds

- and tides in the lower thermosphere: 1. Aliasing and sampling issues, *J. Geophys. Res.*, *112*(D21). [22](#)
- McLandress, C., M. J. Alexander, and D. L. Wu (2000), Microwave Limb Sounder observations of gravity waves in the stratosphere: A climatology and interpretation, *J. Geophys. Res.*, *105*(D9), 11,947–11,967. [20](#), [22](#)
- McLennan, J., and G. Shrum (1925), On the Origin of the Auroral Green Line 5577 angstrom, and Other Spectra Associated with the Aurora Borealis, *Proc. R. Soc. Lond. Series A*, *A108*, 501–512. [39](#)
- Meinel, I. (1950), OH Emission Bands in the Spectrum of the Night Sky., *Astrophys. J.*, *111*, 555. [42](#)
- Meriwether, J. W. (1989), A review of the photochemistry of selected nightglow emissions from the mesopause, *J. Geophys. Res.*, *94*(D12), 14,629–14,646. [42](#)
- Meriwether, J. W., and C. S. Gardner (2000), A review of the mesosphere inversion layer phenomenon, *J. Geophys. Res.*, *105*(D10), 12,405–12,416. [31](#), [158](#)
- Meriwether, J. W., and A. J. Gerrard (2004), Mesosphere inversion layers and stratosphere temperature enhancements, *Rev. Geophys.*, *42*(3). [xv](#), [4](#), [5](#), [31](#), [32](#), [158](#)
- Meriwether, J. W., and M. G. Mlynczak (1995), Is chemical heating a major cause of the mesosphere inversion layer?, *J. Geophys. Res.*, *100*(D1), 1379–1387. [31](#), [158](#)
- Meriwether Jr, J. (1984), Ground based measurements of mesosphere temperatures by optical means, *Middle Atmosphere Handbook*, *13*, 1–18. [61](#), [62](#), [63](#)

- Mertens, C. J., M. G. Mlynczak, M. López-Puertas, P. P. Wintersteiner, R. Picard, J. R. Winick, L. L. Gordley, and J. M. Russell (2001), Retrieval of mesospheric and lower thermospheric kinetic temperature from measurements of  $CO_2$  15  $\mu\text{m}$  Earth Limb Emission under non-LTE conditions, *Geophys. Res. Lett.*, 28(7), 1391–1394. [67](#), [77](#), [169](#)
- Mies, F. H. (1974), Calculated vibrational transition probabilities of  $OH(X^2\Pi)$ , *J. Mol. Spect.*, 53(2), 150–188. [62](#), [63](#)
- Mukherjee, B., and B. Ramanamurty (1972), High level warmings over a tropical station, *Monthly Weather Review*, 100, 674–681. [167](#)
- Mukhtarov, P., et al. (2007), Large-scale thermodynamics of the stratosphere and mesosphere during the major stratospheric warming in 2003/2004, *J. Atmos. Solar Terr. Phys.*, 69(17), 2338–2354. [30](#)
- Murphy, D., W. French, and R. Vincent (2007), Long-period planetary waves in the mesosphere and lower thermosphere above Davis, Antarctica, *J. Atmos. Solar Terr. Phys.*, 69(17), 2118–2138. [23](#)
- Murtagh, D., G. Witt, J. Stegman, I. McDade, E. Llewellyn, F. Harris, and R. Greer (1990), An assessment of proposed  $O(^1S)$  and  $O_2(b^1\Sigma_g^+)$  nightglow excitation parameters, *Planet. Space Sci.*, 38(1), 43–53. [39](#), [171](#)
- Murtagh, D., et al. (2002), An overview of the Odin atmospheric mission, *Can. J. Phys.*, 80(4), 309–319. [77](#)
- Murthy, B. K. (1998), Middle atmosphere-upper atmosphere coupling, *Proc. Ind. Nat. Sc. Acad.*, 64(3), 303–313. [13](#)
- Myrabø, H., C. Deehr, and B. Lybekk (1984), Polar cap OH airglow rotational temperatures at the mesopause during a stratospheric warming event, *Planet. Space Sci.*, 32(7), 853–856. [30](#)

- Nakamura, T., A. Higashikawa, T. Tsuda, and Y. Matsushita (1999), Seasonal variations of gravity wave structures in OH airglow with a CCD imager at Shigaraki, *Earth, planets and space*, 51(7-8), 897–906. [114](#)
- Nappo, C. J. (2013), *An introduction to atmospheric gravity waves*, Academic Press, California. [16](#), [18](#)
- Nastrom, G., D. Fritts, and K. Gage (1987), An investigation of terrain effects on the mesoscale spectrum of atmospheric motions, *J. Atmos. Sci.*, 44(20), 3087–3096. [19](#)
- Pallamraju, D., U. Das, and S. Chakrabarti (2010), Short-and long-timescale thermospheric variability as observed from OI 630.0 nm dayglow emissions from low latitudes, *J. Geophys. Res.*, 115(A6), doi:10.1029/2009JA015042. [89](#), [115](#)
- Pallamraju, D., et al. (2014), Daytime wave characteristics in the mesosphere lower thermosphere region: Results from the Balloon-borne Investigations of Regional-atmospheric Dynamics experiment, *J. Geophys. Res.*, 119(3), 2229–2242, doi:10.1002/2013JA019368. [4](#), [54](#)
- Pancheva, D., et al. (2008), Planetary wave coupling (5–6-day waves) in the low-latitude atmosphere–ionosphere system, *J. Atmos. Solar Terr. Phys.*, 70(1), 101–122. [128](#)
- Pendleton, W., P. Espy, and M. Hammond (1993), Evidence for non-local-thermodynamic-equilibrium rotation in the OH nightglow, *J. Geophys. Res.*, 98(A7), 11,567–11,579. [62](#)
- Pertsev, N., and V. Perminov (2008), Response of the mesopause airglow to solar activity inferred from measurements at Zvenigorod, Russia, *Ann. Geophys.*, 26(5), 1049–1056. [104](#)

- Pfister, L., W. Starr, R. Craig, M. Loewenstein, and M. Legg (1986), Small-scale motions observed by aircraft in the tropical lower stratosphere: Evidence for mixing and its relationship to large-scale flows, *J. Atmos. Sci.*, *43*(24), 3210–3225. [20](#)
- Phadke, K. A., R. Narayanan, R. P. Singh, and D. Pallamraju (2014), An Automated CCD-based Multi-wavelength Airglow Photometer (CMAP) for Optical Aeronomy Studies, *PRL Tech. Note, PRL-TN-2014-107*. [69](#), [134](#), [203](#)
- Piani, C., D. Durran, M. Alexander, and J. Holton (2000), A numerical study of three-dimensional gravity waves triggered by deep tropical convection and their role in the dynamics of the QBO, *J. Atmos. Sci.*, *57*(22), 3689–3702. [20](#)
- Pitteway, M., and C. Hines (1963), The viscous damping of atmospheric gravity waves, *Can. J. Phys.*, *41*(12), 1935–1948. [153](#)
- Prakash, S., B. Subbaraya, and S. Gupta (1972), Rocket measurements of ionization irregularities in the equatorial ionosphere at Thumba & identification of plasma instabilities, *Ind. J. Radio and Space Phys.*, *1*, 72–80. [35](#)
- Pramitha, M., M. Venkat Ratnam, A. Taori, B. Krishna Murthy, D. Pallamraju, and S. Vijaya Bhaskar Rao (2015), Evidence for tropospheric wind shear excitation of high-phase-speed gravity waves reaching the mesosphere using the ray-tracing technique, *Atmos. Chem. Phys.*, *15*(5), 2709–2721. [135](#)
- Press, W. H., and G. B. Rybicki (1989), Fast algorithm for spectral analysis of unevenly sampled data, *Astrophys. J.*, *338*, 277–280. [80](#), [81](#)
- Ramesh, K., S. Sridharan, and S. Vijaya Bhaskara Rao (2013), Dominance of chemical heating over dynamics in causing a few large mesospheric inversion layer events during January–February 2011, *J. Geophys. Res.*, *118*(10), 6751–6765. [31](#), [158](#)

- Rapp, M., B. Strelnikov, A. Müllemann, F.-J. Lübken, and D. Fritts (2004), Turbulence measurements and implications for gravity wave dissipation during the MaCWAVE/MIDAS rocket program, *Geophys. Res. Lett.*, *31*(24). [35](#)
- Reddi, C. R. (1998), Middle atmospheric dynamics, *Proc. Ind. Nat. Sc. Acad.*, *64*(A(3)), 289–301. [13](#)
- Reed, R. J. (1966), Zonal wind behavior in the equatorial stratosphere and lower mesosphere, *J. Geophys. Res.*, *71*(18), 4223–4233. [25](#)
- Reid, I. M., A. J. Spargo, and J. M. Woithe (2014), Seasonal variations of the nighttime  $O(^1S)$  and  $OH(8-3)$  airglow intensity at Adelaide, Australia, *J. Geophys. Res.*, *119*(11), 6991–7013. [110](#)
- Remsberg, E., et al. (2008), Assessment of the quality of the Version 1.07 temperature-versus-pressure profiles of the middle atmosphere from TIMED/SABER, *J. Geophys. Res.*, *113*(D17). [77](#)
- Remsberg, E. E., P. P. Bhatt, and L. E. Deaver (2002), Seasonal and longer-term variations in middle atmosphere temperature from HALOE on UARS, *J. Geophys. Res.*, *107*(D19). [25](#)
- Richter, J. H., F. Sassi, and R. R. Garcia (2010), Toward a physically based gravity wave source parameterization in a general circulation model, *J. Atmos. Sci.*, *67*(1), 136–156. [8](#)
- Rienecker, M. M., et al. (2011), MERRA: NASA’s Modern-Era Retrospective analysis for Research and Applications, *J. climate*, *24*(14), 3624–3648. [78](#)
- Russell III, J. M., M. G. Mlynczak, L. L. Gordley, J. Tansock, and R. Esplin (1999), An overview of the SABER experiment and preliminary calibration results, in *Proc. SPIE*, 3756, pp. 277–288. [76](#), [174](#)

- Salby, M. L. (1981), Rossby normal modes in nonuniform background configurations. Part I: Simple fields, *J. Atmos. Sci.*, *38*(9), 1803–1826. [128](#)
- Salby, M. L. (1996), *Fundamentals of atmospheric physics, International geophysics series*, vol. 61, Academic Press, California. [23](#), [24](#)
- Salby, M. L., D. L. Hartmann, P. L. Bailey, and J. C. Gille (1984), Evidence for equatorial Kelvin modes in Nimbus-7 LIMS, *J. Atmos. Sci.*, *41*(2), 220–235. [23](#)
- Sarkhel, S., R. Sekar, D. Chakrabarty, and S. Sridharan (2010), A case study on the possible altitude-dependent effects of collisions on sodium airglow emission, *J. Geophys. Res.*, *115*(A10). [41](#)
- Sasi, M., and B. Krishna Murthy (1990), Diurnal and semidiurnal tides in the middle atmosphere over Balasore (21.5 N, 86.9 E), *J. Atmos. Sci.*, *47*(17), 2101–2107. [22](#)
- Sasi, M., G. Ramkumar, and V. Deepa (1998), Nonmigrating diurnal tides in the troposphere and lower stratosphere over Gadanki (13.5°N, 79.2°E), *J. Geophys. Res.*, *103*(D16), 19,485–19,494. [22](#)
- Sasi, M., G. Ramkumar, and V. Deepa (2001), Tidal wind oscillations in the tropical lower atmosphere as observed by Indian MST Radar, *Ann. Geophys.*, *19*(8), 991–999. [22](#)
- Sasi, M., G. Ramkumar, and B. K. Murthy (2005), Studies on equatorial waves over the Indian zone, *Curr. Sci.*, *89*(3), 475–487. [128](#)
- Sato, K. (1992), Vertical wind disturbances in the afternoon of mid-summer revealed by the MU radar, *Geophys. Res. Lett.*, *19*(19), 1943–1946. [20](#)
- Sato, K. (1993), Small-scale wind disturbances observed by the MU radar during the passage of Typhoon Kelly, *J. Atmos. Sci.*, *50*(4), 518–537. [20](#)



- Savigny, C. v., I. McDade, K.-U. Eichmann, and J. Burrows (2012), On the dependence of the OH\* Meinel emission altitude on vibrational level: SCIAMACHY observations and model simulations, *Atmos. Chem. Phys.*, *12*(18), 8813–8828. [171](#)
- Scargle, J. D. (1982), Studies in astronomical time series analysis. II-Statistical aspects of spectral analysis of unevenly spaced data, *Astrophys. J.*, *263*, 835–853. [80](#), [107](#), [116](#)
- Scheer, J., E. Reisin, and C. Mandrini (2005), Solar activity signatures in mesopause region temperatures and atomic oxygen related airglow brightness at El Leoncito, Argentina, *J. Atmos. Solar Terr. Phys.*, *67*(1), 145–154. [104](#)
- Schlapp, R. (1937), Fine Structure in the  $^3\Sigma$  Ground State of the Oxygen Molecule, and the Rotational Intensity Distribution in the Atmospheric Oxygen Band, *Phys. Rev.*, *51*(5), 342–345. [64](#)
- Schulz, M., and M. Mudelsee (2002), REDFIT: estimating red-noise spectra directly from unevenly spaced paleoclimatic time series, *Computers & Geosciences*, *28*(3), 421–426. [84](#), [89](#), [90](#), [91](#), [115](#), [142](#)
- Sharma, S., H. Chandra, G. Beig, P. Kumar, and R. Vaishnav (2016), Investigations of mesospheric temperature inversions over sub-tropical location using lidar and satellites measurements, *J. Atmos. Solar Terr. Phys.*, *138*, 54–65. [31](#)
- Sheese, P., E. Llewellyn, R. Gattinger, A. Bourassa, D. Degenstein, N. Lloyd, and I. McDade (2010), Temperatures in the upper mesosphere and lower thermosphere from OSIRIS observations of  $O_2$  A-band emission spectra, *Can. J. Phys.*, *88*(12), 919–925. [77](#)
- Sheese, P., E. Llewellyn, R. Gattinger, and K. Strong (2014), OH Meinel band

- nightglow profiles from OSIRIS observations, *J. Geophys. Res.*, *119*(19).  
[171](#)
- Shepherd, T. G. (2000), The middle atmosphere, *J. Atmos. Solar Terr. Phys.*,  
*62*(17), 1587–1601. [4](#)
- Shimizu, A., and T. Tsuda (1997), Characteristics of Kelvin waves and grav-  
ity waves observed with radiosondes over Indonesia, *J. Geophys. Res.*,  
*102*(D22), 26,159–26,171. [20](#)
- Shiokawa, K., et al. (2007), Development of airglow temperature photometers  
with cooled-CCD detectors, *Earth, planets and space*, *59*(6), 585–599. [61](#)
- Singh, R., P. Thapliyal, C. Kishtawal, P. Pal, and P. Joshi (2007), A new  
technique for estimating outgoing longwave radiation using infrared window  
and water vapor radiances from Kalpana very high resolution radiometer,  
*Geophys. Res. Lett.*, *34*(23). [78](#)
- Singh, R. P., and D. Pallamraju (2015), On the latitudinal distribution of  
mesospheric temperatures during sudden stratospheric warming events, *J.*  
*Geophys. Res.*, *120*(4), 2926–2939, doi:10.1002/2014JA020355. [68](#), [202](#)
- Singh, R. P., and D. Pallamraju (2016), Effect of cyclone Nilofar on meso-  
spheric wave dynamics as inferred from optical nightglow observations from  
Mount Abu, India, *J. Geophys. Res.*, *121*(6), 5856–5867, doi:10.1002/  
2016JA022412. [20](#), [107](#), [114](#), [115](#), [121](#), [200](#)
- Singh, R. P., and D. Pallamraju (2017a), Near InfraRed Imaging Spectrograph  
(NIRIS) for ground-based mesospheric  $OH(6 - 2)$  and  $O_2(0 - 1)$  intensity  
and temperature measurements, *J. Earth Sys. Sci.*, *126*(88), doi:10.1007/  
s12040-017-0865-4. [xvi](#), [50](#), [89](#), [105](#), [134](#), [201](#), [202](#)
- Singh, R. P., and D. Pallamraju (2017b), Large-and small-scale period-  
icities in the mesosphere as obtained from variations in  $O_2(0 - 1)$  and

- OH*(6 – 2) nightglow emissions, *Ann. Geophys.*, 35(2), 227–237, doi:10.5194/angeo-35-227-2017. [20](#), [199](#), [200](#)
- Sinha, H., and S. Prakash (1996), Electron densities in the equatorial lower ionosphere over Thumba and SHAR, *Adv. Space Res.*, 18(6), 311–318. [35](#)
- Siskind, D., L. Coy, and P. Espy (2005), Observations of stratospheric warmings and mesospheric coolings by the TIMED SABER instrument, *Geophys. Res. Lett.*, 32(9). [167](#)
- Siskind, D., S. Eckermann, J. P. McCormack, L. Coy, K. W. Hoppel, N. L. Baker, et al. (2010), Case studies of the mesospheric response to recent minor, major, and extended stratospheric warmings, *J. Geophys. Res.*, 115(D3). [30](#)
- Sivakandan, M., I. Paulino, A. Taori, and K. Niranjana (2016), Mesospheric gravity wave characteristics and identification of their sources around spring equinox over Indian low latitudes, *Atmos. Meas. Tech.*, 9(1), 93–102. [114](#)
- Slanger, T. G., et al. (2005), Variability of the mesospheric nightglow sodium D2/D1 ratio, *J. Geophys. Res.*, 110(D23). [41](#)
- Smith, A. K. (2012a), Global dynamics of the MLT, *Surv. Geophys.*, 33(6), 1177–1230. [xv](#), [8](#), [9](#), [10](#), [11](#)
- Smith, A. K. (2012b), Interactions between the lower, middle and upper atmosphere, *Space Sci. Rev.*, 168(1), 1–21. [4](#)
- Smith, A. K., R. R. Garcia, D. R. Marsh, and J. H. Richter (2011), WACCM simulations of the mean circulation and trace species transport in the winter mesosphere, *J. Geophys. Res.*, 116(D20), doi:10.1029/2011JD016083. [8](#)
- Sridharan, S., K. Raghunath, S. Sathishkumar, and D. Nath (2010), First results of warm mesospheric temperature over Gadanki (13.5°N, 79.2°E) dur-

- ing the sudden stratospheric warming of 2009, *J. Atmos. Solar Terr. Phys.*, *72*(14), 1139–1146. [167](#)
- Suzuki, S., K. Shiokawa, Y. Otsuka, T. Ogawa, K. Nakamura, and T. Nakamura (2007), A concentric gravity wave structure in the mesospheric airglow images, *J. Geophys. Res.*, *112*(D2). [20](#)
- Suzuki, S., S. Vadas, K. Shiokawa, Y. Otsuka, S. Kawamura, and Y. Murayama (2013), Typhoon-induced concentric airglow structures in the mesopause region, *Geophys. Res. Lett.*, *40*(22), 5983–5987. [131](#)
- Swenson, G., R. Haque, W. Yang, and C. Gardner (1999), Momentum and energy fluxes of monochromatic gravity waves observed by an OH imager at Starfire Optical Range, New Mexico, *J. Geophys. Res.*, *104*(D6), 6067–6080. [20](#)
- Taori, A., M. J. Taylor, and S. Franke (2005), Terdiurnal wave signatures in the upper mesospheric temperature and their association with the wind fields at low latitudes (20°N), *J. Geophys. Res.*, *110*(D9). [61](#)
- Taori, A., N. Dashora, K. Raghunath, J. Russell, and M. G. Mlynczak (2011), Simultaneous mesosphere-thermosphere-ionosphere parameter measurements over Gadanki (13.5°N, 79.2°E): First results, *J. Geophys. Res.*, *116*(A7). [62](#)
- Taylor, M. J., and M. Hapgood (1988), Identification of a thunderstorm as a source of short period gravity waves in the upper atmospheric nightglow emissions, *Planet. Space Sci.*, *36*(10), 975–985. [20](#), [131](#)
- Taylor, M. J., P. Espy, D. Baker, R. Sica, P. Neal, and W. Pendleton (1991), Simultaneous intensity, temperature and imaging measurements of short period wave structure in the OH nightglow emission, *Planet. Space Sci.*, *39*(8), 1171–1188. [121](#)

- Taylor, M. J., W. Pendleton, S. Clark, H. Takahashi, D. Gobbi, and R. Goldberg (1997), Image measurements of short-period gravity waves at equatorial latitudes, *J. Geophys. Res.*, *102*(D22), 26,283–26,299. [20](#), [114](#)
- Taylor, M. J., W. Pendleton, C. Gardner, et al. (1999), Comparison of terdiurnal tidal oscillations in mesospheric OH rotational temperature and Na lidar temperature measurements at mid-latitudes for fall/spring conditions, *Earth, planets and space*, *51*(7-8), 877–885. [61](#), [62](#)
- Teitelbaum, H., and F. Vial (1991), On tidal variability induced by nonlinear interaction with planetary waves, *J. Geophys. Res.*, *96*(A8), 14,169–14,178. [128](#)
- Tepley, C., R. Burnside, and J. Meriwether (1981), Horizontal thermal structure of the mesosphere from observations of OH (8-3) band emissions, *Planet. Space Sci.*, *29*(11), 1241–1249. [121](#)
- Thorne, A., U. Litzén, and S. Johansson (1999), *Spectrophysics: principles and applications*, Springer-Verlag, Berlin, Heidelberg. [71](#)
- Torr, M. R., D. Torr, and R. Laher (1985), The  $O_2$  atmospheric 0-0 band and related emissions at night from Spacelab 1, *J. Geophys. Res.*, *90*(A9), 8525–8538. [40](#)
- Torrence, C., and G. P. Compo (1998), A practical guide to wavelet analysis, *Bull. Amer. Meteor. Soc.*, *79*(1), 61–78. [80](#), [85](#), [86](#), [87](#), [95](#)
- Tsuda, T., Y. Murayama, H. Wiryosumarto, S. W. B. Harijono, and S. Kato (1994), Radiosonde observations of equatorial atmosphere dynamics over Indonesia: 1. Equatorial waves and diurnal tides, *J. Geophys. Res.*, *99*(D5), 10,491–10,505. [20](#)
- Turnbull, D., and R. Lowe (1989), New hydroxyl transition probabilities and their importance in airglow studies, *Planet. Space Sci.*, *37*(6), 723–738. [63](#)

- Vadas, S., J. Yue, and T. Nakamura (2012), Mesospheric concentric gravity waves generated by multiple convective storms over the North American Great Plain, *J. Geophys. Res.*, *117*(D7). [20](#)
- Vadas, S. L., J. Yue, C.-Y. She, P. A. Stamus, and A. Z. Liu (2009), A model study of the effects of winds on concentric rings of gravity waves from a convective plume near Fort Collins on 11 May 2004, *J. Geophys. Res.*, *114*(D6). [20](#)
- Venkat Ratnam, M., A. Patra, and B. Krishna Murthy (2010), Tropical mesopause: Is it always close to 100 km?, *J. Geophys. Res.*, *115*(D6). [158](#)
- Vincent, R. (1993), Long-period motions in the equatorial mesosphere, *J. Atmos. Solar Terr. Phys.*, *55*(7), 1067–1080. [128](#)
- Vincent, R., and I. Reid (1983), HF Doppler measurements of mesospheric gravity wave momentum fluxes, *J. Atmos. Sci.*, *40*(5), 1321–1333. [20](#)
- Vincent, R., S. Kovalam, D. Fritts, and J. Isler (1998), Long-term MF radar observations of solar tides in the low-latitude mesosphere: Interannual variability and comparisons with the GSWM, *J. Geophys. Res.*, *103*(D8), 8667–8683. [22](#), [34](#)
- Vincent, R. A. (2015), The dynamics of the mesosphere and lower thermosphere: a brief review, *Progress in Earth and Planetary Science*, *2*(1), 4, doi:10.1186/s40645-015-0035-8. [4](#)
- Walterscheid, R., G. Sivjee, and R. Roble (2000), Mesospheric and lower thermospheric manifestations of a stratospheric warming event over Eureka, Canada (80°N), *Geophys. Res. Lett.*, *27*(18), 2897–2900. [30](#), [167](#)
- Whiteway, J. A., and A. I. Carswell (1994), Rayleigh lidar observations of thermal structure and gravity wave activity in the high Arctic during a stratospheric warming, *J. Atmos. Sci.*, *51*(21), 3122–3136. [30](#)

- Widdel, H. (1985), Foil clouds as a tool for measuring wind structure and irregularities in the lower thermosphere (92–50 km), *Radio Sci.*, *20*(4), 803–812. [35](#)
- Wiens, R., and G. Weill (1973), Diurnal, annual and solar cycle variations of hydroxyl and sodium nightglow intensities in the Europe-Africa sector, *Planet. Space Sci.*, *21*(6), 1011–1027. [104](#)
- Wrasse, C., et al. (2006), Mesospheric gravity waves observed near equatorial and low? middle latitude stations: wave characteristics and reverse ray tracing results, *Ann. Geophys.*, *24*(12), 3229–3240. [20](#)
- Wu, D., P. Hays, and W. Skinner (1994), Observations of the 5-day wave in the mesosphere and lower thermosphere, *Geophys. Res. Lett.*, *21*(24), 2733–2736. [23](#)
- Wu, Q., and T. Killeen (1996), Seasonal dependence of mesospheric gravity waves (<100 km) at Peach Mountain Observatory, Michigan, *Geophys. Res. Lett.*, *23*(17), 2211–2214. [xviii](#), [122](#), [123](#)
- Yue, J., et al. (2009), Concentric gravity waves in the mesosphere generated by deep convective plumes in the lower atmosphere near Fort Collins, Colorado, *J. Geophys. Res.*, *114*(D6). [xviii](#), [20](#), [131](#), [132](#)
- Yue, J., L. Hoffmann, and M. Joan Alexander (2013), Simultaneous observations of convective gravity waves from a ground-based airglow imager and the AIRS satellite experiment, *J. Geophys. Res.*, *118*(8), 3178–3191. [20](#)
- Yue, J., S. D. Miller, L. Hoffmann, and W. C. Straka (2014), Stratospheric and mesospheric concentric gravity waves over tropical cyclone Mahasen: Joint AIRS and VIIRS satellite observations, *J. Atmos. Solar Terr. Phys.*, *119*, 83–90. [20](#), [154](#)

